

Advanced Techniques in Optical Diffraction Tomography

Présentée le 28 juillet 2022

Faculté des sciences et techniques de l'ingénieur
Laboratoire d'optique
Programme doctoral en génie électrique

pour l'obtention du grade de Docteur ès Sciences

par

Ahmed Bassam SAYED AYOUB MOHAMED EMAM

Acceptée sur proposition du jury

Prof. M. Unser, président du jury
Prof. D. Psaltis, directeur de thèse
Prof. L. Tian, rapporteur
Dr P. Ferraro, rapporteur
Prof. C. Moser, rapporteur

Acknowledgements

I would like to thank Prof. Demetri Psaltis, without whom I would have never reached that moment. With his priceless guidance and motivation I was able to learn many things and conduct research at EPFL. He has greatly inspired me both on the scientific and the personal level which made me always feel the warmth of a family and that he will be always there for me to help whenever needed.

In addition, I would like to thank the members of the Jury committee; Prof. Michael Unser, Prof. Moser, Prof. Ferrao, and Prof. Lei Tian. The discussion we had during the private thesis defense was very insightful and helped me improve the thesis and gain more understanding about the different topics I worked on.

I would like also to thank the group members who were always kind and willing to help whenever needed. Despite being from different culture, we always find a way to remove the barriers and act as one.

Within the group members, I would like to thank particularly, the lab alumni, Alexandre Goy who helped me a lot in understanding many of the theoretical and the experimental aspects of my work.

In addition, I would like to thank Elizabeth Antoine who helped me a lot in sample preparation and cell culture techniques which I always needed to know while performing experiments.

Last but not least, I would like to thank Joowon lim who I closely worked with during my PhD and helped me understand many of the computational aspects within our research group.

Special thanks goes to Prof. Micheal Unser (biomedical imaging group) and Prof. Harm-Anton Klok (polymers group) for their collaborations. In particular I thank Than-An Pham of the biomedical imaging lab and Tanja Thomsen of the polymers lab for the time we spent on projects to help making the best out of those collaborations.

Finally, I thank my family for bearing up with me along my journey in academia. In particular, I would like to thank my father who raised me with the love of reading and curiosity to always learn more and more. May he rest in peace and may God reward him with the best.

At the end, I thank my lovely wife, Doaa, for being the greatest support in my life. With her I always felt the confidence and the will to continue even in the darkest of times, I owe her everything I achieved and will achieve in the future. God bless her!

Lausanne, February 2022

Abstract

Optical microscopy has been widely used in various fields and especially for biomedical applications. Optical Diffraction tomography (ODT) is a branch of optical microscopy that can be used for quantitative 3D imaging of different samples including biological samples (i.e. cells, tissues) with a label-free, non-invasive approach. The quantitative measure of the 3D reconstruction is referred to as the refractive index which is a distinct property for each material and is cross-linked to the dry mass of biological samples. Being a label-free imaging technique, ODT can be used in diverse studies including immune cells drug delivery applications, red blood cells monitoring and characterization, and live imaging of different samples including human tissues and c-elegans. By changing the angle of illumination of the incident light beam and acquiring intensity and/or holographic measurements for the sample through a limited numerical aperture (NA) imaging system, the 3D shape of the sample can be estimated.

The limited-NA imaging system usually results in the so called “missing cone problem”, where the cone refers to the missing spectral frequencies that are not collected by the limited-NA imaging system which forms a cone-like shape. This “missing cone problem” usually results in an elongation along the optical axis. In addition, the missing cone problem is always accompanied with an underestimation of the 3D refractive index reconstruction which generally degrades the reconstruction quality. Another challenge in ODT is the common need for holographic measurements and phase unwrapping algorithms to reconstruct the 3D refractive index of the sample. While holographic systems could be easy to implement, phase unwrapping could be a serious problem for highly wrapped samples and the vulnerability of the phase unwrapping algorithms to any speckle noise introduced by the highly coherent laser beam.

As mentioned above, the typical approach for 3D reconstruction is to spatially scan the illumination incident k-vectors by the use of galvo-mirrors or the use of spatial light modulators (SLM) which have a better mechanical stability as compared to galvo-mirrors since there is no moving parts. On the other hand, SLMs usually suffer from low frame rate and thus can be hardly used for high-speed live imaging. Another approach is to use digital micro-mirror devices (DMDs) which are much faster than SLMs but suffer from being binary switches (i.e. on/off). The use of time-multiplexing techniques can be a solution for getting greyscale-images (i.e. sinusoidal grating as in structured illumination microscopy) which results in better reconstructions. However, time-multiplexing lowers the speed of DMDs by a factor of 256 for 8-bit greyscale images.

In this thesis, we study the different challenges described above. First, we study different reconstruction techniques and assess the fidelity of each reconstruction results by means of structured illumination and phase conjugation. By reconstructing the 3D refractive index of the sample using different algorithms (i.e. Born, Rytov, and Radon) and then perform a numerical back-propagation of experimentally measured structured illumination pattern we are able to assess the fidelity of each reconstruction algorithms without prior information about the 3D RI distribution of the sample.

The second part of the thesis is concerned with the 3D reconstruction of samples using intensity-only measurements which the need to holographically acquire them. We show that using intensity-only measurements, we could still be able to reconstruct the 3D volume of the sample with edge-enhanced effects which was proven useful for drug delivery applications in which nano-particles were identified on the cell membrane of immune T-cells in a drug delivery studies. Such reconstruction technique would result in more robust imaging system where the commercial imaging microscope systems can be incorporated with LEDs for high-quality speckle noise-free imaging systems. In addition, we show that under certain conditions, we can be able to reconstruct the 3D refractive index distribution of different samples.

The third part of the thesis is contributing to high-speed complex wave-front shaping using DMDs. In that part, new modulation technique is demonstrated that can boost the speed of the current time-multiplexing techniques by a factor of 32. The modulation technique is based on amplitude modulation where an amplitude modulator is synchronized with

the DMD to modulate the intensity of each bit-plane of an 8-bit image and then all the modulated bit-planes are linearly added on the detector. Such modulation technique can be used not only for structured illumination microscopy but also for high-speed 3D printing applications as well as projectors.

The last part is concerned with using deep learning approaches to solve the missing cone problem usually accompanied with optical imaging due to the limited numerical aperture of the imaging system. Two techniques are discussed; the first is based on using a physical model to enhance the quality of the 3D RI reconstruction and the second is based on using deep neural network to solve the missing cone problem.

Keywords

Optical diffraction tomography, 3D refractive index reconstruction, structured illumination, intensity-only measurements, spatial light modulation

Résumé

La microscopie optique a été largement utilisée dans divers domaines et notamment pour des applications biomédicales. La tomographie par diffraction optique (ODT) est une branche de la microscopie optique qui peut être utilisée pour l'imagerie 3D quantitative de différents échantillons, y compris des échantillons biologiques (c'est-à-dire des cellules, des tissus) avec une approche non invasive et sans marquage. La mesure quantitative de la reconstruction 3D est appelée indice de réfraction avec une propriété distincte pour chaque matériau et est réticulée à la masse sèche des échantillons biologiques. Étant une technique d'imagerie sans marquage, l'ODT peut être utilisé dans diverses études, y compris les applications d'administration de médicaments aux cellules immunitaires, la surveillance et la caractérisation des globules rouges et l'imagerie en direct de différents échantillons, y compris les tissus humains et les *c-elegans*. En modifiant l'angle d'éclairage du faisceau lumineux incident et en acquérant des mesures d'intensité et/ou holographiques pour l'échantillon via un système d'imagerie à ouverture numérique (NA) limitée, la forme 3D de l'échantillon peut être estimée.

Le système d'imagerie à NA limité entraîne généralement le « problème du cône manquant », où le cône fait référence aux fréquences spectrales manquantes qui ne sont pas collectées par le système d'imagerie à NA limité qui forme une forme de cône. Ce « problème de cône manquant » se traduit généralement par un allongement le long de l'axe optique. De plus, le problème du cône manquant s'accompagne toujours d'une sous-estimation de la reconstruction de l'indice de réfraction 3D qui dégrade généralement la qualité de la reconstruction. Un autre défi de l'ODT est le besoin commun de mesures holographiques et d'algorithmes de déroulement de phase pour reconstruire l'indice de réfraction 3D de l'échantillon. Alors que les systèmes holographiques pourraient être faciles à mettre en œuvre, le déroulement de phase pourrait être un problème sérieux pour les échantillons d'échantillons fortement enveloppés et la vulnérabilité des algorithmes de déroulement de phase à tout bruit de speckle introduit par le faisceau laser hautement cohérent.

Comme mentionné ci-dessus, l'approche typique pour la reconstruction 3D consiste à balayer spatialement les vecteurs k incidents d'éclairage à l'aide de galvo-miroirs ou à l'aide de modulateurs spatiaux de lumière (SLM) qui ont une meilleure stabilité mécanique par rapport aux galvo-mirrors puisque il n'y a pas de pièces mobiles. D'un autre côté, les SLM souffrent généralement d'une faible fréquence d'images et peuvent donc être difficilement utilisés pour l'imagerie en direct à haute vitesse. Une autre approche consiste à utiliser des dispositifs numériques à micro-miroir (DMD) qui sont beaucoup plus rapides que les SLM mais souffrent d'être des commutateurs binaires (c'est-à-dire marche/arrêt). L'utilisation de techniques de multiplexage temporel peut être une solution pour obtenir des images en niveaux de gris (c. Cependant, le multiplexage temporel réduit la vitesse des DMD d'un facteur 256 pour les images en niveaux de gris 8 bits.

Dans cette thèse, nous étudions les différents défis décrits ci-dessus. Tout d'abord, nous étudions différentes techniques de reconstruction et évaluons la fidélité de chaque résultat de reconstruction au moyen d'un éclairage structuré et d'une conjugaison de phase. En reconstruisant l'indice de réfraction 3D de l'échantillon à l'aide de différents algorithmes (c'est-à-dire Born, Rytov et Radon), puis en effectuant une rétro-propagation numérique du motif d'éclairage structuré mesuré expérimentalement, nous sommes en mesure d'évaluer la fidélité de chaque algorithme de reconstruction sans informations sur la distribution RI 3D de l'échantillon.

La deuxième partie de la thèse s'intéresse à la reconstruction 3D d'échantillons à l'aide de mesures d'intensité seule nécessitant de les acquérir holographiquement. Nous montrons qu'en utilisant uniquement des mesures d'intensité, nous pourrions encore être en mesure de reconstruire le volume 3D de l'échantillon avec des effets d'amélioration des bords, ce qui s'est avéré utile pour les applications d'administration de médicaments dans lesquelles des nanoparticules ont été identifiées sur la membrane cellulaire de la T-immunitaire cellule dans une étude d'administration de médicament. Une telle technique de reconstruction se traduirait par un système d'imagerie plus robuste où les systèmes de microscopes d'imagerie commerciaux peuvent être incorporés avec des LED pour des systèmes d'imagerie sans bruit de chatolement

Résumé

de haute qualité. De plus, nous montrons que sous certaines conditions, nous pouvons être en mesure de reconstruire la distribution 3D de l'indice de réfraction de différents échantillons.

La troisième partie de la thèse contribue à la mise en forme de front d'onde complexe à grande vitesse à l'aide de DMD. Dans cette partie, une nouvelle technique de modulation est démontrée qui peut augmenter la vitesse des techniques de multiplexage temporel actuelles par un facteur de 32. La technique de modulation est basée sur la modulation d'amplitude où un modulateur d'amplitude est synchronisé avec le DMD pour moduler l'intensité de chaque plan binaire d'une image à 8 bits, puis tous les plans binaires modulés sont ajoutés linéairement sur le détecteur. Une telle technique de modulation peut être utilisée non seulement pour la microscopie à illumination structurée, mais également pour les applications d'impression 3D à grande vitesse ainsi que pour les projecteurs.

La dernière partie concerne l'utilisation d'approches d'apprentissage en profondeur pour résoudre le problème du cône manquant généralement accompagné de l'imagerie optique en raison de l'ouverture numérique limitée du système d'imagerie. Deux techniques sont discutées; le premier est basé sur l'utilisation d'un modèle physique pour améliorer la qualité de la reconstruction RI 3D et le second est basé sur l'utilisation d'un réseau neuronal profond pour résoudre le problème du cône manquant.

Mots-clés

Tomographie par diffraction optique, 3D reconstruction d'indice de réfraction, éclairage structuré, mesures d'intensité uniquement, modulation spatiale de la lumière.

Contents

Acknowledgements ii

Abstract iv

Résumé vi

Chapter 1 Introduction..... 13

Chapter 2 Theory 23

2.1. Light Scattering from Inhomogeneous Media.....23

2.2. Optical Diffraction Tomography.....25

2.3. Direct-Inversion Models based on First-order approximation.....25

2.3.1.First-order Born approximation.....25

2.3.2.First-order Rytov approximation.....27

2.3.3.Phase unwrapping for Rytov approximation.....29

2.3.4.Validity of Born and Rytov approximations.....30

2.4. Filling in the K-space using the “Wolf Transform” in transmission.....31

2.5. 3D Refractive Index Reconstruction using Born and Rytov approximations.....33

2.6. Solving the missing cone problem with different imaging scenarios.....35

2.7. Diffraction-Less Optical Tomography (Back-projection algorithm).....40

**Chapter 3 A Method for Assessing the Fidelity of Optical Diffraction Tomography Reconstruction
Methods using Structured Illumination** 43

3.1. Introduction.....43

3.2. Materials and Methods.....45

3.2.1.Experimental setup and samples.....45

3.2.2.Propagation model.....46

3.2.3.Tomographic reconstruction methods.....47

3.3. Assessment results.....48

**Chapter 4 3D Reconstruction of weakly scattering objects from 2D intensity-only measurements
using the Wolf transform**..... 51

4.1. Introduction.....51

4.2. Principle.....52

4.3. Results.....55

4.4. Supplementary information.....58

4.4.1.Defining the modified scattering potential due to the intensity measurement.....58

4.4.2.Mapping of the twin image into 3D kappa space.....60

4.4.3.Effect of numerical aperture of the imaging lens (OBJ2) on the contribution of the twin image
to the 3D reconstruction.....64

Chapter 5 Optical Diffraction Tomography using nearly in-line Holography with broadband LED source.....	66
5.1. Introduction.....	66
5.2. Theory.....	67
5.3. Experimental setup and 3D RI reconstructions.....	70
5.4. Effect of misalignment on the reconstruction quality.....	74
5.5. ODT using wavelength diversity.....	75
Chapter 6 High speed, complex wavefront shaping using the digital micro-mirror device	79
6.1. Introduction.....	79
6.2. Methods.....	80
6.2.1.Complex wavefront shaping with DMD.....	80
6.2.2.Opto-electronic phase conjugation (OEPC) using DMD.....	82
6.3. Results.....	84
6.3.1.OEPC for diffracted pattern after passing through scattering media.....	84
6.3.2.Grayscale modulation using amplitude modulator synchronized with the DMD.....	85
6.4. Discussion.....	89
Chapter 7 High fidelity optical diffraction tomography of strongly scattering samples	93
7.1. Introduction	93
7.2. Results.....	95
7.2.1.Multiple cylinders by using Mie theory.....	96
7.2.2.RBC cluster using discrete dipole approximation.....	97
7.2.3.Cell phantom using discrete dipole approximation.....	99
7.2.4.Experimental validation using a yeast cell.....	100
7.2.5.Data compression demonstrated on experimental data—HCT116 cells.....	103
7.3. Discussion.....	104
7.4. Materials and Methods.....	105
7.4.1.Simulation.....	105
7.4.2.Experiments.....	106
7.4.3.Semisynthetic simulation.....	106
7.4.4.Reconstruction algorithm.....	106
7.4.5.Overall scheme of the learning tomography.....	107
7.4.6.Split-step non-paraxial method.....	107
7.5. Supplementary section.....	108
7.5.1.Split-step non-paraxial method.....	108
7.5.2.Numerical implementation.....	109
7.5.3.Calculation of the gradient.....	109
7.5.4.Experimental setup.....	110
7.5.5.Sample preparation.....	111
Chapter 8 Three-dimensional tomography of red blood cells using deep learning	112
8.1. Introduction.....	112
8.2. Main Idea.....	113
8.3. Method.....	117
8.3.1.Network Training.....	117
8.3.2.Experiment.....	118
8.4. Results.....	119
8.4.1.Synthetic Data.....	119

Contents

8.4.2.Experimental Data.....	121
8.5. Appendix A: Dataset Generation.....	122
8.6. Appendix B: Semisynthetic Simulation.....	123
 Chapter 9 Conclusion	125
 References	131
Curriculum Vitae.....	139

Chapter 1 Introduction

Optical imaging is extensively used in the investigation of different physical and biological phenomena including red blood cells morphology [1-2], cancer detection [3-4], and neuron imaging [5-7]. Compared to transmission electron microscopy and scanning electron microscopy, optical imaging is characterized by being a non-invasive imaging technique, and therefore is considered an important way for biological imaging causing minimal harm to various biological samples while being able to generate high quality images with sub-micron resolution. Owing to these characteristics, optical microscopy has a key role in biomedicine for diagnosis and treatment purposes [8, 9].

Optical imaging can be divided into 2 main branches; fluorescent and label-free imaging. Fluorescent imaging is widely used in biological and medical applications in which the fluorescent markers act as the contrast agents to identify different organelles within cells and/or tissues [10]. By selecting the appropriate dye, one can study the behavior of a specific organelle while suppressing the signal from other organelles. For example, 6-diamidino-2-phenylindole (DAPI) is commonly used for imaging the nucleus where it reaches the maximum efficiency when excited by light with wavelength between 354 nm and 362 nm while the maximum emission is reached at wavelengths between 458 nm and 462 nm. On the other hand, DASPMI (4-Di-1-ASP, D288) and DASPEI (D426) are commonly used for imaging mitochondria.

Optical scattering is governed by the morphology and the refractive index contrast between the sample of interest and the background. Optical scattering is closely related to the contrast of a microscopic image. Depending on how much a sample scatters the light, the contrast can be estimated especially for negligible absorption. Since most optical microscopes use visible light to image biological samples, the absorption is often negligible and only the scattering affects the image contrast. Weak scattering, as in the case of thin tissue slices and cellular imaging, will result in very weak image contrast and the sample is usually referred to as “phase object” since it affects significantly the phase of the incident field while the amplitude is almost the same. This makes it very hard to identify such samples in bright-field imaging mechanism. High contrast images can be recorded either by converting the phase of the sample to a phase-dependent intensity image or by directly measuring the phase of the sample. Intensity images are usually measured by using fluorescent-labels or phase contrast imaging introduced by Zernike [11].

Fluorescent imaging is very popular within the biomedical world especially for imaging of thin tissues which act like transparent objects and thus need a contrast agent to highlight the features inside the cells. However, fluorescent imaging still has some limitations. First, while providing images with high resolution, the images do not represent any quantitative measures of the sample including the dry mass of the samples which can be related to metabolic and cellular functionalities. Second, fluorescent imaging is usually associated with photo-bleaching which make it hard to be used for long-term imaging. Third, while some dyes are appropriate with live cells, many others require that the cells be fixed which limit the functionality of fluorescent imaging for live imaging purposes. In addition, when used with live cells, they can be photo-toxic which usually alters the morphology of the sample and affects its metabolic state.

A breakthrough to enhance the contrast of an intensity image occurred in the 1930s without the use of labelling dyes by Zernike. To understand the mechanism of operation of Zernike's phase contrast microscopy, let's assume the total field, U , as the sum of the incident field U_{in} and the scattered field from the sample under the microscope with the 2 fields interfering with each other in an on-axis interferometer configuration. For weak phase modulation, the total field can be expressed as [12]:

$$\begin{aligned} U(x, y) &= |U| e^{j\phi(x, y)} \approx U_{in} [1 + j\phi(x, y)] \\ \Rightarrow |U|^2 &= |U_{in}|^2 [1 + \phi^2] \approx |U_{in}|^2, \end{aligned} \quad (1.1)$$

where $\phi(x, y)$ is the phase delay map of a sample. As can be seen from equation 1.1, the intensity profile for such sample, denoted as, $|U|^2$, shows weak spatial modulation which results in negligible contrast.

To enhance the contrast of the intensity image, Zernike introduced additional $\pi/2$ phase shift between the scattered and the incident field using a phase mask. By doing so, the total field, U_{pc} (i.e. for phase contrast), is defined as:

$$\begin{aligned} U_{pc}(x, y) &= U_{in} \{j + j\phi(x, y)\} \\ \Rightarrow |U_{pc}|^2 &= |U_{in}|^2 [1 + \phi^2 + 2\phi] \approx |U_{in}|^2 [1 + 2\phi] \end{aligned} \quad (1.2)$$

Equation 1.2 shows that using a phase mask that introduce a $\pi/2$ phase shift and therefore the phase shifts are converted in intensity variations within the image which results in a better contrast.

As a continuation to on-axis interferometry, Gabor introduced the concept of in-line holography where he showed that the intensity image retrieved from the in-line holography is composed of an "in-focus" image in addition to an "out-of-focus" image [13]. Due to this "Twin" image problem, in-line holography usually encounters problems in order to retrieve the phase of the object. To solve this problem, 2 solutions were proposed. The first solution is to use phase-shifting interferometry by assuming that the intensity profile of an image is expressed as [14]:

$$I(x, y) = I_R + I_s(x, y) + 2\sqrt{I_R I_s(x, y)} \cos[\phi(x, y) + \phi_0], \quad (1.3)$$

where ϕ_0 denotes the phase shift between the reference and the scattered field. By tuning the phase shift between the 2 arms at $\phi_0 = 0, \pi/2, \pi, 3\pi/2$, one can solve for the phase of the sample $\phi(x, y)$ as expressed below:

$$I_0 = I_{\phi_0=0}(x, y) = I_R + I_s(x, y) + 2\sqrt{I_R I_s(x, y)} \cos[\phi(x, y)] \quad (1.4)$$

$$I_1 = I_{\phi_0=\pi/2}(x, y) = I_R + I_s(x, y) - 2\sqrt{I_R I_s(x, y)} \sin[\phi(x, y)] \quad (1.5)$$

$$I_2 = I_{\phi_0=\pi}(x, y) = I_R + I_s(x, y) - 2\sqrt{I_R I_s(x, y)} \cos[\phi(x, y)] \quad (1.6)$$

$$I_3 = I_{\phi_0=3\pi/2}(x, y) = I_R + I_s(x, y) + 2\sqrt{I_R I_s(x, y)} \sin[\phi(x, y)] \quad (1.7)$$

And eventually the phase will be given as:

$$\varphi(x, y) = \arg(I_3 - I_1, I_0 - I_2) = \tan^{-1} \frac{I_3 - I_1}{I_0 - I_2} \quad (1.8)$$

While this technique will retrieve the phase accurately, it has the disadvantage of increased time and energy consumption since 4 intensity measurements are needed for the phase retrieval.

The second solution was due to Upatnieks and Leith who proposed to use an off-axis interferometer which use spatial modulation instead of temporal modulation as in phase-shifting interferometry [15]. In this configuration, a small tilt is introduced between the reference arm and the sample arm which results in shifting in the Fourier domain the “out-of-focus” image with respect to the “in-focus” image and thus the phase extraction is done with only 1 intensity measurement which is expressed as:

$$I(x, y) = |U_R + U_t|^2 = |U_R|^2 + |U_t|^2 + U_R U_t^* + U_t U_R^*, \quad (1.9)$$

where $U_R = e^{j(k_x^r x + k_y^r y)}$ is defined by the angle tilt between the reference and the sample beam which translates into shift in the Fourier domain by (k_x^r, k_y^r) , U_t is the total field from the sample. Figure 1-1 shows an example of off-axis interferometry where the DC term ($|U_R|^2 + |U_t|^2$) is centered in the Fourier space while the +1 order ($U_R U_t^*$) and the -1 order ($U_t U_R^*$) are centered-symmetric around the origin.

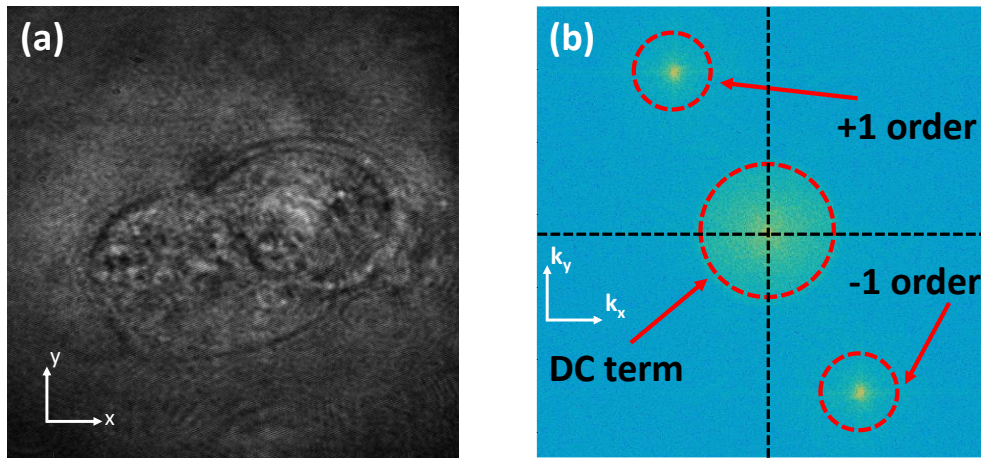


Figure 1-1. Off-axis holography. (a) Hologram of HCT116 cell. (b) Fourier transform of the sample showing the DC term, +1 order and the -1 order.

However, this speed enhancement comes at the expense of a limited space-and-width product. Depending on the field of interest, one should properly choose between phase-shifting or spatial-shifting interferometry to yield the best images of the sample of interest. Nowadays, the recording media (i.e. sensors) and image reconstruction techniques are digital and that is why the whole field is called “Digital Holography” [16]. Both interferometric techniques are generally referred to as quantitative phase imaging (QPI) which are widely used in many digital holographic microscopic systems (DHM) [17-18].

It should be mentioned that a proper selection of the tilt angle is needed to ensure complete isolation of the cross-terms with respect to the DC term and an accurate extraction of the complex field U_t . Given that the numerical aperture of the objective lens is equivalent to a circular low pass filter of

Introduction

radius B in the Fourier domain, we need to select the tilt angle to be large enough to isolate the desired term from the DC term to avoid any distortions in the extracted complex field. This can be estimated if we assumed the maximum coverage in the Fourier space as shown in Figure 1-2.

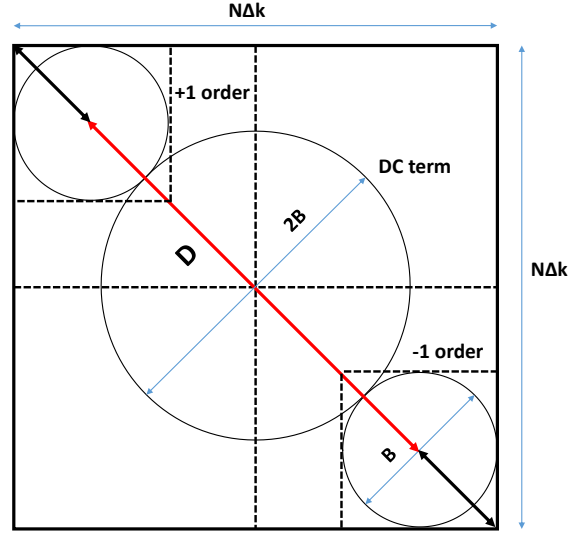


Figure 1-2. Fourier domain for best spectral coverage

From Figure 1-2, to ensure complete separation between the +1 order and the DC term, the reference tilt angle should satisfy the following condition:

$$|k^r| \geq \frac{3B}{2} \quad (1.10)$$

In addition, since for maximum coverage the x and y components of the k-vector should be the same to ensure maximum utilization of space bandwidth, then:

$$\frac{2\pi}{\lambda} \sin(\theta) \geq \frac{3B}{2\sqrt{2}} \quad (1.11)$$

And thus the minimum tilt angle along x and y of the reference beam with respect to the sample beam is given as:

$$\theta_{\min} = \sin^{-1} \frac{3B\lambda}{2\sqrt{2}2\pi} \quad (1.12)$$

On the other hand, the tilt angle should not exceed a certain limit such that the carrier frequency of the reference arm does not exceed Nyquist's limit where the maximum angle is given by:

$$\begin{aligned} \frac{\sin \theta}{\lambda} &\leq \frac{1}{2d} \\ \Rightarrow \theta &\leq \theta_{\max} = \sin^{-1} \frac{\lambda}{2d}, \end{aligned} \quad (1.13)$$

where d is the pixel size on the detector plane and λ is the wavelength of the light source.

Finally, we can identify an inequality for proper selection of the reference tilt angle along x and y axis as below:

$$\sin^{-1} \frac{3B\lambda}{2\sqrt{2}2\pi} \leq \theta \leq \sin^{-1} \frac{\lambda}{2d} \quad (1.14)$$

Having the knowledge on the tilt angle between the reference and the sample arm, we can shift the “-1 order” to the center of the Fourier domain, this is mathematically expressed as:

$$I(x, y)e^{j(k_x^r x + k_y^r y)} = I(x, y)U_R = |U_R|^2 U_R + |U_t|^2 U_R + U_R U_t^* U_R + U_t \quad (1.15)$$

Applying a low pass filter based on the numerical aperture of the objective lens followed by applying an inverse Fourier transform we can finally extract the complex field U_t from which we can obtain with the phase explicitly as shown in Figure 1-3.

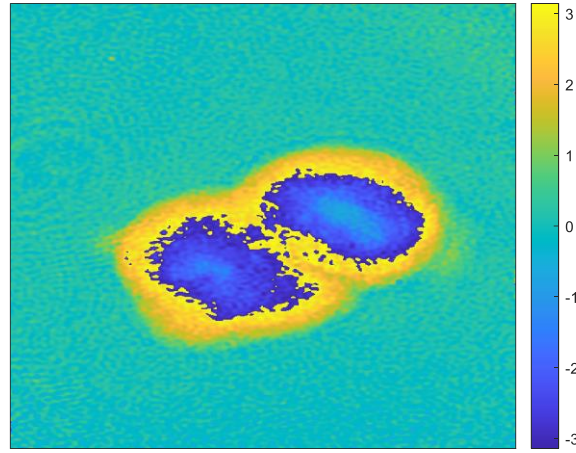


Figure 1-3. Phase extraction for the HCT116 cell shown in Fig. 1 after shifting and filtering the “-1 order”

It should be noted here that the phase shown in Figure 1-3 is wrapped and phase unwrapping will be necessary for correct characterization of the sample as will be shown later in the chapter.

While the complex field extraction shows the relative phase of the sample, it is not sufficient for full characterization of the sample. The phase map shown above is a result of the incident wave propagating through a complex structure and thus for fully recovering of the 3D refractive index map, we need to add another dimension in the data acquisition. This is usually done either by scanning rotating the sample or the rotating the illumination beam.

Sample rotation is used in micro-fluidic channels and optical tweezers, however it suffer from mechanical stability especially when dealing with biological samples. On the other hand, illumination rotation is widely used in tomographic imaging through galvo-mirrors, spatial light modulators (SLM), or digital micro-mirror devices (DMD). While galvo-mirror can be reach higher speed than SLMs, SLMs offer higher mechanical stability. On the other hand, the DMD has been presented as a promising candidate for high speed tomographic imaging based on structured illumination (SI) schemes.

On the other hand, illumination rotation scanning is more feasible for imaging biological samples. However, 3D reconstructions usually have anisotropic resolution with poor axial resolution as compared to lateral resolution which also results in 3D reconstructions suffering from the missing cone problem which results from the limited NA of the imaging objective lens. Figure 1-4 shows the complex field extracted for different illumination angles.

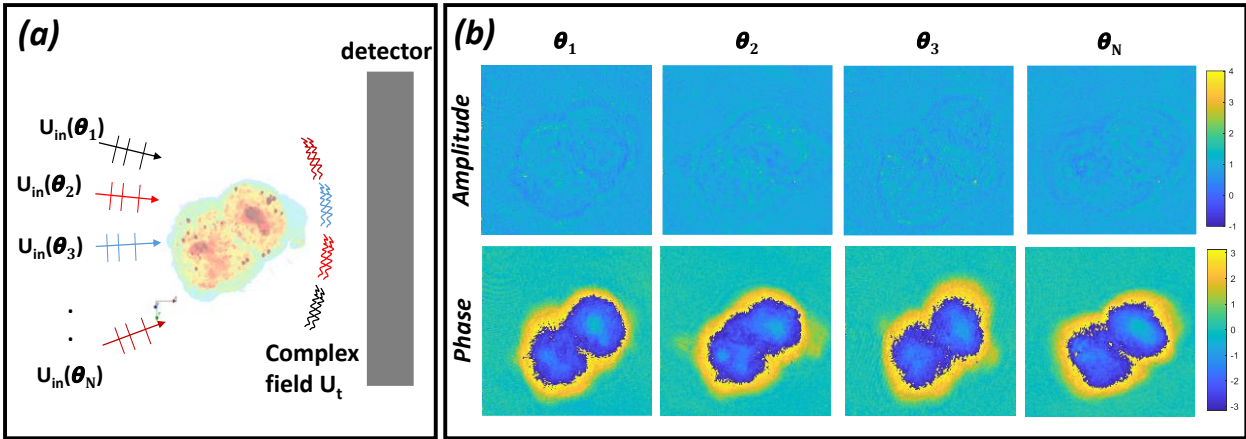


Figure 1-4. Complex field for an HCT116 cell at different illumination angles. As explained earlier, being a “phase object” the amplitude does not add any information while the phase shows high contrast. (a) shows a simplified schematic for the imaging process in which the illumination angle of the incident field is varied and the complex field is measured while (b) shows the complex field extracted from the holographic system.

To reconstruct the 3D RI distribution for a specific sample, we need to combine multiple 2D QPI projections that are acquired from different illumination angle as shown in Figure 1-4. We refer to this process as Optical diffraction tomography (ODT) [9, 12, 19-20]. ODT is capable of decoupling information concerning the morphology and the refractive index from the 2D QPI data without the need for labeling. In addition, the RI can provide information about the dry mass for different cellular organelles inside the cell/tissue and can provide information about the metabolic state and inter-cellular functionalities. However, before going to deep detail about the reconstruction process, we first need to highlight some critical aspects in understanding the optical scattering of samples and how the sample alters the illumination field after passing through it.

To understand the interaction between the optical field and the sample, we need to define a physical model that we usually refer to as the “Forward model” which actually solves Maxwell’s equations that govern the optical scattering within the medium given an incident field which we assume to be a plane wave with a certain illumination wave-vector. The main limitation for accurate solution of the Maxwell-equation is the fact that optical scattering is a non-linear function of the dielectric constant of the scattering medium. This makes it difficult to define a forward model that accurately defines such a non-linear relationship. One way to imagine such relation is to assume a situation where we have a cell phantom and measure the scattered field from this phantom. If we inserted a second, identical cell phantom along the propagation direction, the resulting scattered field would not be a linear summation of the two individual scattered fields. The reason for this is that for multiple scattering events, the scattered field from the first event is considered as the input illumination for the second scattering event and so forth as shown in Figure 1-5 [12].

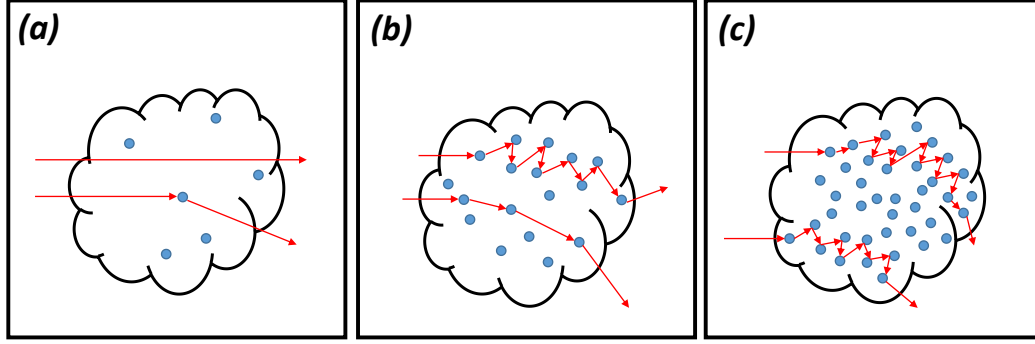


Figure 1-5. Scattering events within the sample for (a) weakly scattering, (b) intermediate scattering and (c) highly scattering samples

To make it easier to reconstruct the 3D RI distribution, it is common to neglect any non-linear effects within the sample and assume linear scattering models. This is usually referred to as weak-scattering model and is valid as long as the scattered field has much lower magnitude than the incident field. Depending on the imaging scheme, one can further neglect the effect of diffraction as would be the case in X-ray computed tomography (CT) where the operating wavelength of the light beam is much smaller than the physical dimensions of the sample being imaged (i.e. human body or complete organs) [21]. However, this is not the case when imaging micro-scale samples in which the wavelength of the visible light is comparable to the physical dimensions of the sample of interest. In that case diffraction should be accounted for. We usually refer to such a model that accounts for diffraction but neglects multiple scattering events as the Wolf transform in which various 2D fields are mapped into the 3D Fourier space for the 3D RI distribution to be reconstructed [12, 19].

The Wolf transform relates the 2D measurements into the 3D frequency space by mapping each 2D field with the corresponding illumination. The k-vectors of the angular spectrum of each 2D measurement is represented as a spherical cap in the 3D Fourier domain governed by the relation:

$$k_z = \sqrt{k^2 - k_x^2 - k_y^2} \text{ assuming coherent illumination with } k = \frac{2\pi}{\lambda} n_0 \text{ where } \lambda \text{ is the wavelength of the}$$

coherent illumination, n_0 is the refractive index of the surrounding medium and (k_x, k_y, k_z) are the coordinates of the k-space. Each spherical cap occupies a different position in the 3D frequency domain depending on the illumination k-vectors (k_x^{in}, k_y^{in}) . In this way the recorded fields will form the limited-NA 3D scattering potential from which we can estimate the 3D spatial distribution of the RI by taking the 3D Fourier transform of the measured 3D spectrum. The process of RI reconstruction, however, holds many challenges and difficulties.

The first problem is inherent and is referred to as the missing cone problem. In order to fully recover the 3D information of the sample, one would need to capture the scattered field from the sample in 360 degrees. However, due to the limited numerical aperture (NA) of the illumination and imaging objective lenses, we are able to only capture the scattered fields that make it through the NA of the objective lens. As a result, the 3D RI reconstruction does not reflect the true RI distribution of the sample. The missing cone problem not only results in under-estimation of the RI but it also results in elongation along the optical axis (i.e. for illumination rotation). If instead of rotating the angle of the illuminating beam we rotate the sample, the missing frequency information along the rotation axis results in the “missing apple core”.

The second problem involved with conventional 3D RI reconstruction is the need for 2D QPI data. In other words, the need for holographic imaging systems. While holographic systems offer access to the complex field (i.e. amplitude and phase), they do suffer from critical problems. The first

problem is the speckle noise introduced with coherent detection which might affect the quality of the 3D reconstruction due to the limited signal to noise ratio (SNR). Another problem is related to phase stability which is related to any laser or mechanical fluctuations which can be fixed by recording holograms without the sample which shall correct to any phase drift but can be time consuming.

Another problem is more related to 3D live imaging. Current technologies usually suffer in terms of speed of the scanning devices that are available, typically Galvo-mirrors, SLM and DMDs. While galvo-mirrors are widely used in ODT, they usually suffer from the mechanical stability and can thus affect the quality of the 3D RI reconstruction. On the other hand, SLMs offer much better mechanical stability. However, this comes at the expense of the modulation speed of the SLM to generate plane waves with different illumination k-vectors. Recently, DMD has been increasingly used in ODT applications in a structured illumination scheme. While DMD offers high mechanical stability and also high “amplitude” modulation speed, to incorporate the DMD into structured illumination scheme, time-multiplexing has been used. However, this will dramatically limit the modulation speed by a factor of 256 of the original binary modulation speed.

In the course of my Ph.D., we tried to address the 3 problems mentioned above. In the upcoming chapters we will address each problem separately and try to tackle each one.

In Chapter 2, we go through the theory governing our work that will be used repetitively through the thesis. We start from the wave equation and derive the Helmholtz equation which governs light scattering inside inhomogeneous media, and it is followed by the first-order approximations: Born and Rytov. Afterward, the Wolf-transform is explained. In addition, we go through the Radon transform which neglects any diffraction from the sample. 3D RI reconstruction of a sample measured in transmission configuration usually suffers from the so-called “missing cone” problem. Different imaging scenarios are discussed to solve this problem including sample rotation or using a 90 degrees imaging modality which does not suffer from this limitation.

In chapter 3, we present a method that provides a quantitative metric of the accuracy of the three dimensional reconstruction for optical tomography. The method relies on spatial light modulation of the illumination beam through the sample and numerical back-propagation of the phase conjugated experimentally measured optical field through the 3D reconstruction of the object. The fidelity of this reconstruction provides a quantitative measure of the accuracy of the 3D reconstruction without direct access to the ground truth about the 3D object.

In chapters 4 & 5, a new approach to optical diffraction tomography (ODT) based on intensity measurements is presented. By applying the Wolf transform directly to intensity measurements, we observed unexpected behavior in the 3D reconstruction of the sample. Such a reconstruction does not explicitly represent a quantitative measure of the refractive index of the sample; however, it contains interesting qualitative information. This 3D reconstruction exhibits edge enhancement and contrast enhancement for nanostructures compared with the conventional 3D refractive index reconstruction and thus could be used to localize nanoparticles such as lipids inside a biological sample. When the illumination and the imaging NA are identical, we show that using our technique the 3D RI distribution can be reconstructed.

In chapter 6, DMD will be discussed for high speed complex field representation. Digital micro-mirror devices (DMDs) have been deployed in many optical applications. As compared to spatial light modulators (SLMs), they are characterized by their much faster refresh rates (full-frame refresh rates up to 32 kHz for binary patterns) compared to 120 Hz for most liquid crystal SLMs. DMDs however can only display binary, unipolar patterns and utilize temporal modulation to repre-

sent with excellent accuracy multiple gray-levels in display applications. We used the built-in time domain dynamic range representation of the DMD to project 8-bit complex-fields. With this method, we demonstrated 8-bit complex field modulation with a frame time of 38.4 ms (around 0.15 s for the entire complex-field). We performed phase conjugation by compensating the distortions incurred due to propagation through free-space and a scattering medium. For faster modulation speed, an electro-optic modulator was used in synchronization with the DMD in an amplitude modulation mode to create grayscale patterns with frame rate ~ 833 Hz with display time of only 1.2 ms instead of 38.4 ms for time multiplexing gaining a speed up by a factor of 32.

The last 2 chapters introduce of concept of using deep learning approaches to solve the missing cone problem previously mentioned in this chapter.

In chapter 7, we propose an iterative reconstruction scheme for optical diffraction tomography which exploits the split-step non-paraxial (SSNP) method as the forward model. Compared to the beam propagation method used in learning tomography (LT-BPM), the improved accuracy of SSNP maximizes the information retrieved from measurements without relying on prior assumptions about the sample. Rigorous evaluation of learning tomography based on SSNP (LT-SSNP) using both synthetic and experimental measurements confirms its outstanding performance for various samples.

In Chapter 8, we accurately reconstruct three-dimensional (3-D) refractive index (RI) distributions from highly ill-posed two-dimensional (2-D) measurements using a deep neural network (DNN). Strong distortions are introduced on reconstructions obtained by the Wolf transform inversion method due to the ill-posed measurements acquired from the limited numerical apertures (NAs) of the optical system. Despite the recent success of DNNs in solving ill-posed inverse problems, the application to 3-D optical imaging is particularly challenging due to the lack of the ground truth. We overcome this limitation by generating digital phantoms that serve as samples for the discrete dipole approximation (DDA) to generate multiple 2-D projection maps for a limited range of illumination angles. The presented samples are red blood cells (RBCs), which are highly affected by the ill-posed problems due to their morphology. The trained network using synthetic measurements from the digital phantoms successfully eliminates the introduced distortions. Most importantly, we obtain high fidelity reconstructions from experimentally recorded projections of real RBC sample using the network that was trained on digitally generated RBC phantoms. Finally, we confirm the reconstruction accuracy using the DDA to calculate the 2-D projections of the 3-D reconstructions and compare them to the experimentally recorded projections.

Chapter 2 Theory

1. Light Scattering from Inhomogeneous Media

Maxwell's equations describes the light interaction with matter. To describe the effect of an inhomogeneous medium on an incident electric field, we first start by the “wave equation” which can be derived from Maxwell's equation.

The “wave equation” can be formulated as follows [12]:

$$\nabla^2 \mathbf{E}(\mathbf{r}, t) - \frac{\varepsilon(\mathbf{r})\mu(\mathbf{r})}{c^2} \frac{\partial^2 \mathbf{E}(\mathbf{r}, t)}{\partial t^2} = -\nabla \tilde{\mu}(\mathbf{r}) \times (\nabla \times \mathbf{E}(\mathbf{r}, t)) - \nabla(\mathbf{E}(\mathbf{r}, t) \cdot (\nabla \tilde{\varepsilon}(\mathbf{r}))) , \quad (2.1)$$

where \mathbf{E} is the electric field vector, c is the speed of light in vacuum. ε and μ are the relative electric permittivity and relative magnetic permeability of the inhomogeneous medium, respectively. $\tilde{\varepsilon}$ and $\tilde{\mu}$ are the natural logarithms of ε and μ , respectively.

Assuming a monochromatic plane wave given by:

$$\mathbf{E}(\mathbf{r}, t) = A e^{j(\mathbf{k} \cdot \mathbf{r} - \omega t)} \Rightarrow \frac{\varepsilon\mu}{c^2} \frac{\partial^2 \mathbf{E}}{\partial t^2} = -\frac{\varepsilon\mu}{c^2} \omega^2 \mathbf{E}, \quad (2.2)$$

where ω is the angular frequency given by $\omega = k_0 c$, where k_0 is the wavenumber in free-space. Hence equation 1 can be rewritten as follows:

$$\nabla^2 \mathbf{E}(\mathbf{r}, t) + \frac{\varepsilon(\mathbf{r})\mu(\mathbf{r})}{c^2} \omega^2 \mathbf{E}(\mathbf{r}, t) = -\nabla \tilde{\mu}(\mathbf{r}) \times (\nabla \times \mathbf{E}(\mathbf{r}, t)) - \nabla(\mathbf{E}(\mathbf{r}, t) \cdot (\nabla \tilde{\varepsilon}(\mathbf{r}))) \quad (2.3)$$

By further assuming (1) a non-magnetic medium with $\mu(\mathbf{r}) = 1$ and thus neglecting the first term on the right hand side and (2) slowly varying electric permittivity along the spatial coordinates, equation 3 can be further simplified to:

$$\nabla^2 \mathbf{E} + k_0^2 n^2(\mathbf{r}, \omega) \mathbf{E} = 0, \quad (2.4)$$

where $n(\mathbf{r})$ is the 3D refractive index in the spatial domain and is related to the relative electric permittivity by $n(\mathbf{r}) = \sqrt{\varepsilon(\mathbf{r})}$.

By further assuming an isotropic medium, we will focus on the scalar version of equation 2.4:

Theory

$$\nabla^2 U(\mathbf{r}, w) + k_0^2 n^2(\mathbf{r}) U(\mathbf{r}, w) = 0 \quad (2.5)$$

For an object whose refractive index distribution is $n(\mathbf{r})$ in a surrounding medium with refractive index n_0 , we define the scattering potential as $F(\mathbf{r}, w) = \frac{k_0^2}{4\pi} (n^2(\mathbf{r}, w) - n_0^2)$. Equation 2.5 can then be expressed as:

$$\nabla^2 U(\mathbf{r}, w) + k_0^2 n_0^2 U(\mathbf{r}, w) = -4\pi F(\mathbf{r}, w) U(\mathbf{r}, w) \quad (2.6)$$

The total field $U(\mathbf{r})$ can be described as the sum of the incident field $U_i(\mathbf{r})$ and the scattered field $U_s(\mathbf{r})$ and equation 6 can be decomposed into 2 equations:

$$\nabla^2 U_i(\mathbf{r}, w) + k_0^2 n_0^2 U_i(\mathbf{r}, w) = 0 \quad (2.7)$$

In which equation 2.7 satisfies propagation in a homogenous medium (i.e. $F(\mathbf{r}, w) = 0$). The second equation is concerned with the scattered field and given equation 2.6 and 2.7, the scattered field should satisfy the following the equation:

$$(\nabla^2 + k^2) U_s(\mathbf{r}, w) = -4\pi F(\mathbf{r}, w) U(\mathbf{r}, w), \quad (2.8)$$

where $k = k_0 n_0$.

To solve equation 2.8, one could use the Helmholtz equation for the Green's function $G(\mathbf{r} - \mathbf{r}')$:

$$(\nabla^2 + k^2) G(\mathbf{r} - \mathbf{r}') = -4\pi \delta(\mathbf{r} - \mathbf{r}'), \quad (2.9)$$

where $\delta(\mathbf{r} - \mathbf{r}')$ is the three-dimensional Dirac delta function. A valid expression for the Green's function that satisfies equation 2.9 would be:

$$G(\mathbf{r} - \mathbf{r}') = \frac{e^{jk|\mathbf{r} - \mathbf{r}'|}}{|\mathbf{r} - \mathbf{r}'|} \quad (2.10)$$

Using equations 2.8-2.10, the scattered field $U_s(\mathbf{r})$ can be expressed as follows:

$$U_s(\mathbf{r}) = \int_V F(\mathbf{r}') U(\mathbf{r}') G(\mathbf{r} - \mathbf{r}') d\mathbf{r}' \quad (2.11)$$

And hence the total field can be expressed as

$$U(\mathbf{r}) = U_i(\mathbf{r}) + \int_V F(\mathbf{r}') U(\mathbf{r}') G(\mathbf{r} - \mathbf{r}') d\mathbf{r}' \quad (2.12)$$

While equation 2.12 is linear with respect to the incident fields, it is nonlinear with respect to the scattering potential distribution. In order to accurately solve this equation nonlinear techniques are

usually used to account for such nonlinearity (i.e. multiple scattering). However, for weakly scattering semi-transparent samples, equation 2.12 can be linearized and the weakly scattering approximations can be used to reconstruct a reasonable estimate 3D distribution for the refractive index map. In the following section different models accounting for weakly scattering samples will be discussed along with 3D reconstructions. Such models are referred to as “Inverse models based on first-order approximations”.

2. Optical Diffraction Tomography

Optical diffraction tomography (ODT) is the process of acquiring different projections from multiple angles and then use the information to reconstruct the 3D refractive index distribution. To do so, equation 2.12 is used to relate the measured total field to the scattering potential. However, as mentioned before, such equation is nonlinear with respect to the scattering potential and a direct-inverse model cannot be utilized to solve such equation. However, for weakly scattering transparent samples, this equation can be linearized and a linear relation between the scattered field and the scattering potential can be retrieved and a good estimate for 3D refractive map can be reconstructed.

3. Direct-Inversion Models based on First-order approximation

1. First-order Born approximation

For weakly scattering objects, we can assume that the measured total field is approximately equal to the incident field plus the component of the field that was scattered only once.

Under this assumption, equation 2.11 can be approximated as follows:

$$U_s(\mathbf{r}) = \int_V F(\mathbf{r}') U_i(\mathbf{r}') G(\mathbf{r} - \mathbf{r}') d\mathbf{r}' \quad (2.13)$$

Equation 2.13 is linear in terms of the scattered field and the scattering potential and a direct-inverse model can be used to reconstruct the scattering potential from the measured scattered field. Equation 2.13 is usually referred to as the “Born approximation” or more precisely “First-order Born approximation”.

To solve the integral term on the right-hand side of equation 2.13, we use the integral form of the Green’s function given by:

$$G(\mathbf{r} - \mathbf{r}') = \frac{e^{jk|\mathbf{r} - \mathbf{r}'|}}{|\mathbf{r} - \mathbf{r}'|} = \frac{ik}{2\pi} \int_{-\infty}^{\infty} \int_{-\infty}^{\infty} \frac{1}{s_z} e^{jk[s_x(x-x') + s_y(y-y') + s_z(z-z')]} ds_x ds_y, \quad (2.14)$$

where $\mathbf{k} = k\mathbf{s} = (ks_x, ks_y, ks_z)$ denotes the k-vector along the three coordinates while s_z satisfies the following equation:

$$\begin{aligned} s_z &= \sqrt{1 - s_x^2 - s_y^2}, \quad s_x^2 + s_y^2 \leq 1 \\ &= j\sqrt{s_x^2 + s_y^2 - 1}, \quad s_x^2 + s_y^2 \geq 1, \end{aligned} \quad (2.15)$$

Theory

where the former equation describe a homogenous wave that propagate away from the scatterer while the latter express an evanescent wave that exponentially decays along $|z|$.

Assuming plane-wave illumination:

$$U_i(\mathbf{r}) = e^{j(\mathbf{k}_0 \cdot \mathbf{r})} = e^{j(k_{0x}x + k_{0y}y + k_{0z}z)}, \quad (2.16)$$

where $\mathbf{k}_0 = k\mathbf{s}_0 = (k s_{0x}, k s_{0y}, k s_{0z})$ is the illumination k-vector of the incident plane wave. By substituting equations 2.15-2.16 into equation 2.13, we get:

$$U_s(\mathbf{r}) = \int_V F(\mathbf{r}') e^{j(k s_{0x}x' + k s_{0y}y' + k s_{0z}z')} \left[\frac{ik}{2\pi} \int_{-\infty}^{\infty} \int_{-\infty}^{\infty} \frac{1}{s_z} e^{jk[s_x(x-x') + s_y(y-y') \pm s_z(z-z')]} ds_x ds_y \right] d\mathbf{r}', \quad (2.17)$$

Eq. 2.17 can be expressed as:

$$U_s(\mathbf{r}) = \int_{-\infty}^{\infty} \int_{-\infty}^{\infty} a^{(\pm)}(s_x, s_y; s_{0x}, s_{0y}) e^{jk[s_x x + s_y y \pm s_z z]} ds_x ds_y, \quad (2.18)$$

where $a^{(\pm)}(s_x, s_y; s_{0x}, s_{0y})$ is the 2D Fourier transform of the 2D measurements (the projections) obtained by illuminating the sample with a plane wave in a direction (s_{0x}, s_{0y}) and it is given by:

$$a^{(\pm)}(s_x, s_y; s_{0x}, s_{0y}) = \frac{ik}{2\pi s_z} \int_V F(\mathbf{r}') e^{-jk[(s_x - s_{0x})x' + (s_y - s_{0y})y' + (\pm s_z - s_{0z})z']} d\mathbf{r}', \quad (2.19)$$

From equations 2.18 and 2.19, we obtain the following equation:

$$a^{(\pm)}(s_x, s_y; s_{0x}, s_{0y}) = \frac{1}{(2\pi)^2} k^2 \tilde{U}_s(k s_x, k s_y) e^{\mp j k s_z z^\pm} = \frac{jk}{2\pi s_z} \tilde{F}[k(s_x - s_{0x}), k(s_y - s_{0y}), k(\pm s_z - s_{0z})], \quad (2.20)$$

where $\tilde{F}(\dots)$ is the 3D Fourier transform of the scattering potential $F(\mathbf{r})$. Hence,

$$\tilde{F}[k(s_x - s_{0x}), k(s_y - s_{0y}), k(\pm s_z - s_{0z})] = \frac{k s_z}{2\pi j} \tilde{U}_s(k s_x, k s_y) e^{\mp j k s_z z^\pm} \quad (2.21)$$

Equation 2.21 relates directly the 2D Fourier transforms of the measured scattered fields to the scattering potential of the 3D object in the Fourier space. In practice, objective lenses are used to image biological samples and hence in the Fourier space the spectrum of the sample is low pass filtered by a circular filter whose radius is proportional to the numerical aperture (NA) of the objective lens. The 2D Fourier transform of the scattered field is mapped as a spherical cap into the 3D Fourier space of the object governed by the relation $s_z = \sqrt{1 - s_x^2 - s_y^2}$. We refer to the 3D Fourier space of the object as the kappa space ($\boldsymbol{\kappa} = \mathbf{k} - \mathbf{k}_0$) depending on the illumination k-vector \mathbf{k}_0 as shown in Figure 2-1. The process of mapping the 2D scattered field into the kappa space is the foundation of the Fourier diffraction theory and was first described in a paper by Wolf [19]. We refer to it as the “Wolf Transform”.

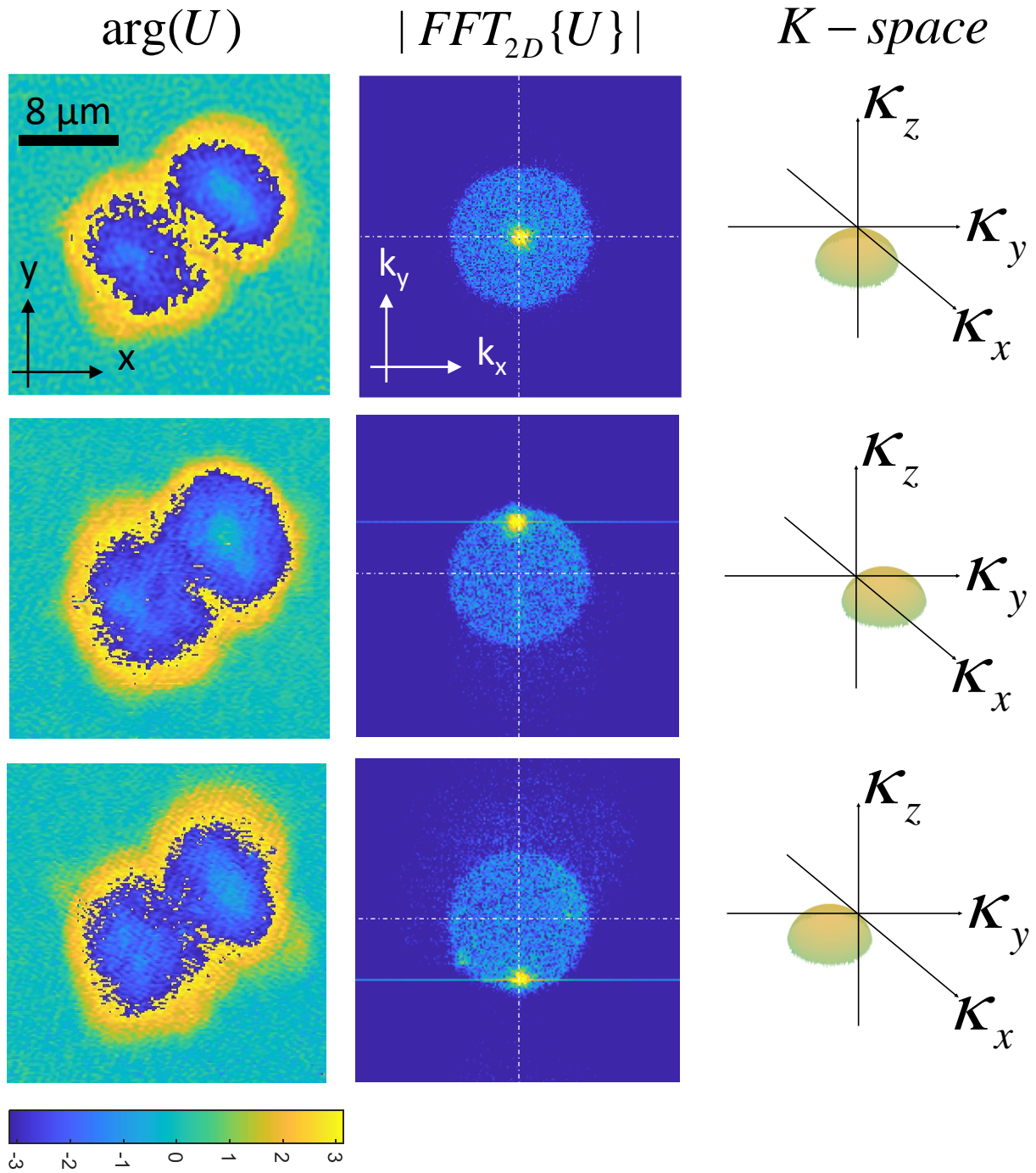


Figure 2-1. Wolf Transform procedures. First, the complex field is extracted from the holograms as shown in the left-hand side of the figure, then the 2D Fourier transform is computed as shown in the middle column and then the 2D Fourier transform is computed as a spherical cap in the kappa-space as shown in the right-hand column.

2. First-order Rytov approximation

The Rytov method of reconstructing a 3D object from its 2D projections is a close relative of the Wolf transform.

Theory

The first-order Rytov approximation can be derived starting from equation 2.6:

$$\nabla^2 U(\mathbf{r}) + k^2 U(\mathbf{r}) = -4\pi F(\mathbf{r}) U(\mathbf{r})$$

If we assume that the total field is purely phase modulated by the object then it takes the form $U(\mathbf{r}) = e^{\psi(\mathbf{r})}$ where $\psi(\mathbf{r}) = \psi_i(\mathbf{r}) + \psi_s(\mathbf{r})$ is the phase of the total field assumed to be the sum of the phase of the incident wave and the phase due to the object. This is the first-order Rytov expansion [12]. Substituting in Eq. (2.6) we get the following set of equations:

$$\nabla^2 e^{\psi(\mathbf{r})} + k^2 e^{\psi(\mathbf{r})} = -4\pi F(\mathbf{r}) e^{\psi(\mathbf{r})} \quad (2.22)$$

$$\nabla(\nabla e^{\psi(\mathbf{r})}) + k^2 e^{\psi(\mathbf{r})} = -4\pi F(\mathbf{r}) e^{\psi(\mathbf{r})} \quad (2.23)$$

$$\nabla(\nabla \psi(\mathbf{r}).e^{\psi(\mathbf{r})}) + k^2 e^{\psi(\mathbf{r})} = -4\pi F(\mathbf{r}) e^{\psi(\mathbf{r})} \quad (2.24)$$

$$\nabla^2 \psi(\mathbf{r}).e^{\psi(\mathbf{r})} + (\nabla \psi(\mathbf{r}))^2 .e^{\psi(\mathbf{r})} + k^2 e^{\psi(\mathbf{r})} = -4\pi F(\mathbf{r}) e^{\psi(\mathbf{r})} \quad (2.25)$$

$$\nabla^2 \psi(\mathbf{r}) + (\nabla \psi(\mathbf{r}))^2 + k^2 = -4\pi F(\mathbf{r}) \quad (2.26)$$

$$\nabla^2 \psi_i(\mathbf{r}) + \nabla^2 \psi_s(\mathbf{r}) + (\nabla \psi_i(\mathbf{r}))^2 + (\nabla \psi_s(\mathbf{r}))^2 + 2\nabla \psi_i(\mathbf{r}).\nabla \psi_s(\mathbf{r}) + k^2 = -4\pi F(\mathbf{r}) \quad (2.27)$$

Equation 2.27 can be decomposed into 2 equations for the incident field and with perturbation as follows:

$$\nabla^2 \psi_i(\mathbf{r}) + (\nabla \psi_i(\mathbf{r}))^2 + k^2 = 0 \quad (2.28)$$

By plugging in equation 2.28 into 2.27 we get:

$$\nabla^2 \psi_s(\mathbf{r}) + (\nabla \psi_s(\mathbf{r}))^2 + 2\nabla \psi_i(\mathbf{r}).\nabla \psi_s(\mathbf{r}) = -4\pi F(\mathbf{r}) \quad (2.29)$$

Considering the following identity:

$$\nabla^2(g(\mathbf{r})h(\mathbf{r})) = \nabla^2 g(\mathbf{r}).h(\mathbf{r}) + g(\mathbf{r}).\nabla^2 h(\mathbf{r}) + 2\nabla g(\mathbf{r}).\nabla h(\mathbf{r}) \quad (2.30)$$

And assuming plane wave illumination, $U_i(\mathbf{r}) = e^{j\psi_i(\mathbf{r})} = A(\mathbf{r})e^{j(\mathbf{k}_{in}.\mathbf{r})} \Rightarrow \nabla^2 U_i(\mathbf{r}) = -k^2 U_i(\mathbf{r})$, equation 2.30 becomes:

$$\nabla^2(U_i(\mathbf{r})\psi_s(\mathbf{r})) = -k^2 U_i(\mathbf{r}).\psi_s(\mathbf{r}) + U_i(\mathbf{r}).\nabla^2 \psi_s(\mathbf{r}) + 2\nabla \psi_s(\mathbf{r})U_i(\mathbf{r}).\nabla \psi_i(\mathbf{r}) \quad (2.31)$$

Re-ordering equation 2.31:

$$U_i(\mathbf{r}).\nabla^2 \psi_s(\mathbf{r}) + 2U_i(\mathbf{r}).\nabla \psi_i(\mathbf{r}).\nabla \psi_s(\mathbf{r}) = \nabla^2(U_i(\mathbf{r})\psi_s(\mathbf{r})) + k^2 U_i(\mathbf{r}).\psi_s(\mathbf{r}) \quad (2.32)$$

Multiplying equation 2.29 by $U_i(\mathbf{r})$ we get:

$$U_i(\mathbf{r}).\nabla^2 \psi_s(\mathbf{r}) + 2U_i(\mathbf{r}).\nabla \psi_i(\mathbf{r}).\nabla \psi_s(\mathbf{r}) = -[(\nabla \psi_s(\mathbf{r}))^2 + 4\pi F(\mathbf{r})] U_i(\mathbf{r}) \quad (2.33)$$

By equating the left-hand side of equation 2.32 and 2.33 we get:

Theory

$$\nabla^2(U_i(r)\psi_s(\mathbf{r})) + k^2 U_i(r)\psi_s(\mathbf{r}) = -[(\nabla \psi_s(\mathbf{r}))^2 + 4\pi F(\mathbf{r})] U_i(\mathbf{r}) \quad (2.34)$$

For weakly scattering objects, we can neglect the effect of this term $(\nabla \psi_s(\mathbf{r}))^2$ and equation 2.34 becomes:

$$(\nabla^2 + k^2)U_i(r)\psi_s(\mathbf{r}) = -4\pi F(\mathbf{r}) U_i(\mathbf{r}) \quad (2.35)$$

By noting the similarity between this equation and equation 2.8, we solve for $U_i(r)\psi_s(\mathbf{r})$ using the same Green's function integral we used before:

$$U_i(r)\psi_s(\mathbf{r}) = \int_V F(\mathbf{r}') U_i(\mathbf{r}') G(\mathbf{r} - \mathbf{r}') d\mathbf{r}', \quad (2.36)$$

where $\psi_s(\mathbf{r}) = \ln \frac{U}{U_i} = \ln \frac{|U|}{|U_i|} + j\phi$, where ϕ is the unwrapped phase after passing through the sample. Equation 2.36 looks similar to equation 2.11 except for replacing $U_s(r)$ by $U_i(r)\psi_s(\mathbf{r})$.

3. Phase unwrapping for Rytov approximation

As shown in Eq. 2.36, an accurate measure of the phase is required to reconstruct the scattering potential. A common problem when extracting the phase from the hologram is that for thicker samples, the phase becomes wrapped and thus an efficient phase unwrapping algorithm is needed to retrieve the true phase [22]. Phase wrapping problem can be expressed mathematically as:

$$e^{j\phi} = e^{j(\phi+2\pi)} \quad (2.37)$$

This problem results in wrong calculation of the phase along the 2D (x, y) grid. Figure 2-2 shows the effect of applying phase unwrapping on the wrapped phase.

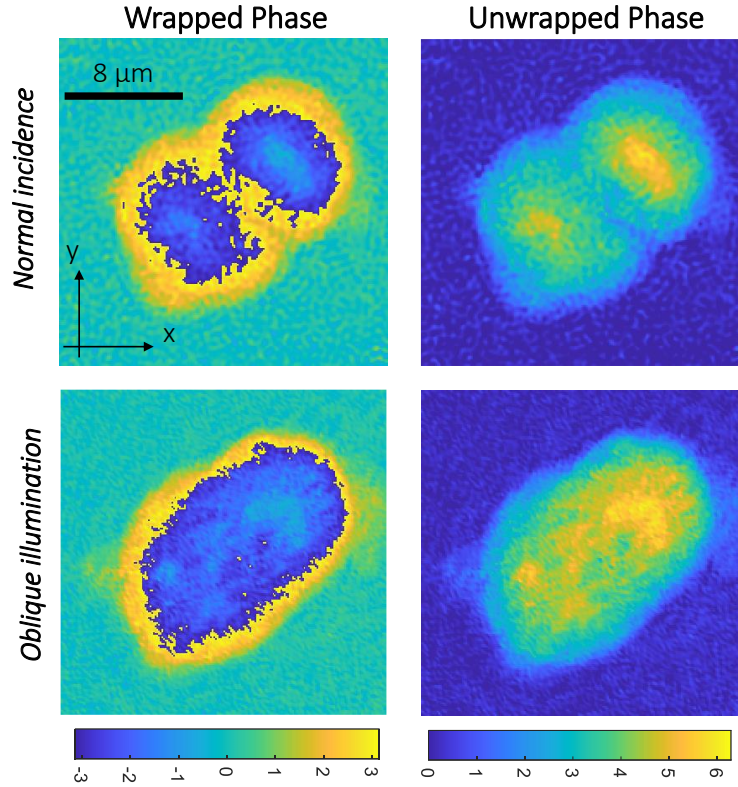


Figure 2-2. Phase unwrapping. The right column shows how the phase profile is highly different than the one in the left column.

4. Validity of Born and Rytov approximations

The validity of the first-order Born approximation is limited to the phase shift from the sample does not exceed π as explained in [23]:

$$phase\ shift = \frac{2\pi}{\lambda} \Delta n \cdot L \leq \pi \text{ [Born Approx.]}, \quad (2.38)$$

where L is the thickness of the sample. Equation 2.38 highly limits the applicability of Born approximation for biological samples which usually have wrapped phases and Born approximation will not be valid in that case.

On the other hand, the Rytov approximation is only valid when:

$$(\nabla \psi_s(\mathbf{r}))^2 + 4\pi F(\mathbf{r}) \approx 4\pi F(\mathbf{r}), \quad (2.39)$$

where $F(\mathbf{r}) = \frac{k_0^2}{4\pi}(n^2(\mathbf{r}) - n_0^2)$. For weakly scattering objects, $F(\mathbf{r})$ can be approximated to

$$F(\mathbf{r}) = \frac{k_0^2}{2\pi}(n_0\Delta n) \text{ and equation 2.39 becomes}$$

$$(\nabla \psi_s(\mathbf{r}))^2 + 2k_0^2 n_0 \Delta n \approx 2k_0^2 n_0 \Delta n, \quad (2.40)$$

which is only valid when $(\nabla \psi_s(\mathbf{r}))^2 \ll k_0^2 n_0 \Delta n$ and therefore we reach the condition for the validity of the Rytov approximation as follows [23]:

$$\Delta n \gg \frac{(\nabla \psi_s(\mathbf{r}))^2 \lambda^2}{4\pi^2 n_0} \quad [\text{Rytov Approx.}] \quad (2.41)$$

An interesting fact in the Rytov approximation is that the size of the sample L is not a factor in the Rytov approximation as the case in the Born approximation. However, it is the gradient of $\psi_s(\mathbf{r})$ over one wavelength that is important and not the actual phase shift. Therefore Rytov approximation will be valid as long as the phase shift over a single wavelength is small.

4. Filling in the K-space using the “Wolf Transform” in transmission

As mentioned before, each projection is mapped as a spherical cap in the kappa-space and then an inverse 3D Fourier transform is applied to get the final scattering potential in the spatial domain from which we get an estimate about the 3D refractive index distribution. We usually refer to the 3D kappa-space as the Ewald’s sphere in which each projection is mapped as a spherical cap (i.e. diffraction models) into the Ewald’s sphere depending on the imaging scenario.

To understand more, let’s first have a look about the Ewald’s sphere in the spectral domain to gain an understanding about the mapping process. We first assume that we only change the illumination angle of the incident field without any sample rotation and without changing the operating wavelength of the laser source. Figure 2-3(a, i) shows the case for normal incidence onto the sample. Since we are imaging with an objective lens with a limited numerical aperture (NA), we cannot cover all the scattered frequencies of the sample. However, we only capture a portion of those frequencies that makes it through the objective lens NA. Thus, we can represent those collected frequencies as a spherical cap whose projection in the (k_x, k_z) plane would be a circular arc represented by the red arc in Figure 2-3(a, i). This result in underestimation and elongation of the retrieved 3D RI distribution along the optical axis as will be shown later.

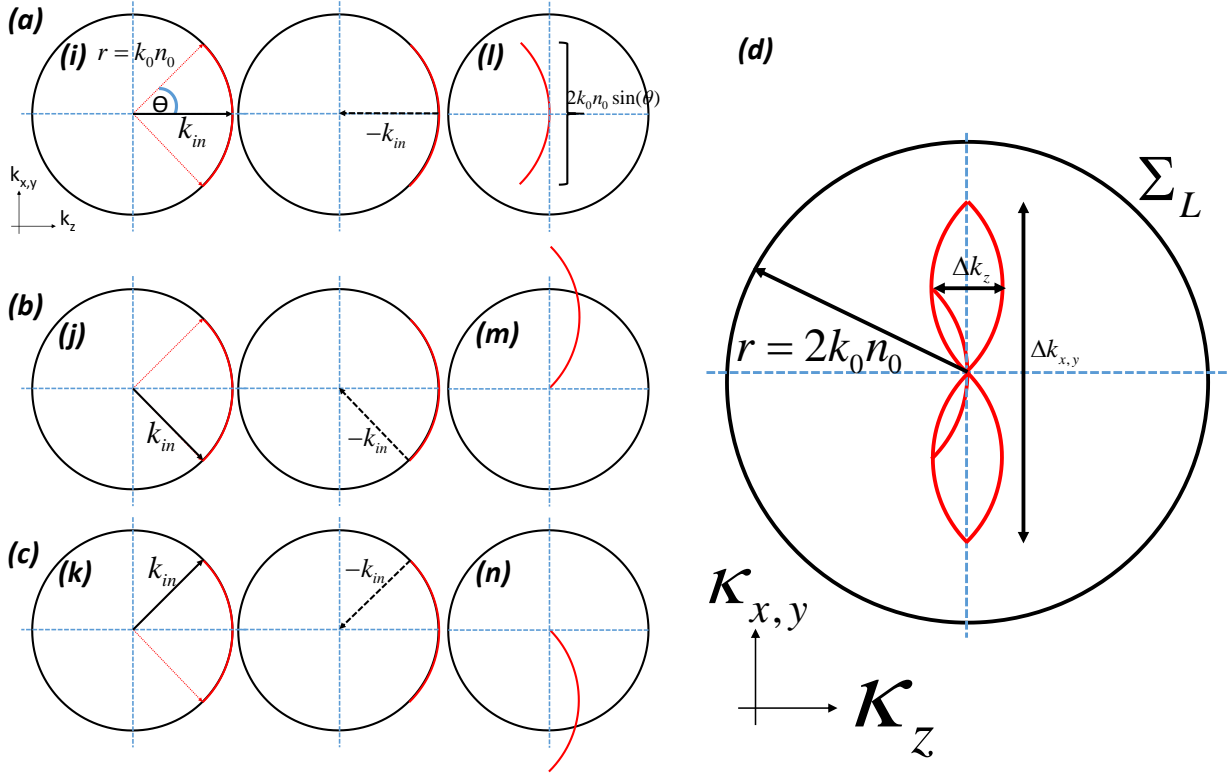


Figure 2-3 Mapping the scattered frequencies of the object into the Ewald's sphere in transmission for (a) normal incidence and (b, c) oblique illumination. (i, j, k) show the object scattered frequencies distributed on the spherical cap (i.e. red arc) defined by the numerical aperture of the objective lens. (l, m, n) show the mapping of different spherical caps onto the Ewald's sphere support for different illumination angles. Illumination angles cannot reach higher value than θ which is defined by the numerical aperture of the objective lens. (d) shows the Ewald's sphere support after mapping all the projections, changing the illumination angles to cover the whole numerical aperture of the objective lens results in the donut shape. Σ_L is the limiting Ewald's sphere which is the largest frequency domain covered by the scattered frequencies when all the possible incidence directions are mapped. Note that a transmission imaging system can only collect angle subtended by $\theta = 90^\circ$.

Σ_L is the limiting Ewald's sphere which is the largest frequency domain covered by the scattered frequencies when all the possible incidence directions are mapped. Note that a transmission imaging system can only collect angle subtended by $\theta = 90^\circ$.

Depending on the illumination and imaging modalities, the resolution will vary [24]. The illumination scanning transmission configuration for spiral scanning results in a lateral ($r_{x,y}$) and axial (r_z) resolution of the 3D reconstruction as follows:

$$r_{x,y}^{spiral} = \frac{2\pi}{\Delta k_{x,y}} = \frac{2\pi}{4k_0 n_0 \sin(\theta)} = \frac{2\pi}{4 \frac{2\pi}{\lambda} NA} = \frac{\lambda}{4NA} \quad (2.42)$$

$$r_z^{spiral} = \frac{2\pi}{\Delta k_z} = \frac{2\pi}{2k_0 n_0 [1 - \cos(\theta)]} = \frac{2\pi}{2 \frac{2\pi}{\lambda} n_0 [1 - \cos(\theta)]} = \frac{\lambda}{2n_0 [1 - \cos(\theta)]}, \quad (2.43)$$

Theory

while for circular scanning, we get the following:

$$r_{x,y}^{circular} = \frac{2\pi}{\Delta k_{x,y}} = \frac{2\pi}{4k_0 n_0 \sin(\theta)} = \frac{2\pi}{4 \frac{2\pi}{\lambda} NA} = \frac{\lambda}{4NA} \quad (2.44)$$

$$r_z^{circular} = \frac{2\pi}{\Delta k_z} = \frac{2\pi}{k_0 n_0 [1 - \cos(\theta)]} = \frac{2\pi}{\frac{2\pi}{\lambda} n_0 [1 - \cos(\theta)]} = \frac{\lambda}{n_0 [1 - \cos(\theta)]} , \quad (2.45)$$

where n_0 is the immersion medium for the objective lens and $NA = n_0 \sin(\theta)$ is the numerical aperture for liquid immersion objectives.

For $n_0 = 1$ and assuming low NA objective lens, equations 2.44 and 2.46 can be rewritten using Taylor's approximation:

$$r_z^{spiral} = \frac{2\pi}{\Delta k_z} = \frac{2\pi}{2k_0 [1 - \cos(\theta)]} = \frac{2\pi}{2 \frac{2\pi}{\lambda} [1 - \sqrt{1 - \sin^2(\theta)}]} = \frac{\lambda}{2 \cdot \frac{1}{2} \cdot \sin^2(\theta)} = \frac{\lambda}{NA^2} \quad (2.46)$$

$$r_z^{circular} = \frac{2\pi}{\Delta k_z} = \frac{2\pi}{k_0 n_0 [1 - \cos(\theta)]} = \frac{2\pi}{\frac{2\pi}{\lambda} [1 - \sqrt{1 - \sin^2(\theta)}]} = \frac{\lambda}{\frac{\sin^2(\theta)}{2}} = \frac{2\lambda}{NA^2} \quad (2.47)$$

Please notice how that different illumination schemes result in different axial resolution as given by equations 2.43 and 2.45 in which the spiral scanning (i.e. filling in the whole NA of the objective lens) results in a better axial resolution by a factor of 2 than in the case of the circular scanning.

5. 3D Refractive Index Reconstruction using Born and Rytov approximations

From Born and Rytov approximations:

$$U_s(\mathbf{r}) = \int_V F(\mathbf{r}') U_i(\mathbf{r}') G(\mathbf{r} - \mathbf{r}') d\mathbf{r}' \quad (\text{Born})$$

$$U_i(\mathbf{r}) \psi_s(\mathbf{r}) = \int_V F(\mathbf{r}') U_i(\mathbf{r}') G(\mathbf{r} - \mathbf{r}') d\mathbf{r}' \quad (\text{Rytov})$$

It is noticed that the right hand side of the 2 equations are identical and thus the same procedures can be followed for the 3D RI reconstruction by simply replacing the scattered field $U_s(\mathbf{r})$ by $U_i(\mathbf{r}) \psi_s(\mathbf{r})$. However, for accurate substitution of $\psi_s(\mathbf{r})$, we need to first applying the phase unwrapping algorithm as previously explained in section III(c). Figure 2-4 shows the different reconstruction from the Born and Rytov approximation for the same HCT116 cell shown in Figure 2-2.

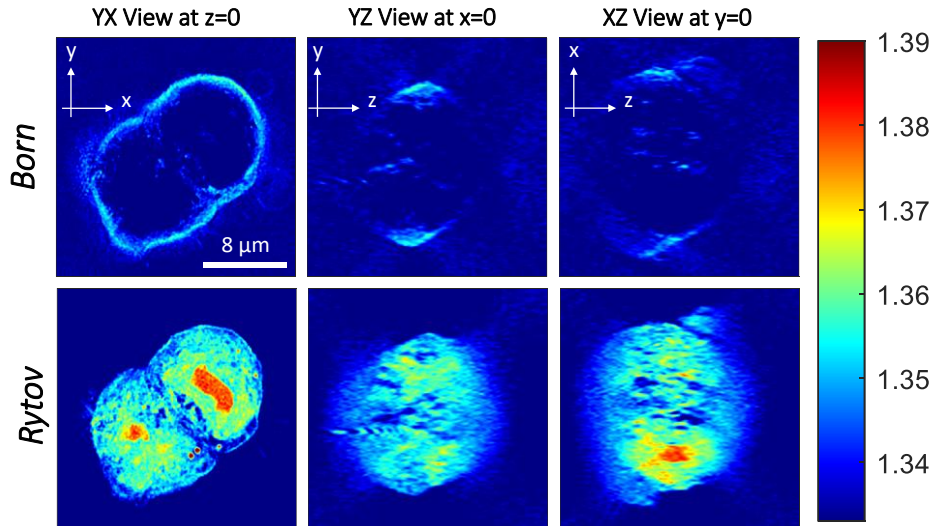


Figure 2-4. Difference between 3D refractive index distribution based on Born and Rytov approximation. It is noted that the Born approximation suffers from underestimation in the RI distribution which might be attributed to the phase wrapping phenomenon shown in Fig. 2-2.

Figure 2-4 shows how the Rytov approximation is able to get a better estimate of the refractive index reconstruction. For example, literature shows that for biological samples the refractive index of the cytoplasm is around 1.35-1.37 while that lipids have the higher index around 1.4 which is highly matching with the 3D RI estimate from the Rytov approximation. Figure 2-5 shows the YX view at different depths for the Rytov approximation which shows how the image gets out of focus as we move away from the best plane of focus of the imaging system.

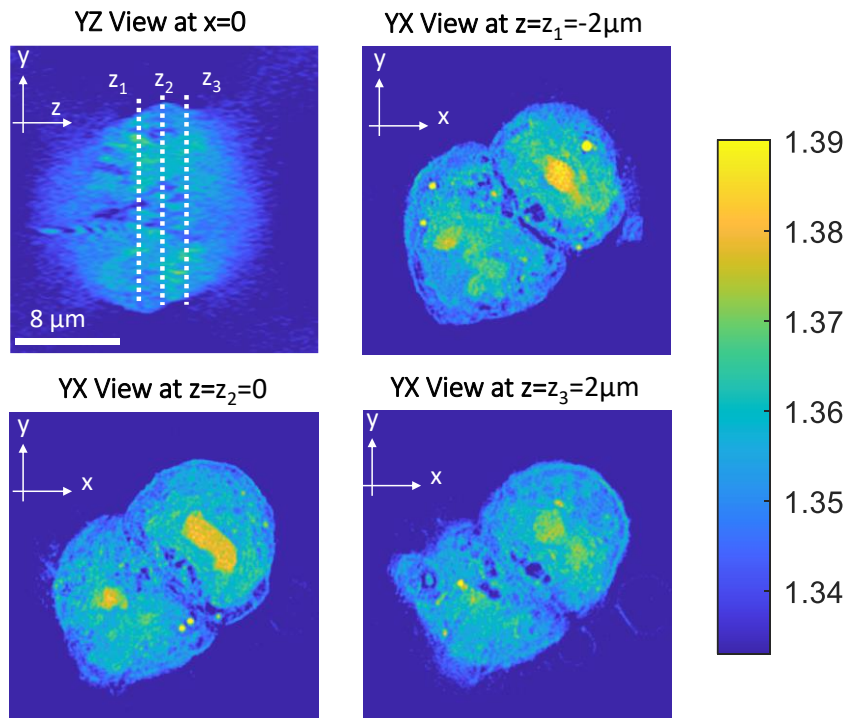


Figure 2-5. Defocusing problem in the Rytov reconstruction when we move away from the best plane of focus of the objective lens.

It is also noticed how the YZ view is elongated along the direction of propagation (z-axis) which is a consequence of the so-called “missing cone” problem. The missing cone problem comes from the fact that we can only collect the scattered frequencies within the numerical aperture of the objective lens and therefore missing the scattering frequencies along κ_z as shown in Figure 2-6. This result in an elongation along the optical axis as observed in Figure 2-5 and Figure 2-6.

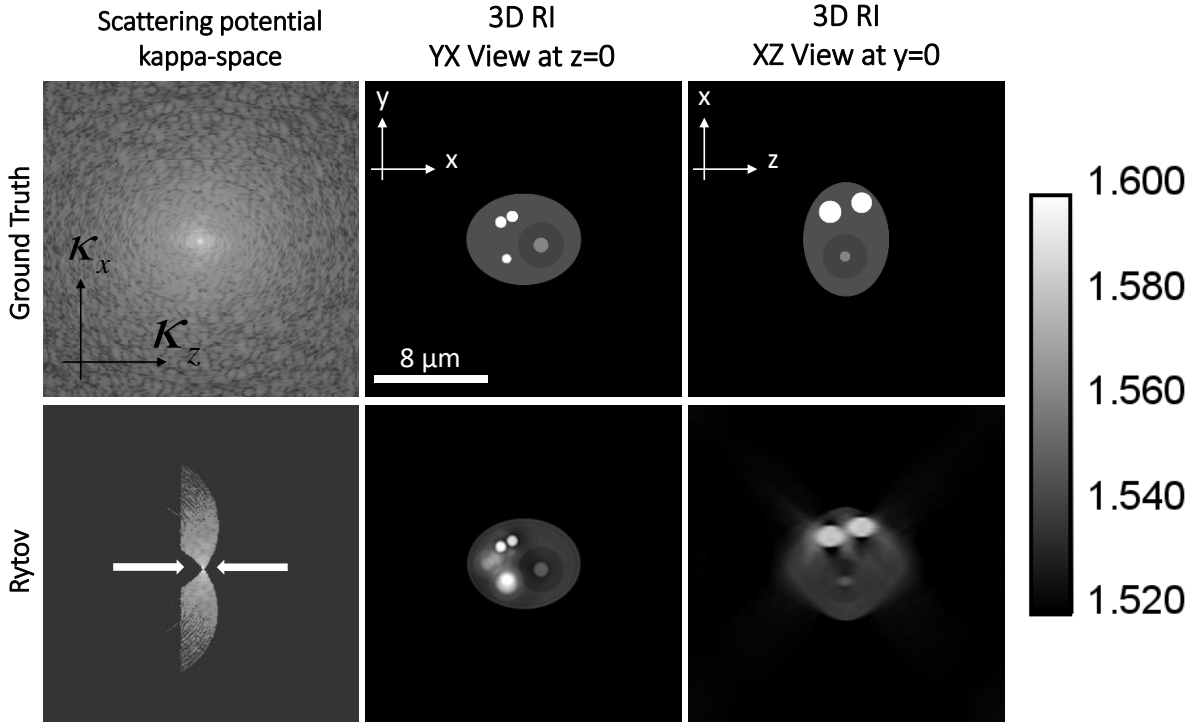


Figure 2-6. Missing cone problem. The left-column shows how the frequency components are low pass filtered by the limited NA of the objective lens which results in an elongation as shown in the right-most column. In addition, it is noticed how the RI map is underestimated in the bottom row as compared to the upper row. This underestimation is a consequence of blocking a portion of the energy in the spectral domain and thus the same amount will be blocked in the spatial domain which results in lower RI value.

Another limitation shown in Figure 2-6 is underestimation of the RI value of the Rytov as compared to the ground truth. The reason for this is that the limited NA objective lens blocks part of the energy components in the Fourier domain, and since energy is conserved in the spectral and spatial domain, this translates into less energy in the spatial domain which translates to lower RI value in the reconstruction process.

6. Solving the missing cone problem with different imaging scenarios

In this section we propose different illuminations scenarios to solve the missing cone problem including 90 degrees geometry and sample rotation configuration as shown in Figure 2-7.

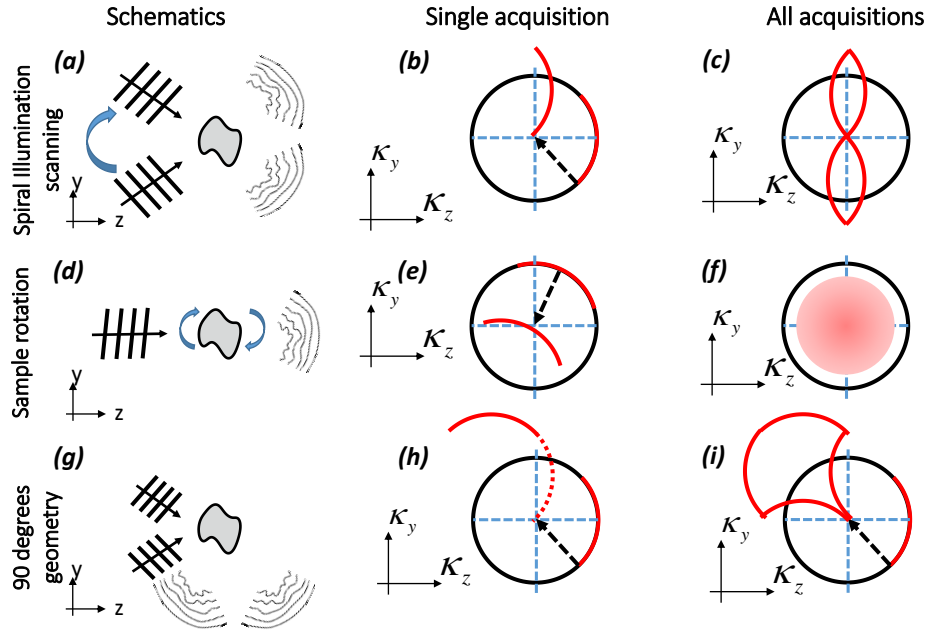


Figure 2-7. Illustrative schematics and Ewald's sphere for different imaging scenarios. (a)–(c) spiral Illumination scanning method. (a) Schematic for transmission configuration. (b) Mapping of single acquisition into the Ewald's sphere. (c) Mapping all the acquisitions using illumination scanning in transmission configuration. (d)–(f) Sample rotation method. (d) Sample rotation while the illumination beam is fixed. (e) Mapping of single acquisition into the Ewald's sphere for sample rotation. (f) Mapping all the acquisitions using sample rotation in transmission configuration. (g)–(i) 90 degrees geometry. (g) Schematic for 90 degrees configuration. (h) Mapping of single acquisition into the Ewald's sphere. (i) Mapping all the acquisitions using 90 degrees configuration.

Figure 2-8 shows the frequency support for transmission, and 90 degrees geometry. While transmission yields slightly higher RI contrast, 90 degrees geometry is able to minimize the elongation along the optical axis.

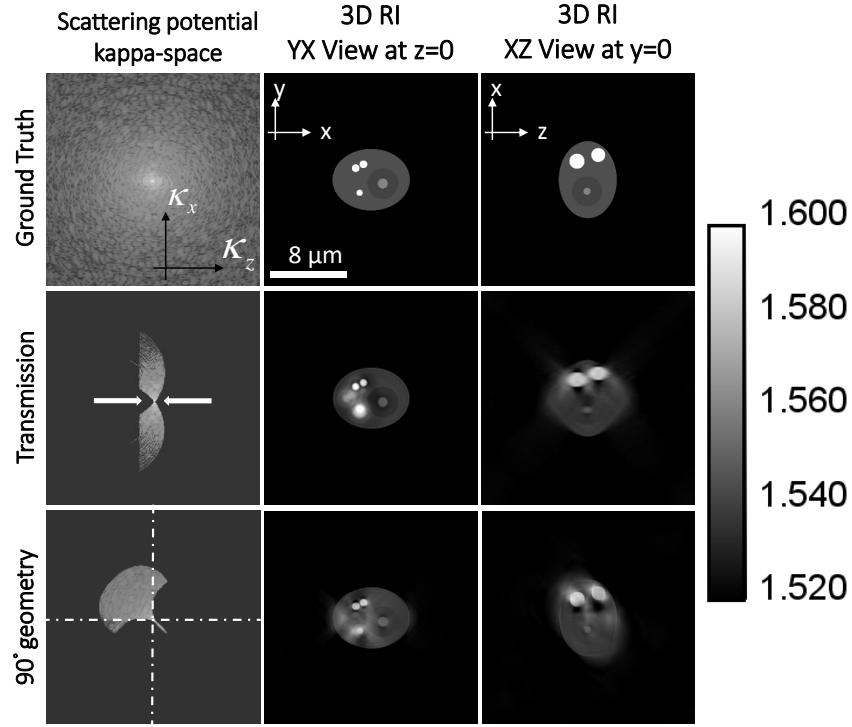


Figure 2-8. Coverage of the k-space of the object depending on the imaging geometry.

Another way to minimize the missing cone problem is to rotate the object instead of scanning the illumination angle as shown in Figure 2-9 (i.e. rotation around x-axis) [25].

On the other hand, sample rotation usually suffers from worse lateral resolution as compared to illumination scanning configuration as given by:

$$r_{x,y}^{illumination} = \frac{2\pi}{\Delta k_{x,y}} = \frac{2\pi}{4k_0 n_0 \sin(\theta)} = \frac{2\pi}{4 \frac{2\pi}{\lambda} NA} = \frac{\lambda}{4NA} \quad (2.48)$$

$$r_z^{illumination} = \frac{2\pi}{\Delta k_z} = \frac{2\pi}{2k_0 n_0 [1 - \cos(\theta)]} = \frac{2\pi}{2 \frac{2\pi}{\lambda} n_0 [1 - \cos(\theta)]} = \frac{\lambda}{2n_0 [1 - \cos(\theta)]} \quad (2.49)$$

$$r_x^{sample} = \frac{2\pi}{\Delta k_x} = \frac{2\pi}{2k_0 n_0 \sin(\theta)} = \frac{2\pi}{2 \frac{2\pi}{\lambda} NA} = \frac{\lambda}{2NA} \quad (2.50)$$

$$r_{y,z}^{sample} = \frac{2\pi}{\Delta k_{y,z}} = \frac{2\pi}{4k_0 n_0 \sin(\frac{\theta}{2})} = \frac{2\pi}{4 \frac{2\pi}{\lambda} n_0 \sin(\frac{\theta}{2})} = \frac{\lambda}{4n_0 \sin(\frac{\theta}{2})} \quad (2.51)$$

This is evident in Figure 2-10 where we can see that high frequency features can be captured by scanning the illumination angle but not with sample rotation.

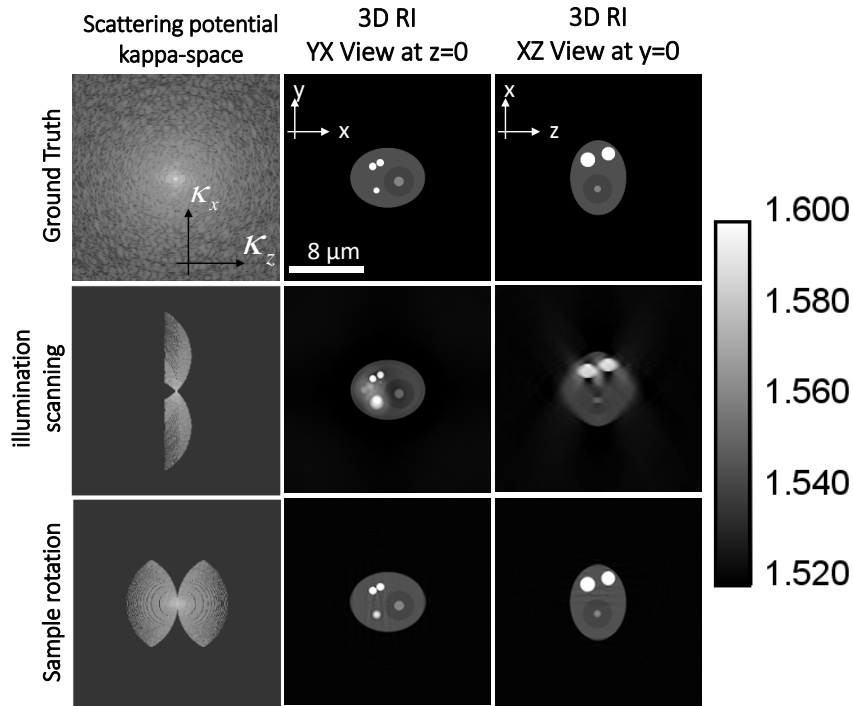


Figure 2-9. Illumination scanning and sample rotation coverage in the kappa-space. We see how the missing cone problem is solved when rotating the sample while the illumination direction is fixed to normal incidence. However, we see how the frequency support is similar to an apple core, this is called “missing apple core” problem.

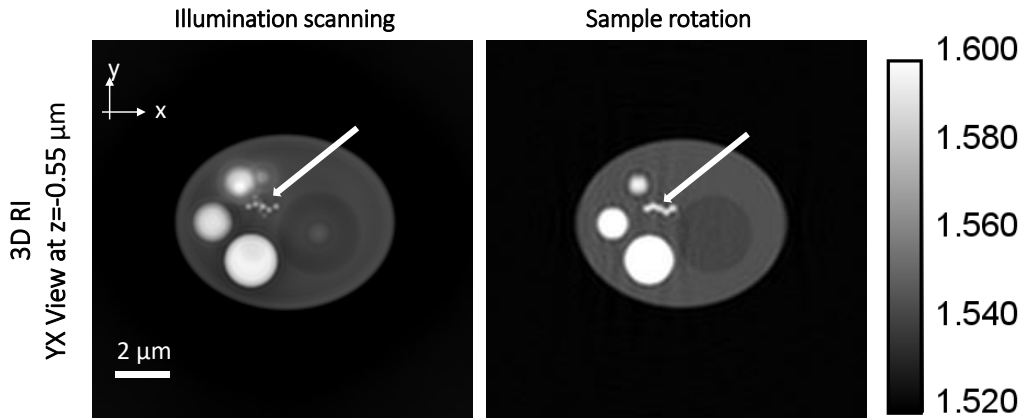


Figure 2-10. Lower resolution in the sample rotation in which the illumination scanning scenario is able to detect the high frequency features of the sample.

The best way is to combine both the angular scanning and the sample rotation for an isotropic resolution in 3D and to solve the missing cone problem along the direction of propagation as shown in Figure 2-11 where a better frequency support is visible when combining both scenarios. Figure 2-12 shows an example in which the combination of the 2 techniques resulted in better resolving power at the respective depth.

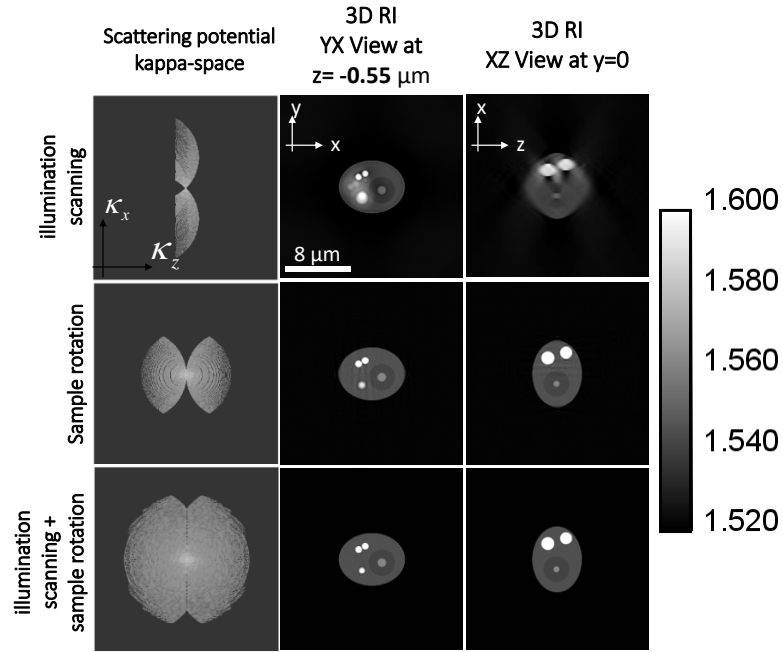


Figure 2-11. Illumination scanning, sample rotation, “illumination scanning + sample rotation” coverage in the kappa-space.

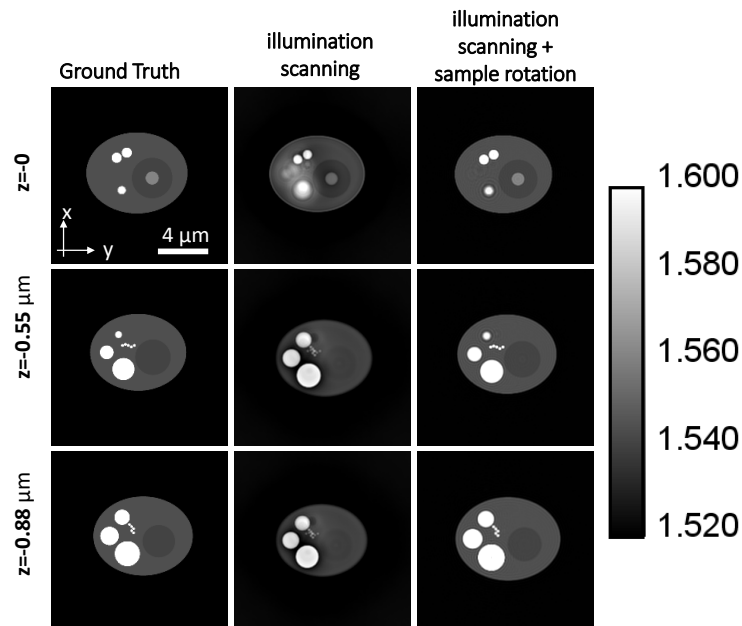


Figure 2-12. Comparison between different imaging modalities at different depths.

The best quality attained is reached by combining mesh scanning with sample rotation which can be described by Figure 2-13. In Figure 2-13 (a) we see the well-known doughnut shape with the missing cone problem along K_z while (b) and (c) shows the case when the mesh scanning is combined with sample rotation around y-axis with angle (0, 90) and (0,45,90,135), respectively. Figure 2-13 (d) shows an almost isotropic sphere along the 3 coordinates when mesh scanning is combined with sample rotation between 0 and 360 degrees with step size of 20 degrees. Such a perfect sphere which we refer to as “illumination scanning sample rotation – ISSR” results in an isotropic resolution along the 3 spatial coordinates given by [25]:

$$r_{x,y,z}^{ISSR} = \frac{2\pi}{\Delta k_{x,y,z}} = \frac{2\pi}{4k_0 n_0 \sin(\theta)} = \frac{2\pi}{4 \frac{2\pi}{\lambda} NA} = \frac{\lambda}{4NA} \quad (2.52)$$

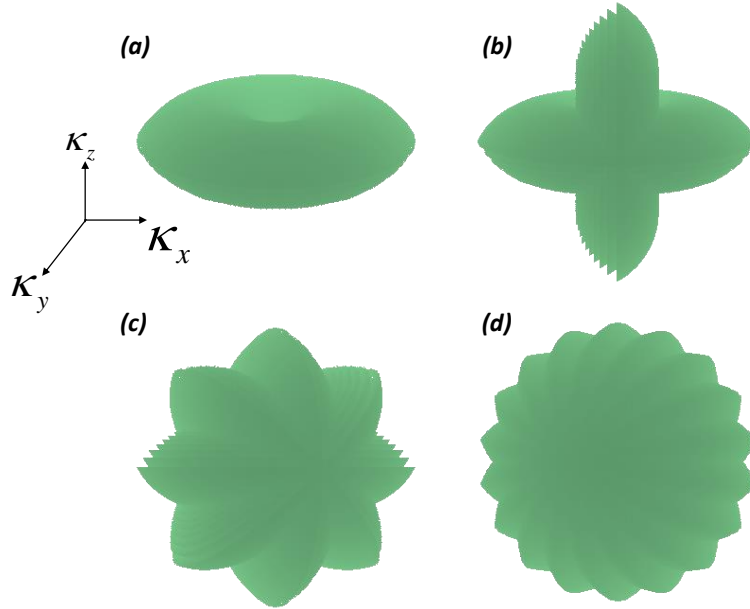


Figure 2-13. Frequency support for different imaging modalities. (a) Illumination mesh scanning only, (b) illumination mesh scanning and sample rotation by 0 and 90 degrees, (c) illumination mesh scanning and sample rotation by 0, 45, 90, and 135 degrees, and (d) illumination mesh scanning and rotation between 0 and 360 degrees with step of 20 degrees.

An alternative to the direct inversion methods (Born and Rytov) that rely on ignoring the effects of multiple scattering, is to use a nonlinear forward model that accounts for multiple scattering and iterative optimization and also solve the missing cone problem based on different computational forward models explained in [26-30].

7. Diffraction-Less Optical Tomography (Back-projection algorithm)

Unlike diffraction tomography described in the previous sections, filtered-back projection tomography does not solve the Helmholtz equation [21]. However, it assume that the measured phase is the integration of the RI distribution along a straight line and totally ignores light diffraction inside the sample. As a result, it deals with the measured complex field as the projection of the 3D map along the direction of the incident plane wave. Therefore, one could build the 3D k-space by simple mapping the 2D Fourier transform of the measured fields with the corresponding incidence angle which is followed by an inverse 3D Fourier transform to reconstruct the 3D RI distribution. The back-projection algorithm is valid as long as the features size of the sample is much bigger than the operating wavelength and that is why this approach is in X-ray CT scan in which the wavelength is much smaller than the size of the organs. However, for biological imaging when the imaging cells and/or tissues, the visible wavelength is comparable to the features size and this limits the reconstruction quality. Ignoring the wavelength value with respect to the features size of the sample results in mapping in the 3D k-space as a straight line instead of a spherical cap as shown in Figure 2-14. Usually we refer to the back-projection reconstruction as the “Radon” reconstruction.

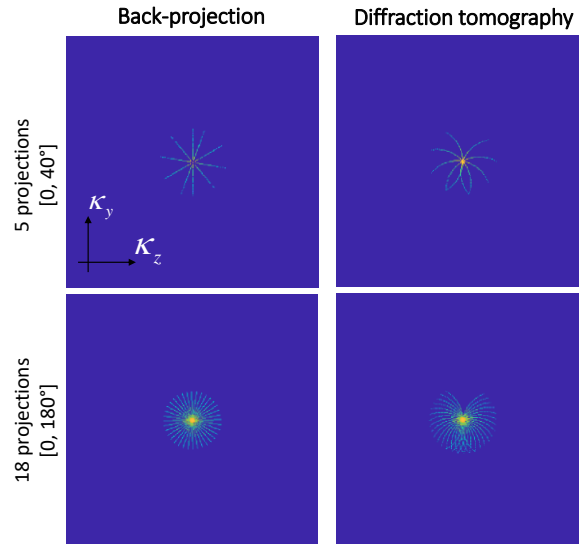


Figure 2-14. K-space coverage: Back-projection versus diffraction tomography

Figure 2-15 shows an image reconstruction using the radon transform for different number of projections. As can be observed, the higher the number of projections the better the reconstruction quality.

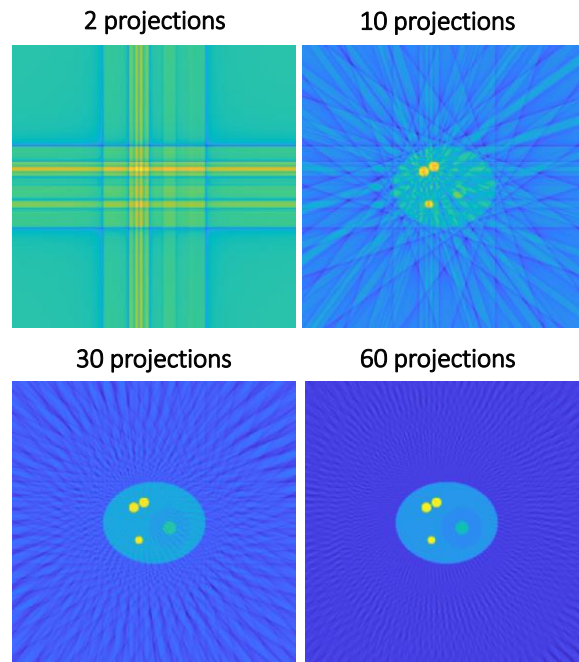


Figure 2-15. Effect of the number of projections on the reconstruction quality

The term “filtered” comes from the fact that we apply a filter for each projection to correct for the blurring associated with the back-projections. In other word, each projection is filtered before the back-projection process to correct the blurring effect. Figure 2-16 shows the difference between filtered and unfiltered back-projection algorithm for the same image in Figure 2-15 for 2 projections and 60 projections in which the blurring is completely removed by the filtered back-projection.

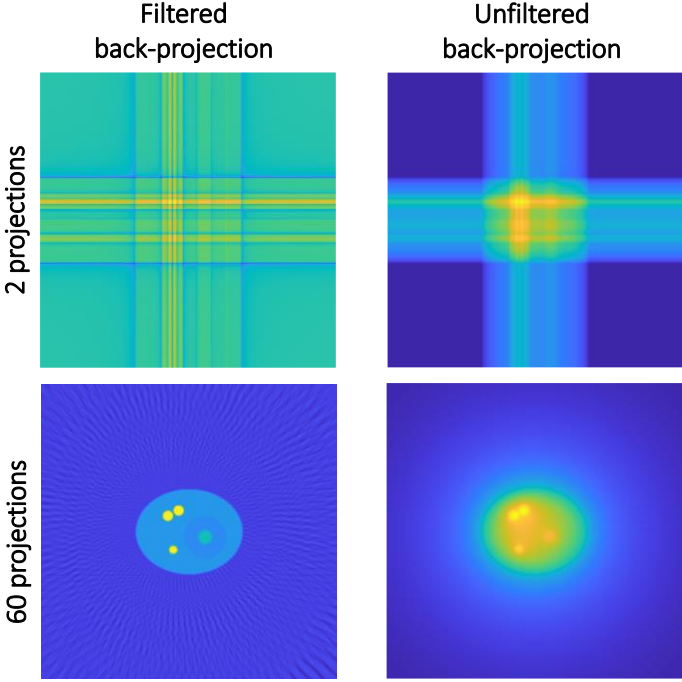


Figure 2-16. Filtered versus Unfiltered back-projection

Chapter 3 A Method for Assessing the Fidelity of Optical Diffraction Tomography Reconstruction Methods using Structured Illumination

This work has been published in [A. B. Ayoub, T.-A. Pham, J. Lim, M. Unser, and D. Psaltis, “A method for assessing the fidelity of optical diffraction tomography reconstruction methods using structured illumination,” Opt. Commun. 454, 124486 (2020)].

A.B. Ayoub built the optical setup, carried out the experiments, and the assessment.

1. Introduction

Light microscopy plays an important role in many fields and especially in label-free detection and characterization of microstructures and biological cells/specimens which becomes a primary goal for biomedical applications. Optical Diffraction Tomography (ODT) is an example of such quantitative characterization of biological specimens by reconstructing the 3D refractive index (RI). Several reconstruction methods have been employed for the RI reconstruction [9, 13, 19, 31-47]. Since ODT does not require staining, it can be used in various biological studies including immune cells [48], red blood cells [49], and embryos [50]. ODT images are formed by first recording the complex field of projections taken at different illumination angles. Excluding digital phantoms and samples for which we have a-priori knowledge (i.e. 3D printed samples), we generally lack information about the ground truth of 3D samples. This lack of information becomes particularly serious in biomedical applications since accurate characterization is necessary for diagnosis and cure. For example, in cellular imaging, this lack of information leads to uncertainty in the calculation of the RI of the sample which is interrelated to the protein concentration inside the cells. One way to quantify this uncertainty is through the use of phantom objects such as beads or microspheres. However, this way cannot be generalized to biological samples since their ground truth is not available.

In this paper we describe and experimentally demonstrate a method that provides a comparative metric for assessing the relative performance of reconstruction algorithms for arbitrary 3D objects without having access to their ground truth. To do this, digital phase conjugation and back-propagation through inhomogeneous media were used. The distortion imposed on an optical field propagating through an inhomogeneous medium with negligible absorption can be undone

if the transmitted field is holographically recorded and the phase conjugate reconstruction of the hologram is made to propagate backwards through the sample [51-54]. This is conveniently done in the optical domain by illuminating the recorded hologram with a plane wave counter-propagating to the plane wave used to record the hologram. When the incident beam illuminating the object is spatially modulated by a 2D pattern (an image), the field arriving at the hologram plane is a distorted version of the 2D illumination pattern. Through phase conjugation, this distortion is removed and the field arriving back at the input plane is ideally an exact replica of the original image. Deviations from this ideal condition can occur due to limited spatial bandwidth, absorption or other losses in the optical path. Any imperfection in the holographic recording and play-back of the hologram (including speckle) can also contribute to deviations of the phase conjugate reconstruction from the original image projected through the sample. In a carefully designed optical system in which the coherent noise is minimal (i.e. due to dust particles or multiple reflections from optical elements), we can generally obtain excellent phase conjugate reconstructions since the medium where the beam propagates through is well defined. The phase conjugate image is also strongly affected by any changes in the 3D object in the time between the recording of the hologram and the play-back. If the effect of noise is negligible, then any distortions in the phase conjugate image can be attributed to changes in the object itself. This effect has been used for many applications including imaging through diffusing media [51], turbidity suppression in biological samples [52, 53] and imaging through turbid media [54]. In this paper we use this effect to assess the accuracy of the estimate of a 3D reconstruction.

Figure 3-1 shows the overall idea behind the proposed assessment technique. First, different holograms from different illumination angles of the 3D object are recorded on a sCMOS camera using the experimental setup that is described below. Using this information, we can reconstruct the 3D refractive index map using well known algorithms (i.e. Radon [38], Born [19] and Rytov [35]). On the same setup, we illuminate a known pattern onto the sample with structured illumination by recording a pattern on the spatial light modulator (SLM). The pattern gets distorted by the 3D sample as it propagates through the 3D sample along the optical path. Phase conjugation of the distorted pattern is performed digitally by computationally propagating the conjugate of the experimentally measured field through the 3D object whose index distribution has been estimated using the above mentioned algorithms. Using accurate digital wave propagation and assuming perfect 3D reconstruction, we expect a faithful digital reconstruction of the pattern that was presented on the SLM. Distortions in the digital reconstruction of the 2D pattern that was placed on the SLM are partially due to inaccuracies of the 3D reconstruction algorithm. Measurement of the degree of distortion in the digital reconstruction of the SLM pattern provides a quantitative metric which we can use to compare ODT reconstruction algorithms.

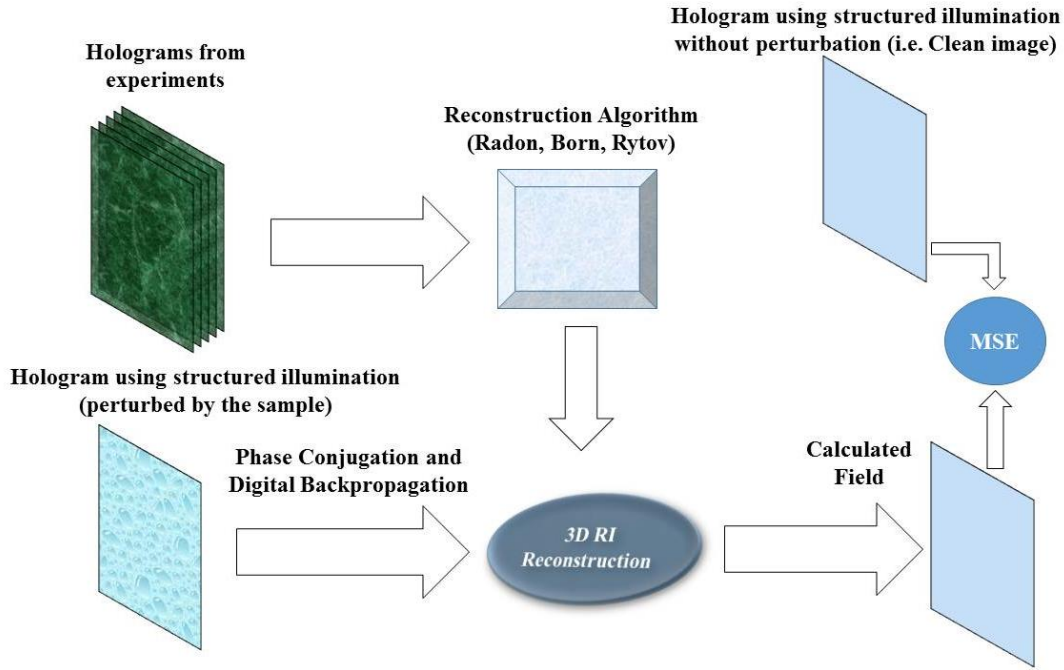


Figure 3-1. The overall scheme of the proposed assessment technique

The three commonly used reconstruction algorithms were tested: Radon [38], Born [19] and Rytov [35]. Comparisons between Born and Rytov have been performed in literature in different optical regimes [55-56]; however, such studies cannot directly be translated to arbitrary shaped samples such as biological samples. The proposed method in the paper can work as a good reconstruction assessment tool for any other reconstruction method [46, 57, 58]. The goal of this paper is to present the assessment method and therefore we did not include a comprehensive comparison of the entire set of reconstruction algorithms.

2. Materials and Methods

2.1. Experimental setup and samples

The optical system shown in Figure 3-2 used a diode pumped solid state (DPSS) 532 nm laser. The laser beam was first spatially filtered using a pinhole. A beam-splitter separated the input beam into a signal and a reference beam in an off-axis geometry. The signal beam was directed to the sample at different angles of incidence using a reflective liquid crystal on silicon (LCOS) spatial light modulator (SLM) (Holoeye PLUTO VIS, pixel size: 8 μm , resolution: 1080x1920 pixels) that modulates the phase of the incident beam. Different illumination angles were obtained by displaying blazed gratings on the SLM. In the experiments presented here, a blazed grating with a period of 25 pixels (200 μm) was rotated a full 360° with a resolution of 1 degree for a total of 361 projections, including normal incidence to be able to measure the shift of the k vectors with respect to it. Two 4f systems between the SLM and the sample permitted filtering of higher orders reflected from the SLM (due to the pixilation of the device) as well as 240x angular magnification of the SLM projections onto the sample. Using a 100X oil immersion objective lens (OBJ1) with NA 1.4 (Olympus), the incident angle on the sample corresponding to the 200 μm grating was about 37°. A third 4f system after the sample includes a 100X oil immer-

sion objective lens (OBJ2) with NA 1.45 (Olympus). The sample and reference beams were collected on a second beam-splitter and projected onto a scientific complementary metal-oxide-semiconductor (sCMOS) camera (Andor Neo 5.5 sCMOS, pixel size: 6.5 μm , resolution: 2150 x 2650 pixels). The samples used were HCT-116 human colon cancer cells and Panc-1 human pancreas cancer cells which were cultured in McCoy 5A growth medium (Gibco) supplemented with 10% fetal bovine serum (Gibco). #1 coverslips were treated with a 5 $\mu\text{g/mL}$ solution of fibronectin (Sigma) in phosphate-buffered saline (PBS) and let it to dry at room temperature. Cells at passage 18 were removed from culture flasks using trypsin, seeded directly onto the fibronectin-treated coverslips, and incubated 24 hours in a 37C/5% CO₂ atmosphere until cells adhered and spread on the coverslips. Each sample was fixed for 10 minutes at room temperature in 4% paraformaldehyde in PBS, rinsed twice with PBS, and sealed with a second coverslip.

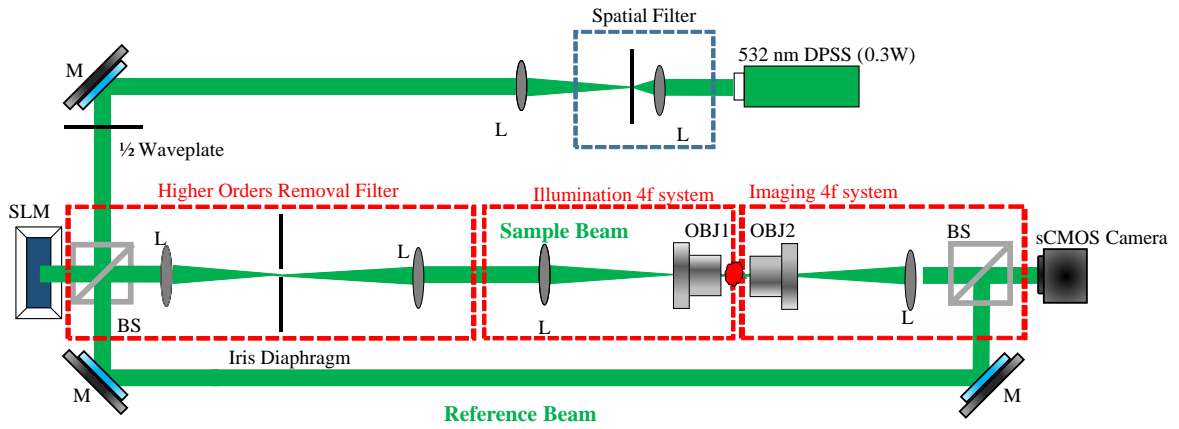


Figure 3-2. Experimental tomographic setup. (M: Mirror, L: Lens, OBJ: Objective lens, BS: Beam splitter). Pinhole-based spatial filter cleans out the beam spatially. The Higher orders cleaning filter removes the unneeded higher orders that might interfere at the image plane on the sample causing image deterioration.

2.2. Propagation model

To ensure accurate propagation through inhomogeneous medium, we used the Lippmann-Schwinger Equation (LSE) [59, 60]. The Lippmann-Schwinger equation is the same as the integral equation described in Born and Wolf [12]. This integral equation is formulated as follows

$$E(\mathbf{r}) = E_{\text{inc}}(\mathbf{r}) + \int G(\mathbf{r} - \mathbf{r}') E(\mathbf{r}') \eta(\mathbf{r}') d\mathbf{r}' \quad (3.1)$$

Where E_{inc} and E are the incident and total field respectively of wavelength λ . $G(\mathbf{r})$ denotes the

Green function, $\eta(\mathbf{r}) = k^2 \left(\frac{n^2(\mathbf{r})}{n_m^2} - 1 \right)$ is the scattering cross-section of the sample of refractive index

$n(\mathbf{r})$ with $k = \frac{2\pi}{\lambda} n_m$ the optical wavenumber in the medium of refractive index n_m .

Our numerical propagation is divided in two sequential steps:

$$E = (I - G \eta)^{-1} E_{\text{inc}} \quad (3.2)$$

$$E^{\text{meas}} = G^{\text{meas}} (E \eta) + E_{\text{inc}}^{\text{meas}} \quad (3.3)$$

Where η , E_{inc} denote the scattering cross-section of the sample and the incident field discretized in the region of interest (i.e., which includes the sample), and G denotes the discrete convolution with the Green function. Similarly, G^{meas} denotes the discrete convolution with the Green function that gets the scattered field at the sensors position and $E_{\text{inc}}^{\text{meas}}$ is the incident field at the sensors position. In Eq. (3.2), we compute the discrete total field E in the region of interest by inverting a matrix. In this work, we use the BiConjugate Gradients Stabilized Method to iteratively compute the matrix inverse [61]. In Eq. (3.3), E^{meas} refers the total field at the sensor positions. The LSE method is very accurate since beyond the scalar assumption, there is no further approximation. The multiple scattering events (including reflections) are fully accounted for as opposed to the beam propagation method.

2.3. Tomographic reconstruction methods

For 3D RI reconstruction, three computational techniques were considered; Radon, Born, and Rytov. ODT was first described by Wolf [19, 31] and refined by Devaney [35]. Like the first order Born approximation, the first order Rytov approximation is also a linearization of the inverse scattering problem but it has been found to yield superior results for biological cells and has been the most commonly used technique for linear ODT [35, 47]. One of the main differences between the Rytov and the Born models is the phase unwrapping that is explicit in the Rytov model [23]. This unwrapped phase is used instead of the field in the inversion formula introduced by Wolf (which we refer to as the Wolf transform). The third technique, the Radon direct inversion based reconstruction [38], is a filtered back-projection reconstruction algorithm that is based on diffraction-free model thus it generates errors when it comes to diffracting objects with spatial variations comparable to the wavelength of light. A phase unwrapping algorithm was used to unwrap the phase [22] of the holographically recorded projections. Two examples of such projections are shown in Figure 3-3. In the studied samples (i.e. HCT-116 cells and Panc-1 cells), the accumulated phase from the samples, whose thickness is around 8 μm , exceeds 2π at some regions depending on the proteins distributions as shown in Figure 3-3 (a, b). Both Radon and Born fail to reconstruct the 3D refractive index distribution due to considerable diffraction, and high phase accumulation by the sample, respectively. Slices in x-y and x-z of the 3D reconstructions of the two cells are shown in Figure 3-4. Notice that the methods based on the Born and Rytov approximations are significantly different in estimating the refractive index distribution.

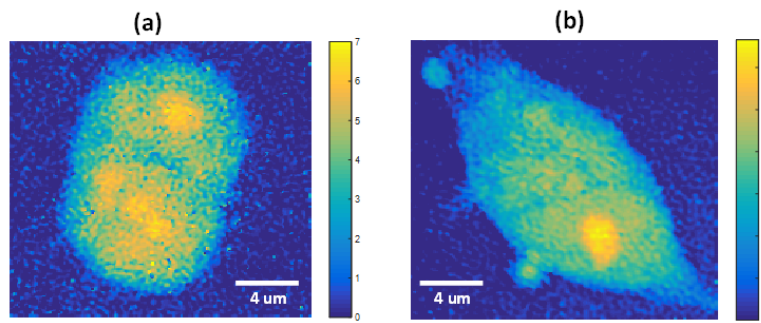


Figure 3-3. Unwrapped phase of (a) HCT-116 cell and (b) Panc-1 cell for normal incidence. Phase unwrapping was done using PUMA algorithms. Color bars are in Radians.

Cancer cells usually have a RI of cytoplasm that range between 1.36-1.39 due to excess RNA and protein [36]. As observed in Figure 3-4(a), this index range is probably under-estimated (i.e. around 1.32) due to high phase delay that Born cannot deal with. On the contrary, the Rytov approximation shows better agreement with what is expected from the biology of cells. The estimated index of the cytoplasm is around 1.365 which is within the expected range. Another interesting feature is the lipids which are composed of fats, sugars and proteins and are characterized by their high proteins concentrations and thus high RI value. This is in agreement with the Rytov reconstructions where we can see bright spots which do not show up in the Born approximation [36]. In Figure 3-4(b), it is obvious how the Born under-estimates the RI value of the nucleus as well where it should have much higher RI than the surrounding media (i.e., water) [36]. This could be because phase unwrapping is not considered and that is why we can see enhanced edges at the boundaries of the cell at the point where the phase wraps while the higher phase is under estimated. In addition the RI contrast between nucleus and medium is quite low in case of Born. On the other hand, Rytov agrees with literature where the high RI contrast is clear [36, 62-64].

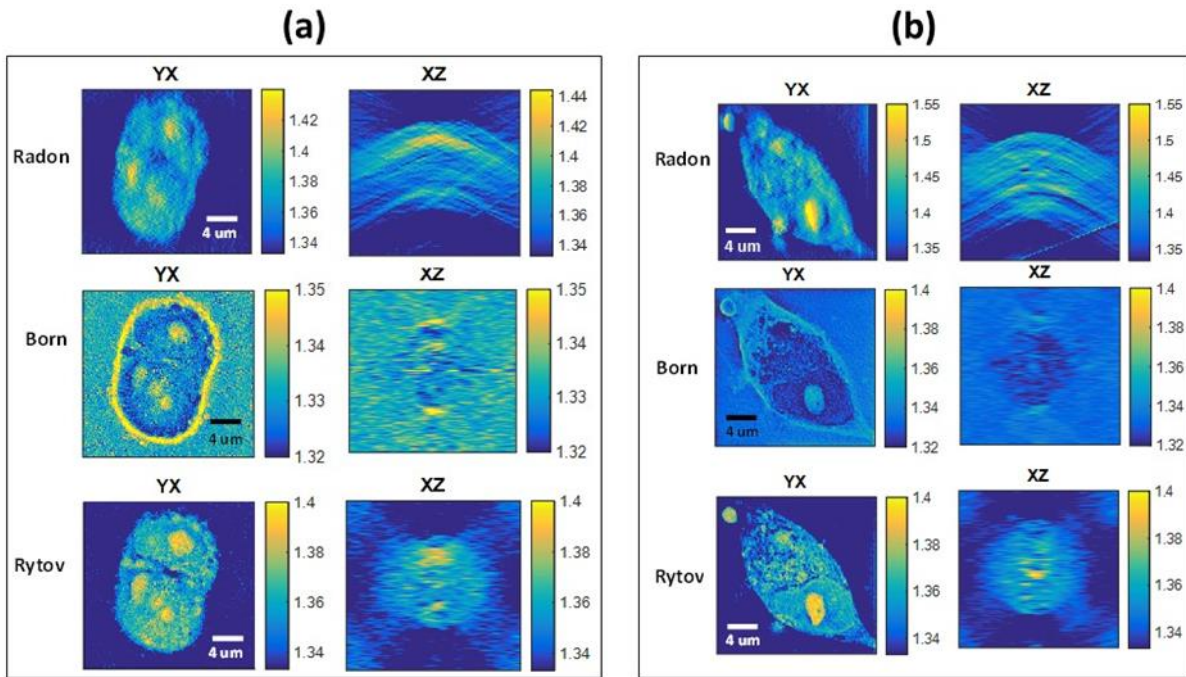


Figure 3-4. 3D reconstruction based on Radon, Born, and Rytov techniques for (a) HCT-116 cell and (b) Panc-1 cell.

3. Assessment results

We quantitatively assess the performance of each of the three reconstruction methods (i.e. Radon, Born, and Rytov) in the same experimental setup using digital phase conjugation method as described earlier. First we illuminated the 3D sample with a phase modulated beam with an image of Einstein or the 1951 USAF resolution test chart that are displayed on the SLM. The phase modulated beam that comes through the sample is holographically recorded on the sCMOS camera. The wrapped phase of such an image is shown in Figure 3-5. Structured illumination was used instead of plane waves since structured illumination by its own can be thought of as many plane waves propa-

gating at the same time and hence probe a larger portion of the 3D spectrum of the object. In addition, assessment using structured illumination ensures fairness as these patterns were not used in the tomographic reconstruction. In order to measure the incident field, we repeat the exact same measurement by propagating through the media (clear PBS liquid between two coverslips). We consider the measurement we obtain from this step as the “Original” pattern since there is minimal distortion along the optical path. The second step in the assessment is done computationally by back-propagating the modulated output (i.e. picture of Einstein or the USAF resolution test chart modulated with the HCT-116/Panc-1 phase delay) through the reconstructed 3D refractive index (RI) map. We use the Lippmann-Schwinger Equation (LSE) propagation model described above [59, 60]. The LSE method requires a larger memory and longer processing time (as compared to the beam propagation method [65] where reflections are neglected) however this method is more accurate. From these two steps, we expect an accurate refractive index reconstruction to result in a clean reconstruction of the original structured illumination pattern. Comparison with the original pattern measured from the experiment without the cell gives us a quantitative measure of the accuracy of the ODT method. Figure 3-6 shows the retrieved Einstein and 1951 USAF resolution test chart for the case of Radon, Born, and Rytov approximations as compared to the original field using this procedure.

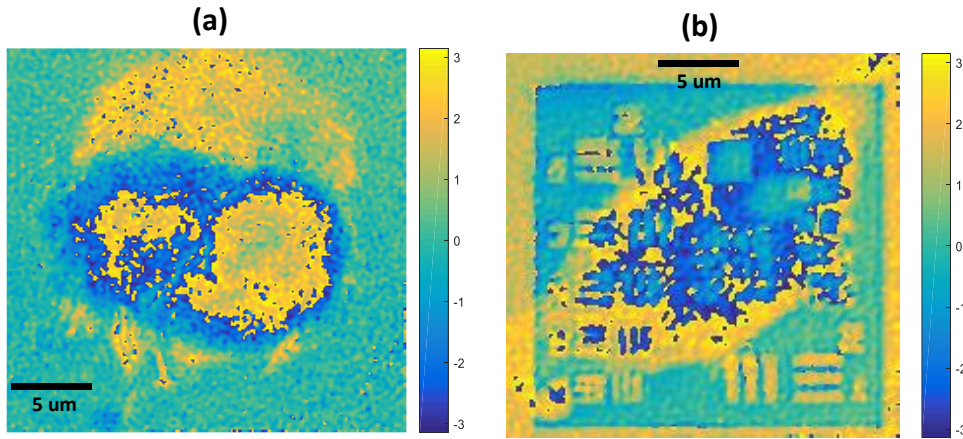


Figure 3-5. Wrapped phase of Einstein/USAF chart after propagating through the HCT-116/Panc-1 cell.

To quantify the error, the mean square error (MSE) between the measured and retrieved fields is calculated. Assessment was done for reconstructions provided by Radon, Born, and Rytov approximations as shown in Tables 1, and 2. The MSE in the case of Born reconstruction is high as compared to Radon and Rytov (at least 3 times higher than MSE for Rytov). This is due to the fact that both Radon and Rytov make use of the unwrapped phase whereas the Born reconstruction algorithm is implemented on the complex field. The Radon reconstruction scheme depends on the unwrapped phase; however it ignores diffraction which limits its performance as compared to Rytov which have the best performance by taking into account phase unwrapping, and diffraction.

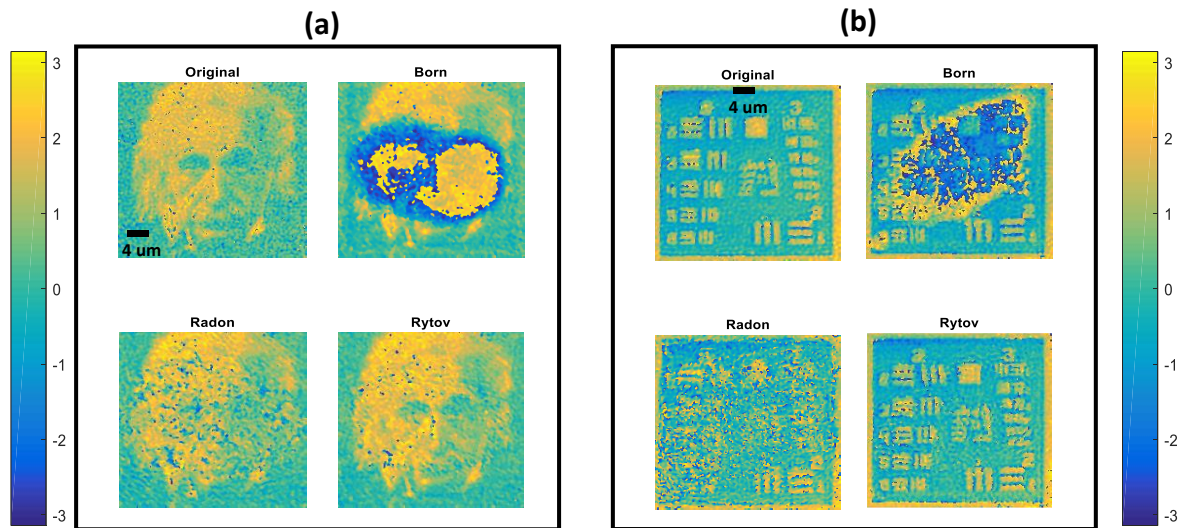


Figure 3-6. Retrieved projected fields using Radon, Born, and Rytov for (a) Einstein through HCT-116 cell, and (b) USAF chart through Panc-1 cell.

Table 1. MSE percentage for Radon, Born and Rytov based Reconstruction techniques for Einstein

Radon	Born	Rytov
8.83%	34.73%	6.39%

Although the MSE values are changing from one case to another (depending on phase profile, dimensions and diffraction strength), the three reconstructions follow the same trend where Born has the worst performance as compared to Radon and Rytov.

Table 2. MSE percentage for Radon, Born and Rytov based Reconstruction techniques for USAF chart

Radon	Born	Rytov
16.19%	24.58%	7.97%

Chapter 4 3D Reconstruction of weakly scattering objects from 2D intensity-only measurements using the Wolf transform

This work has been published in [A.B. Ayoub, Joowon Lim, Elizabeth E. Antoine, and Demetri Psaltis, "3D reconstruction of weakly scattering objects from 2D intensity-only measurements using the Wolf transform," Opt. Express 29, 3976-3984 (2021)].

A.B. Ayoub built the optical setup, carried out the experiments, and reconstructions.

1. Introduction

Optical Diffraction Tomography (ODT) is a powerful label-free measurement tool which can be used for high-speed live imaging of transparent objects in three-dimensional space [9, 19, 23, 32, 36-37, 66-68]. By acquiring 2D projections from different illumination angles and extracting their complex amplitudes, an estimate of the 3D refractive index (RI) distribution of an object can be reconstructed using inverse scattering models [23]. To obtain the complex amplitude, a digital holographic microscopy (DHM) setup is needed. An advantage of ODT over conventional phase imaging techniques is that, by recording both amplitude and phase of the scattered field, it can provide quantitative information about the sample. An alternative to using DHM to measure both the amplitude and phase at the detector is the measurement of only the intensity of the total field, which can subsequently be used to retrieve the phase. For example, phase can be inferred from non-holographic intensity measurements using the transport of intensities principle [69]. In the context of ODT, M. Maleki *et al.* used an iterative scheme based on the Gerchberg-Saxton algorithm (GS) [70] to retrieve the phase map from the intensity profile for each 2D projection [71]. The same group used intensity measurements to retrieve an RI estimate through a direct inversion procedure [72]. In their work, the intensity of the far-field was measured for different illumination angles. The intensity measurement includes not only a component from which the 3D object can be reconstructed, but also a twin image whose contribution to the final 3D reconstruction was negligible in their study. More recently, other works that used a direct inversion approach to retrieve the refractive index distribution out of the intensity measurements have also been demonstrated using detailed modeling of the propagation of light through the 3D sample in reflection geometry [73-75]. An alternative approach to direct inversion is a reconstruction of the 3D RI distribution of a sample from far-field intensity by using complex iterative schemes which minimize an error function [59, 30, 76-82]. Tian and Waller used this approach with LED illumination [78], and more recently, Pham *et al.* [80] used an iterative reconstruction scheme based on the Lippmann-Schwinger forward model using intensity measurements. Chowdhury *et al.* used a beam propagation model (BPM) as the forward model [81] to estimate the 3D refractive index from intensity-only measurements, where high-resolution reconstructions were obtained with lateral and axial resolutions of ≤ 240 nm and \leq

900 nm, respectively. R. Ling et al. [82] took yet another approach to intensity diffraction tomography, deriving phase and absorption transfer functions as a function of the pupil function, power of illumination beam, and the Green's function. In their work, the cost function consists of (1) the data fidelity term which is the difference between the actual measurement and the predicted measurement from the forward model and (2) Tikhonov regularization which was the l_2 regularization of the permittivity. By imposing a minimum total energy constraint on the cost function, a closed form for the real and imaginary part of the permittivity by manipulating the regularization parameters. While this approach produces a refractive index measurement from intensity-only measurements, it only accounts for single scattering events and requires regularization and minimization operations.

The Wolf transform [19] is a well-known operator which maps the 2D Fourier transform of the measured field for each 2D projection onto a spherical cap in the 3D Fourier domain to reconstruct the scattering potential. Multiple 2D projections are measured, and their Fourier transform is incorporated in the 3D Fourier domain of the object. This is followed by an inverse 3D Fourier transform to reconstruct the refractive index map spatially. The *Born* reconstruction is obtained when the complex field of the 2D projections that serve as the input to the Wolf transform is used without unwrapping the phase while the *Rytov* reconstruction is obtained by utilizing the unwrapped phase [23]. In this paper, we apply the Wolf transform to the amplitude only of the total field, which can be obtained from an intensity-only measurement and obtain 3D reconstructions. We show that we obtain reconstructions whose shape is same as the *Born* and *Rytov* methods but the contrast mechanism is different, displaying a strong enhancement of nanostructures within the 3D sample. The aims of this work are to examine the effect of applying the Wolf transform on intensity-only measurements and to elucidate the physical phenomena seen in the resulting reconstructions. We provide a theoretical analysis for the twin image effect, usually seen in on-axis holography (i.e., Gabor holography) [83], which we observe using the Wolf transform. Finally, we demonstrate the effect of the twin image on the final 3D reconstruction using experimental measurements and suggest possible biological applications of the present study.

2. Principle

The experimental system we used is shown in Figure 4-1[84]. A diode-pumped solid-state (DPSS) 532 nm laser was used. The laser beam is spatially filtered and collimated with a pinhole and a pair of lenses. Signal and reference beams are separated in an off-axis configuration using a non-polarizing beam splitter. The signal beam illuminates the sample with oblique illuminations in a conical illumination scenario over a full 360° rotation with a resolution of 1° for a total of 361 projections, including normal incidence. Oblique illuminations are obtained using blazed gratings written on a spatial light modulator (SLM) (Holoeye; pixel size = $8\ \mu\text{m}$ and resolution = 1080×1920 pixels). Higher orders from the SLM are filtered using an iris diaphragm. Using an objective lens OBJ1 (Olympus: numerical aperture = 1.4, 100X, oil immersion) as the illuminating lens, the angle of incidence on the sample is 35° . A 4f system after the sample includes an objective lens OBJ2 (Olympus: numerical aperture = 1.45, 100X, oil immersion) and a regular lens to image the sample onto the detector. For holographic detection, the signal and reference beams are combined using a non-polarizing beam splitter and projected onto a scientific complementary metal-oxide-semiconductor (sCMOS) camera (Andor Neo 5.5 sCMOS, pixel size = $6.5\ \mu\text{m}$, resolution = 2150×2650 pixels). HCT116 human colon cancer cells were cultured in McCoy 5A growth medium (Gibco) supplemented with 10% fetal bovine serum (Gibco). #1 coverslips were treated with a $5\ \mu\text{g/mL}$ solution of fibronectin (Sigma) in phosphate-buffered saline (PBS) and air-dried at room temperature. Cells at passage 11 were detached from culture flasks using trypsin, seeded directly onto the fibronectin-treated coverslips, and incubated 24 hours in a $37^\circ\text{C}/5\%\ \text{CO}_2$ atmosphere until cells adhered and spread on the coverslips. Each sample was fixed for 10 minutes at room

temperature in 4% paraformaldehyde in PBS, rinsed twice with PBS, and sealed with a second coverslip.

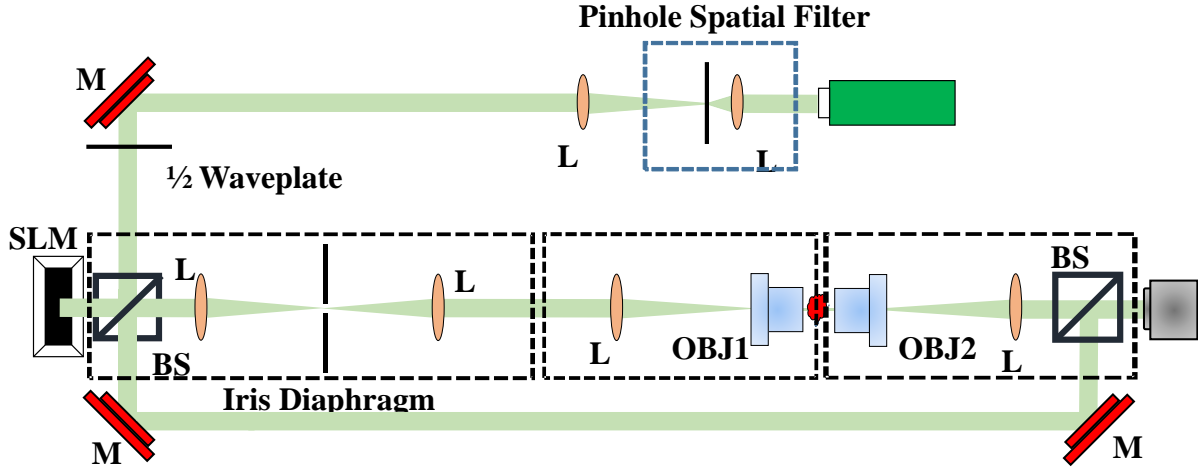


Figure 4-1. Experimental tomographic setup. (M: Mirror, L: Lens, OBJ: Objective lens, BS: Beam splitter) An iris diaphragm is used to block the extra orders generated by the SLM due to its limited fill factor. 4f systems represented by the dotted rectangular blocks are used to obtain an imaging plane at the best plane of focus of the immersion objective lenses.

The 2D field incident in the detector of the ODT system is $E_t(x, y, z = z_0)$ where x, y, z are the Cartesian coordinates of the system and z_0 is the plane of best focus along the optical axis. The detected intensity is

$$|E_t|^2 = |E_i|^2 + |E_s|^2 + 2|E_i||E_s|\cos(\phi_s - \phi_i) \quad (4.1)$$

where $|E_t|$ is the amplitude of the total field, $|E_i|$ is the amplitude of the incident field, $|E_s|$ is the amplitude of the scattered field, and $\phi_s - \phi_i$ is the difference between the phases of the scattered and incident fields. For weakly scattering objects ($|E_s| \ll |E_i|$) and defining $E_i = e^{j\phi_i}$, $|E_i| = 1$, then equation (4.1) can be rewritten as follows:

$$\begin{aligned} |E_t|^2 &\approx 1 + 2|E_s|\cos(\Delta\phi) \\ \Rightarrow |E_t| &= \sqrt{1 + 2|E_s|\cos(\Delta\phi)} \end{aligned} \quad (4.2)$$

where $\Delta\phi = \phi_s - \phi_i$. Due to the assumption of weakly scattering objects ($|E_s| \ll 1$), $|E_t|$ can be approximated as follows:

$$\begin{aligned} |E_t| &= \sqrt{1 + 2|E_s|\cos(\Delta\phi)} \\ |E_t| &\approx 1 + \frac{1}{2}(2|E_s|\cos(\Delta\phi)) \\ &= 1 + \frac{1}{2}|E_s|e^{j\Delta\phi} + \frac{1}{2}|E_s|e^{-j\Delta\phi} \end{aligned} \quad (4.3)$$

Multiplying both sides of equation (4.3) by $E_i = e^{j\phi_i}$, we obtain:

$$\begin{aligned}
 |E_t| e^{j\phi_t} &= \frac{1}{2} |E_s| e^{j\phi_s} + e^{j\phi_t} + \frac{1}{2} |E_s| e^{-j\phi_s} e^{2j\phi_t} \\
 &= \frac{1}{2} E_s + e^{j\phi_t} + \frac{1}{2} E_s^* e^{2j\phi_t} \\
 &= \frac{1}{2} E_s + e^{j\phi_t} \left(1 + \frac{1}{2} E_s^* e^{j\phi_t} \right)
 \end{aligned} \tag{4.4}$$

Although the term on the left-hand side of equation (4.4) is not the complex scattered field, it does include the phase information contained in the scattered field term E_s . We refer to E_s as the principal image to differentiate it from the twin image (the 3rd term in Eq. 4.4). Equation 4 relates the measurement obtained from an intensity-only imaging system (i.e., $|E_t| e^{j\phi_t}$) to the information accessible only when using a holographic setup (i.e. E_s). Equation 4 includes the contribution of the scattered field to the intensity measurement. However, it also contains the contributions of the twin image $\frac{1}{2} E_s^* e^{2j\phi_t}$ in addition to $e^{j\phi_t}$.

Since $e^{j\phi_t}$ does not include the scattering effect of the sample, it does not result in any index perturbation and does not contribute to the final 3D reconstruction. We will show that under certain conditions the term $E_s^* e^{2j\phi_t}$ (the complex conjugate of E_s shifted by $2\vec{k}_i$ in Fourier domain where \vec{k}_i is the propagation vector of the incident plane wave), results in an inverted phase and negative RI contrast compared to E_s and acts approximately as a cancelling term to E_s . When the numerical aperture of the optical system (OBJ2 in Figure 4-1) is large enough to allow the twin image to reach the detector, then this approximate cancelation effect is most prominent for the plane of best focus. This is experimentally observed as we report later in this paper. Figure 4-2 demonstrates the importance of multiplying the total field amplitude $|E_t|$ (middle column) by the incident field $e^{j\phi_t}$ (right column) for correct mapping in the Fourier domain before applying the Wolf transform (c.f. Equation (4.4)). Although this step is not critical for reconstructions using iterative schemes as in [21-24], it is crucial for reconstructions using the Wolf transform, which relies on the direct inversion of the scattering potential. With normal incidence (top row), the scattered field $\frac{1}{2} E_s$ (solid red circle) and twin image $e^{j\phi_t} (\frac{1}{2} E_s^* e^{j\phi_t})$ (orange dashed circle) are both centered in the Fourier domain, overlapping. However, under oblique plane wave illumination (second and third rows), the scattered field and its twin image are both shifted off-center when the uncorrected total field is plotted (middle column). Multiplying by the incident field $e^{j\phi_t} = e^{i(\vec{k}_i \cdot \vec{r})}$ (right column) results in the scattered field remaining fixed at the center (as with normal incidence) while only the twin image is shifted. This has a profound effect on the summation of projections used to obtain the scattering potential, as it means that the summed scattered fields are mapped correctly in 3D Fourier-space. In contrast, their twin images rotate around them according to the k-vectors of the incident field.

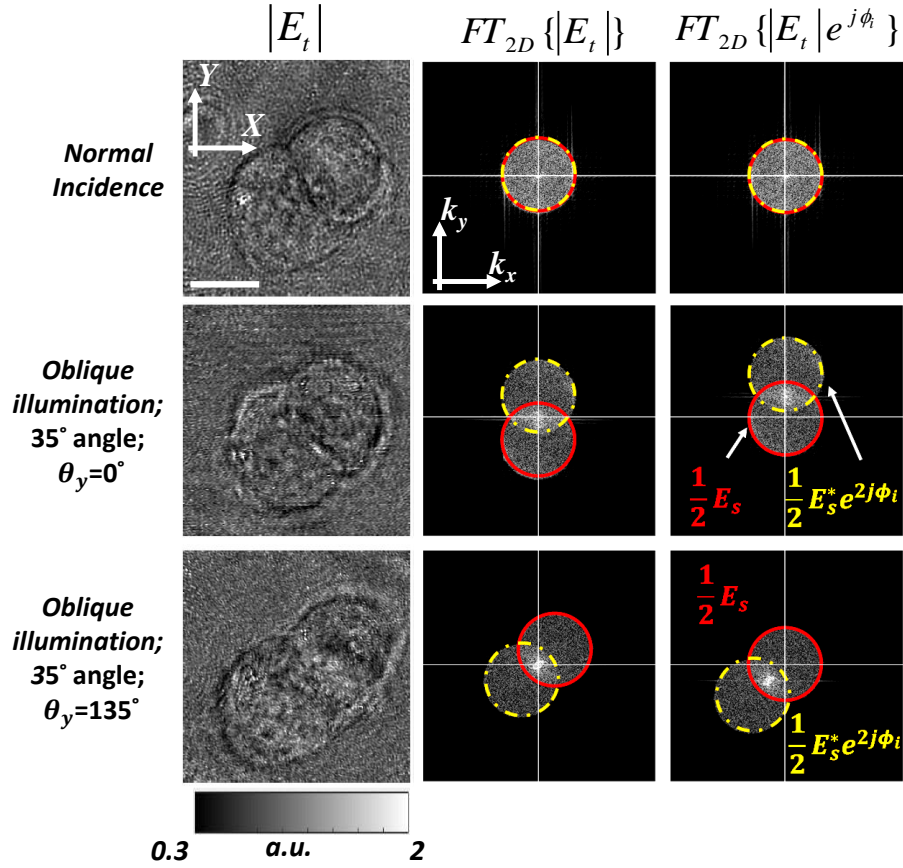


Figure 4-2. The amplitude of measured total field and associated 2D Fourier transforms (logarithmic scale). The middle column shows the Fourier transform of the raw intensity map where the principal image (red circle) and the twin image (orange circle) appear concentric for normal illumination and symmetrically shifted around the origin for different oblique illuminations. The right-most column shows the Fourier transform of the raw intensity map after shifting by k_i in the frequency domain as a result of multiplying by the incident wave in the spatial domain. Scale bar = 9 μm .

3. Results

The contribution of the scattered field and its twin image to the total scattering potential is demonstrated in Figure 4-3 for various projections taken at different illumination angles. θ_y refers to the inclination angle of the conical illumination from the y-axis where $\theta_y=0$ refers to $k_x=0$ while $\theta_y=90$ refers to $k_y=0$. Fig. 3A shows the fields shown in the third column of Figure 4-2 after masking out frequencies outside the limited NA of the imaging system. Figure 4-3(B) shows the summation over all projections when each is mapped with its own k-vector. For the scattered field ($\frac{1}{2}E_s$), all frequency components are retained by the NA filter (Figure 4-3(B-I)); however, since $e^{j\phi_i}(\frac{1}{2}E_s^* e^{j\phi_i})$ is not centered around the origin, the high frequency components are removed by the NA of the imaging lens (OBJ2) as seen in Figure 4-3(B-II). This term therefore affects the contrast in the 3D reconstruction.

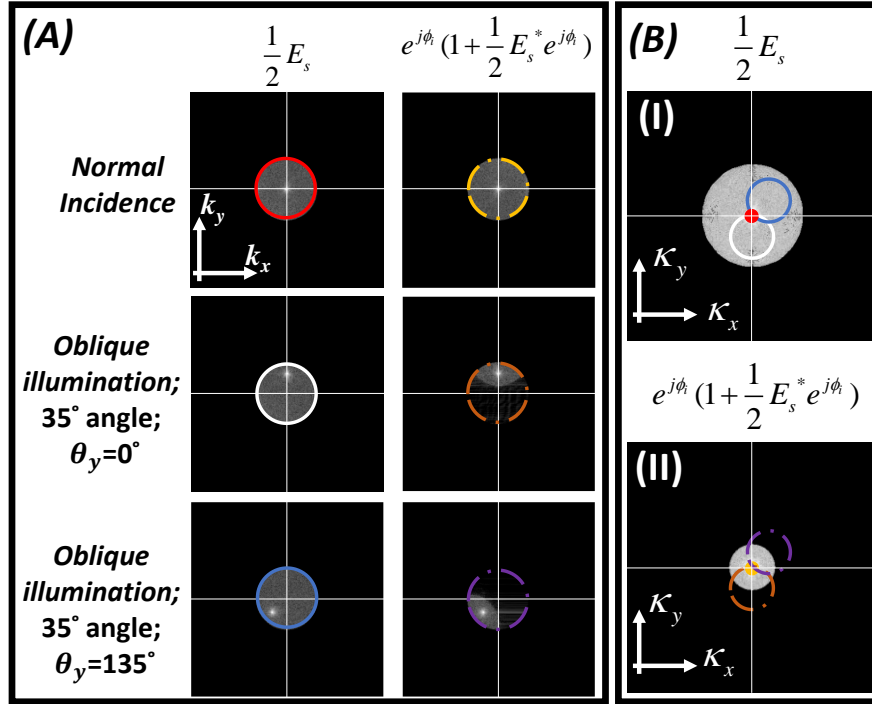


Figure 4-3. (A), The spectrum of the different field components as a function of (k_x, k_y) of the scattered field (left) and its twin image (right) for different illumination angles, (B) 3D Fourier transform of the estimated scattering potential as a function of the spatial frequency components $(\kappa_x, \kappa_y, \kappa_z)$ of the object plotted in 2D at $\kappa_z = 0$ for (I) the scattered fields and (II) the twin images. Panel (B) shows how the 2D projections are mapped inside the 3D Fourier space of the object where the colored circles in Panel (A) are mapped according to the incident \vec{k} -vector \vec{k}_i . Note that the size of the scattering potential in B(I) at is not $(4k \cdot NA)$ as shown by the green dotted line since we are not illuminating with the maximum possible angle allowed by the numerical aperture of the objective lens.

In Figure 4-4, we see the contributions of each component of the recorded field amplitude (c.f. Eq. 4.4) at different axial slices in the 3D reconstruction of an HCT116 cell. We first note that the reconstruction based only on $\frac{1}{2} E_s$ (Figure 4-4(A), also shown in Fourier space in Figure 4-3(B-I)) is materially the same as the *Born* reconstruction (scaled by $\frac{1}{2}$). This reconstruction was obtained using the holographic recording mode of our experimental set-up. The inverted contrast of the twin image component (Figure 4-4(B)) is evident at all planes.

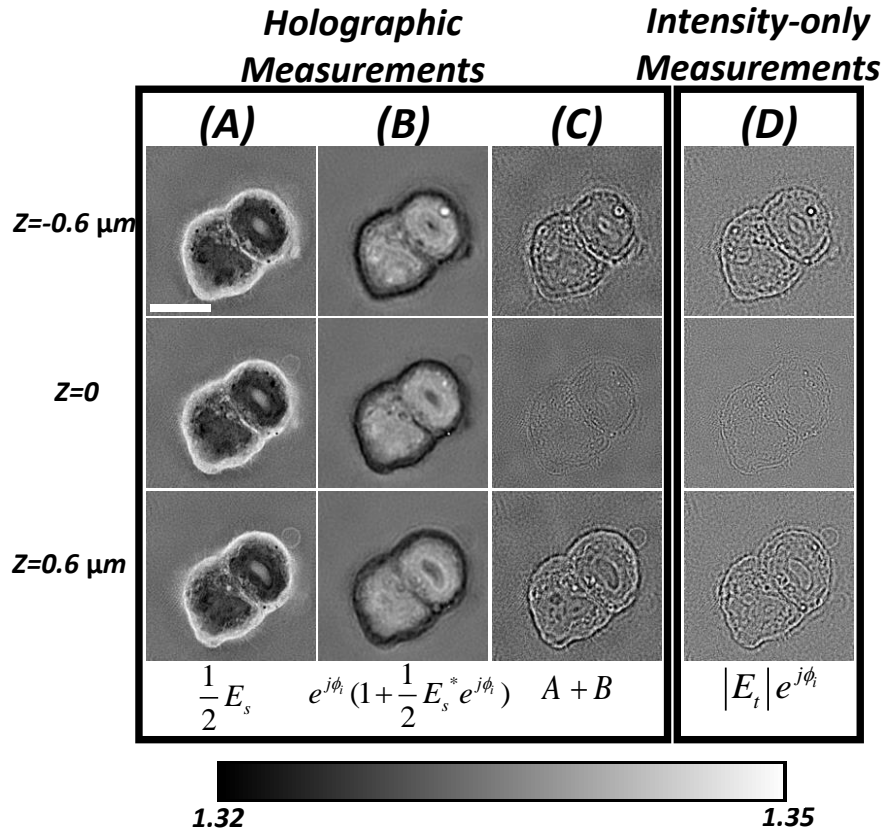


Figure 4-4. HCT116 cell XY slices of 3D reconstructions at different depths obtained from (left) holographic measurements of the complex field and (right) intensity-only measurements. Columns (A), (B) and (C) were retrieved using the holographic mode in our optical setup, while column (D) represents the intensity-only measurement, Columns (C) and (D) show high structural similarity index which validate the proposed study. Scale bar = 9 μm. Colorbar shows the estimated RI map for (A) and (B) while it shows the modified refractive index map for (C) and (D) using the proposed method.

The sum of the principal image and the twin image is shown in Figure 4-4(C). In the plane of best focus $z=0$, the low frequencies cancel one another and disappear almost entirely due to the inverted sign of the twin image. However, because the high-frequency components of the twin image are outside the NA filter (c.f. Figure 4-3), this component only contributes to the low frequencies of the scattering potential, resulting in an edge-enhanced image at different planes along z (where z is the propagation direction). Figure 4-4(D) shows the 3D reconstruction obtained directly using intensity-only measurements as input to the Wolf transform. According to our analysis, this reconstruction is equivalent to the reconstruction obtained using the full complex field (Figure 4-4(C)). We confirmed the similarity between columns C and D by calculating the structural similarity index (SSIM) [85]. The SSIM, computed for each XY slice and averaged over all slices (160 slices in our analysis), was $99 \pm 0.2\%$ over the 3D volume, quantitatively validating the approximations used to derive equation (4.4). This result demonstrates the feasibility of applying this method for intensity-only 3D reconstruction of complex samples and confirms our explanation for the qualitative observations of contrast phenomena. The observed increase in contrast as we move away from the plane of best focus is due to the fact the principal image diffracts differently from the twin image due to the conjugation. Finally, we compare our proposed intensity-only 3D reconstruction with those obtained using the classical *Born* and *Rytov* approximations (Figure 4-5). As the *Born* reconstruction is retrieved by using the complex field (i.e. no phase unwrapping involved), we observed that it shows an inverted contrast in specific regions within the cell as compared to the *Rytov* reconstruction which is implemented based on the unwrapped phase. Compared to *Born* and *Rytov*, which give a quantitative estimate of the RI, the amplitude-only reconstructions produce a modified RI-like measurement with artificially enhanced edges in regions of high phase gradients. For cellu-

lar imaging, this enables efficient localization of elements such as lipids and the cell membrane which are difficult to identify from RI alone. Despite not getting the true refractive index map, the proposed technique is able to highly localize nanostructures inside the sample or on the surface (i.e. lipids in biological samples). This is demonstrated in Thomsen et al. [86], in which we used the 3D reconstructions from intensity measurements to localize Polylactic acid (PLA) particles with 200-220 nm diameter on the membranes of T-cells. These measurements were used to validate results obtained from standard fluorescence-based imaging.

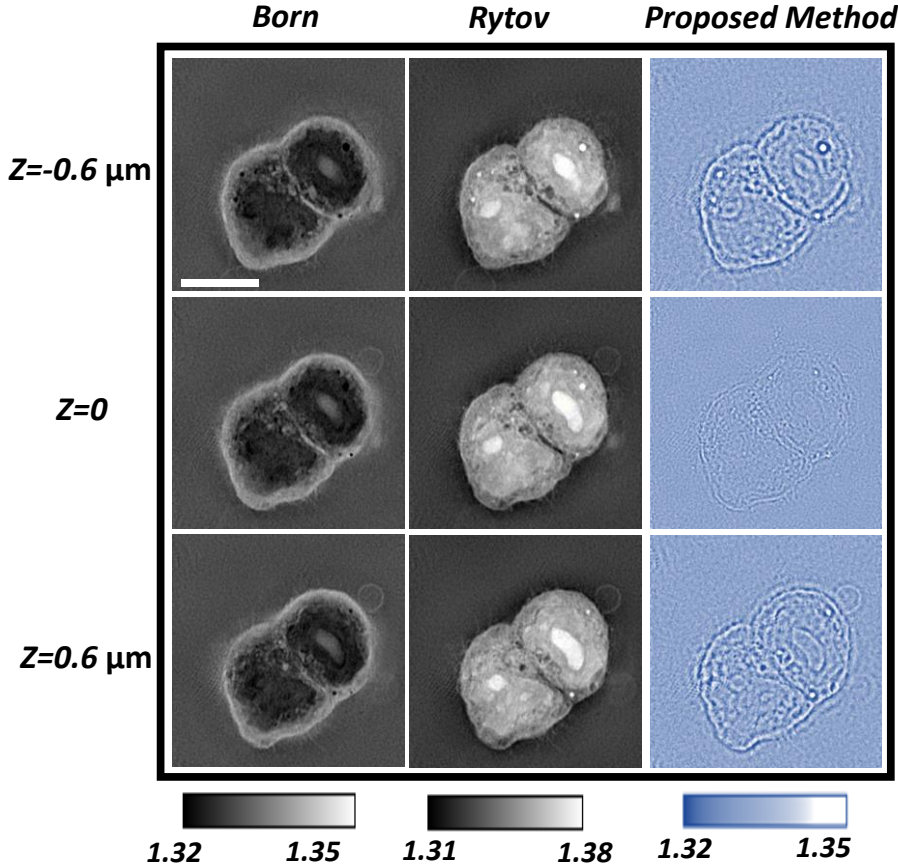


Figure 4-5. HCT116 cell XY slices of 3D reconstructions at different depths obtained using Born, Rytov, and intensity-based reconstruction methods. While Born and Rytov provide a quantitative estimate of the 3D refractive index map, intensity-based reconstruction shows a modified refractive index map where only the high frequency components inside the cell (i.e. cell membrane and lipid structures). Scale bar = 9 μm .

4. Supplementary information

4.1. Defining the modified scattering potential due to the intensity measurement

Starting from equation 4.4:

$$\begin{aligned} |E_t| e^{j\phi_t} &= \frac{1}{2} |E_s| e^{j\phi_s} + e^{j\phi_t} + \frac{1}{2} |E_s| e^{-j\phi_s} e^{2j\phi_t} \\ &= \frac{1}{2} E_s + e^{j\phi_t} + \frac{1}{2} E_s^* e^{2j\phi_t} \\ &= \frac{1}{2} E_s + e^{j\phi_t} \left(1 + \frac{1}{2} E_s^* e^{j\phi_t} \right) \end{aligned}$$

Although the term on the left hand side of equation (4.4) is not the complex scattered field, it does include the phase information contained in the scattered field term E_s . We will refer to E_s as the principal image in

order to differentiate it from the twin image due to the third term in Equation (4.4). Equation 4.4 is the key formula for this work, as it relates the measurement obtained from an intensity-only imaging system to the information accessible only when using a holographic setup, E_s . In what follows, we analyze the effect of the additional terms, $e^{j\phi} (1 + \frac{1}{2} E_s^* e^{j\phi})$, on the final 3D reconstruction from both theoretical and experimental perspectives.

We assume that the incident field is a plane wave with propagation vector \vec{k}_i . By measuring the scattered field at $z=0$ along the direction $\vec{k} = (k_x, k_y, k_z)$, one Fourier component of the 3D spectrum of the scattering potential $\tilde{F}(\vec{k})$ can be retrieved:

$$\tilde{F}(\vec{k}) = \frac{k_z}{2\pi j} \tilde{E}_s(k_x, k_y) \quad (4.5)$$

where

$$\vec{k} = \vec{k} - \vec{k}_i = \begin{bmatrix} k_x - k_{ix} \\ k_y - k_{iy} \\ \sqrt{(k_0 n_0)^2 - k_x^2 - k_y^2} - k_{iz} \end{bmatrix},$$

where $\tilde{E}_s(k_x, k_y)$ is the 2D Fourier transform of $E_s(x, y, z=0)$, \vec{k} is the 3D spatial frequency of the scattering potential, $k_0 = \frac{2\pi}{\lambda}$, λ is the wavelength of the illumination beam, and n_0 is the refractive index of the surrounding medium. Equation (4.5) is referred to as the Wolf transform.

By applying equation (4.5) for different 2D projections and integrating in the 3D Fourier domain, the 3D spectrum $\tilde{F}(\vec{k})$ can be measured. Subsequently, $F(r)$ can be spatially reconstructed using an inverse 3D Fourier transform. Finally, $n(r)$ is retrieved using the following equation:

$$F(r) = \frac{k_0^2}{4\pi} (n^2(r) - n_0^2) \approx \frac{k_0^2}{2\pi} n_0 \Delta n \quad (4.6)$$

where $\Delta n = n(r) - n_0$ and the approximation holds for small Δn .

Similar to equation 4.5, we can define a modified scattering potential, $\tilde{F}_m(\vec{k})$, that is related to the 2D Fourier transform of the modulated amplitude of the total field $|E_t|e^{j\phi}$ rather than the complex scattered field E_s .

The modified scattering potential $\tilde{F}_m(\vec{k})$ is calculated by applying a 2D Fourier transform to equation (4.4) as follows:

$$\begin{aligned} \tilde{F}_m(\vec{k}) &= \frac{k_z}{2\pi j} FT_{2D}\{|E_t|e^{j(k_{ix}x + k_{iy}y)}\} \\ &= \frac{k_z}{2\pi j} \left[\frac{1}{2} \tilde{E}_s(\vec{k}_x, \vec{k}_y) + \delta(k_x - k_{ix}, k_y - k_{iy}) + \frac{1}{2} \tilde{E}_s^*(-k_x + 2k_{ix}, -k_y + 2k_{iy}) \right] \end{aligned} \quad (4.7)$$

where $FT_{2D}\{.\}$ denotes the 2D Fourier transform. Since $\delta(k_x - k_{ix}, k_y - k_{iy})$ does not contain any scattering from the sample. As shown in Figure 4-6, using this term only to reconstruct the 3D shape of the sample results in no RI contrast since this term does not contains any scattering effects from the sample.

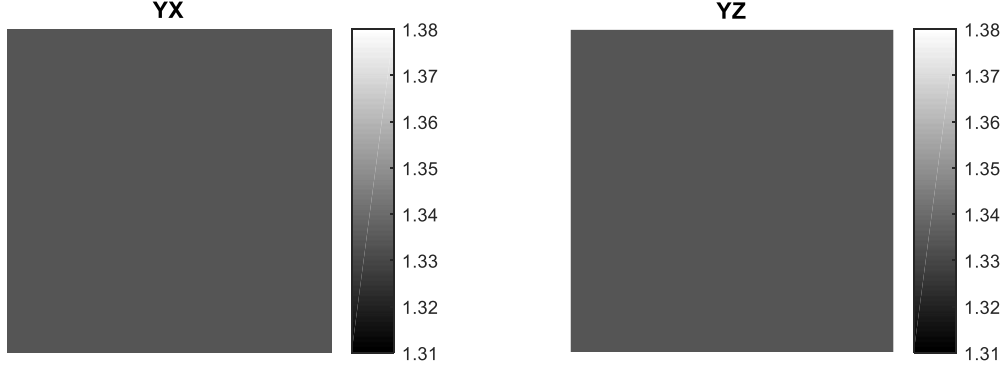


Figure 4-6. RI reconstruction from applying the Wolf transform on the incident field ($\delta(k_x - k_{ix}, k_y - k_{iy})$).

Therefore, the modified scattering potential is further simplified to:

$$\begin{aligned} \tilde{F}_m(\vec{k}) &= \frac{k_z}{2\pi j} FT_{2D}\{|E_t|e^{j(k_{ix}x + k_{iy}y)}\} \\ &= \frac{k_z}{2\pi j} \left[\frac{1}{2} \tilde{E}_s(\vec{k}_x, \vec{k}_y) + \frac{1}{2} \tilde{E}_s^*(-k_x + 2k_{ix}, -k_y + 2k_{iy}) \right] \end{aligned} \quad (4.8)$$

4.2. Mapping of the twin image into 3D kappa space

We use Equation 4.8 to examine how the modified reconstruction ($\tilde{F}_m(\vec{k})$) is affected by the twin image by plotting the twin image in 2D Fourier space (Figure 4-7). Figure 4-7(a) shows the 2D Fourier transform of $\tilde{E}_s^*(-k_x + 2k_{ix}, -k_y + 2k_{iy})$ where the blue dotted circle indicates the $2k_{iy}$ shift. The “rugby-ball” overlap shown in red corresponds to the part of the twin image that passes through the numerical aperture of the objective lens (OBJ2) and contributes to the reconstruction. When the 2D spectrum is mapped to 3D kappa space, the rugby-ball spectrum is distributed over a spherical cap given by $(k_x, k_y, k_z = \sqrt{(k_0 n_0)^2 - k_x^2 - k_y^2})$ as shown in Figure 4-7 (b). Figure 4-7(b) includes a 3D rendering of the spherical cap as well as its 2D projections. Note that the center point of rugby-ball spectrum (marked with a blue X in Figure 4-7), representing the DC term of the scattered field (located at \vec{k}_i), is mapped to the origin in 3D kappa space according to the relation $\vec{k} = \vec{k} - \vec{k}_i$. The mapping in Figure 4-7(b) indicates that there is a low-pass filtering effect on the twin image, as its higher frequency components are outside the NA and excluded from the final result. We can infer from Figure 4-7 that illumination at the NA-limited maximum angle would eliminate overlap between the twin image and the optical system NA in Fourier space, reducing the rugby-ball spectrum to zero.

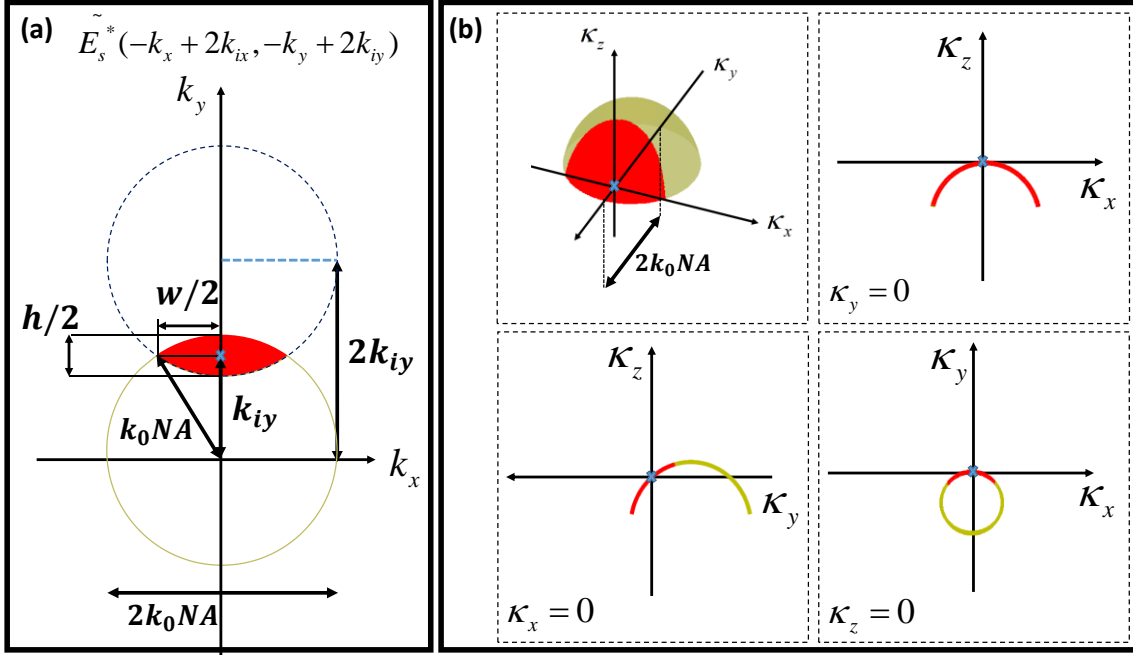


Figure 4-7. Mapping of the twin image from 2D Fourier space to in 3D object spectrum space (kappa space).

(a) The blue dashed circle represents the spectrum of the twin image for $(k_{ix} = 0, k_{iy} \neq 0, k_{iz} = \sqrt{k_i^2 - k_{iy}^2})$ while the green circle represents the numerical aperture of the optical system. The red “rugby-ball” region represents the portion of the twin image that passes through the numerical aperture. (b) Mapping of the twin image into the 3D spectrum of the object space results in distribution of the 2D rugby-ball shaped spectrum onto a 3D spherical cap.

From Figure 4-7, we conclude that $h = 2(k_0 NA - k_t)$ and $w = 2\sqrt{(k_0 NA)^2 - k_t^2}$, where k_t is the tangential illumination vector.

When the sample is illuminated in a conical pattern (as in our illumination scenario), k_t is given as:

$$k_t = \sqrt{k_{ix}^2 + k_{iy}^2} = \sqrt{(k_0 n_0 \sin \alpha_{ill} \sin \theta_i)^2 + (k_0 n_0 \sin \alpha_{ill} \cos \theta_i)^2} = k_0 n_0 \sin \alpha_{ill} \quad (4.9)$$

where $[k_{ix}, k_{iy}, k_{iz}] = [k_0 n_0 \sin \alpha_{ill} \sin \theta_i, k_0 n_0 \sin \alpha_{ill} \cos \theta_i, k_0 n_0 \cos \alpha_{ill}]$, α_{ill} is the conical illumination angle and θ_i is the azimuthal angle along the cone.

In order to estimate the individual contributions of the principal and twin images to the spatial distribution of the 3D reconstruction, their spatial frequencies must be mapped accurately. To this end, we compared the mapping into 3D kappa space of the spatial frequencies of the principal image with those of the conjugated principal image and those of the twin image (Figure 4-8). Figure 4-8 (a) shows the $(k_y - k_z)$ cross-section of the 3D spherical cap at $k_x = 0$ for the principal image, where colored spots are used to indicate a set of distinct spatial frequencies. By taking the conjugate of the scattering potential in the spatial domain, we obtain the spectrum shown in Figure 4-8 (b). The mirroring of the spherical cap around the origin is as expected, since conjugation in spatial domain results in conjugation and mirroring in the frequency domain (equation 4.7):

$$\begin{aligned} \because F(r) &\Leftrightarrow \tilde{F}(\vec{k}) \\ \therefore F^*(r) &\Leftrightarrow \tilde{F}^*(-\vec{k}) \end{aligned} \quad (4.10)$$

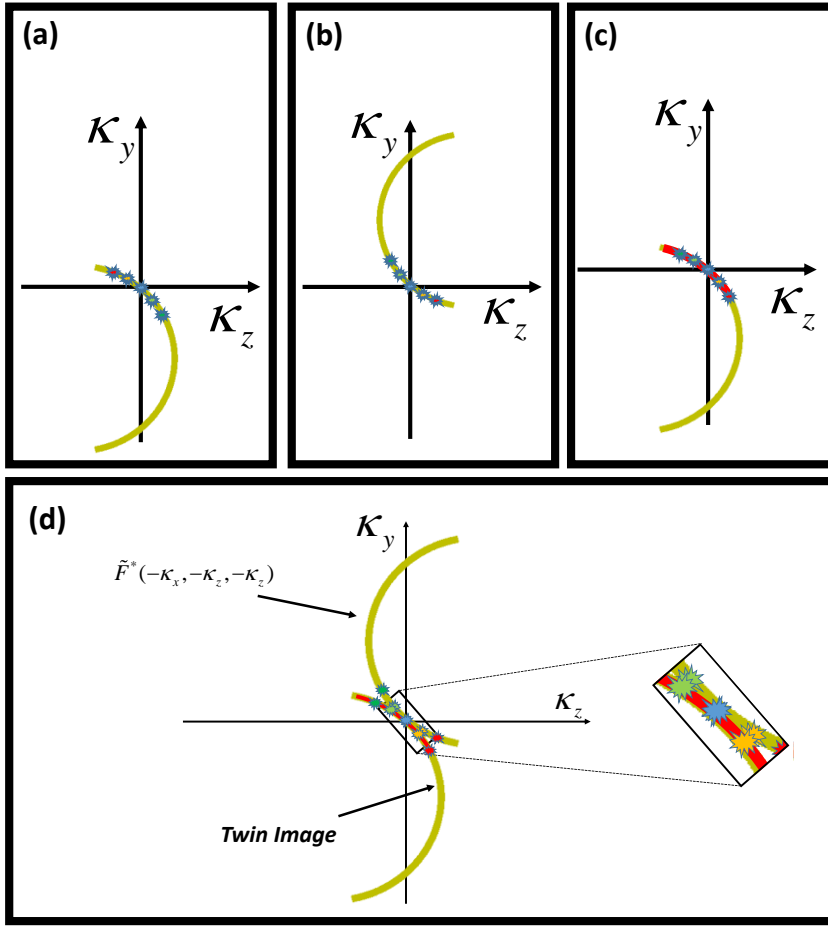


Figure 4-8. Cross-section of the spherical cap, at $\kappa_x = 0$, in the (κ_y, κ_z) plane for the (a) principal image, (b) conjugated principal image $\tilde{F}^*(-\vec{\kappa})$, (c) twin image, and (d) overlaid conjugated principal image and twin image. In parts (c) and (d), the red part of the line corresponds to the red rugby-ball of Figure 4-7. The colored spots show the same set of spatial frequencies for the four plots.

In contrast, the spherical cap of the twin image (Figure 4-8 (c)) is in exactly the same position as that of the principal image (Figure 4-8(a)) because both share the same $\vec{\kappa}$ vector. However, because the 2D spectra of both the principal and twin images are centered around k_i (which is mapped to the origin of 3D Kappa space as shown in Figure 4-7), the positions of the frequencies in the example set (colored spots) are reversed. Comparison of the twin image with the conjugated principal image (Figure 4-8 (d)) shows that their spatial frequencies are closely aligned (highlighted by the black rectangle in Figure 4-8 (d)), resulting in the twin image producing a similar reconstruction to that which would be obtained from the conjugated principal image.

Another observation related to the twin image is that it shows an inverted contrast compared to the conjugated principal image. This inversion is attributed to the missing minus sign in the twin image term ($\frac{k_z}{2\pi j} \frac{1}{2} \tilde{E}_s^*(-k_x + 2k_{ix}, -k_y + 2k_{iy})$) as compared to the conjugated principal image (minus sign in the right hand side multiplied by k_z in $\tilde{F}^*(\vec{\kappa}) = -\frac{k_z}{2\pi j} \tilde{E}_s^*(k_x, k_y)$).

From the previous discussion in Figure 4-7 and Figure 4-8, it is reasonable to rewrite the modified scattering potential as follows:

$$\begin{aligned}
 \tilde{F}_m(\vec{k}) &= \frac{k_z}{2\pi j} \left[\frac{1}{2} \tilde{E}_s(\vec{k}_x, \vec{k}_y) + \frac{1}{2} \tilde{E}_s^*(-k_x + 2k_{ix}, -k_y + 2k_{iy}) \right] \\
 &\approx \tilde{F}(\vec{k}) - LPF\{\tilde{F}^*(-\vec{k})\} + \hat{O}(\vec{k}) \\
 \Rightarrow F_m(\vec{r}) &= FT_{3D}^{-1}\{\tilde{F}_m(\vec{k})\} = F(\vec{r}) - LPF\{F^*(r)\} + O(\vec{r})
 \end{aligned} \tag{4.11}$$

where $FT_{3D}^{-1}\{.\}$ is the inverse 3D Fourier transform, $LPF\{.\}$ is the low pass filtering from the rugby-ball shaped spectrum as shown in Figure 4-7, $\hat{O}(\vec{k})$ is the error resulting from the imperfect alignment between $\tilde{F}^*(-\vec{k})$ and the twin image as shown in Figure 4-8, and $O(\vec{r})$ is the corresponding error function in the spatial domain. Equation 4.11 can be further simplified by assuming non-absorbing objects ($F^*(\vec{r}) = F(\vec{r})$) and hence the modified scattering potential in the 3D object space can be retrieved as follows:

$$\begin{aligned}
 F_m(\vec{r}) &= F(\vec{r}) - LPF\{F(\vec{r})\} + O(\vec{r}) \\
 \Rightarrow F_m(\vec{r}) &= HPF\{F(\vec{r})\} + O(\vec{r})
 \end{aligned} \tag{4.12}$$

where $HPF\{.\}$ is high pass filtering applied to $F(\vec{r})$. Figure 4-9 shows the 3D reconstruction using conventional Rytov reconstruction and our approach for Jurkat cells (T lymphocytes) modified with nanoparticles in PBS where the high pass filtering effect is observed. Jurkat cells (clone E6-1, cat. no. TIB-152) were obtained from ATCC. Nanoparticle-modified cells and unmodified control cells were fixed for 20 min in 4% paraformaldehyde solution in PBS, washed twice with PBS, and sedimented on a coverslip by centrifugation (3 min, 200g). Cells were then left for 15-minutes to maintain perfect adherence to the coverslip.

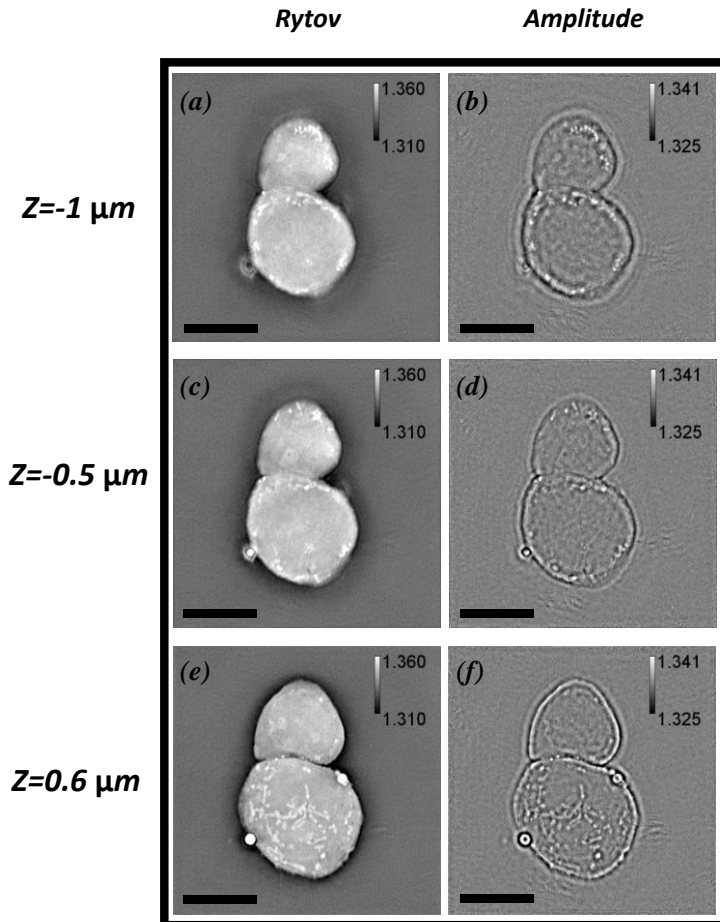


Figure 4-9. 3D reconstruction using intensity measurements at the different axial positions. Scale bar = 10 μm .

The effect of this filtering is also evident in the RI reconstruction at the best plane of focus ($z=0$) (Figure 4-10), where high frequency features appear sharp while low frequency features are blurred.

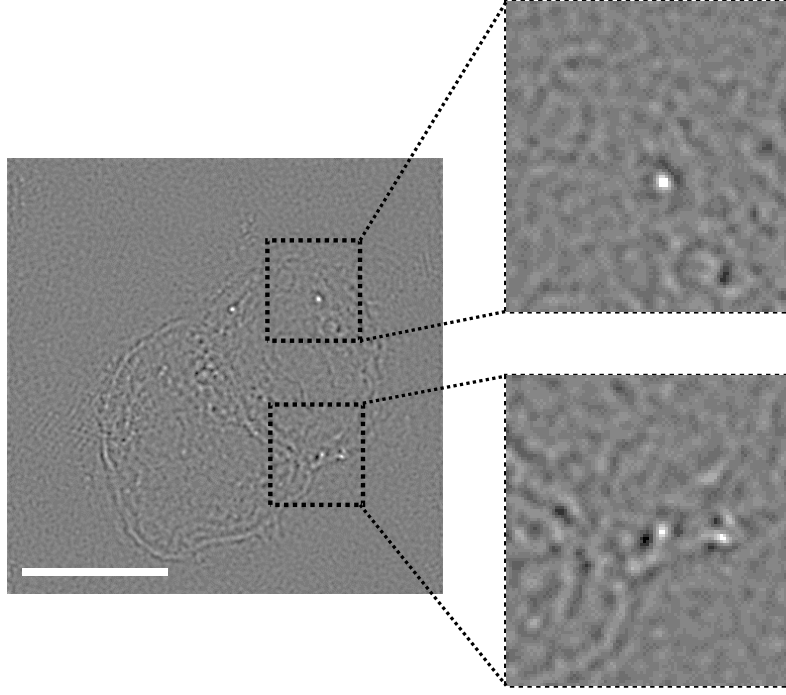


Figure 4-10. 3D reconstruction using intensity measurements at the best plane of focus. Scale bar = 9 μm .

4.3. Effect of numerical aperture of the imaging lens (OBJ2) on the contribution of the twin image to the 3D reconstruction

To further investigate the relationship between the twin image and the final reconstruction, we numerically varied the NA of the imaging objective lens from 0.8 to 1.333 (Figure 4-11). Figure 4-11 shows the modified refractive index map in the 3D object space (n_m) governed by equation (4.13):

$$F_m(r) = \frac{k_0^2}{4\pi} (n_m^2(r) - n_0^2) \quad (4.13)$$

$$\Rightarrow n_m = \text{Re} \left\{ \sqrt{\frac{4\pi}{k_0^2} F_m(r) + n_0^2} \right\}$$

As expected from the visualization of the relationship between NA and the twin image (Figure 4-7), reducing the NA weakens the contribution of the twin image to the final reconstruction and the reconstruction from the intensity-only measurement approaches the reconstruction obtained using the Born approximation with complex measurements. In comparison, increasing the NA increases the contribution of the twin image, producing a reconstruction with reduced contrast. At the maximum NA of 1.333 (limited by the use of a water-based medium surrounding the sample), only the very highest frequencies remain in the reconstruction. Lower contrast was seen as the contribution of the

twin image is getting higher as we increase the NA of the objective. Figure 4-11, the contribution of the twin image is increased as NA increased but with the illumination angle fixed which is why the when the illumination angle matches exactly with the numerical aperture, the twin image will be eliminated. In other words, regardless the numerical aperture, when the illumination angle is exactly the same as the maximum angle allowed by the numerical aperture, the twin image will be completely eliminated. This was expressed in Figure 4-11 but with changing “digitally” the numerical aperture while the illumination angle was fixed. By decreasing the NA of the imaging system (i.e. illumination angle is approaching more the maximum angle from this digitally-modified NA), the contribution of the twin image appears to decrease and thus better contrast is revealed. Better SNR can be achieved by using a laser diode (bandwidth of few nanometers) which significantly reduce the speckle noise (improve the SNR) as compared to solid state laser.

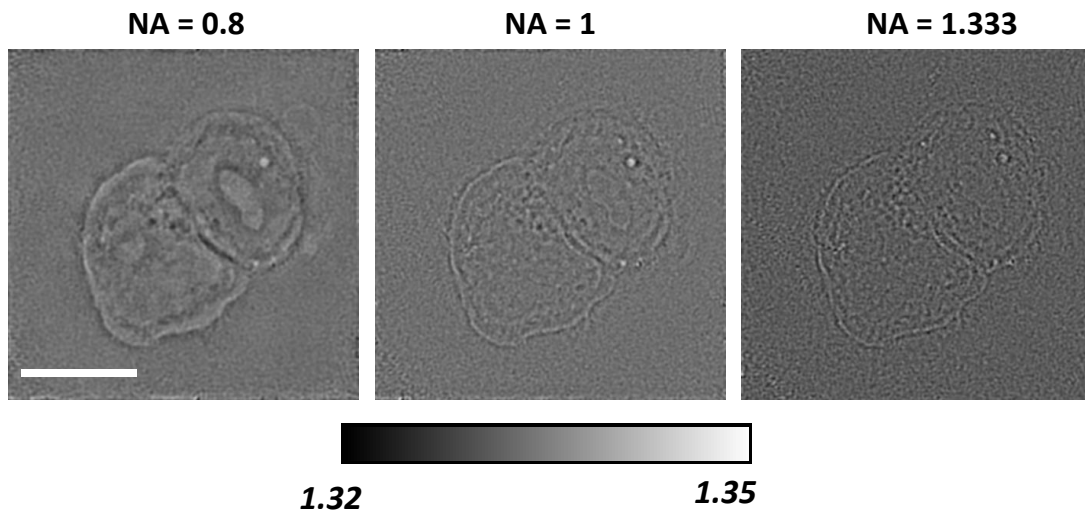


Figure 4-11. Modified RI reconstruction for numerical apertures (a) 0.8, (b) 1.0, and (c) 1.333. Increasing the numerical aperture increases the contribution of the twin image to the reconstruction, eliminating low-frequency information and reducing overall contrast. Scale bar = 9 μm .

Chapter 5 Optical Diffraction Tomography using nearly in-line Holography with broadband LED source

This work has been published in [Ayoub, A.B.; Roy, A.; Psaltis, D. Optical Diffraction Tomography Using Nearly In-Line Holography with a Broadband LED Source. Appl. Sci. 2022, 12, 951. <https://doi.org/10.3390/app12030951>].

A.B. Ayoub calibrated the optical setup, carried out the experiments, and performed the reconstructions.

1. Introduction

Optical Diffraction Tomography (ODT) has been an emerging tool for label-free imaging of different semi-transparent samples in three-dimensional space [9, 19, 23, 32, 36-37, 47, 66-68]. Being semi-transparent, such objects do not strongly alter the amplitude of the field. However, the total phase delay at a particular wavelength as a function of the refractive index contrast between the sample and the surrounding medium, the thickness of the sample. Due to this ambiguity, one cannot distinguish between those parameters from just 2D images and 3D imaging would be essential to decouple the refractive index contrast from the thickness of the sample by reconstructing the 3D map of the refractive index contrast (3D RI). Hence, to reconstruct the 3D RI map of different semi-transparent samples, a holographic detection is needed to extract the phase of the field after passing through the sample. Then, by acquiring different holograms from different illumination angles, the 3D RI map can be reconstructed using inverse scattering models [23].

Holographic detection was introduced by Gabor who used “in-line” holography. He showed that the intensity image retrieved from the in-line holography is composed of an “in-focus” image in addition to an “out-of-focus” image (i.e. “Twin” image) [13]. Due to this “Twin” image problem, in-line holography usually encounters problems in order to retrieve the phase of the object. Upatnieks and Leith proposed “off-axis” holography [15]. In this configuration, a small tilt is introduced between the reference arm and the sample arm which results in shifting in the Fourier domain the “out-of-focus” image with respect to the “in-focus”. Since then, “off-axis” interferometry has been widely used in ODT by first extracting the phase before using the inverse models [17-18, 33].

Several limitations remain that limit the use of ODT in biological imaging. These limitations include phase instability due to interferometry and laser fluctuations, and speckle artifacts due to the high coherence of the laser source. To overcome these limitations, Lei Tian, Laura Waller and co-workers used a relatively broadband source (i.e. LED illumination) to illuminate the sample for Fourier ptychographic and 3D imaging [78, 87-89]. In particular, in [78], Tian and Waller used LED illumination and demonstrated an iterative reconstruction scheme with a multi-slice forward model to estimate the 3D complex RI distribution by minimizing an error function between the intensity patterns estimated from the forward model. Their approach showed in-focus reconstruction at different depths while taking multi scattering phenomena into account.

In recent years, this approach was demonstrated both in reflection and transmission configurations [73-75, 90-92]. For example, a motion-free illumination scanning scheme was demonstrated for 3D RI reconstruction using an LED ring that mimics a circular scanning approach [82]. Other approaches to intensity diffraction tomography include the use of iterative schemes to reconstruct the 3D RI map from 2D intensity images using non-linear iterative schemes that minimize an error function [80, 81]. These models usually starts with an initial guess of the 3D RI that it keep modifying by minimizing the error between the actual measurement from the experiment and the intensity profile from the forward physical model.

In the earlier work [78] the phase and absorption transfer functions were calculated in the spatial domain using the intensity images as a function of the illumination angle. In this work, we use LED illumination and apply the Fourier diffraction theorem or Wolf Transform [19, 93] in order to reconstruct the 3D scattering potential in the 3D Fourier space followed by a 3D inverse Fourier transform to produce the 3D RI distribution. The reconstructions showed higher resolution, lower speckle noise and high contrast reconstructions compared to the results we presented earlier for a Wolf transform reconstruction applied to projections obtained with a laser illumination [93].

We begin by discussing the use of the Fourier diffraction theorem on the “on-line” intensity data for the retrieval of the 3D RI map of the sample. We describe the theory behind our work, we then show the reconstructed 3D RI map. After that, we show the effect of slight misalignment of the illumination on the quality and contrast of the 3D RI reconstruction. Finally, we show the effect of adding different wavelength on the final reconstruction.

2. Theory

The intensity pattern captured by the detector of the ODT system is $I_t(x, y)$ with x and y being the horizontal and the vertical dimensions of the 2D intensity pattern. The detected intensity is given by:

$$I_t = |U_i|^2 + |U_s|^2 + 2|U_i||U_s|\cos(\varphi_s - \varphi_i) \quad (5.1)$$

, where I_t is the intensity pattern after passing through the sample, $|U_i|$ is the amplitude of the incident field, $|U_s|$ is the amplitude of the scattered field, and $\varphi_s - \varphi_i$ is the difference between the phases of the complex scattered and the incident field which carry the phase information of the sample. For weakly scattering samples (i.e. Born approximation) we can assume that $(|U_s| \ll |U_i|)$ and defining $U_i = e^{j\varphi_i}$, $|U_i| = 1$, then equation (5.1) can be rewritten as follows:

$$I_t \approx 1 + 2|U_s|\cos(\Delta\varphi) \quad (5.2)$$

, where $\Delta\varphi = \varphi_s - \varphi_i$. Equation 5.2 can be further simplified to:

$$\begin{aligned} I_t &= 1 + 2|U_s|\cos(\Delta\phi) \\ \Rightarrow I_t &= 1 + |U_s|e^{j\Delta\phi} + |U_s|e^{-j\Delta\phi} \end{aligned} \quad (5.3)$$

Multiplying both sides of equation (5.3) by $E_i = e^{j\phi_i}$, we obtain:

$$\begin{aligned}
I_t e^{j\phi_i} &= |U_s| e^{j\phi_s} + e^{j\phi_i} + |U_s| e^{-j\phi_s} e^{2j\phi_i} \\
&= U_s + e^{j\phi_i} + U_s^* e^{2j\phi_i} \\
&= U_s + e^{j\phi_i} (1 + U_s^* e^{j\phi_i})
\end{aligned} \tag{5.4}$$

Equation 4 includes the effect of the scattered field (i.e. U_s) which we refer to as the “Principal” image and its complex conjugate (i.e. $U_s^* e^{2j\phi_i}$) which we refer to as the twin image. As has been shown previously [93], at illumination angles less than the numerical aperture, the two terms tend to cancel each other which results in a low contrast 3D reconstruction while maintaining the high frequency features of the sample. Figure 5-1 shows the effect of changing the illumination angle on the 2D intensity image of a simulated digital phantoms where different illumination angles were assumed. Please note the 2D Fourier transform of the corresponding intensity images includes two circles in the Fourier domain. Each circle is the result of the spectral filtering applied by the limited numerical aperture of the objective lens. From equation 5.3, we see that we have 3 terms; Zero-order term (first term on the right-hand side), and the two cross terms. The shift of the two circles from the DC term depends on the illumination angle of the incident plane wave (i.e. E_i).

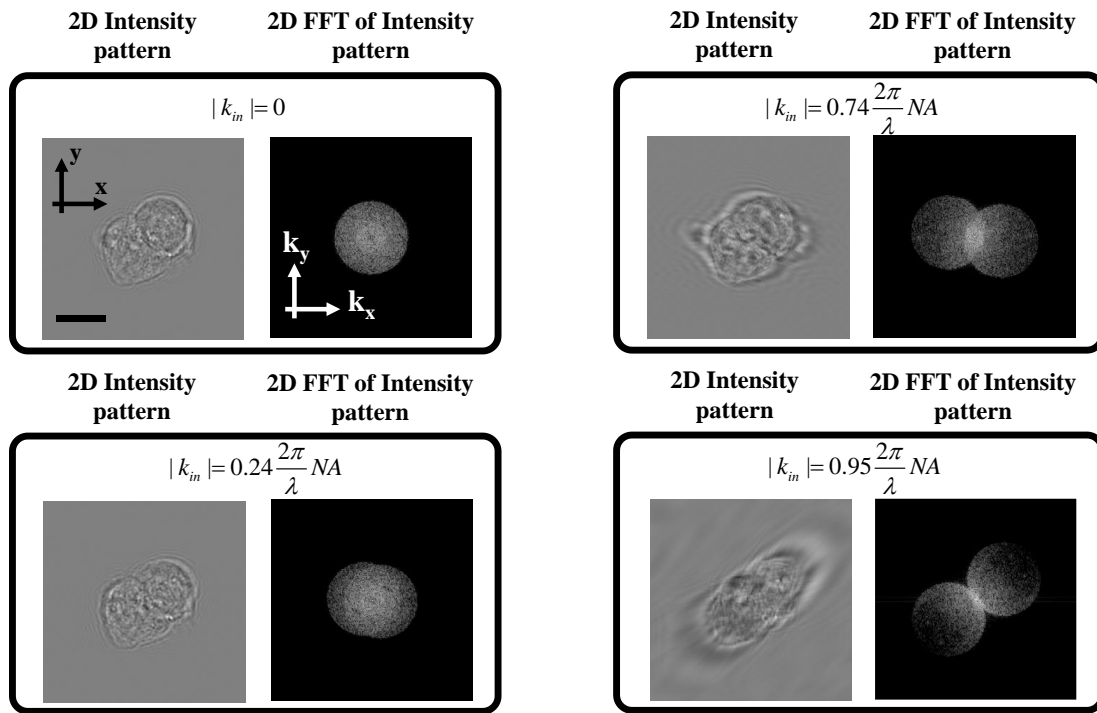


Figure 5-1. Intensity images and its 2D Fourier transforms for on-axis and off-axis configurations with different illumination angles. As can be seen from the figures, as the incident illumination vector approaches the numerical aperture of the objective lens, the 2 cross terms can be decoupled and the principal term can be retrieved. Scale bar = 8 μm .

In other words, for normal incidence, the two circles completely overlap with each other. However, as we increase the illumination angle, the shift between the two circles increases until we reach the limit of the numerical aperture, at which point we see that the two circles are tangent to each other. Only when the illumination is at the maximum angle permitted by the NA of the objective lens, the complex field can be retrieved from the intensity image as would be the case for an off-axis interferometric setup with a separate reference arm for holographic detection.

Figure 5-1 shows that for an accurate extraction of the scattered field, the sample should be illuminated with the maximum angle permitted by the NA of the objective lens. The scattered field can be extracted by simply multiplying the intensity measurement with the incident plane wave which results in shifting the spectrum in the Fourier domain. This is followed by spectral filtering of the “Principal” image with a circular filter whose size is dependent on the NA of the objective lens as shown in Figure 5-2.

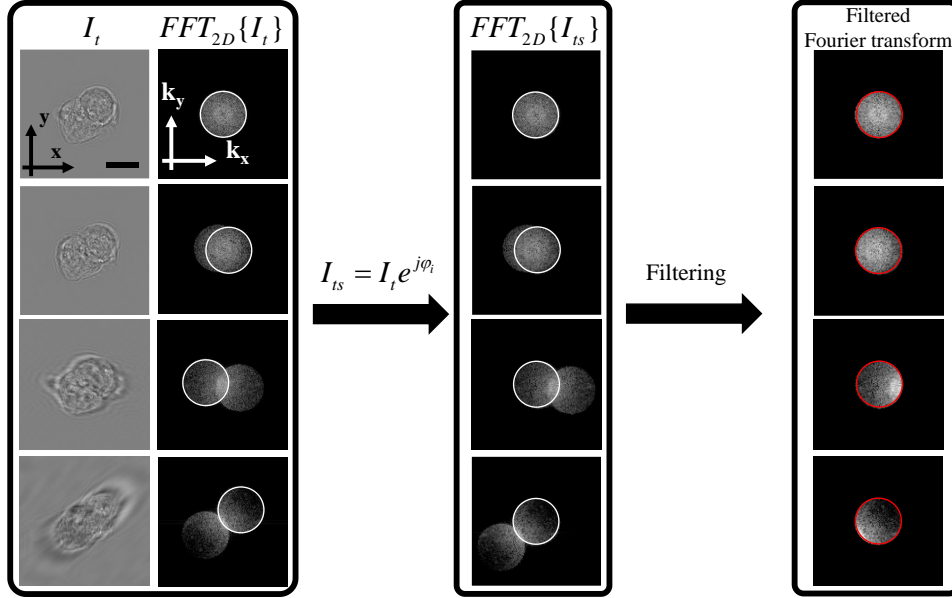


Figure 5-2. Processing of the 2D intensity images before mapping into the 3D Fourier space. The left-most panel shows the intensity measurements and the corresponding Fourier transform. The middle panel shows the effect of multiplying by the incident plane wave which results in centring the scattered field highlighted by the white circles. The final step is the filtering of the scattered field with a circular filter whose size matches the size of the numerical aperture in the Fourier space declared by the red circle. Scale bar = 8 μm .

From Figure 5-2, it can be seen that only when the illumination and imaging NA are matched, we can extract the complex scattered field from the intensity image. This can be experimentally demonstrated by illumination along a circular cone whose center is perfectly aligned with the imaging objective lens. This is demonstrated in the experimental setup described in the following section.

By multiplying the intensity image with the incident plane-wave to shift the spectrum in the Fourier domain, the scattered field spectrum becomes centered around the origin. To filter out the complex scattered field in the Fourier domain, we apply a low pass filter given by the following equation:

$$\tilde{U}_s(k_x, k_y) = LPF\{FFT_{2D}\{I_t e^{j\phi_i}\}\} \quad (5.5)$$

, where $\tilde{U}_s(k_x, k_y)$ is the 2D Fourier transform of $U_s(x, y)$, $LPF\{.\}$ represents a circular low pass filter whose radius is given by $k_0 NA$, where k_0 is the wave number in free-space.

By extracting the complex field along the direction $k = (k_x, k_y, k_z)$ for each illumination k-vector

$k_{in} = (k_x^{in}, k_y^{in}, k_z^{in})$, one Fourier component of the 3D spectrum of the scattering potential $\tilde{F}(\vec{k})$ can be retrieved:

$$\tilde{F}(\vec{\kappa}) = \frac{k_z}{2\pi j} \tilde{E}_s(k_x, k_y) \quad (5.6)$$

where

$$\vec{\kappa} = \vec{k} - \vec{k}_i = \begin{bmatrix} k_x - k_x^{in} \\ k_y - k_z^{in} \\ \sqrt{(k_0 n_0)^2 - k_x^2 - k_y^2} - k_z^{in} \end{bmatrix}$$

where $\tilde{E}_s(k_x, k_y)$ is the 2D Fourier transform of $E_s(x, y)$, $\vec{\kappa}$ is the 3D spatial frequency of the scattering potential, $k_0 = \frac{2\pi}{\lambda}$, λ is the wavelength of the illumination beam, and n_0 is the refractive index of the surrounding medium. Equation (2) is referred to as the Wolf transform [19].

By applying equation (5.6) for different 2D projections and integrating in the 3D Fourier domain, the 3D spectrum $\tilde{F}(\vec{\kappa})$ can be measured. Subsequently, $F(r)$ can be spatially reconstructed using an inverse 3D Fourier transform. Finally, $n(r)$ is retrieved using the following equation:

$$n(r) = \sqrt{\frac{4\pi}{k_0^2} F(r) + n_0^2} \quad (5.7)$$

3. Experimental setup and 3D RI reconstructions

The experimental setup used in our experiments combines a standard bright field microscope (AmScope T490B-DK 40X-2000X) with an LED ring illumination unit (Adafruit, ID: 1586, 24 LED pixels) that replaces the existing LED in the microscope as shown in Figure 5-3. The LED ring has a radius of around 30 mm. For imaging, an objective lens of magnification 40x and NA of 0.65 was used (Plan Achromatic). Images were captured using a scientific color CMOS camera (Thorlabs Zelux, resolution: 1440x1080, pixel size: 3.45 μm). The LED ring was driven using an Arduino kit (Arduino Uno). For proper synchronization, Matlab script was used to synchronize the LED ring with the camera for different illumination angles.

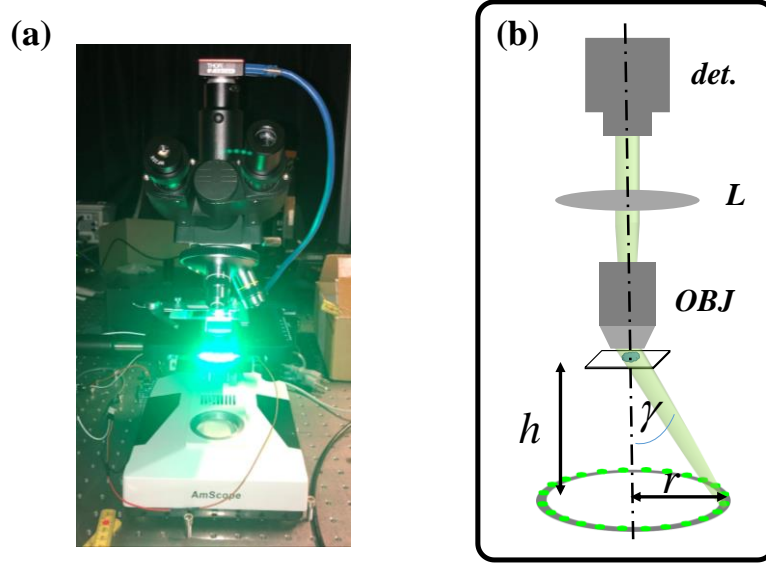


Figure 5-3. Experimental setup. (a) bright-field microscope equipped with an LED ring. (b) Schematic of the system with its different parts. (OBJ: objective lens, L: lens, det.: detector). The LED ring is perfectly aligned with the optical axis for better quality of the reconstruction. The distance (h) is controlled to ensure perfect match between the illumination and imaging NA.

Practically, as described in the previous section, the center of the LED ring was aligned with the optical axis. As we will show later, any misalignment will severely affect the quality of the reconstruction. In addition, the illumination and imaging NA were matched by controlling the distance between the sample and the LED ring to ensure proper extraction of the “Principal” field only from the intensity measurement.

As shown in Figure 5-3(b), the distance (h) is controlled so that the illumination and imaging NA are perfectly matched. In other words, the distance (h) should satisfy the following condition:

$$\sin \gamma = \frac{r}{\sqrt{r^2 + h^2}} = NA_{OBJ} \quad (5.8)$$

Figure 5-4 shows an example for a raw image taken for a cheek cell extracted from human mouth. Figure 5-3(b) shows the 2 circles (i.e. cross terms) as expected from the theory. As explained in the previous section by carefully aligning the LED ring to match the imaging NA, we are able to completely decouple the 2 cross terms for proper reconstruction of the 3D RI distribution.

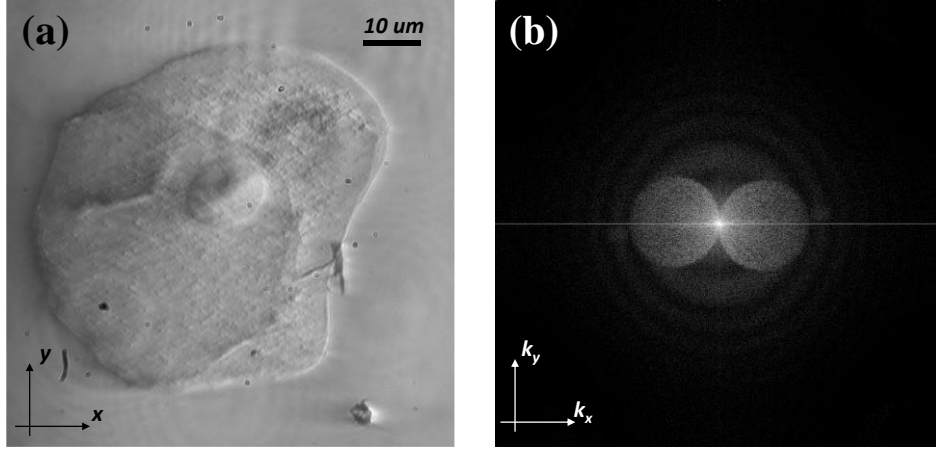


Figure 5-4. Intensity raw image from the experimental setup. (a) 2D intensity image for human cheek cell. (b) 2D Fourier transform of the image shown in (a).

Pre-processing of the images is done by subtracting the background from the raw images to remove any noise from the camera or the ambient environment, the background is retrieved by applying a low pass filter onto the raw images. The normalized intensity profile is then calculated as follows:

$$I_n = \frac{I_t - I_{Bkg}}{I_{Bkg}} \quad (5.9)$$

To retrieve the illumination angle, we adopted a previously developed algorithm which retrieve the illumination angle by detecting the boundaries and distance between the center of the circle and the DC point [94]. After acquiring different projections by illuminating individual the LEDs sequentially, the 3D RI reconstruction is retrieved by mapping the filtered Fourier transform shown in Figure 5-2 into the 3D kappa-space. This is followed by taking the 3D inverse Fourier transform of the scattering potential in the kappa-space to calculate the 3D RI distribution. Figure 5-5 shows an example for the 3D RI reconstruction for the cheek cell shown in Figure 5-4.

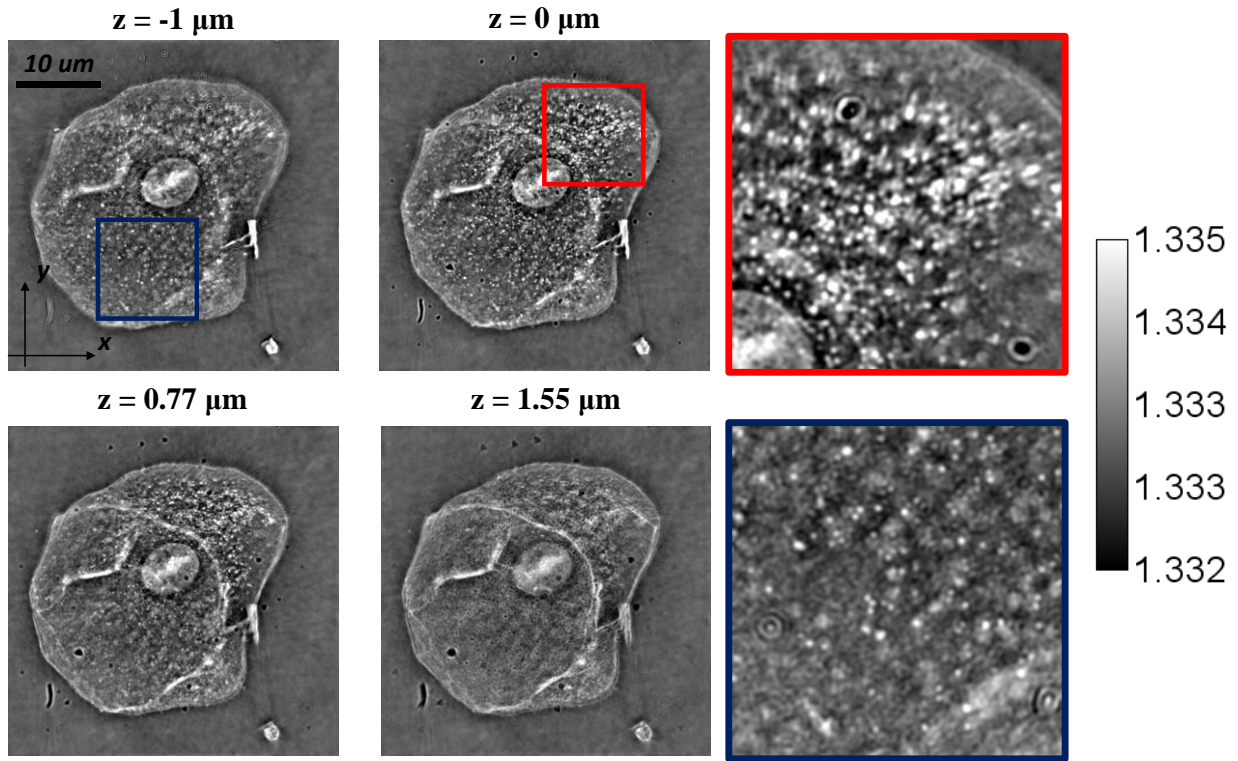


Figure 5-5. 3D RI reconstruction at different depths the left column is the highlighted regions at $z = -1 \mu\text{m}$ (dark blue) and $z = 0 \mu\text{m}$ (red). The images show the high resolution due to the use of partially incoherent LED source in which the speckle noise is highly minimized.

Figure 5-6 shows another example for a Human Cheek cell where the bacterial structures are clearly detected with their refractive index contrast higher than the cytoplasm of the cell agreeing with results reported in the literature [75, 95].

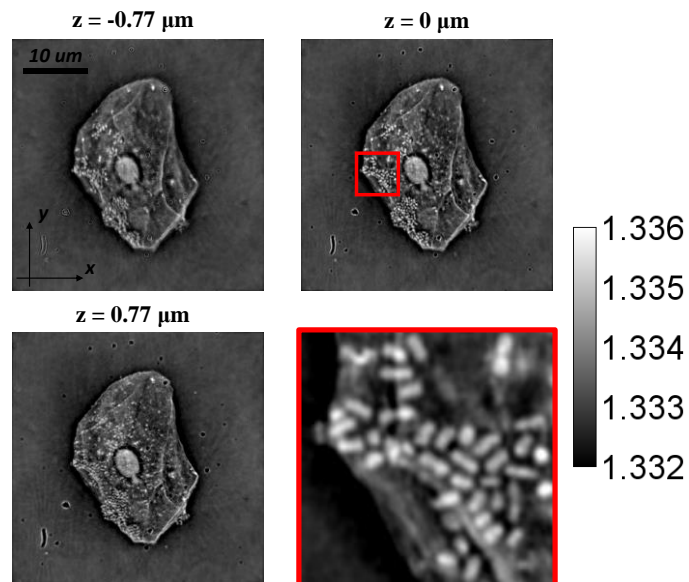


Figure 5-6. 3D RI reconstruction at different depths. The red box is a magnified picture of the highlighted red region. It shows the higher refractive index of this bacterial structures as compared to the cytoplasm of the cell.

4. Effect of misalignment on the reconstruction quality

In this section we study the effect of optical misalignment on the quality of the 3D reconstruction. As described in the above sections, it is critical that the illumination and imaging NA are identical (i.e. conical illumination with the center aligned with the optical axis). Any misalignment will result that the “Principal” and the “Twin” images overlapping which will alter the contrast quality of the final 3D RI reconstruction. To study this, the same optical setup was used, however, the LED was slightly misaligned from the optical axis. Figure 5-7 show an image for 2 LED illumination. As clearly seen, when the “Principal” and the “Twin” image overlap (i.e. in Fourier transform) we see very low contrast in the intensity images since the “Principal” and the “Twin” image tend to cancel each other [93]. However, for the other case when they do not overlap, we see that the contrast is enhanced. As a result of this effect, the final 3D RI reconstruction will not reflect the true 3D refractive index distribution of the sample since we cannot retrieve the complex scattered field “alone” from the intensity images because of the overlapping circles for certain projections. Fig. 8 shows the retrieved 3D RI distribution as a result of optical misalignment. From the figure, it is observed how the bacteria highlighted in blue box takes an RI value less than the surrounding medium (i.e. water) which does not agree with literature [75, 95] this is also contradict the reconstruction shown in Figure 5-6 when the LED where perfectly aligned and the illumination and imaging NA were matched. This error in the 3D RI re-construction might be attributed to the twin image and the principal image overlapping which results in wrong calculation of the 3D reconstructions. In addition we see that the refractive index contrast decreased due to the cancelation of the low frequency components from the overlapping of the principal and the twin image.

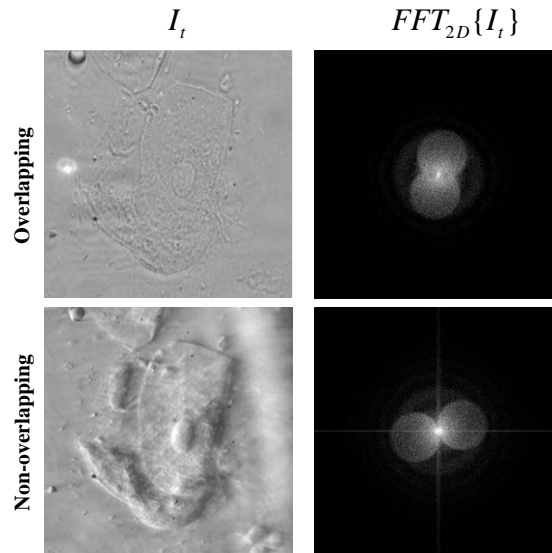


Figure 5-7. Effect of misalignment on the captured intensity images. For overlapping circles we see the low contrast images which is not the case when they minimally or do not overlap.

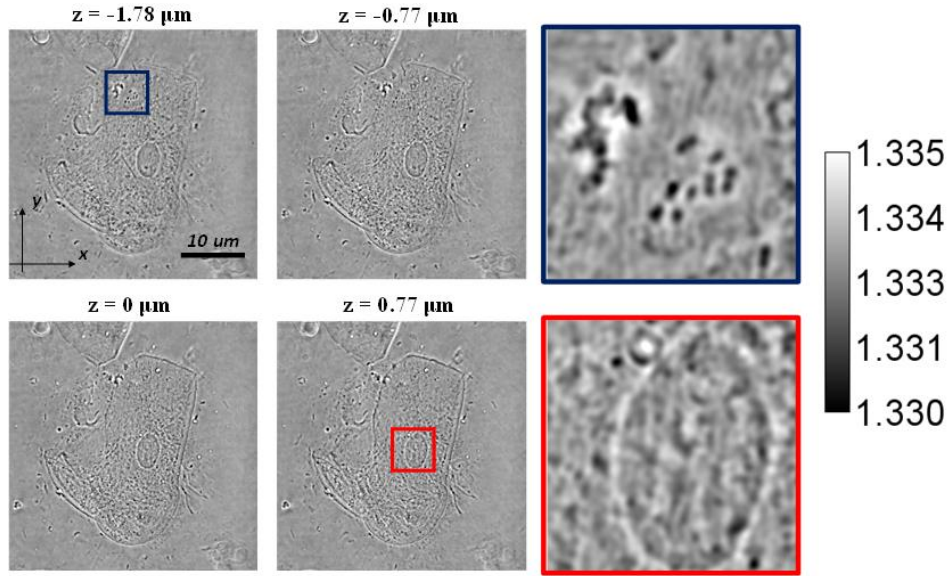


Figure 5-8. 3D RI reconstruction for misaligned LED ring. As shown in the red box, the contrast is highly suppressed as a result of the cancelation of the low spatial frequency due to the overlap between the two circles in some of the projections. On the other hand, as shown in the dark blue box, we see an artifact where the contrast is inverted for the bacterial structure which does not agree with literature [75, 95] where the bacterial structures have higher refractive index than cytoplasm.

5. ODT using wavelength diversity

Finally, 3D RI reconstruction based on wavelength diversity is discussed in this section. Since the LED ring supports “RGB” colors, we captured images at 3 different wavelengths; red (623 nm), green (515 nm) and blue (468 nm). Theoretically, this corresponds to mapping at different Ewald’s

sphere with different radius $k = \frac{2\pi}{\lambda_{illum}}$ as shown in Figure 5-9.

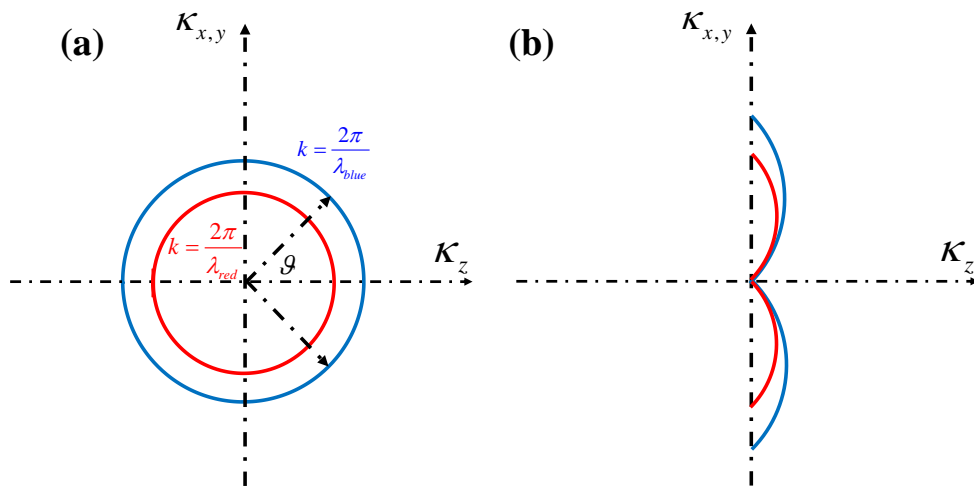


Figure 5-9. Filling of the Ewald’s sphere for 2 projections at different illumination wavelength (i.e. red and blue).

Practically, objective lenses suffer from chromatic aberrations which results in the image not being in best focus at different wavelength as shown in Figure 5-9. This results in mismatching when mapping the projections onto the Ewald's sphere which results in an inaccurate estimation of the final 3D RI distribution. One as to correct for this is by acquiring different intensity images at different focal planes and correct for the aberrations by calculating the cross-correlation function between those images and a reference image [96] which effectively corrects for these aberrations.

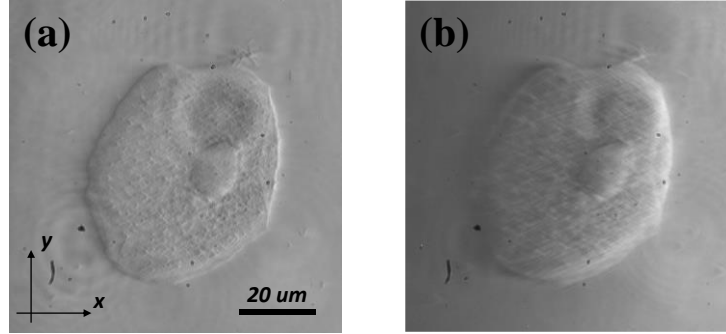


Figure 5-10. Chromatic aberrations of the objective lens. (a) Sample is in focus at Green illuminations whereas in (b) we see that at blue illumination the sample is out of focus due to the aberrations.

To correct for the chromatic aberrations we took a different approach using Fresnel propagation to refocus the image digitally since we have access to the scattered field in that case. This was performed on two steps; first we reconstruct the 3D RI distribution without calibrating for the aberrations at Red and Blue (given that green channel is in focus). Then, by monitoring the reconstructions, the fields are back-propagated by the distance where the sample is displaced from the best plane of focus ($z=0$). Figure 5-11 shows an example for the reconstructions along YZ for Green and Blue. Note how the reconstruction for blue illumination is displaced along the optical axis.

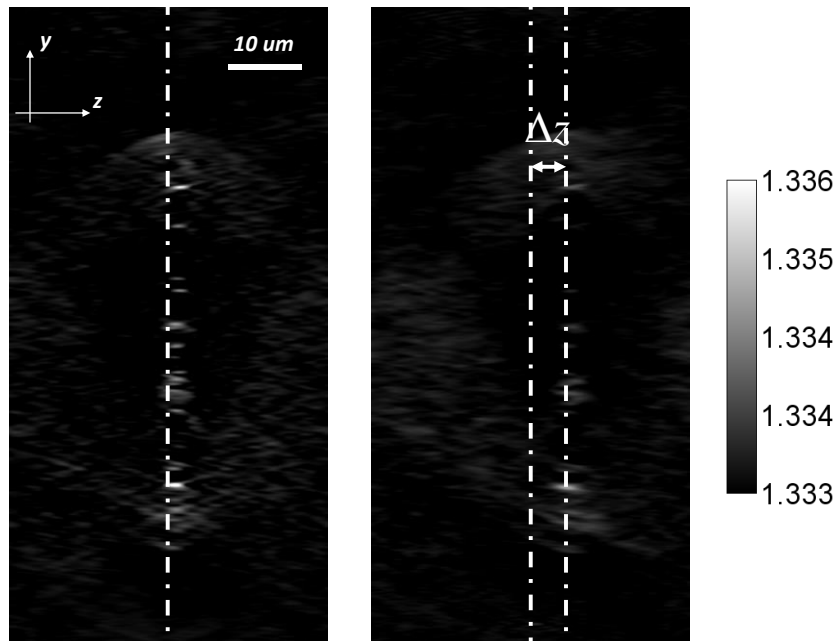


Figure 5-11. Effect of chromatic aberrations on the 3D RI reconstruction at green illumination (left) and blue illumination (right). Please note how the 3D reconstruction at blue is shifted from the $z=0$ plane due to chromatic aberrations.

The second step is to back-propagate the complex field extracted from the intensity image by the distance Δz to refocus it using Fresnel propagation as follows:

$$E_{calib} = IFFT\{FFT\{E_{uncalib}\}e^{jK_z\Delta z}\} \quad (5.10)$$

Figure 5-12 shows the effect of refocusing on the displacement along the optical axis on the XY slice at $z=0$ (best plane of focus) in which the image become in focus after calibrating for the chromatic aberrations.

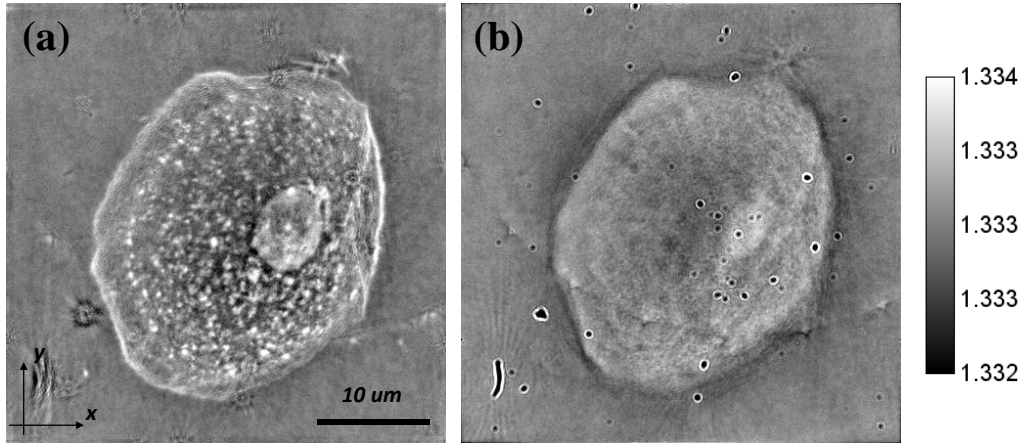


Figure 5-12. Calibration of the chromatic aberrations for blue illumination. (a) XY slice at $z=0$ after calibration and (b) before calibration.

After calibrating each wavelength channel, the 3D RI distribution is retrieved by combining all the calibrated projections into the 3D kappa-space which results in additional filling of the Ewald's sphere and hence more accurate reconstructions. However, this is based on the assumption that the sample does not have strong dispersion and thus the RI value is almost constant at different wavelengths. Figure 5-13 shows the frequency support in the kappa-space and the corresponding XY slices at different depths. While we don't observe enhancement in the optical resolution by going from 1 wavelength to 3 wavelengths, imaging at multiple wavelengths can still be advantageous in other aspects. For example, instead of capturing 24 projections each projection corresponds to each LED, we can simultaneously operate 3 LED pixels each with different color and then decouple them in the post processing since we have an RGB camera. This increases the throughput of the system by a factor of 3 [96, 97]. In addition the incoherent superposition of the 3 RGB images increases the SNR of the reconstructed 3d object. This is not visually evident in Fig. 13 because the image quality was already high with a single color but in cases where we want to carry out high speed recording and we operate at low light levels, the aid of the RGB illumination can prove helpful. Finally, we can use the wavelength scanning in reflection or 90 degree configuration. This would result in a resolution enhancement along the axial direction helping resolve the missing cone problem.

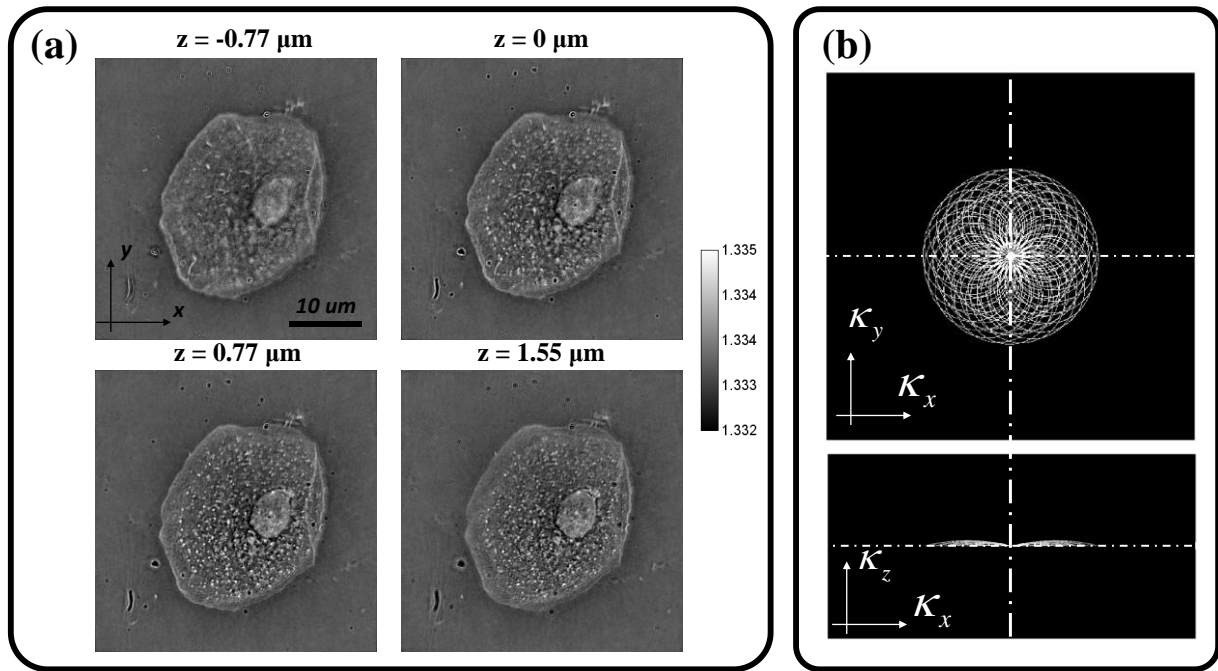


Figure 5-13. 3D RI reconstruction using wavelength diversity. (a) XY slices at different propagation depth. (b) Ewald's sphere frequency support.

Chapter 6 High speed, complex wavefront shaping using the digital micro-mirror device

This work has been published in [Ayoub, A.B., Psaltis, D. High speed, complex wavefront shaping using the digital micro-mirror device. Sci Rep 11, 18837 (2021). <https://doi.org/10.1038/s41598-021-98430-w>].

A.B. Ayoub built the optical setup, carried out the experiments, and the simulations.

1. Introduction

SLMs have been widely used in optical applications including wave-front shaping and light focusing [52, 98-104]. A main limitation of liquid crystal SLMs is their low refresh rates, typically less than 120 Hz. This limitation can make it impossible to achieve high performance in applications that require high speed such as beam focusing in live samples. This has opened the door for another technology, DMDs, to be used for similar applications [67, 105-109]. As opposed to SLMs, DMDs are characterized by their much faster refresh rates. DMD devices have a maximum refresh rate of 32 KHz [110]. However, as an “on-off” device, DMD allows only binary amplitude-modulation as compared to the grayscale and phase modulation that is possible with SLMs. Despite its binary amplitude-modulation, it was shown that DMDs can outperform SLMs in beam-shaping applications [111]. In [112], Conkey et.al demonstrated the use of Lee computer generated holograms [113] to achieve beam focusing in scattering media with signal to background ratio up to ~160 in ~34 ms. An improved optical performance was achieved by projecting Lee holograms on the DMD along with spatial filtering and misaligned optical lenses for phase modulation using “Super-pixel” technique where each super-pixel is composed of multiple pixels of the DMD [114]. In [115], Drémeau et.al used the DMD as a binary input in a reference-less optical system for beam focusing. A Bayesian phase retrieval algorithm [116] was used to precisely estimate the transmission matrix as well as for beam focusing through a white paint layer which acted as the highly scattering medium. In recent years [117], Wang et.al implemented a binary-based digital optical phase conjugation (DOPC) system based on the use of DMD instead of SLMs. They used phase retrieval methods to design a binary computer generated hologram and demonstrated speed enhancement by approximately 2 orders of magnitude as compared to a liquid crystal SLM with a low playback latency of ~5 ms.

In display application, the DMD is used to modulate the time integrated light intensity through sequential pulse width modulation [118-121]. In the context of optical diffraction tomography [122], Lee et.al demonstrated a time-multiplexing structured illumination control scheme using DMDs [123]. In their paper, the authors showed an improved performance by using time-multiplexed 8-bit amplitude modulation as compared to binary amplitude modulation (i.e. Lee holograms) in which the unwanted artifacts were diminished.

In this paper, we use a DMD to perform complex (amplitude and phase) modulation. We used the built-in dynamic range feature of the DMD device and to control the frame time of the DMD, to project an 8-bit image in 38.4 ms (256x150 μ s). We show that by splitting the complex field into

real and imaginary parts and using the time modulation scheme of the DMD we were able to synthesize a complex signal. We demonstrated this method for wavefront shaping by phase conjugating a measured field in free space and/or passing through a scattering medium. This paves the way for imaging and optical phase conjugation systems that are fast, digital accuracy without compromising light efficiency. Finally, to increase further the frame rate for grayscale modulation using the DMD, we modulated the intensity of the illuminating beam for each bit-plane while fixing the time for each bit-plane. Using this modulation scheme, the frame time for each grayscale image was reduced to 1.2 ms ($8 \times 150 \mu\text{s}$).

In what follows, we first introduce the basic concept we use in the paper. After that, in the next sub-section in the methods section, we show how we used this technique for phase conjugation applications. We refer to this method as Opto-Electronic Phase Conjugation (OEPC) to distinguish it from conventional Digital Phase Conjugation. The results section was divided into 3 sub-sections. The first two are experiments that demonstrate phase conjugation conducted using our time-multiplexed technique. The last sub-section shows a new modality for using the DMD which is amplitude modulation scheme.

2. Methods

2.1. Complex wavefront shaping with DMD

We consider a complex field $f(x, y) = A(x, y)e^{j\varphi(x, y)}$ where $A(x, y)$ is the 2D amplitude and $\varphi(x, y)$ is the 2D phase pattern. We represent a complex pattern on the DMD by presenting positive and negative portions of real and imaginary parts of the complex field, sequentially. In order to represent the grayscale of the real and imaginary parts of the complex field, we take advantage of the time modulation feature of the DMD. $f(x, y)$ can be written as follows:

$$\begin{aligned} f(x, y) &= \text{Re}\{f(x, y)\} + i * \text{Im}\{f(x, y)\} \\ &= \sum_{\alpha=1}^8 BR_{\alpha} 2^{\alpha-1} + i * \sum_{\alpha=1}^8 BI_{\alpha} 2^{\alpha-1} \end{aligned} \quad (6.1)$$

Where BR_{α} and BI_{α} are the α bit-planes for the real and imaginary parts, respectively. In our optical system, the field is interferometrically measured at the detector. This allows us to reconstitute the complete complex field by temporal integration on the detector which aggregates the contributions of each of the bit planes of both real and imaginary parts. Alternatively, the summation can be done post-detection on the computer.

We used the experimental setup shown in Figure 6-1.

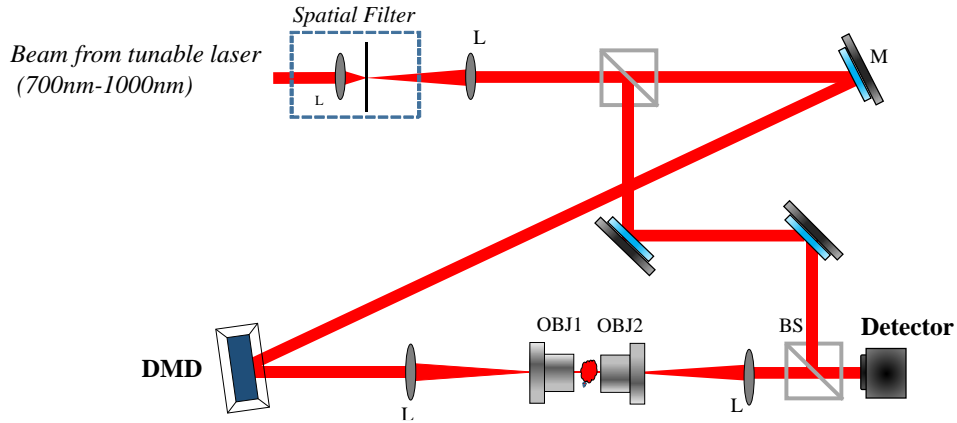


Figure 6-1. Optical setup. (M: Mirror, L: Lens, OBJ: Objective lens, BS: Beam splitter). 4f systems are used to image DMD pattern onto the detector with a spatial magnification defined by the 4f systems.

A continuous wave (CW) laser at 725nm was used in all our experiments. The laser beam is spatially filtered and collimated with a pinhole and a pair of lenses. The signal beam is reflected from the DMD device (DLP4500NIR .45 WXGA near-Infrared, resolution: 912x1140, pixel pitch: 10.8 μm , Ajile Light Industries). A 4f system was used to image the DMD plane onto the detector plane to retrieve in-focus images. For holographic detection, the signal and reference beams are combined using a non-polarizing beam splitter and projected onto a complementary metal-oxide-semiconductor (CMOS) camera (Edmund optics, pixel size=3.45 μm , resolution=2056 \times 1542 pixels). Although in the current experiment there is no object to be imaged, objective lenses were used to allow the DMD to be used for imaging applications.

The grayscale image was translated into 8 binary bit-planes (corresponding to the 8-bit image) and the 8 binary images were displayed onto the DMD sequentially to be captured onto the detector within a limited exposure time in a time-multiplexing manner. Since time-multiplexing is used, this means that the least significant bit-plane will be displayed for 1 time unit while the most significant bit-plane will be displayed for 128 time units (i.e. 1 time unit = 150 μs). This was repeated for both the real and the imaginary parts of the image. Figure 6-2 demonstrates successful phase modulation as a result of this technique. Each of the real and the imaginary parts were projected, one at a time, onto the DMD in a time multiplexing fashion. After capturing the two grayscale mages of the real and the imaginary parts, they were added digitally onto the computer which is equivalent to phase modulation by the DMD as seen in Figure 6-2.

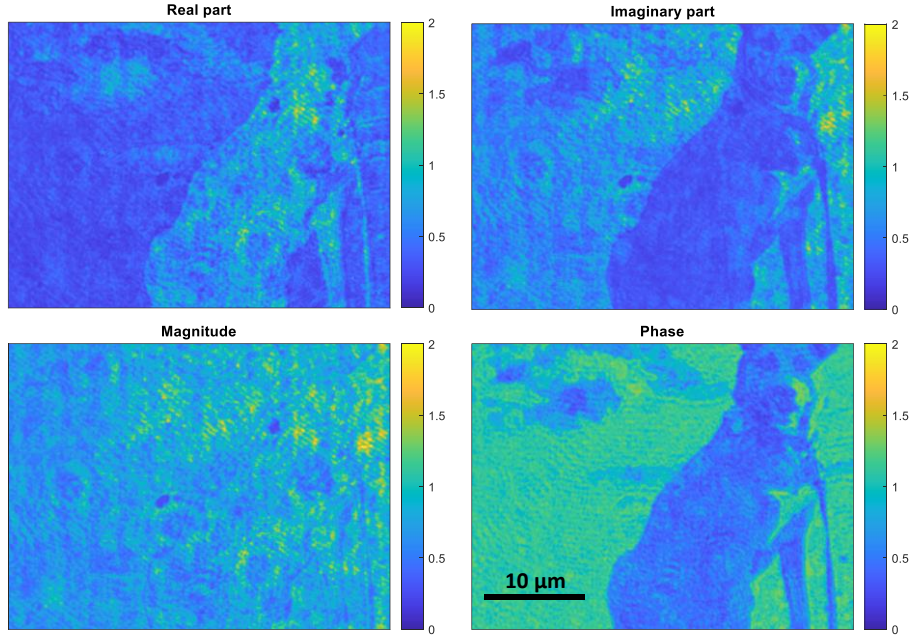


Figure 6-2. Phase modulation using DMD where no amplitude modulation is observed.

For phase maps whose phase exceeds $\pi/2$ radians, we split the real and imaginary parts into positive and negative values and displayed each one separately onto the DMD. This is expressed by Eq. 6.2:

$$\begin{aligned}
 f(x, y) &= \text{Re}\{f(x, y)\} + i * \text{Im}\{f(x, y)\} \\
 &= \left[\sum_{\alpha=1}^8 BR_{\alpha}^p 2^{\alpha-1} - \sum_{\alpha=1}^8 BR_{\alpha}^n 2^{\alpha-1} \right] \\
 &+ i * \left[\sum_{\alpha=1}^8 BI_{\alpha}^p 2^{\alpha-1} - \sum_{\alpha=1}^8 BI_{\alpha}^n 2^{\alpha-1} \right]
 \end{aligned} \tag{6.2}$$

Where BR_{α}^p and BR_{α}^n are the α bit-planes for the positive and negative parts of the real component, respectively, while BI_{α}^p and BI_{α}^n are the α bit-planes for the positive and negative parts of the imaginary component, respectively.

2.2. Opto-electronic phase conjugation (OEPC) using DMD

Assuming an initial complex field (U_i) incident on a scattering medium, we can write the output as follows:

$$U_o = T_{io} U_i \tag{6.3}$$

, where T_{io} is the transmission matrix describing the propagation of U_i through the scattering medium. After taking the complex conjugate of this function and propagate through the same medium, we get:

$$\begin{aligned}
 U_{final} &= T_{oi} U_o^* \\
 &= T_{oi} (T_{io} U_i)^* = T_{oi} T_{io}^* U_i^*
 \end{aligned} \tag{6.4}$$

Assuming a perfect time-symmetric system (i.e. $T_{oi}^{-1} = T_{io}^*$), equation 6.4 simplifies to:

$$U_{final} = T_{oi} T_{io}^* U_i^* = T_{oi} T_{oi}^{-1} U_i^* = U_i^* \tag{6.5}$$

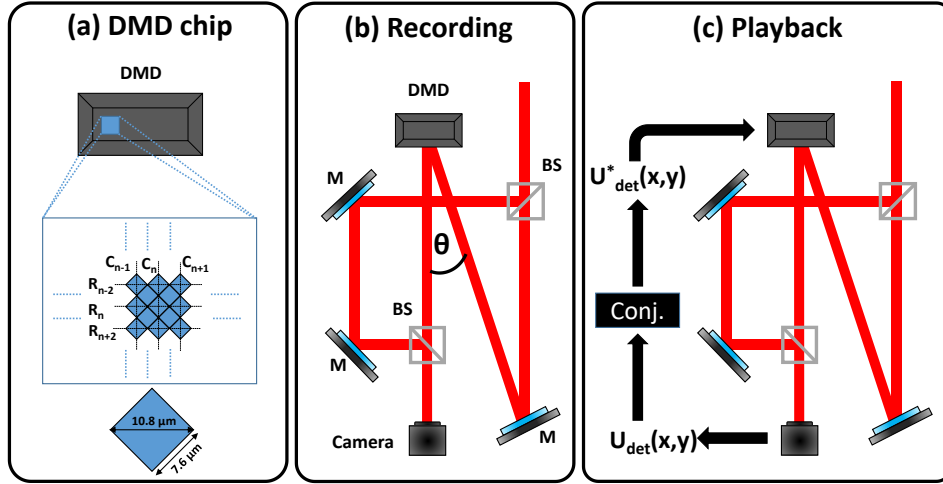


Figure 6-3. OEPC optical setup. (a) DMD projector grid showing the pixel orientation (b) Recording step is performed first to record the hologram after free-space propagation. The second step is the (c) playback where the complex conjugate of the detected field is displayed onto the DMD and the original field is retrieved. M: Mirror, BS: Beamsplitter.

Equation (6.5) shows how OEPC removes the aberrations associated with the medium (i.e. free space propagation or mouse liver tissue in our experiments) and the input field is retrieved. In order to demonstrate OEPC using the DMD, a simplified interferometric setup was used as shown in Fig. 3. The detector used in this experiment is a CMOS camera (Photonfocus Inc., resolution: 1312x1280, pixel size: 8 μm). First, the setup was calibrated to ensure pixel-to-pixel alignment between the DMD and the camera. The incident angle is chosen to be at θ degrees with respect to the direction normal to the DMD surface. Given that the DMD has an “on” and “off” state beam at $\pm 12^\circ$ with respect to the normal direction, θ was chosen to be around 12° relative to the normal direction as shown in Fig. 3(b). Owing to the specific distribution of the pixels in the DMD, (Figure 6-3(a)), interpolation was used in order to successfully align the pixels of the DMD and SLM. As seen in Figure 6-3(a), the center-to-center distance between two successive columns (i.e. C_{n-1} and C_n) is 10.8 μm while the distance between two successive rows is equal to 5.4 μm (i.e. 10.8/2 μm) as given by the DMD specification. This difference was accommodated by the use of interpolation to ensure successful mapping of the detector image onto the DMD screen. After calibrating the system, the recording step (Figure 6-3(b)) was performed to by displaying phase and/or amplitude maps as expressed by equation (6.2). After acquiring the image on the CMOS detector, the hologram was processed and the complex field was extracted on a personal computer and its complex conjugate was displayed back onto the DMD (Figure 6-3(c)) and finally the original non-distorted image is reconstructed by adding the real and the imaginary parts digitally.

3. Results

3.1. OEPC for diffracted pattern after passing through scattering media

An experiment was performed with a scattering medium in between the DMD and the detector as shown in Figure 6-4. The scattering medium was a 10 μm -thick fixed mouse liver-tissue sandwiched between a standard cover-slide of 1mm thickness and a coverslip of 170 μm thickness.

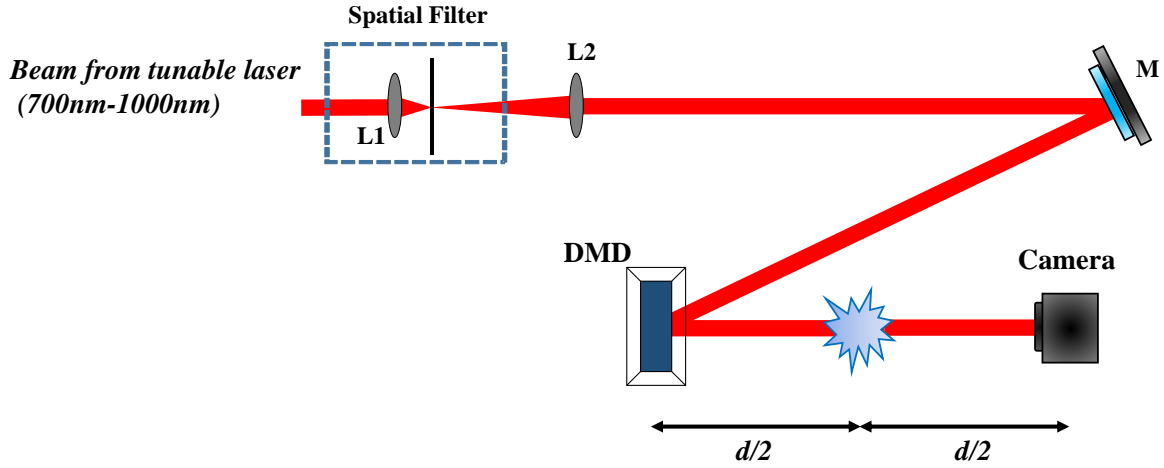


Figure 6-4. Experimental setup with the scattering medium inserted in between the DMD and the camera (M: Mirror, L1&L2: Lenses, $d = 28 \text{ cm}$).

In the OEPC experiment, a simple object (a binary amplitude circular mask of $\sim 430 \mu\text{m}$ diameter) was displayed on the DMD and the reflected light was captured by the detector. By extracting the complex field of the acquired hologram, taking its complex conjugate and feeding it back to the DMD with the scattering medium in place, we were able to retrieve the original pattern. Figure 6-5 shows the diffracted and the refocused spot after OEPC. The right panel of Figure 6-5 shows how we get a full-width at half-maximum (FWHM) of $250 \mu\text{m}$ whereas the defocused spot has a FWHM of $400 \mu\text{m}$.

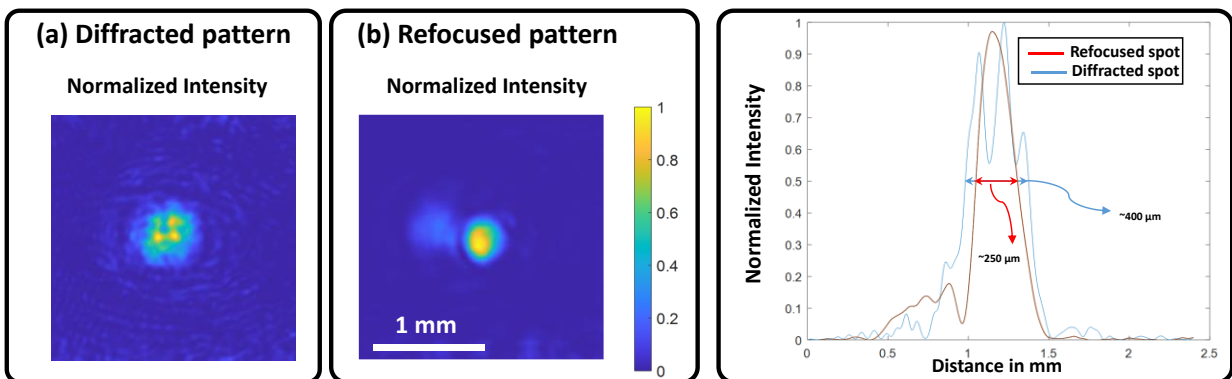


Figure 6-5. Intensity pattern before and after refocusing using OEPC technique. (a) Diffracted intensity pattern after propagating through the scattering medium path while (b) shows the intensity pattern after OEPC.

A similar experiment was performed with the USAF target being the input amplitude-only field passing through the same scattering medium (i.e. liver tissue). The image on the left hand-side of

Figure 6-6 shows the diffracted intensity pattern through the sample while the right hand-side image shows the refocused USAF target after compensating the effect of defocusing and scattering through the sample.

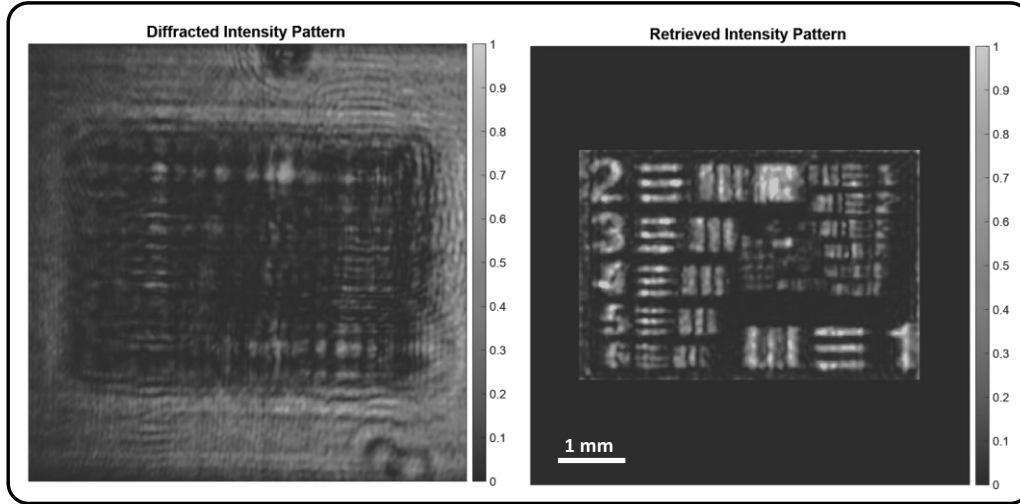


Figure 6-6. Intensity pattern before and after refocusing using OEPC. (a) Diffracted intensity pattern after propagating through the scattering medium while (b) shows the intensity pattern after OEPC.

3.2. Grayscale modulation using amplitude modulator synchronized with the DMD

In order to boost further the speed of grayscale modulation using the DMD, amplitude modulation was used instead of time modulation. As shown in Figure 6-7, an electro-optic modulator (Thorlabs, EO-AM-NR-C1) was used to modulate the light intensity for each bit-plane. In this case we used light intensity instead of light amplitude since holographic recording was not used on the camera. Therefore the calibration was done for intensity recording. The NI PCIe-6321 data acquisition tool was used for fast synchronization permitting speeds up to 90 KHz which is much faster than the DMD speed (6.6 KHz). Figure 6-7 shows the calibration process of the amplitude modulator (AM). A photodetector (Thorlabs, PDA36A-EC) was used to measure the voltage signal from the AM as a function of the applied voltage. As the characteristic half-wave voltage (V_π) at 725nm for the AM was around 240V, high voltage was needed to get the full modulation range which was generated using a high voltage amplifier (HVA200, $V_{in}=-10:10$, $V_{out}=-200:200$, Thorlabs). A quarter wave plate (QWP) was used to get the full range since V_π is higher than the maximum possible voltage generated by the voltage amplifier.

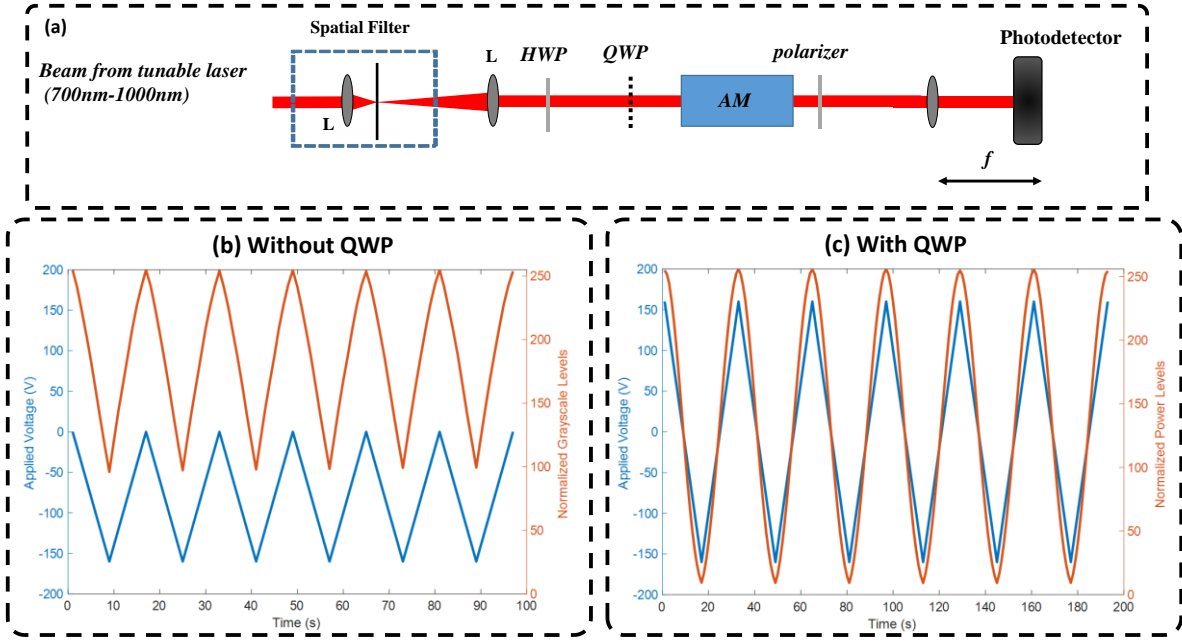


Figure 6-7. Amplitude modulation. (a) Calibration system for the amplitude modulator. (b) Amplitude modulation (orange) as a function of the applied voltage (blue) without the QWP. (c) Amplitude modulation (orange) as a function of the applied voltage (blue) with the QWP. Comparing (b) and (c), adding the QWP resulted in creating an input circular polarization which resulted in getting the complete modulation range.

A look-up-table (LUT) is extracted from Figure 6-7(c) to modulate the 8 bit-planes of the 8-bit grayscale image. After calibrating the AM, the amplitude modulator was synchronized with the DMD and images were recorded using the camera as shown in Figure 6-8. With such modulation scheme a maximum achievable frame rate of 833 Hz could be reached (i.e. $\frac{1}{150\mu s \times 8}$). Using this amplitude-modulation scheme, we showed efficient grayscale modulation for sinusoidal grating using the DMD.

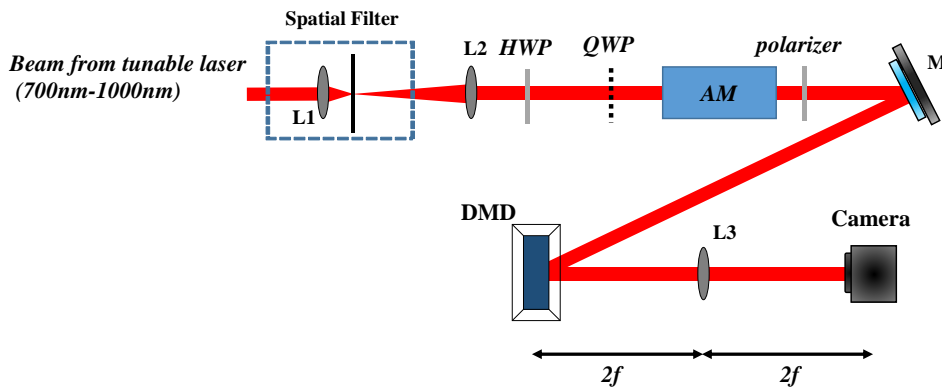


Figure 6-8. Amplitude modulation using AM synchronized with the DMD.

Figure 6-9 shows an example of amplitude modulation for a sinusoidal grating with a grating period of 15 pixels displayed onto the DMD and imaged by the camera where it shows the effectiveness of our proposed scheme as compared to binary grating where the higher diffraction orders are visible as shown in Figure 6-9 (b1). For the amplitude modulation case, higher orders are highly suppressed while the 0th, +1, -1 orders are dominant.

The DMD consists of individually-controlled mirrors, and this creates many diffraction orders [124]. This phenomenon is shown in Figure 6-10 where the pattern recorded on the DMD (a square) is repeated multiple times. The photograph in Figure 6-10 was taken by placing the camera close to the DMD in order to capture the multiple patterns and demonstrate the effect.

During the performance of the experiment it was noticed that using a lens (L3 in Figure 6-8) with higher focal length showed better reconstructed images. This is due to the fact that as the lens gets far from the DMD, additional diffracted orders from the DMD miss the lens and are not captured by the camera while only the zero-diffracted beam is able to pass through the lens and be captured by the camera. Notice that in practice, this approach is not light efficient, and a lens design such as the one used in display applications [125, 126] that captures all the diffracted orders and superimposes them on the camera is preferable.

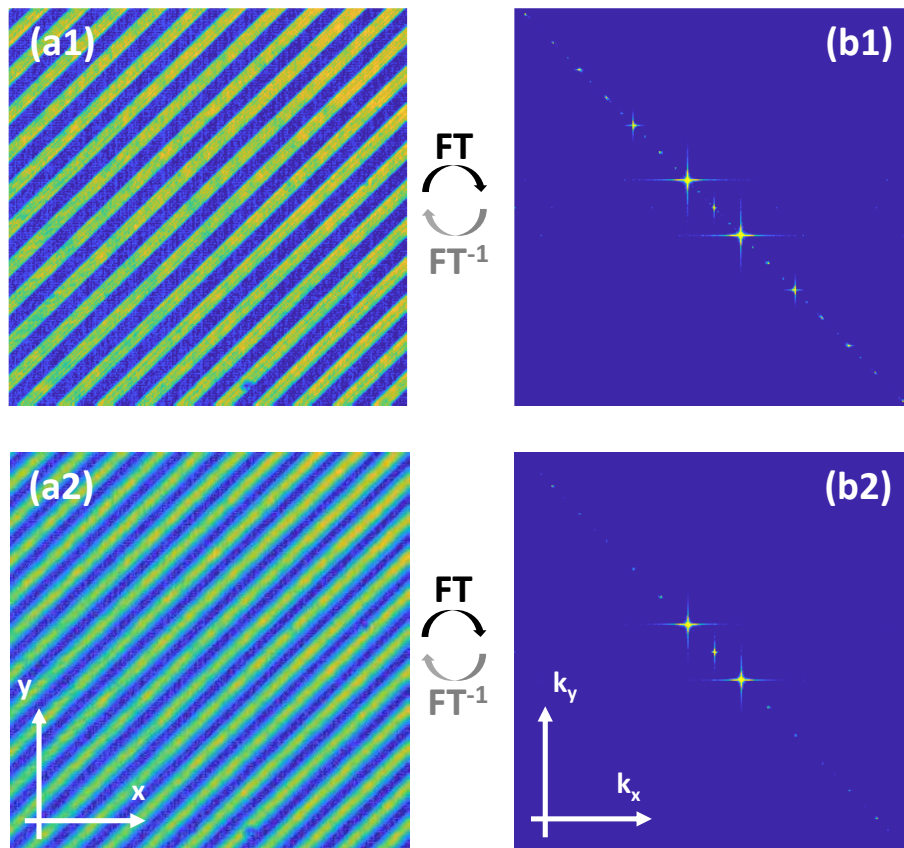


Figure 6-9. Sinusoidal grating projected from the DMD using amplitude modulation scheme. (a1-a2) The recorded gratings. (b1-b2) Fourier transform of recorded gratings. (a1, b1) show the binary grating and the associated Fourier transform where the diffraction noise (artifacts) are dominant. (a2, b2) show the sinusoidal grating and the associated Fourier transform in which the 3 main orders are visible with no visible diffraction artifacts.

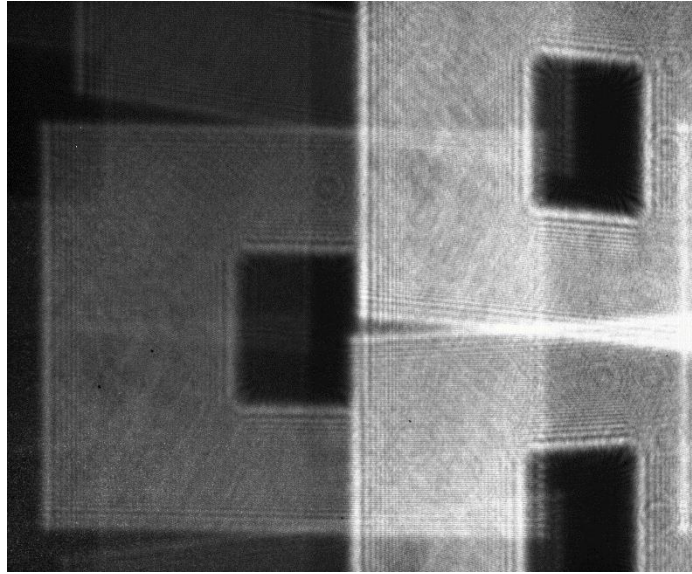


Figure 6-10. Diffraction patterns from the DMD as a result of mirror deflections.

To further validate our results, phase modulation was performed as described earlier in which the complex field is divided into real and imaginary components and then each component was presented separately using the electro-optic amplitude modulation scheme. We recorded directly intensity on the camera where the signals corresponding to the different bit planes were integrated on the camera. The real and imaginary parts were read-out and were added digitally on the pc to form the complex field. A blazed grating and a binary phase grating were synthesized on the DMD. As shown in Figure 6-11, the blazed grating shows all the power focused into the +1 order. On the other hand, the binary phase grating resulted in multiple orders as expected.

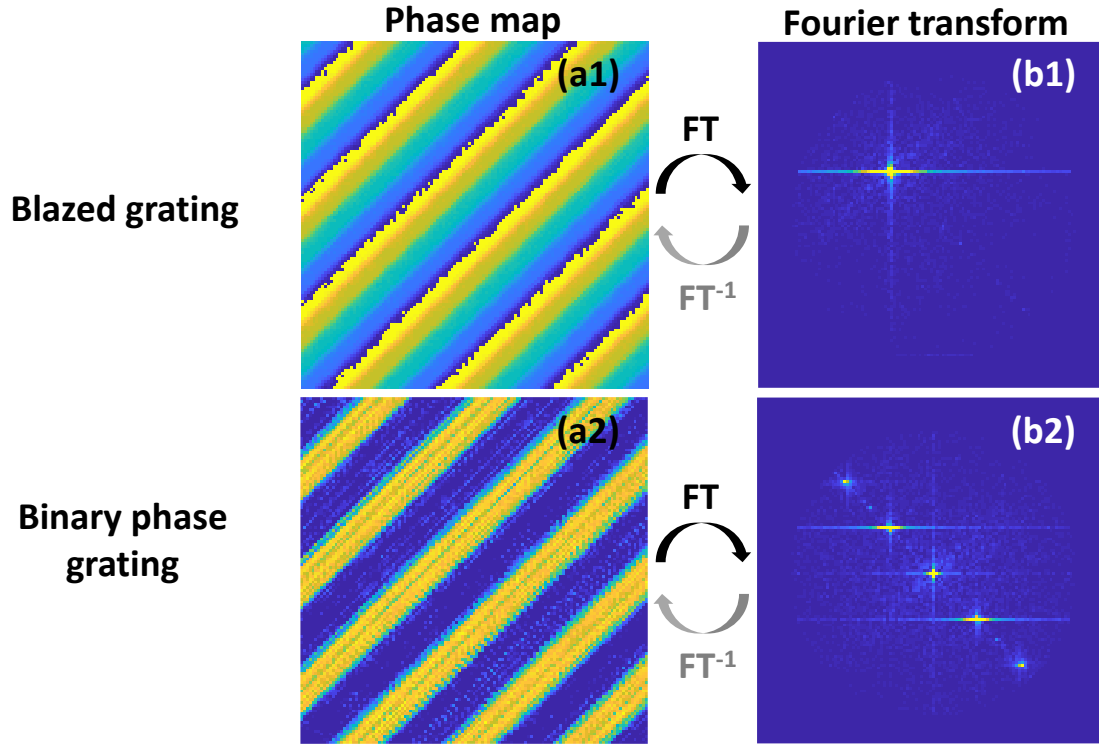


Figure 6-11. Phase gratings projected from the DMD using amplitude modulation scheme. (a1-a2) The recorded gratings. (b1-b2) Fourier transform of recorded gratings. (a1, b1) show the blazed grating and the associated Fourier transform where the diffraction noise (artifacts) are dominant. (a2, b2) show the binary phase grating and the associated Fourier transform in which the multiple orders are present.

4. Discussion

In the optical OEPC experiments, the curvature of the DMD surface was corrected digitally by acquiring another hologram with all the DMD pixels in the “on” state (i.e. background hologram), then all the collected holograms for the real and the imaginary parts were corrected by dividing the extracted fields over the background field, this resulted in a clean image without phase-artifacts as shown in Figure 6-2-Figure 6-6. For the time-multiplexing scheme, the 8-bit frame rate is rather low (~26 frames per second). This speed can be further boosted using a faster commercially available DMD [127] (refresh rates ~ 32 KHz instead of 6.6 KHz) and also reducing the region of interest (ROI) on the DMD if the application allows a smaller number of pixels. For instance, using the same DMD we used in our study, by decreasing the ROI to 16x1140 instead of 912x1140, refresh rates can be boosted to 100 KHz (corresponding to a complex-field display rate ~110 frames per second). The speed of time modulation technique can be further enhanced by using 4-bit images instead of 8-bit images which will yield a speed enhancement by a factor of 16. Figure 6-12 shows the effect of changing the number of bits used in the DMD when carrying out OEPC on the focusing quality after passing through the scattering medium (the liver tissue). It is observed that both 4-bit and 8-bit modulation depth resulted in a well preserved focused spot however with a speed enhancement factor of 16 with a display time of 2.4ms ($2.4\text{ms} = 150\mu\text{s} \times 16$) with an effective frame rate of 415 frames per second.

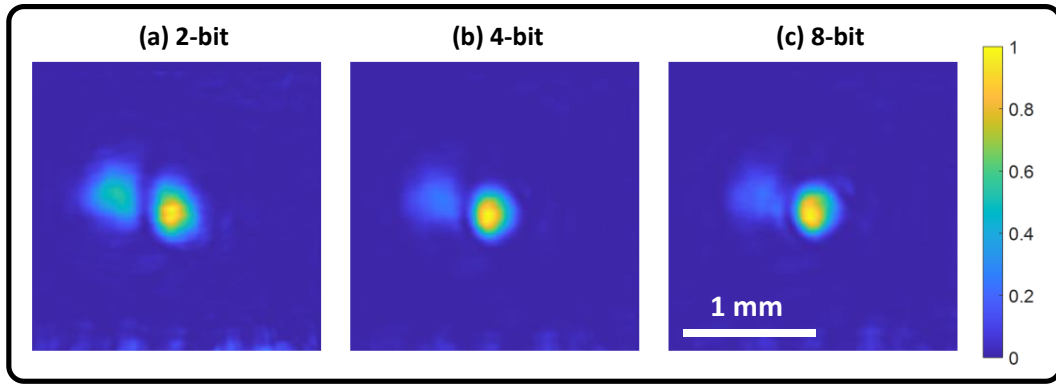


Figure 6-12. Effect of changing the modulation depth on the focusing quality. (a) 2-bit, (b) 4-bit, (c) 8-bit. (b), and (c) show well preserved focused spot while (a) shows stronger artifacts.

Table 1 shows a comparison between amplitude and time modulation schemes in terms of the frame rate for the used DMD whose refresh rate is 6.66 KHz.

Table 1. Comparison between different modulation schemes in terms of frame rate/display time

Modulation\specs	Frame rate	Minimum Display time
Binary (1-bit)	6.6KHz	150μs
Time (8-bit)	$26Hz = \frac{6.66KHz}{2^8}$	$38.4ms = 150\mu s \times 2^8$
Time (4-bit)	$416Hz = \frac{6.66KHz}{2^4}$	$2.4ms = 150\mu s \times 2^4$
Amplitude (8-bit)	$833Hz = \frac{6.66KHz}{8}$	$1.2ms = 150\mu s \times 8$
Amplitude (4-bit)	$1665Hz = \frac{6.66KHz}{4}$	$0.6ms = 150\mu s \times 4$

Current DMD technologies have refresh rate as high as 32 KHz which would scale up the modulation speed as shown in Table 2.

Table 2. Comparison between different modulation schemes in terms of frame rate/display time for DMD with refresh rate of 32 KHz.

Modulation\specs	Frame rate	Minimum Display time
Binary (1-bit)	32KHz	31.25μs
Time (8-bit)	$125Hz = \frac{32KHz}{2^8}$	$8ms = 31.25\mu s \times 2^8$
Time (4-bit)	$2KHz = \frac{32KHz}{2^4}$	$0.5ms = 31.25\mu s \times 2^4$
Amplitude (8-bit)	$4KHz = \frac{32KHz}{8}$	$250\mu s = 31.25\mu s \times 8$

High speed, complex wavefront shaping using the digital micro-mirror device

Amplitude (4-bit)	$8\text{KHz} = \frac{32\text{KHz}}{4}$	$125\mu\text{s} = 31.25\mu\text{s} \times 4$
--------------------------	--	--

Chapter 7 High fidelity optical diffraction tomography of strongly scattering samples

This work has been published in [Lim, J., Ayoub, A.B., Antoine, E.E. et al. High-fidelity optical diffraction tomography of multiple scattering samples. Light Sci Appl 8, 82 (2019). <https://doi.org/10.1038/s41377-019-0195-1>].

A.B. Ayoub built the optical setup, and carried out the experiments.

1. Introduction

Quantitative-phase imaging (QPI) enables the measurement of the phase-contrast information of transparent samples such as biological cells. QPI contrast is generated from the refractive index (RI) contrasts within and around a sample. Because this contrast mechanism is endogenous, quantitative-phase information does not require external labeling, such as immunostaining, which may perturb the sample. QPI contains the coupled information of sample thickness and RI contrast. Optical diffraction tomography (ODT) provides the 3D RI distribution of a sample by combining multiple 2D QPI measurements from various illumination angles [12, 34]. Reconstructed tomograms provide structural information that has been extensively utilized to study hematology [128, 129], morphological parameters [130], and biochemical information [68] which are summarized in several review papers [34, 122, 131, 132]. In ODT, the way in which multiple 2D measurements are combined into unified 3D information is critical. Under the assumption of a weakly scattering sample, the Wolf transform [19] has been widely used. Depending on how the 2D projections are processed, we obtain either the Born or Rytov approximations for the Wolf transform¹. Each method has its limitations [23], but the Rytov approximation is known to be more appropriate than the Born approximation for many biological applications [47]. However, when a sample is thicker and more complex, the Rytov approximation is no longer valid. This limits the usefulness of ODT for imaging complex samples.

Recently, methods have emerged to overcome the limitations of the Born and Rytov approximations by taking multiple scattering into account [57, 59, 60, 76, 78, 80]. It was shown using Mie theory [57] that learning tomography (LT) [26,76], an approach that exploits the beam propagation method (BPM) as the forward model to capture multiple scattering, has superior performance compared with that of the conventional imaging method based on the Rytov approximation. We refer to it as LT-BPM. LT uses the forward model of dividing 3D samples into multislices followed by slice-by-slice propagations. Due to the multislice modeling of forward models by LT, the resulting structure is similar to that of a neural network, and we can use the error back-propagation algorithm to calculate the gradient. The BPM consists of two steps: non-paraxial diffraction followed by phase modu-

High fidelity optical diffraction tomography of strongly scattering samples

lation. The diffraction step used in the BPM assumes $k_0 n(x, y, z) \approx k_0 n_0$, where k_0 is the free-space wavenumber, n_0 is the RI of the medium, and $n(x, y, z)$ represents RI variations. In addition, the phase modulation steps use a distance, $dz/\cos\theta$, to modulate the phase throughout propagation, given the propagation step (dz) and the illumination angle (θ). However, for thicker and more complex samples, as light propagates through the samples, multiple diffracted beams of light are generated, and it is not valid to use one single value, $dz/\cos\theta$, to represent optical path lengths. This deviation from the fixed distance, $dz/\cos\theta$, increases with increasing the illumination angle due to the nature of the cosine function [27].

In this chapter, we show that the accuracy of LT reconstructions of a 3D object is increased when we use the split-step non-paraxial (SSNP) method rather than the BPM. We refer to it as LT-SSNP. The SSNP method exploits not only the field but also the derivative of the field along the optical axis to model the propagation [28, 29]. While the BPM requires this approximation, $k_0 n(x, y, z) \approx k_0 n_0$, to decouple diffraction from phase modulation, SSNP does not require the approximation, benefiting from propagating the derivative of the field at the same time. Phase modulation affects the derivative and is used concurrently in the next step of the diffraction calculation. LT-SSNP uses the same iterative scheme used in LT-BPM. To fairly assess LT-SSNP and compare it with the LT-BPM, synthetic measurements are generated using Mie theory and the discrete dipole approximation (DDA). For spherical and cylindrical objects, Mie theory provides the analytical solution to the Helmholtz equation [133]. Therefore, the solution of Mie theory takes into account multiple scattering. Here, we also use the DDA to simulate light scattering by an arbitrarily shaped sample to generate more complex synthetic data. The DDA is a general method for calculating the scattering and absorption caused by an arbitrarily shaped sample represented by finite discrete dipoles [134]. These dipoles react not only to incident light but also to one another, which places the resulting fields under high orders of scattering. It has been shown that the DDA works well for samples whose RI values fairly match those of the surroundings, such as biological cells in a liquid medium [135]. Therefore, we use Mie theory for multiple cylinders and the DDA for a cell phantom, as well as a cluster of 15 red blood cells (RBCs). After generating synthetic measurements by using either Mie theory or the DDA, the LT-BPM and LT-SSNP are used to reconstruct the 3D RI of each sample, and the accuracy of each reconstruction is evaluated quantitatively.

In this analysis, we include an investigation of the performance of each algorithm with respect to regularization. The iterative reconstruction scheme used for both the LT-BPM and LT-SSNP minimizes a cost function that comprises two terms: data fidelity and regularization. The data fidelity term is defined by whether the forward model applies either the BPM or the SSNP, and the regularization term introduces prior knowledge about the sample characteristics such as edge sparsity and non-negativity. The relative importance of the two terms in the cost function is controlled by the regularization parameter. We compare the LT-BPM and LT-SSNP by using varying regularization parameters with the goal of minimizing the influence of the regularization term so that the results are primarily based on the forward model rather than on prior knowledge. For the simulations described, we confirm that LT-SSNP shows lower dependency on the regularization parameter due to the accuracy of SSNP. In other words, the use of a more accurate forward model permits LT-SSNP to extract more information from the measurements and to rely less on regularization. More im-

High fidelity optical diffraction tomography of strongly scattering samples

portantly, for highly aggregated samples subject to significant multiple scattering, LT-SSNP allows individual objects and structures to be clearly distinguished, while this observation cannot be made when using the LT-BPM.

We validate the proposed method by using experimental ODT data from a yeast cell and from HCT116 human colon cancer cells. To image biological cells with fine details, it is critical to reduce the influence of the regularization term, as high regularization not only smooths out the imaging artifacts but also useful information, leading to deterioration in the quality of the reconstruction. Tomograms of a yeast cell reconstructed by using LT-SSNP show successful results with high quality even with a very low regularization parameter, while the LT-BPM fails to recover fine details within and around the cells. In the case of experimental measurements of biological cells, the true RI distribution is not known, which prevents the direct assessment of the accuracy of the various ODT methods. To overcome this issue, we generate two sets of semisynthetic measurements by using the DDA for each of the RI reconstructions from the LT-BPM and LT-SSNP. A comparison of the discrepancies between the semisynthetic and experimental measurements reflects the proximity of each solution to the real RI values.

Finally, we explore the capacity of LT-SSNP to produce accurate reconstructions with a reduced number of illumination angles [136, 137]. This is of particular interest because the number of scanning angles is directly related to the measurement time. A comparison of each reconstruction method for a varying number of scanning angles indicates that learning approaches provide a dramatic improvement over conventional methods. Overall, the more accurate forward model used in LT-SSNP translates to excellent results even with low regularization and a small number of illumination angles.

2. Results

In this section, we compare the LT-BPM and LT-SSNP, which belong to the same family of LT reconstruction schemes, except for the forward models, namely, the BPM and the SSNP, respectively. LT minimizes the cost function, which consists of two terms as follows:

$$\hat{x} = \arg \min_{x \in P} \frac{1}{2L} \sum_{l=1}^L \|y_K^{(l)} - S_K^{(l)}(x)\|_2^2 + \tau R(x) \quad (7.1)$$

where the first term is the data fidelity term and R is the 3D total variation (TV) [138] regularization term to impose edge sparsity on the solution. The relative importance between two terms is controlled by the regularization parameter, τ . $y_K^{(l)} \in \mathbb{C}^M$ denotes the experimental measurements at the K th slice for each illumination angle l , and L is the total number of angles. $S_K^{(l)}(x)$ represents the estimate by a forward model (either the BPM or the SSNP) at the K th slice, which is the last slice of the volume, to be compared with $y_K^{(l)}$ given a current solution, $x \in \mathbb{R}^N$. $P \in \mathbb{R}^N$ is a convex set that imposes a non-negativity constraint. In the supplementary section, we describe the calculation of the gradient for SSNP. Once we calculate the gradient of the data fidelity term in Eq. (7.1), the optimization scheme uses the fast iterative shrinkage-thresholding algorithm (FISTA) [139] as ex-

High fidelity optical diffraction tomography of strongly scattering samples

plained in [26] for 3D isotropic TV regularization, with eight randomly chosen angles in each iteration.

2.1. Multiple cylinders by using Mie theory

We applied the LT-BPM and LT-SSNP on a highly scattering simulated sample consisting of a 3×3 grid of cylinders. Each cylinder is $6 \mu\text{m}$ in diameter with an RI of 1.05 immersed in air. The center-to-center distance is $9 \mu\text{m}$. We varied the regularization parameter to investigate the accuracy of the forward model for each algorithm. The results are presented by mapping the difference between the reconstructed tomogram for each method and the known solution, as shown in Figure 7-1 (a). The LT-BPM shows many artifacts inside the cylinders and smearing of the RI in the region between the cylinders. These artifacts of the forward model cannot be eliminated even by increasing the regularization parameter. Regularization only smooths out the overall reconstruction. In contrast, LT-SSNP clearly distinguishes each cylinder without interstitial artifacts even with the weakest regularization parameter tested, that is, $0.25\tau = 0.01$. Interestingly, increasing the regularization parameter to $4\tau = 0.16$ reduces the reconstruction quality when using the LT-SSNP algorithm. The total Error, which is defined as follows:

$$\text{Error}(x_{recon}, x_{true}) = \frac{\|x_{recon} - x_{true}\|^2}{\|x_{true}\|^2} \quad (7.2)$$

was also calculated as a function of the iteration number, as shown in Figure 7-1 (b). x_{recon} is the reconstructed RI contrast from the medium RI, and x_{true} is the ground truth RI contrast. Figure 7-1 (b) displays the Error plots of the LT-BPM and LT-SSNP by using the regularization parameter that produced the lowest Error value for each algorithm: $4\tau = 0.16$ for the LT-BPM and $\tau = 0.04$ for LT-SSNP. This analysis quantitatively confirms the better accuracy of LT-SSNP. In the case of multiple cylinders, it is critical to model distortions in the wavefront (phase modulation) introduced by the precedent samples, which determine the illumination on subsequent samples. We further analyzed this scenario by varying the number of layers in multiple cylinders and summarized the results in the supplementary section.

High fidelity optical diffraction tomography of strongly scattering samples

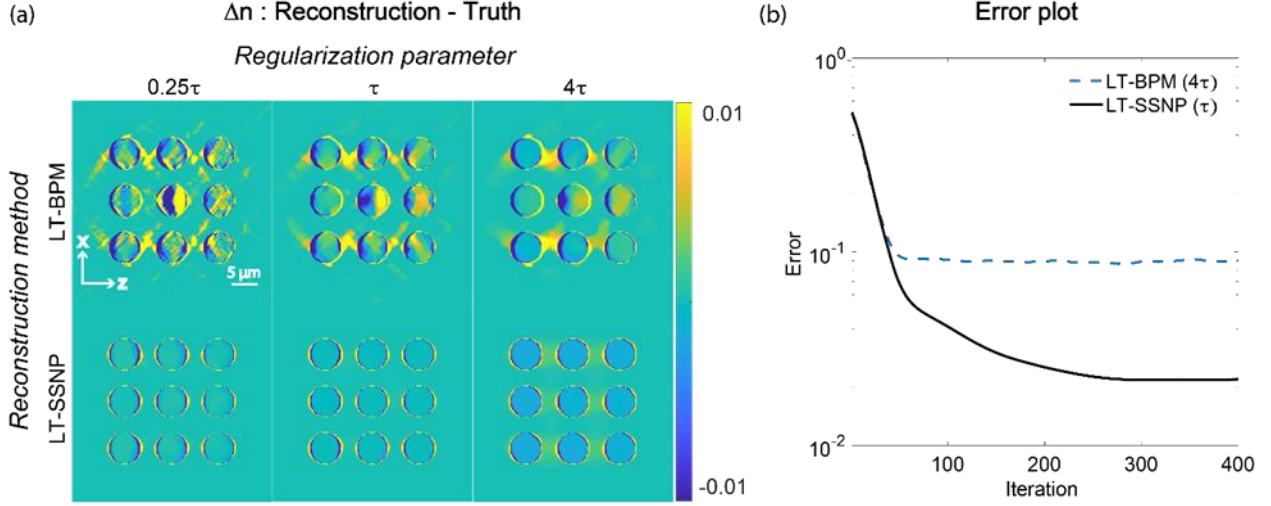


Figure 7-1. Reconstruction results of cylinders using the LT-BPM and LT-SSNP for various regularization parameters ($\tau = 0.04$). (a) Difference maps between reconstructions from the LT-BPM/LT-SSNP and the ground truth (reconstruction—truth). (b) Plots of the Error of the LT-BPM and LT-SSNP by using the regularization parameter that produced the minimum Error value

2.2. RBC cluster using discrete dipole approximation

To investigate the performance of each algorithm with highly scattering samples in 3D, we performed a similar test on a simulated cluster of RBCs. The shape of a single RBC is sketched in Figure 7-2 (a), while the organization of the cluster is shown in Figure 7-2(b). Reconstructions were performed by using various regularization parameters; for each algorithm, we show only the reconstruction by using the regularization parameter that gives the lowest Error: $8\tau = 0.2$ for the LT-BPM and $\tau = 0.025$ for LT-SSNP.

High fidelity optical diffraction tomography of strongly scattering samples

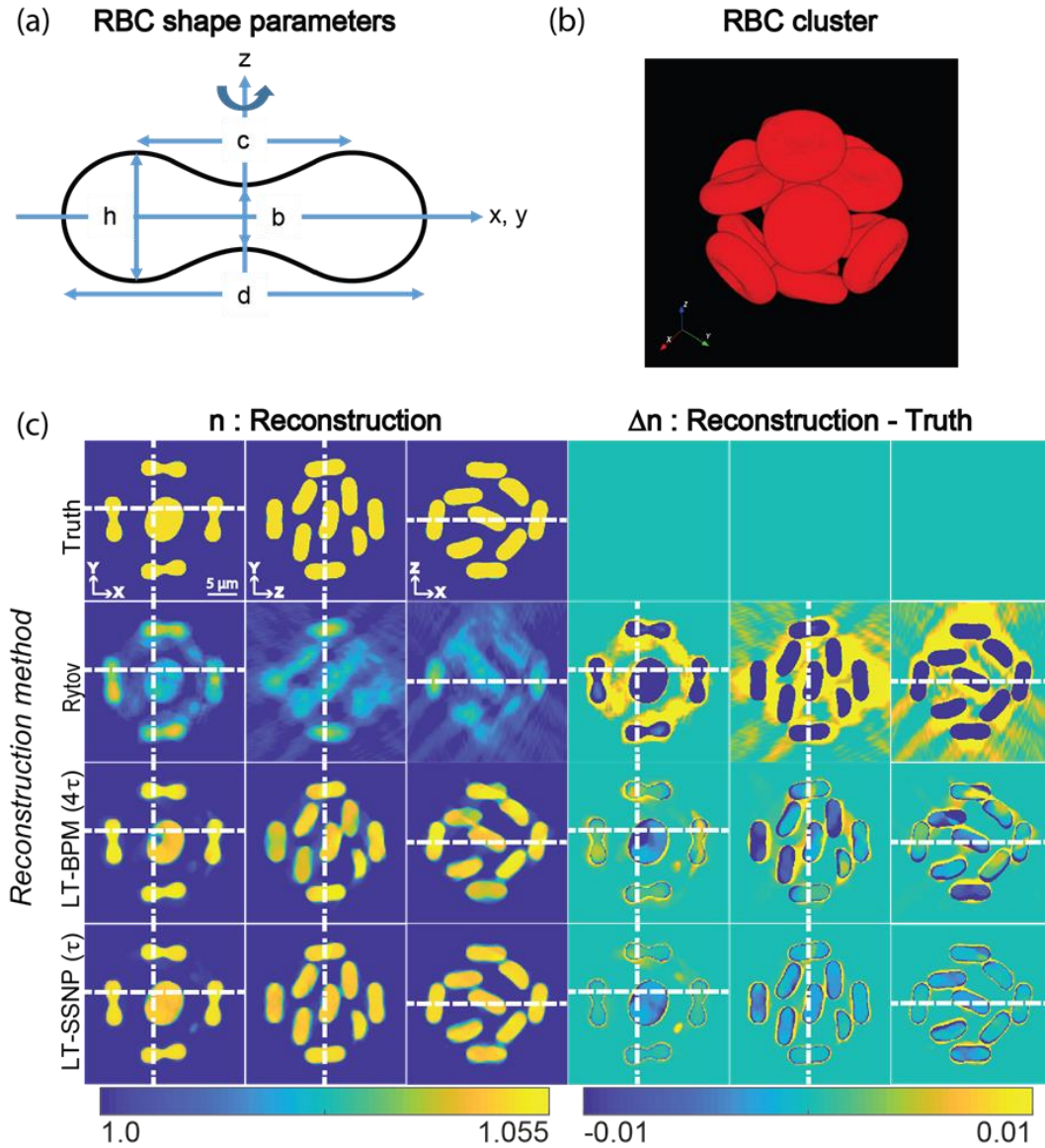


Figure 7-2. Reconstruction results of a RBC cluster using the LT-BPM and LT-SSNP. (a) Parameters used to define the shape of the RBC. (b) 3D rendering of the RBC cluster, which consists of 15 identical RBCs. (c) 3D RI and difference maps for a cluster of 15 RBCs. Top to bottom: ground truth, Rytov approximation, LT-BPM, and LT-SSNP ($\tau = 0.025$). Left: xy, yz, and xz slices of the 3D RI. Right: difference maps between the reconstructed RI and the ground truth.

In Figure 7-2 (c), Figure 7-3, different slices (xy, yz, and xz) of the 3D RI distributions resulting from each method are presented, along with the difference map with respect to the ground truth. Both the LT-BPM and LT-SSNP show better reconstructions compared with reconstructions based on the Rytov approximation, which is expected since Rytov does not consider multiple scattering. By comparing the LT-BPM and LT-SSNP, we can see that the RI tomogram resulting from LT-SSNP shows clearer and more accurate reconstructions of each RBC, producing homogeneous RI distributions within each RBC.

High fidelity optical diffraction tomography of strongly scattering samples

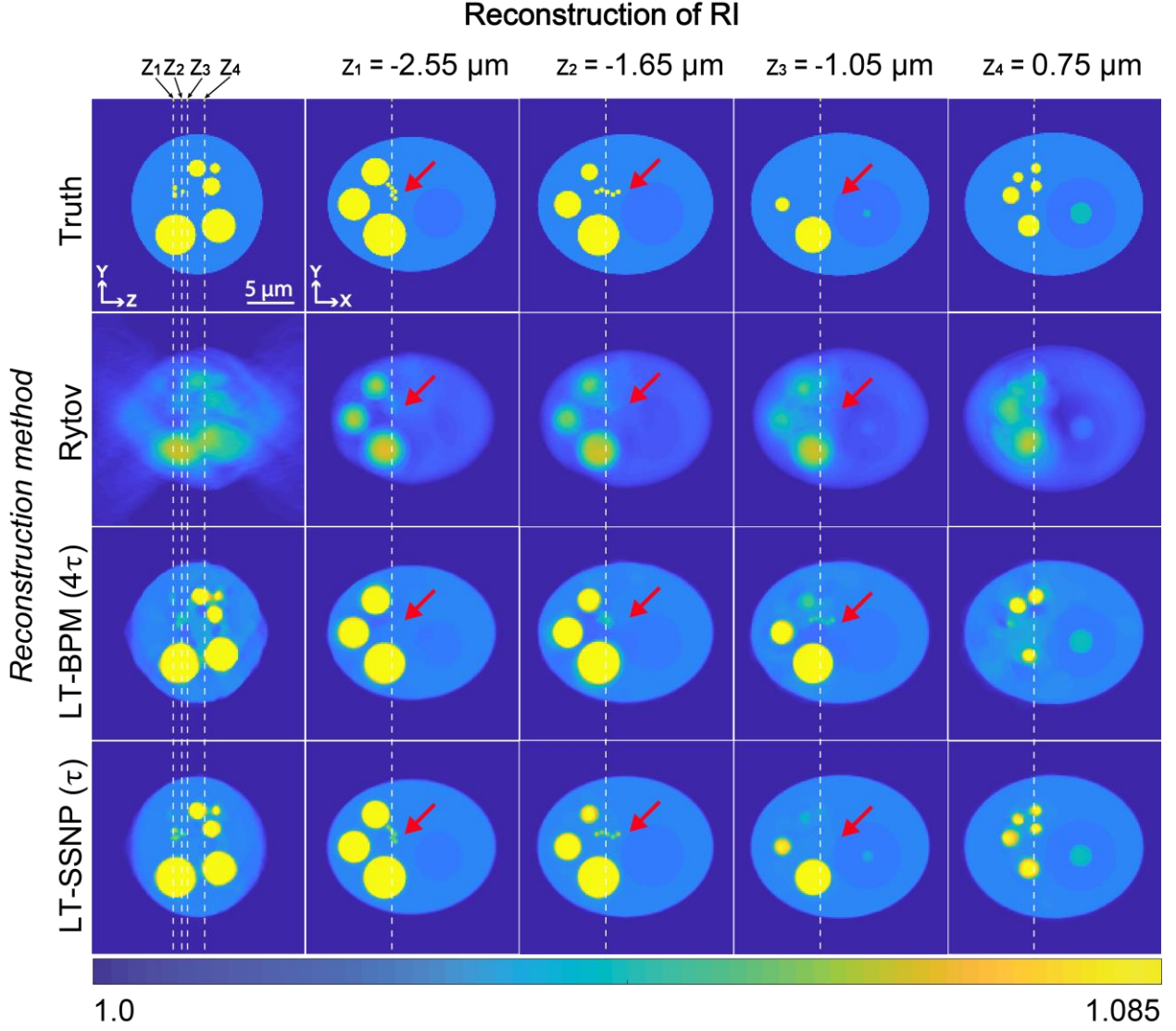


Figure 7-3. Reconstruction results of a cell phantom by using Rytov, the LT-BPM, and LT-SSNP at four different z planes ($\tau = 0.025$). Left column: the yz slice, with the z -positions of the yx slices indicated by using dashed lines. Second through fifth columns: yx slices at the positions indicated in the left column.

2.3. Cell phantom using discrete dipole approximation

To evaluate the LT-BPM and LT-SSNP algorithms on a sample whose RI values are not homogeneous and which contains fine details, we generated a synthetic cell phantom. The phantom contains four different RI values corresponding to the cytoplasm, nucleus, nucleolus, and lipids [140]. Synthetic measurements were made by using the DDA in the same manner as for the RBCs. Again, we present for each algorithm only the results obtained by using the regularization parameter that produced the lowest Error value ($4\tau = 0.1$ for the LT-BPM and $\tau = 0.025$ for LT-SSNP). The reconstruction results are shown in Figure 7-3. The reconstructions obtained with the LT-BPM show that the cytoplasmic regions are highly distorted, similar to the artifacts observed inside the cylinders and RBCs. More importantly, the small lipids indicated by the red arrows are hardly distinguishable due to the inaccuracy of the BPM. By contrast, the LT-SSNP not only distinguishes the shapes of fine structures but also correctly positions them along the optical axis.

High fidelity optical diffraction tomography of strongly scattering samples

2.4. Experimental validation using a yeast cell

To validate the relative performances of the LT-BPM and LT-SSNP on experimental data, we acquired ODT images of a yeast cell. Again, we evaluated different regularization parameters for the reconstructions obtained by using the LT-BPM and LT-SSNP. Figure 7-4 shows the reconstruction results for a slice close to the image plane. For both the LT-BPM and LT-SSNP, the high regularization parameter $4\tau=0.1$ results in too much smoothing, and it becomes difficult to resolve fine details. Therefore, it is necessary to reduce the regularization parameter.

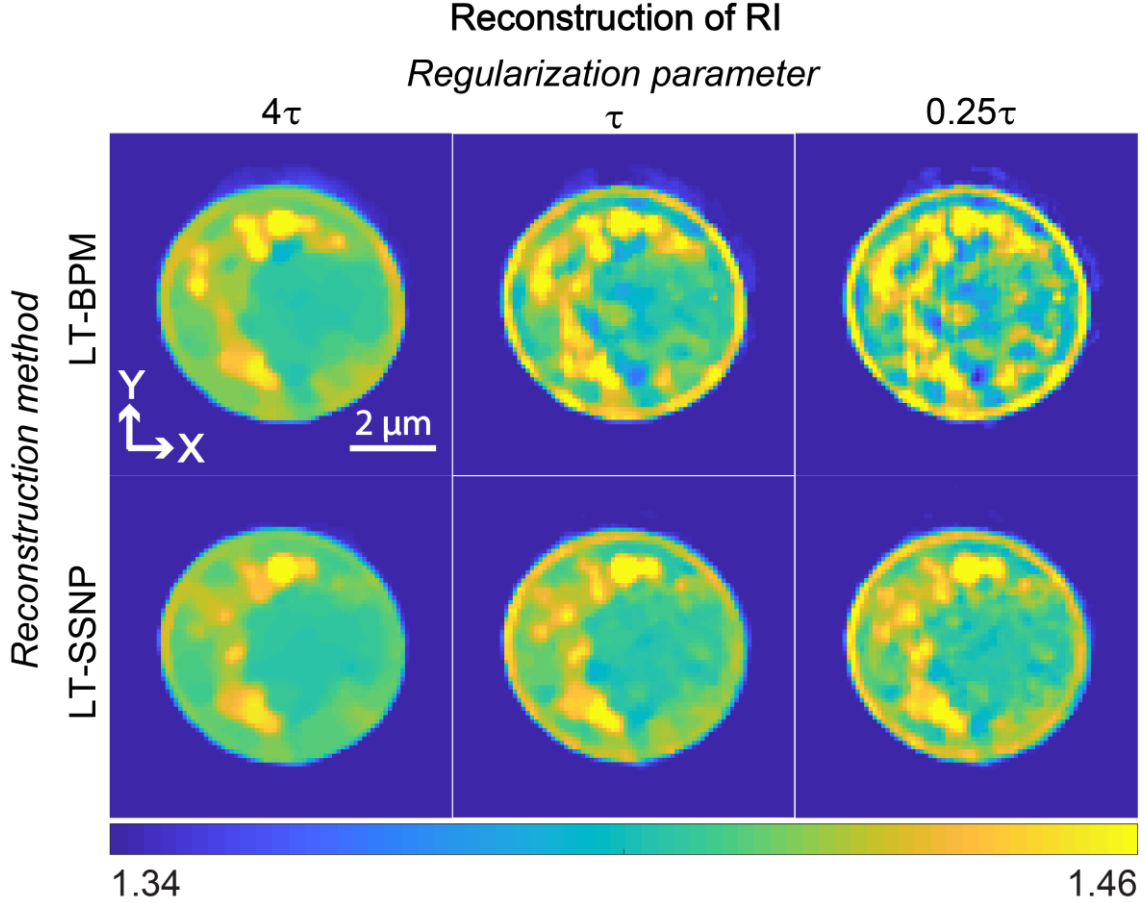


Figure 7-4. Reconstruction results of a yeast cell by using the LT-BPM and LT-SSNP for various regularization parameters ($\tau = 0.025$)

However, in the case of the LT-BPM, lowering the value of the regularization parameter introduces artifacts similar to those present in the simulation results in the previous section. By contrast, the LT-SSNP can reconstruct fine details without introducing strong artifacts. Therefore, we used $\tau = 0.025$ for the LT-BPM and $\tau/4 = 0.00625$ for LT-SSNP and further analyzed the sample for different z planes, as shown in Figure 7-5. Since we used higher regularization for the LT-BPM, we can clearly see that images tend to be smoothed out and fine details are lost, as indicated by the red arrows in Figure 7-5. By contrast, the LT-SSNP reveals structures that are not observable in the Rytov and LT-BPM reconstructions. In addition, even with the higher regularization, the LT-BPM still shows several artifacts, as indicated by the black arrows in Figure 7-5.

High fidelity optical diffraction tomography of strongly scattering samples

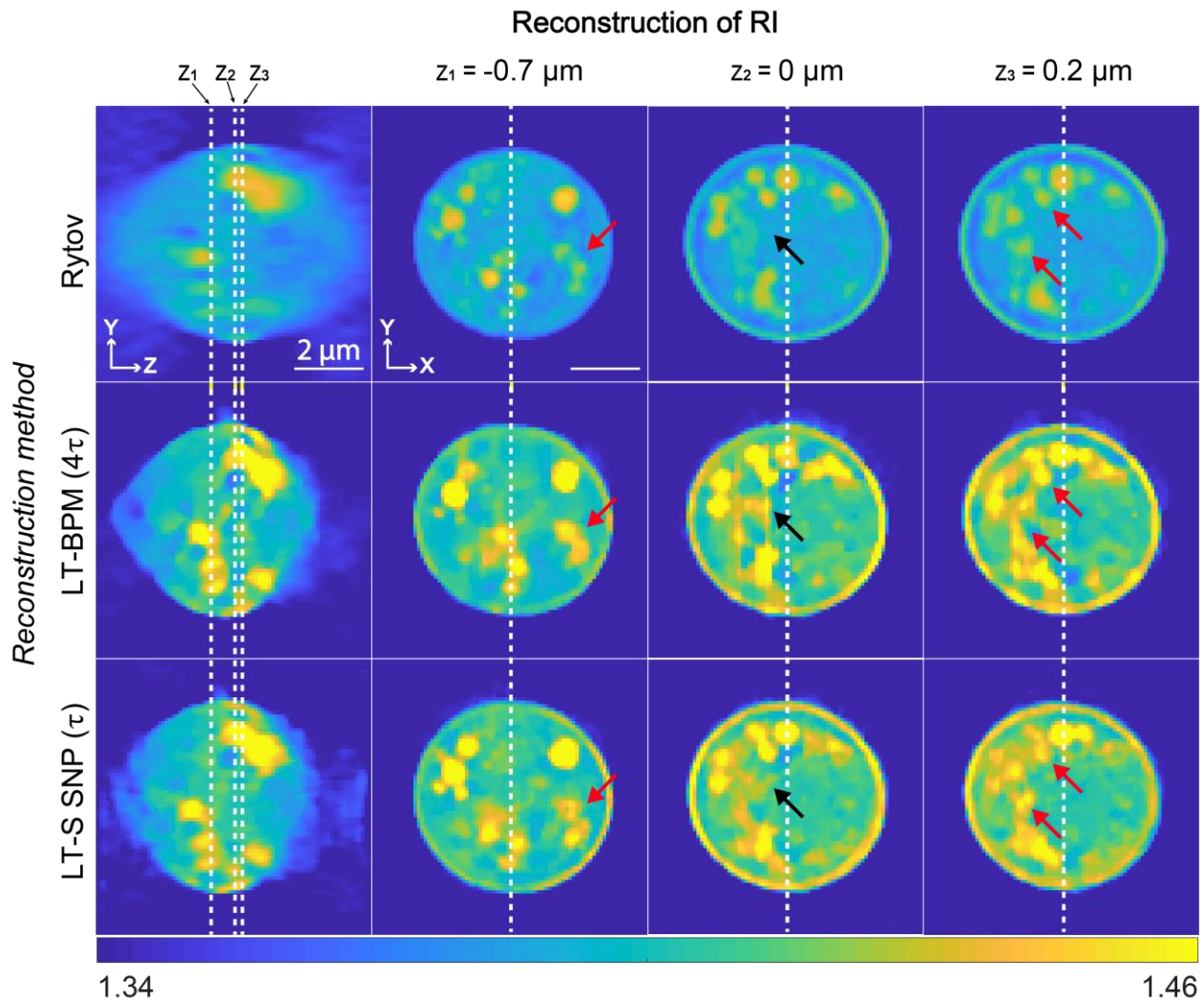


Figure 7-5. Reconstruction results of yeast cell using Rytov, LT-BPM and LT-SSNP at three different z planes ($\tau = 0.025$).

A serious limitation for quantification of the reconstruction accuracy for real biological samples such as this yeast cell is the fact that the true RI distribution is unknown. However, we were able to further evaluate the differences between the LT-BPM and the LT-SSNP by using the semisynthetic measurements generated by using the DDA as shown in Figure 7-6.

High fidelity optical diffraction tomography of strongly scattering samples

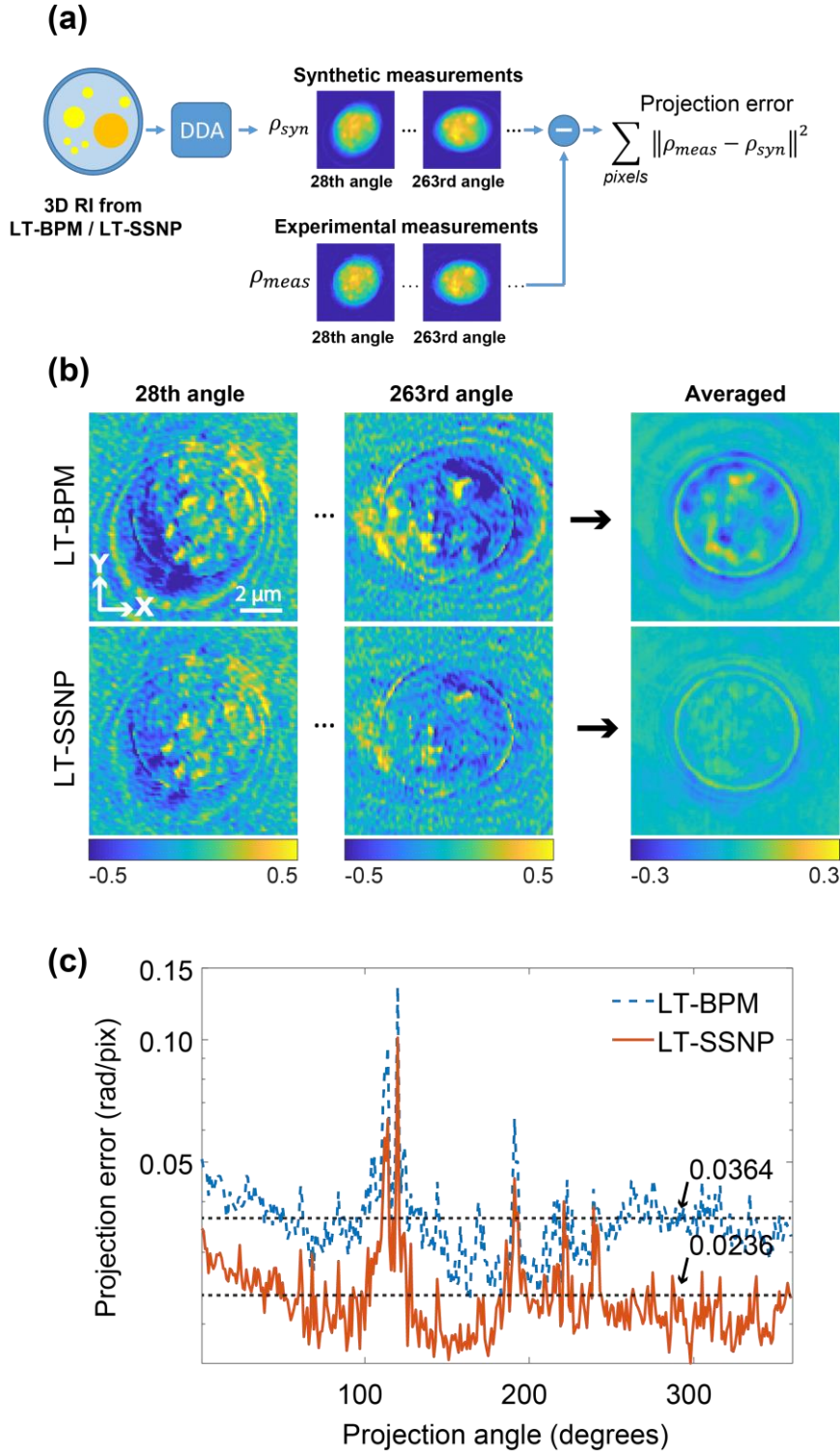


Figure 7-6. (a) Overall scheme of semisynthetic measurement generation by using the DDA. (b) Phase-difference maps for two randomly selected angles and the average for all angles. The color bar is in radians. (c) Calculation of the projection error in retrieved-phase information from experimental measurements and semisynthetic data.

While we generated synthetic measurements by using synthetic samples in all previous cases, the RI reconstructions obtained by using the LT-BPM and the LT-SSNP served as samples for the DDA to generate semisynthetic measurements in this case. The projection error—the difference in phase

High fidelity optical diffraction tomography of strongly scattering samples

information between the experimental data and these simulated measurements—reflects how close the solution is to the true RI distributions, as shown in Figure 7-6 (a). Figure 7-6 (b) maps the 2D projection error for two randomly selected angles as well as the average across the full set of angles for each algorithm. In the case of the LT-BPM, differences are clearly observed when compared with the LT-SSNP, which shows remarkable consistency with the experimental measurements. We quantified the mean projection error (radians/pixel) for each and used this metric to quantify the accuracy of the LT-SSNP compared with that of the LT-BPM (Figure 7-6(c)). The average projection error across all angles was 65% lower for the LT-SSNP than for the LT-BPM.

2.5. Data compression demonstrated on experimental data—HCT116 cells

The tomographic reconstruction based on the Wolf transform and the Rytov approximation directly maps multiple 2D measurements into the 3D Fourier space. Therefore, any missing information in measurements directly deteriorates the final reconstruction. However, the LT-SSNP is an iterative reconstruction scheme. The iterative reconstruction begins with an initial guess (usually based on the Rytov approximation), and the initial solution is updated based on the calculated error gradient by using the forward model. In addition, prior knowledge about the sample is imposed on the current guess during the iterative process. Therefore, even if the measurements are underdetermined due to missing measurements, the learning approaches can fill in some of the missing information. This idea was validated by reducing the number of illumination angles used for each method. The experimental data used for this investigation were ODT images of a pair of HCT116 human colon cancer cells. These cancerous epithelial cells contain information in small structures relative to the size of the cell and highlight the importance of reconstructions that can capture these fine details. Reconstructions were performed by using Rytov, linear tomography [57], and the LT-SSNP by using different numbers of projection angles (45, 24, 12, and 4) uniformly spaced in the range from 0 to 360°. The linear tomography method uses the same iterative reconstruction scheme as the LT-SSNP, except with single scattering as the forward model. For the quantitative analysis, we also compare the structural similarity index (SSIM) [141] for reconstructions from compressed measurements with the full measurement case, namely, 360 angles at the focal plane. The results, plotted in Figure 7-7, show a dramatic improvement in the reconstruction quality for linear tomography and the LT-SSNP because the two methods iteratively fill up empty components introduced from missing measurements but using different forward models. In the case of the HCT116 cells, Rytov produces fairly good reconstructions that reveal intracellular structures with 360 full projections, despite the underestimation due to the missing-cone problem. The Rytov reconstructions, on the other hand, rapidly deteriorate as the number of illumination angles decreases. Compared with Rytov and linear tomography, the LT-SSNP is more robust in the number of projections, providing reconstructions with only four scanning angles with nearly the same quality as reconstructions by using the full 360-angle data, as confirmed by the SSIM in Figure 7-7(b). We believe that the LT-SSNP can benefit from both the iterative scheme and an accurate forward model. In addition, we further tested the compression using the cell phantom, which has higher RI contrasts; the results have been added to the supplementary section.

High fidelity optical diffraction tomography of strongly scattering samples

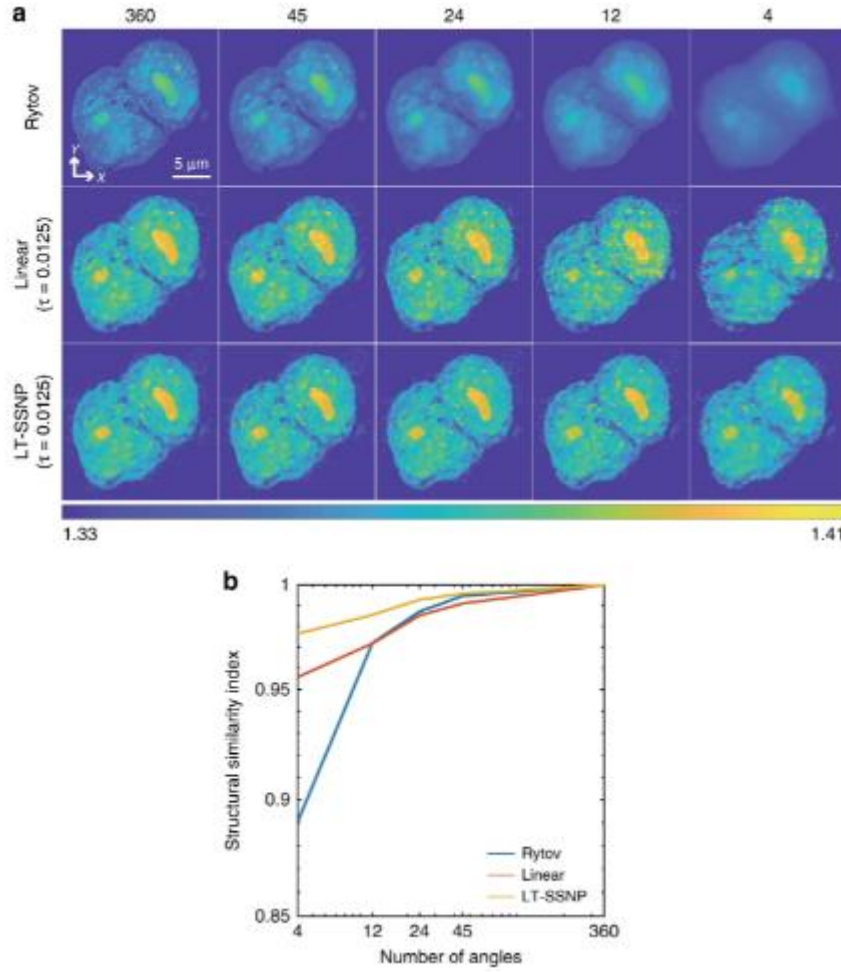


Figure 7-7. (a) Reconstruction results of HCT116 human colon cancer cells by using Rytov, linear tomography, and the LT-SSNP for a downsampled number of scanning angles. (b) Structural similarity index plot with respect to the reconstruction by using each method with full measurements.

3. Discussion

In this study, we have proposed a new tomographic reconstruction algorithm, the LT-SSNP, which is based on the SSNP forward model, for imaging complex highly scattering samples with fine details. By benefiting from the accuracy of the SSNP, the LT-SSNP extracts a maximum amount of information from measurements rather than relying on prior assumptions and generalizations about the sample structure. The LT-SSNP was quantitatively evaluated and compared with the previous algorithm, the LT-BMP, by using synthetic measurements. These synthetic measurements with a known solution were generated by using Mie theory for multiple cylinders, and the DDA for an arbitrarily shaped cluster of RBCs and a cell phantom.

In the case of multiple cylinders, the LT-SSNP shows clear reconstruction of each sample without introducing artifacts. The more interesting point is that the LT-SSNP does not require strong regularization. This is because the SSNP forward model is accurate enough that regularization is not necessary to compensate for poor data fidelity, while the LT-BPM could not properly carry out the reconstruction even with high regularization. For the RBC cluster in 3D, the LT-SSNP returns more homogeneous distributions even with a lower value of the regularization parameter than that of the

High fidelity optical diffraction tomography of strongly scattering samples

LT-BPM. This fact is critical when imaging complex samples because too much regularization smooths out fine structures and makes them impossible to resolve. The cell phantom simulation confirms the performance of the LT-SSNP on a sample with high-resolution information. The LT-SSNP is more accurate and permits the use of a lower regularization parameter, which allows details of the 3D refractive index to be identified without artificially being smoothed out by regularization.

Importantly, the added capabilities of the LT-SSNP are dramatic for imaging biological samples containing information across many scales, as confirmed by applying it to tomographic images of a yeast cell. The reconstructed tomograms by using the LT-SSNP clearly reveal structures that are not observable in the case of Rytov and the LT-BPM. Semisynthetic measurements based on the RI reconstructions of the LT-BPM and the LT-SSNP numerically validate the accuracy of the LT-SSNP reconstructions. The averaged phase-difference map represents how close the reconstruction using each method is to the real sample. In contrast to the averaged phase-difference map of the LT-BPM, which produces many discrepancies inside the sample, LT-SSNP shows consistency with the experimental measurements. The numerical evaluation shows that the LT-SSNP produces a 65% reduction in the projection error compared with that of the LT-BPM.

Furthermore, we explored the capacity of learning approaches to enable data compression by reducing the number of scanning angles. The LT-SSNP shows a dramatic improvement in image quality by using a small number of illumination angles when compared with the conventional direct inverse method by using the Rytov approximation. Even with a low number of projections, the LT-SSNP benefits from its weak dependency on the regularization parameter.

4. Materials and Methods

4.1. Simulation

We used Mie theory to derive the field scattered by multiple cylinders (2D) [142]. A total of 101 illumination angles uniformly distributed between -45° and 45° were used. To perform a deeper assessment of the LT-BPM and LT-SSNP algorithms, we also tested on synthetic measurements in arbitrary-shaped samples: an RBC cluster and a cell phantom.

For RBC simulations, the discrete dipole approximation [134, 143] was applied to an RBC cluster, in which the surface of each RBC is defined by using the following equation:

$$\rho^4 + 2S\rho^2z^2 + z^4 + P\rho^2 + Qz^2 + R = 0 \quad (7.3)$$

where ρ is the radius in cylinder coordinates ($\rho^2 = x^2 + y^2$) and S , P , Q , and R are parameters derived from d , h , b , and c shown in Figure 7-2 (a), respectively. In this paper, d , h/d , b/d , and c/d were set to $7.7 \mu\text{m}$, 0.3542 , 0.1752 , and 0.6196 , respectively, as suggested in ref. 36. We refer interested readers to previous studies [144, 145] for a more complete presentation of the DDA simulation of an RBC. By using a single simulated RBC, a cluster consisting of 15 identical RBCs was generated, as shown in Figure 7-2 (b). In addition, we generated a synthetic cell phantom with four different RI values corresponding to the cytoplasm, nucleus, nucleolus, and lipids [140]. To derive the scattered field from the cluster and the cell phantom, samples were scanned by using 40 uniformly distributed illumination angles on a circle with an incident angle of 45° . For every simulation mentioned above,

High fidelity optical diffraction tomography of strongly scattering samples

the sample with an RI of n was immersed in air, and the wavelength used was 600 nm. This is equivalent to a case in which the RI of the medium is n_0 and the sample with an RI of $n \times n_0$ is illuminated at a wavelength of $600 \times n_0$ nm. The number of dipoles per wavelength for both simulations was set to 12. Table 1 summarizes the numerical and experimental parameters used for the simulations as well as for the experiments.

Table 7-1. Reconstruction parameters

	Size	$\mu\text{m} / \text{pixel}$	n	γ	C	Iterations
Cylinders	1024×256	0.15	1.05	1e-3	90	400
RBCs	$512 \times 512 \times 180$	0.15	1.05	1e-3	57	200
Cell phantom	$350 \times 350 \times 128$	0.15	1.0245(cytoplasm), 1.0210(nucleus) 1.0413(nucleolus), 1.0886(lipids)	1e-3	57	200
Yeast	$150 \times 150 \times 80$	0.1	NA	0.25e-3	163	200
HCT116	$256 \times 256 \times 170$	0.1	NA	0.25e-3	160	200

4.2. Experiments

The experiments were performed by using a conventional optical diffraction tomography configuration in which a spatial light modulator was used to control the illumination angle. A total of 360 holograms were recorded for each sample in a circular pattern with 1° resolution at an incidence angle of 35° . Additional details about the optical setup and sample preparation are provided in the supplementary section.

4.3. Semisynthetic simulation

The semisynthetic measurements were calculated by using the reconstruction results acquired from the LT-BMP and the LT-SSNP as samples for the DDA. The size of the dipole was set to $\lambda/12n_0=0.033\text{nm}$, where $\lambda = 0.532 \text{ nm}$ is the wavelength of the laser and $n_0 = 1.338$. Both the values were set from the values used in the experiments. The grid size of the reconstructions from the LT-BPM and the LT-SSNP was 99 nm. The reconstruction results were interpolated to a grid, one pixel of which was the size of a dipole. Then, we quantized the RI values by using the following equation: $\text{round}(n_{\text{reconn}} \times 1000)/1000$, where n_{recon} denotes the reconstructed RI values. Simulations were performed for 160 nonoverlapping angles, which were calculated from the experiments.

4.4. Reconstruction algorithm

We implemented the algorithms by using custom scripts in MATLAB R2018a (MathWorks Inc., Natick, MA, USA) on a desktop computer (Intel Core i7-6700 CPU, 3.4 GHz, 32 GB of RAM). To accelerate the computation, a graphic-processing unit (GPU, GeForce GTX 1070) with custom-made functions based on the compute unified device architecture (CUDA) was utilized. The gradi-

High fidelity optical diffraction tomography of strongly scattering samples

ent, calculated from a data fidelity term, $D(x)$, was $\partial D(x)/\partial x$, the amplitude of which is proportional to the amplitude of $D(x)$. The LT-BPM and the LT-SSNP use different data fidelity terms. The LT-BPM calculates the difference in the fields $u(x,y,z)$. In contrast, the LT-SSNP requires differences in both $u(x,y,z)$ and its derivative $du(x,y,z)/dz$. Therefore, calibration of the optimization parameters between the methods is necessary to make the LT-BPM and the LT-SSNP use similar optimization parameters. The FISTA requires two parameters: step size (γ) and regularization parameter (τ). The calibration of those parameters can be performed by calculating the ratio C between $\|u(x, y, z)\|_2^2$ and $\|u(x, y, z) + du(x, y, z)\|_2^2$. We approximated this as the average value of $(1 + ik_z)^2$ for the illumination k_z s, which corresponds to a case in which $u(x,y,z)$ is replaced with a planar wave, $e^{1i(k_{xx}+k_{yy}+k_{zz})}$. Therefore, the LT-BPM, which uses the parameters γ and τ , can be directly compared with the LT-SSNP, which uses the parameters γ/C and $\tau \times C$. For convenience, we labeled the figures according to the parameters used for the LT-BPM. The actual parameter values for the LT-SSNP can be easily calculated given C , which is provided in Table 1. The total number of iterations used in the FISTA is also provided in Table 1. Twenty iterations were used for the TV optimization step in all cases.

4.5. Overall scheme of the learning tomography

Both algorithms (LT-BPM and LT-SSNP) start from measured electric fields (including both amplitude and phase information) from the holographic data. An initial guess of the RI distributions is obtained by using the Rytov tomographic reconstruction method. By using either the BPM or the SSNP as the forward model, the scattered field is estimated given the plane-wave illumination propagating through this initial guess. The square of the difference between the estimated and the measured fields is the cost function, which is minimized by adjusting the index values contained in the forward model through the FISTA. At the same time, an intermediate step of regularizations such as smoothness and non-negativity is included. This process is repeated until the total cost function converges.

4.6. Split-step non-paraxial method

In this section, we briefly describe the SSNP in 3D [28, 29], which is the physical forward model used in the LT-SSNP. Bhattacharya and Sharma [146] implemented this method by using a matrix formalism for wave propagation in 3D. Here, we describe a fast Fourier transform implementation for more efficient use of memory. The propagation of a scalar wave $u(x,y,z)$ through a medium $n(x,y,z)$ in 3D must satisfy the following wave equation:

$$\left(\frac{\partial^2}{\partial x^2} + \frac{\partial^2}{\partial y^2} + \frac{\partial^2}{\partial z^2}\right)u(x, y, z) + k_0^2 n^2(x, y, z)u(x, y, z) = 0 \quad (7.4)$$

where $k_0 = 2\pi/\lambda$ is the free-space wavenumber for a given wavelength λ in a vacuum. Eq. (7.4) can be written in matrix form as:

$$\frac{d\mathbf{v}(x, y, z)}{dz} = \mathbf{H}(x, y, z)\mathbf{v}(x, y, z) \quad (7.5)$$

High fidelity optical diffraction tomography of strongly scattering samples

where,

$$\mathbf{v}(x, y, z) = \begin{bmatrix} u(x, y, z) \\ \frac{\partial u(x, y, z)}{\partial z} \end{bmatrix} \quad (7.6)$$

and

$$\mathbf{H}(x, y, z) = \begin{bmatrix} 0 & 1 \\ -(\frac{\partial^2}{\partial x^2} + \frac{\partial^2}{\partial y^2} + k_0^2 n^2(x, y, z)) & 0 \end{bmatrix} \quad (7.7)$$

When we consider an inhomogeneous sample immersed in a homogeneous medium, n_0 , it is possible to split the matrix \mathbf{H} into two terms that correspond to diffraction and phase modulation. Note that no approximation is assumed up to this point. We refer interested readers to the supplementary section for a detailed explanation.

5. Supplementary section

5.1. Split-step non-paraxial method

By applying the finite difference method for a small step, Δz to solve Eq. 7.5, we can get the following equation:

$$\mathbf{v}(x, y, z + \Delta z) = \exp(\mathbf{H}(x, y, z)\Delta z)\mathbf{v}(x, y, z). \quad (7.8)$$

When we consider an inhomogeneous sample immersed in a homogeneous medium, n_0 , it is possible to split the matrix \mathbf{H}_1 and \mathbf{H}_2 which correspond to diffraction and refraction, respectively,

$$\mathbf{H}(x, y, z) = \mathbf{H}_1(x, y, z) + \mathbf{H}_2(x, y, z) = \begin{bmatrix} 0 & 1 \\ -(\frac{\partial^2}{\partial x^2} + \frac{\partial^2}{\partial y^2} + k_0^2 n_0^2) & 0 \end{bmatrix} + \begin{bmatrix} 0 & 0 \\ k_0^2(n_0^2 - n^2(x, y, z)) & 0 \end{bmatrix}. \quad (7.9)$$

Using Eq. 7.9, we can define $\mathbf{P} = \exp(\mathbf{H}_1\Delta z)$ and $\mathbf{Q} = \exp(\mathbf{H}_2\Delta z)$, then Eq. 7.8 can be split into two steps,

$$\mathbf{v}(x, y, z + \Delta z) = \mathbf{Q}\mathbf{P}\mathbf{v}(x, y, z). \quad (7.10)$$

We omitted the notation of (x, y, z) in \mathbf{P} , \mathbf{H}_1 , \mathbf{Q} and \mathbf{H}_2 for the sake of brevity. Using the Taylor series expansion, \mathbf{P} can be written as

$$\mathbf{P} = \begin{bmatrix} I & 0 \\ 0 & I \end{bmatrix} + \mathbf{H}_1\Delta z + \frac{(\mathbf{H}_1\Delta z)^2}{2!} + \frac{(\mathbf{H}_1\Delta z)^3}{3!} + \dots \quad (7.11)$$

\mathbf{Q} can be simplified as follows:

High fidelity optical diffraction tomography of strongly scattering samples

$$\mathbf{Q} = \begin{bmatrix} I & 0 \\ 0 & I \end{bmatrix} + \mathbf{H}_2 \Delta z, \quad (7.12)$$

since (\mathbf{H}_2^m) is $\mathbf{0}$ when m is higher than 1.

5.2. Numerical implementation

We will denote the scalar field at the k -th slice by the vector $\mathbf{u}_k \in \mathbb{C}^M$ and the derivative of the field with respect to the optical axis, z , by the vector $\mathbf{u}'_k \in \mathbb{C}^M$. The RI contrast of an inhomogeneous medium in 3D is represented by the vector $\mathbf{x} = \mathbf{n} - n_0 \in \mathbb{R}^N$ and $\mathbf{x}_k \in \mathbb{R}^M$ denotes the k -th slice of \mathbf{x} . Derivative operations \mathbf{H}_1 in Eq. 7.9 can be implemented by taking the discrete Fourier transform (DFT) of the input signal, followed by Fourier kernel, and taking the inverse DFT again. Using Eq. 7.11 and Eq. 7.12, we can rewrite a discretized version of Eq. 7.10 for numerical implementation as follows:

$$\begin{bmatrix} \mathbf{u}_k \\ \mathbf{u}'_k \end{bmatrix} = \begin{bmatrix} \mathbf{I} & 0 \\ \mathbf{G}_{21} & \mathbf{I} \end{bmatrix} \begin{bmatrix} \mathbf{K}_{11} & \mathbf{K}_{12} \\ \mathbf{K}_{21} & \mathbf{K}_{22} \end{bmatrix} \begin{bmatrix} \mathbf{u}_{k-1} \\ \mathbf{u}'_{k-1} \end{bmatrix}, \quad (7.13)$$

$$\begin{aligned} \mathbf{G}_{21} &= \text{diag}\{\mathbf{g}(\mathbf{x}_k)\} \\ \mathbf{K}_{11} &= \mathbf{F}^H \left[\mathbf{I} + \sum_{j=1}^{\infty} \text{diag}(-\mathbf{s})^j \frac{\Delta z^{2j}}{(2j)!} \right] \mathbf{F} \\ \mathbf{K}_{12} &= \mathbf{F}^H \left[\mathbf{I} \Delta z + \sum_{j=1}^{\infty} \text{diag}(-\mathbf{s})^j \frac{\Delta z^{2j+1}}{(2j+1)!} \right] \mathbf{F} \\ \mathbf{K}_{21} &= \mathbf{F}^H [\text{diag}(-\mathbf{s}) \mathbf{K}_{12}] \mathbf{F} \\ \mathbf{K}_{22} &= \mathbf{F}^H [\mathbf{K}_{11}] \mathbf{F} \end{aligned} \quad (7.14)$$

where $\mathbf{g}(\mathbf{x}_k) = -k_0^2 (2n_0 \mathbf{x}_k + \mathbf{x}_k \circ \mathbf{x}_k) \Delta z$, where \circ represents the hadamard product.

5.3. Calculation of the gradient

In previous work [26], it has been shown that the gradient of $D^{(l)}(\mathbf{x})$ and its Hermitian can be written as:

$$[\nabla D^{(l)}(\mathbf{x})] = \left[\frac{\partial D^{(l)}(\mathbf{x})}{\partial x_1} \dots \frac{\partial D^{(l)}(\mathbf{x})}{\partial x_N} \right] = \text{Re} \left\{ (\mathbf{S}_K^{(l)}(\mathbf{x}) - \mathbf{y}_K^{(l)})^H \left[\frac{\partial}{\partial \mathbf{x}} \mathbf{S}_K^{(l)}(\mathbf{x}) \right] \right\}. \quad (7.15)$$

In practice, we are interested in the column vector:

$$[\nabla D^{(l)}(\mathbf{x})]^H = \text{Re} \left\{ \left[\frac{\partial}{\partial \mathbf{x}} \mathbf{S}_K^{(l)}(\mathbf{x}) \right]^H (\mathbf{S}_K^{(l)}(\mathbf{x}) - \mathbf{y}_K^{(l)}) \right\}. \quad (7.16)$$

Using Eq. 7.13 and Eq. 7.14, we can calculate the following:

High fidelity optical diffraction tomography of strongly scattering samples

$$\left[\frac{\partial \mathbf{S}_k^{(l)}(\mathbf{x})}{\partial \mathbf{x}} \right] = \begin{bmatrix} \mathbf{K}_{11} & \mathbf{K}_{12} \\ \mathbf{K}_{21} + \mathbf{G}_{21}\mathbf{K}_{11} & \mathbf{K}_{22} + \mathbf{G}_{21}\mathbf{K}_{12} \end{bmatrix} \left[\frac{\partial \mathbf{S}_{k-1}^{(l)}(\mathbf{x})}{\partial \mathbf{x}} \right] + \begin{bmatrix} \mathbf{0} \\ \text{diag}\{(\mathbf{K}_{11}\mathbf{u}_{k-1} + \mathbf{K}_{12}\mathbf{u}_{k-1}')\} \left[\frac{\partial}{\partial \mathbf{x}} \mathbf{g}(\mathbf{x}_k) \right] \end{bmatrix} \quad (7.17)$$

Since $\frac{\partial \mathbf{S}_0^{(l)}(\mathbf{x})}{\partial \mathbf{x}} = 0$, it is possible to calculate the Hermitian of Eq. 7.17 by recursion [26].

5.4. Experimental setup

The optical system shown below used to acquire the data shown in this study used a diode pumped solid state (DPSS) 532 nm laser. The laser beam was first spatially filtered using a pinhole spatial filter. A beamsplitter was used to separate the input beam into a sample beam and a reference beam. The sample beam was directed onto the sample at different angles of incidence using a reflective LCOS spatial light modulator (SLM) (Holoeye) with a pixel size of 8 μm and resolution of 1080x1920 pixels. Different illumination angles were obtained by projecting blazed gratings on the SLM. In the experiments presented here, a blazed grating with a period of 25 pixels (200 μm) was circularly rotated with a resolution of 1 projection per degree for total projections. Two 4f systems between the SLM and the sample permitted filtering of higher orders reflected from the SLM (due to limited fill factor and efficiency of the device) as well as magnification of the SLM projections onto the sample. Using a 100X oil immersion objective lens with NA 1.4 (Olympus), the incident angle on the sample corresponding to the 200 μm grating was 35°. The magnification of the illumination side was defined by the 4f systems we used before the sample. A third 4f system after the sample includes a 100X oil immersion objective lens with NA 1.45 (Olympus). The sample and reference beams were collected on a second beamsplitter and projected onto a scientific CMOS (sCMOS) camera (Neo, Andor) with a pixel size of 6.5 μm and resolution of 2150 x 2650 pixels.

High fidelity optical diffraction tomography of strongly scattering samples

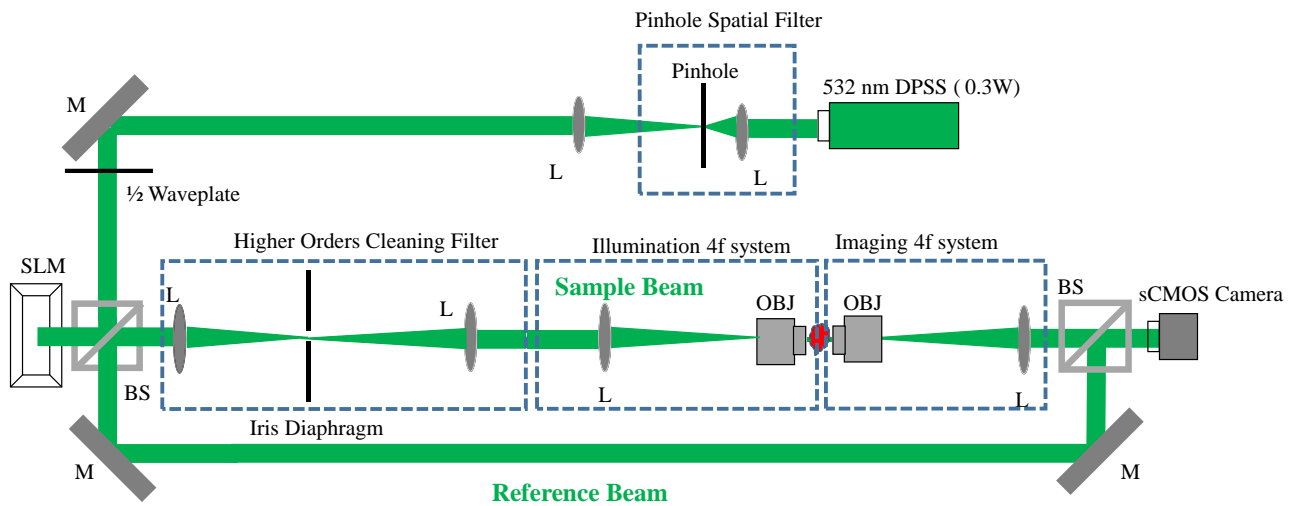


Figure 7-8. Schematic for the experimental setup (M: Mirror, L: Lens, OBJ: Objective lens, BS: Beam splitter).

5.5. Sample preparation

Yeast cells were grown in a solution of agar with a refractive index of 1.338 (a change of 0.00125 for 0.5% increase in the Agar concentration). 2g pure agar powder (AppliChem) was dissolved in 100 mL water, heated to 80C, and subsequently cooled, all while stirring with a magnetic stirrer. Once the solution reached 40C, 2g fresh grocer's yeast was added to the solution. The yeast-agar solution was immediately pipetted onto a #1 coverslip and covered with a second coverslip and finally allowed to cool to room temperature for complete gel formation.

HCT-116 human colon cancer cells were cultured in McCoy 5A growth medium (Gibco) supplemented with 10% fetal bovine serum (Gibco). #1 coverslips were treated with a 5 μ g/mL solution of fibronectin (Sigma) in phosphate-buffered saline (PBS) and air-dried at room temperature. Cells at passage 11 were detached from culture flasks using trypsin, seeded directly onto the fibronectin-treated coverslips, and incubated 24 hours in a 37C/5% CO₂ atmosphere until cells adhered and spread on the coverslips. Each sample was fixed for 10 minutes at room temperature in 4% para-formaldehyde in PBS, rinsed twice with PBS, and sealed with a second coverslip.

Chapter 8 Three-dimensional tomography of red blood cells using deep learning

This work has been published in [Joowon Lim, Ahmed B. Ayoub, and Demetri Psaltis "Three-dimensional tomography of red blood cells using deep learning," Advanced Photonics 2(2), 026001 (24 March 2020). <https://doi.org/10.1117/1.AP.2.2.026001>].

A.B. Ayoub built the optical setup, and carried out the experiments.

1. Introduction

When we look at a three-dimensional (3-D) object in a conventional microscopy, we can only see a two-dimensional (2-D) projection at one time. Therefore, we need more information in order to extract the 3-D shape from the 2-D measurement. If we make a holographic measurement where we record both amplitude and phase, measuring at different z planes is equivalent to a single measurement followed by the digital propagation to multiple planes. Therefore, with coherent detection, a z -scan does not provide extra information compared to the single 2-D recording. Another dimension that can be exploited is the illumination angle θ . The measurements in the x , y , θ dimensions can be converted to the 3-D spatial domain by defining the physical relationship between the illuminating fields at the different angles and the corresponding measurements. However, most of the time, the 2-D measurements are incomplete due to the limited numerical apertures (NAs) of the optics, resulting in an inversion process that is highly ill-posed.

Optical diffraction tomography (ODT) is a 3-D imaging method that utilizes multiple 2-D measurements acquired by changing the angle of illumination. The contrast mechanism in ODT is endogenous index. It, therefore, does not require external labeling. ODT provides 3-D refractive index (RI) distributions [12] that contain morphological and biochemical information, which have been widely used to study various biological samples, which are summarized in recent review papers [34, 122, 131, 132]. Under the assumption of weak scattering, multiple 2-D measurements in (x, y, θ) can be directly inverted to yield the 3-D RI information in (x, y, z) using the Wolf transform [19], which is the transformation that maps the spatial frequencies of the 2-D spectrum of the projections to the spatial frequencies of the 3-D spectrum of the object. However, direct inversion reconstruction methods based on the Wolf transform suffer from the missing cone problem—a consequence of the missing spatial frequencies that are not accessible due to the limited NAs of the optics [77].

Three-dimensional tomography of red blood cells using deep learning

The missing cone problem has been intensively investigated due to its importance [77, 147]. Previous approaches are model-based iterative reconstruction (MBIR) schemes, which exploit regularizations based on our prior knowledge, such as non-negativity or sparsity constraints. In other words, MBIR schemes find a solution that is not only consistent with the measurements but also sparse in the regularization domain. The choice of regularization is critical. However, it requires extensive understanding of the characteristics of the forward models, including the degree of ill-posedness intertwined with the characteristics of the samples. This makes the problem challenging.

Recently, deep neural networks (DNNs) have been successful in various optical applications, such as enhancement of the transverse resolution [148], phase retrieval from intensity measurements [149, 150], digital staining [151, 152], classification/segmentation based on holographic/tomographic measurements [153-155], and others [149, 156, 157]. There are some previous demonstrations of the benefits of applying DNNs to the reconstruction of RI values in ODT [158-160]. As far as we know, nobody has succeeded before in using DNNs to reconstruct arbitrary 3-D RI distributions from limited angle measurements taking diffraction and multiple scattering into account.

In this chapter, we describe a method based on DNNs to solve the long-standing missing cone problem and demonstrate it using red blood cell (RBC) samples. Despite the potential capacity of DNNs, the lack of the ground truth prevents us from applying DNNs on the ODT reconstruction, unlike other DNN optical imaging applications, such as digital staining or phase retrieval where we can access the target images. Our approach relies on the formation of digital phantoms followed by accurate digital models, which provide the 2-D measurements. The digital 2-D projections are used to form a rough 3-D image of the object using the Wolf transform under the Rytov approximation [19]. By training a DNN with the pairs of images from the Wolf transform and the corresponding digital phantoms, we can learn the distortions introduced due to the incomplete measurements in a data-driven way.

2. Main Idea

We demonstrate the method by using RBC samples that are highly affected by the missing cone problem. The shape of RBCs is flat and biconcave showing narrow dimple regions at the center, which requires high-frequency components along the optical axis to fully resolve the structures [2, 49]. In Figure 8-1 (a), we observe that cross sections of the Rytov reconstruction are underestimated and elongated along the z axis when compared with the corresponding sections of the ground truth. The k -space representation of the Rytov reconstruction can be considered as the low-pass filtered version of the k -space of the ground truth under the weak scattering assumption. Looking at the k -space of the ground truth, the frequency components are more broadly distributed in the k_z axis compared to ones in the k_y axis since the sample is broad in the y axis but has the narrow biconcave shape in the z axis. While high-frequency components are required to fully resolve the thin structure, most of them are lost because they are inaccessible due to the limited NAs as indicated by the red triangles. This results in the high distortions in the final Rytov reconstruction. In general, Rytov

Three-dimensional tomography of red blood cells using deep learning

reconstructions of RBCs show holes in the middle making it hard to retrieve meaningful information, such as cell volume, surface, and RI values.

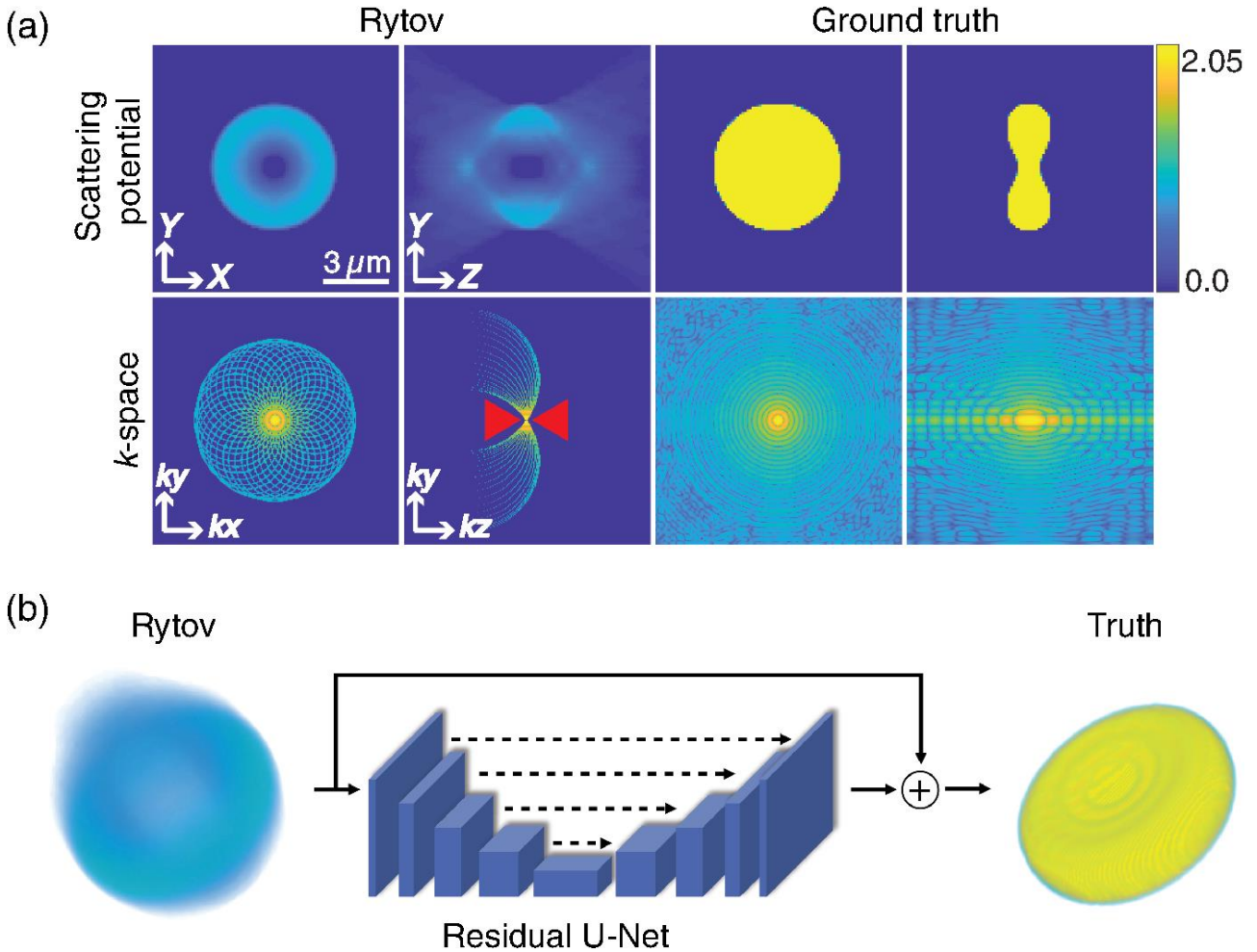


Figure 8-1. The missing cone problem and overall scheme of the main idea. (a) Demonstration of the missing cone problem for a single RBC. The left two columns show the Rytov reconstruction and the right two columns show the ground truth. The first row displays the scattering potential, which can be converted to RI distributions, and the second row displays the k-spaces corresponding to the first row. (b) Overall scheme of the network.

A DNN can be trained to recover those missing high frequencies, which are especially important for forming tomograms of RBCs. The network reconstructs the original RBC with the Rytov reconstruction as the initial condition in the training of the DNN, as shown in Figure 8-1 (b). We refer to the network as TomoNet throughout this paper. The input to the network is the Rytov reconstruction of an RBC and the output is the enhanced image of the same RBC. The input is also relayed directly to the output of the network where it is summed with the correction calculated by the DNN. Therefore, the network learns to extract the difference between the input and the output. In other words, given the low-pass filtered input, the network synthesizes the missing high-pass filtered information using data-driven features from a large number of examples. By combining the low-pass filtered input with the high-pass synthesized output from the network, we can achieve the full resolutions in the transverse and axial planes.

Three-dimensional tomography of red blood cells using deep learning

For training, we digitally generated many RBCs that are different in shape and RI value using the RBC model, as shown in figure 8-2 (a) [144]. For detailed information of the generation of different RBCs, we refer interested readers to Appendix A. Then, each RBC served as a sample for DDA simulations to generate accurate synthetic measurements, as shown in figure 8-2 (b) [134, 143]. A total of 40 uniformly spaced measurements were acquired by scanning on a circular pattern while maintaining a fixed illumination angle of 36 deg with respect to the z axis. The RBC phantoms generated using the model [Figure 8-2 (a)] originally lie in the xy plane. We implemented the various orientations of RBCs that can occur by randomly rotating each sample in the yz and xy planes. The DDA method was then used to calculate the 2-D projections of each 3-D phantom for each of the 40 illumination angles [Figure 8-2 (c)]. These calculations were used to form 3-D reconstructions using the Rytov method, which served as the input to the network.⁶ Each Rytov reconstruction was paired with the corresponding synthetic RBC that was used to generate the calculations. Figure 8-2 (c) shows two example pairs, one without rotation and the other with rotation.

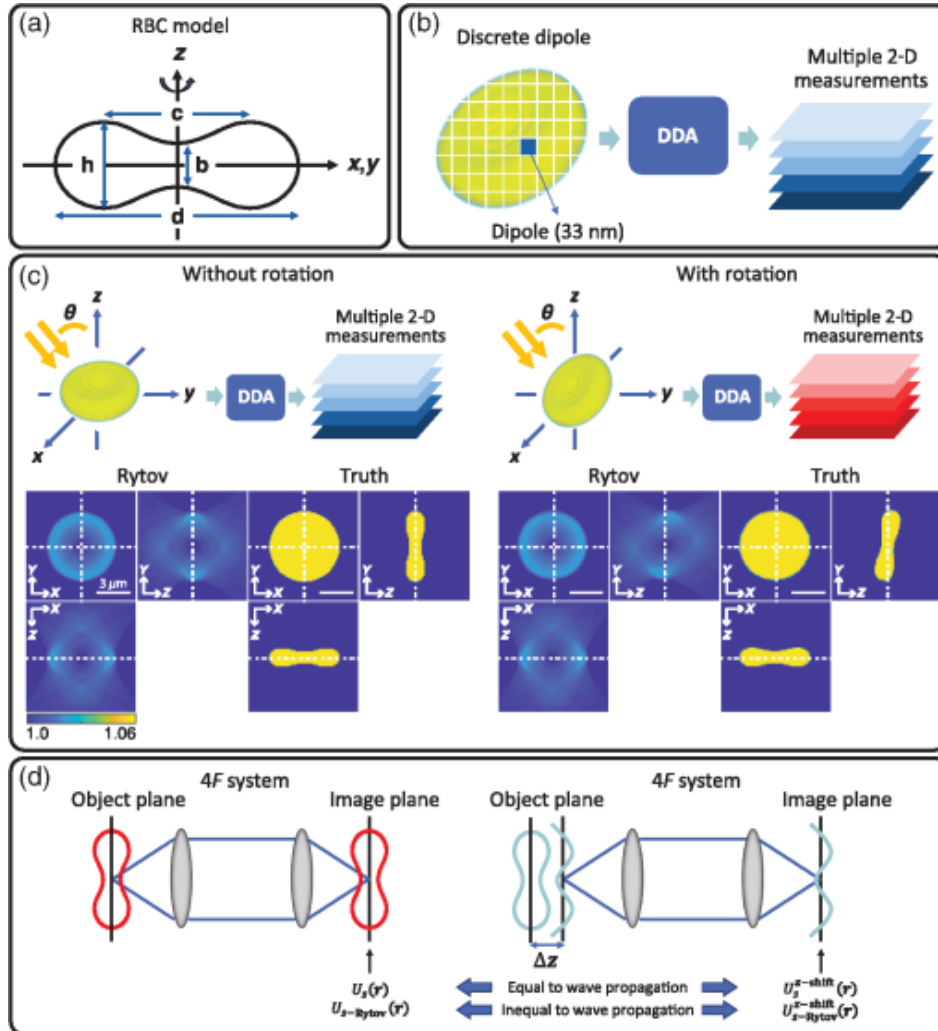


figure 8-2. Dataset generation. (a) RBC model parameters. (b) Synthetic measurements generation using the DDA. (c) Generation of synthetic measurements for two RBCs: one RBC lying in the xy plane and the same RBC but randomly rotated. The pairs of the Rytov reconstructions and the ground truth RBCs are presented. The scale represents the normalized RI, which is calculated by dividing the RI values of a sample by the RI of the background. (d) Schematic description of the z -shift variant property of the Rytov measurement.

Three-dimensional tomography of red blood cells using deep learning

For each RBC pair, we want to augment the dataset by shifting each example in all the axes. To do so, it is important to consider the shift properties of the Rytov reconstruction along each axis. We start from the integral solution to the Helmholtz equation:

$$U_s(\mathbf{r}) = \int_V F(\mathbf{r}') U(\mathbf{r}') G(\mathbf{r} - \mathbf{r}') d\mathbf{r}' \quad (8.1)$$

where $F(\mathbf{r}) = \frac{k^2}{4\pi} (n^2(\mathbf{r}) / n_0^2 - 1)$ is the scattering potential of a sample whose RI distribution is $n(r)$ when immersed in a medium whose RI is n_0 , given a wavenumber for the wavelength λ in vacuum, $k = \frac{2\pi n_0}{\lambda}$. Here $G(\mathbf{r} - \mathbf{r}') = \frac{e^{ik|\mathbf{r}-\mathbf{r}'|}}{|\mathbf{r} - \mathbf{r}'|}$ is the Green's function of the 3-D Helmholtz

equation. The $U_i(\mathbf{r})$ and $U(\mathbf{r})$ are the incident and total electric fields, respectively, and the $U_s(\mathbf{r})$ is the scattered electric field, $U_s(\mathbf{r}) = U(\mathbf{r}) - U_i(\mathbf{r})$. The term $U_s(\mathbf{r})$, on the left-hand side, can be measured at the image plane, as shown in Figure 8-2 (d). It is intuitive to see that moving the sample in the xy plane results in the same shift in the plane of the measurement of the scattered field. When the sample is translated in z, however, the measured scattered field will be the propagated version of the original unshifted measurement. Assuming that the sample is weakly scattering, the Rytov approximation uses the phase of the field itself, and Eq. 8.1 can be rewritten as follows:

$$U_{s-Rytov}(\mathbf{r}) = U_i(\mathbf{r}) \log \frac{U(\mathbf{r})}{U_i(\mathbf{r})} = \int_V F(\mathbf{r}') U_i(\mathbf{r}') G(\mathbf{r} - \mathbf{r}') d\mathbf{r}' \quad (8.2)$$

The left term of Eq. 8.1 $U_s(\mathbf{r}) = U(\mathbf{r}) - U_i(\mathbf{r})$ is replaced with the first Taylor expansion of it

$U_i(\mathbf{r}) \log \frac{U(\mathbf{r})}{U_i(\mathbf{r})}$. It, therefore, loses the propagation property of the scattered field. We refer this

term as $U_{s-Rytov}(\mathbf{r})$. In other words, we must recalculate $U_{s-Rytov}^{z-shift}(\mathbf{r})$ when an object is shifted in the z axis and the result of this calculation is different than distally propagating the field $U_{s-Rytov}(\mathbf{r})$.

Taking these properties into consideration, we augmented the set of training examples by generalizing shifted versions of the original pairs. For the shift in the xy plane, we added an xy-shifted version of each pair in addition to the original pair (without any shift). The shift was randomly selected during training. For the shift in the z axis, after generating the 40 projections for an RBC centered at $z=0$, we digitally propagated the simulated measurements, $U(\mathbf{r})$ and $U_i(\mathbf{r})$, to four different z planes ($-2\Delta z$, $-\Delta z$, $+\Delta z$, and $+2\Delta z$) and calculated the corresponding $U_{s-Rytov}(\mathbf{r})$ values at each plane. This was followed by their Rytov reconstructions to obtain examples of RBCs shifted along

Three-dimensional tomography of red blood cells using deep learning

the z axis. In this work, Δz was set to 122 nm, which corresponds to one pixel of reconstruction grid. Rytov reconstructions were paired with the shifted RBCs in the z axis.

3. Method

3.1. Network Training

We trained a U-Net-type DNN in the regression manner using the following weighted l_2 -norm as the cost function [161, 162]:

$$Error(x_{recon}, x_{true}) = \frac{\|x_{recon} - x_{true}\|^2}{\|x_{true}\|^2} \quad (8.3)$$

where x_{recon} is the output from the network given x_{Rytov} , and x_{true} is calculated from the ground truth RI contrast. Here, x represents the RI contrast multiplied by a scalar value, which is calculated as $c(n - n_0)$, where n represents sample RI distributions and n_0 is the RI of medium. The scalar c was introduced for normalization of values; c can be either 40 for x_{Rytov} or 20 for x_{true} . Negative components of input and output of the network were discarded. We implemented the network using PyTorch (1.2.0) and compute unified device architecture toolkit (10.0) on a desktop computer (Intel Core i7-6700 CPU, 3.4 GHz, 32 GB RAM) with a graphic processing unit (GPU, GeForce GTX 1070). The network was trained using the Adam optimizer with the learning rate of 1×10^{-4} , and it decayed half after every 10 epochs [163]. The mini-batch size was 8 and the total number of epoch was 50.

Figure 8-3 describes the network structure. It is very similar to the U-Net proposed in [161, 162], except for slight modifications [164, 165]. The input is skip-connected and summed to the output of the network. Therefore, the network learns the residual difference between the Rytov reconstruction and the ground truth [162]. All biases in the convolutional layers were set to zero and fixed. Zeros were padded for convolution layers of which kernel sizes are bigger than 1 so that the dimensions stay equal before and after the convolutions. The negative slope of leaky rectified linear unit (RELU) was set to 0.01. For the normalization layer, affine transform was turned off. For the transpose convolutional layers, the kernel size was set to $6 \times 6 \times 6$ with the zero padding of $2 \times 2 \times 2$ and the stride of $2 \times 2 \times 2$.

Three-dimensional tomography of red blood cells using deep learning

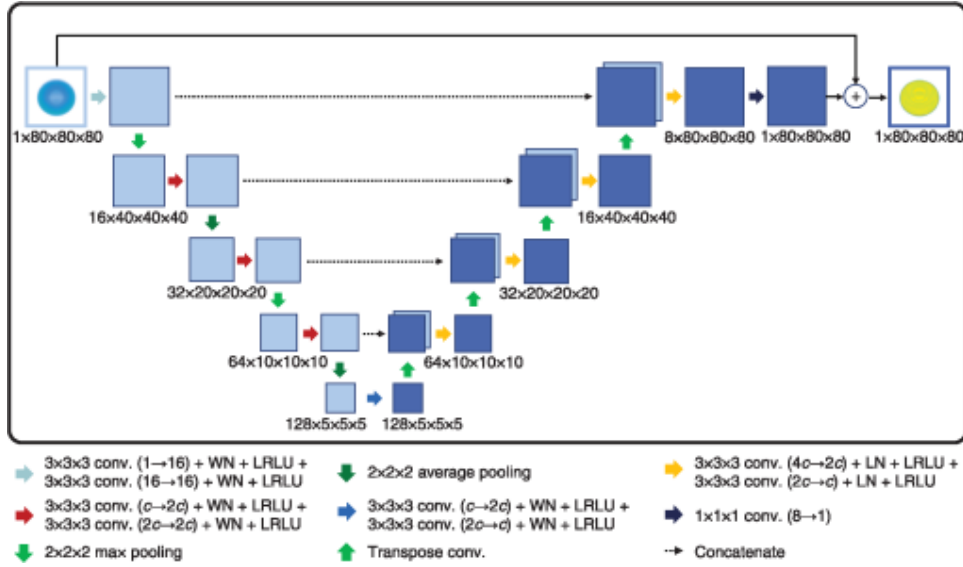


Figure 8-3. Schematic description of the network structure. Here C represents the number of channels written at each block. WN, weight normalization; LRLU, leaky RELU; and LN, layer normalization.

3.2. Experiment

The optical setup is described in Figure 8-4 [84]. It includes a diode pumped solid state 532 nm laser. The laser beam was first spatially filtered using a pinhole spatial filter. A beamsplitter was used to split the input beam into a sample beam and a reference beam. The sample beam was directed onto the sample at different angles of incidence using a reflective liquid crystal on silicon spatial light modulator (SLM) (Holoeye) with a pixel size and resolution of 1080×1920 pixels. Different illumination angles were obtained by projecting blazed gratings on the SLM. In the experiment presented here, a blazed grating with a period of 25 pixels was rotated a full 360 deg. Two 4F systems between the SLM and the sample permitted filtering of higher orders reflected from the SLM (due to limited fill factor and efficiency of the device) as well as magnification of the SLM projections onto the sample. Using a $100\times$ oil immersion objective lens with NA 1.4 (Olympus), the incident angle on the sample corresponding to the grating was 36 deg. The magnification of the illumination side was defined by the 4F systems we used before the sample. A third 4F system after the sample includes a $100\times$ oil immersion objective lens with NA 1.45 (Olympus). The sample and reference beams were collected on a second beamsplitter and projected onto a scientific CMOS (sCMOS) camera (Neo, Andor) with a pixel size and resolution of 2150×2650 pixels.

Three-dimensional tomography of red blood cells using deep learning

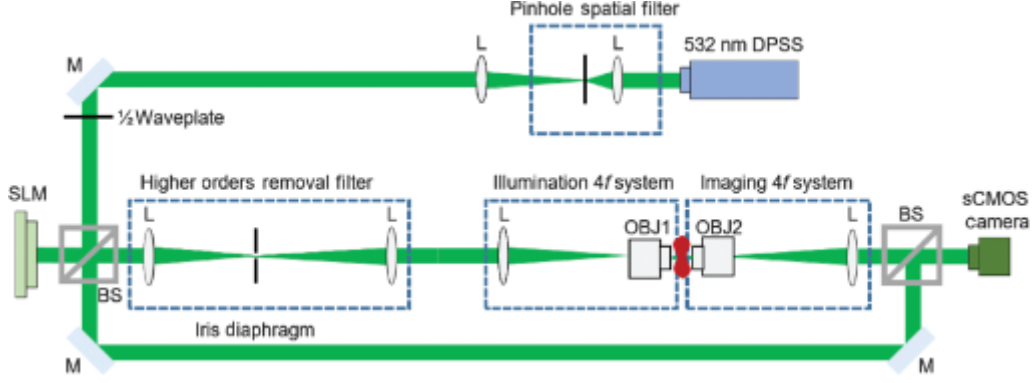


Figure 8-4. Schematic for the experimental setup. M, mirror; L, lens; OBJ, objective lens; and BS, beamsplitter.

Blood sampling was performed by terminal intracardiac puncture on wild-type Balb/cByJ adult mice, in agreement with the Swiss legislation on animal experimentation (authorization number VD3290). RBCs were then isolated from blood plasma by centrifuging using Eppendorf-Centrifuge 5418 at 400 rpm for 3 min. RBCs were then fixed using glutaraldehyde with concentration of 0.25% in phosphate-buffered saline (PBS) followed by centrifuging for 1 min and washing three times with PBS to remove any fixation reagents traces. To ensure strong adhesion between the RBC and the coverslip, coverslip was coated with 0.1% poly L-lysine diluted in PBS with molecular weight ranging between 1000 and 5000gm/mol.

4. Results

4.1. Synthetic Data

Results obtained with the TomoNet are displayed in Figure 8-5 for two different RBCs. Here, we only present centered RBCs without shifts in the xy plane. The first row shows RI reconstructions of Rytov, TomoNet, and the ground truth. The second row displays the difference map from the ground truth (reconstruction – the ground truth). In other words, blue regions in the difference map display underestimated parts and yellow regions show elongated regions. As expected, the Rytov reconstructions underestimate the RI values and elongate the RI distributions along the optical axis. Especially, the central dimple region of the RBC is significantly deteriorated. This is because the dimple region is thin and requires high frequencies for its reconstruction. By contrast, TomoNet shows excellent reconstruction results since it estimates accurately the values of these high frequencies from the data in the training set. In other words, the TomoNet implements super-resolution for 3-D samples revealing spatial details beyond the classical resolution limit. We quantitatively assessed the accuracy of the TomoNet over the Rytov reconstruction by calculating the following metric:

$$Error(\Delta n_{recon}, \Delta n_{true}) = \frac{\|\Delta n_{recon} - \Delta n_{true}\|^2}{\|\Delta n_{true}\|^2} \quad (8.4)$$

where Δn_{recon} is the reconstructed RI contrast and Δn_{true} is the ground truth RI contrast. Here, Δn represents the RI contrast, which is defined as $(n - n_0)$, where n represents the sample RI distri-

Three-dimensional tomography of red blood cells using deep learning

butions and n_0 is the RI of medium. We discarded the negative values when calculating the error metric. The mean error values over all test RBCs are 0.5929 for the Rytov method and 0.0084 for the TomoNet, which confirms the improved performance of the network. The trained network accurately reconstructs RBCs and it does so in less than 10 ms on a GPU (GeForce GTX 1070).

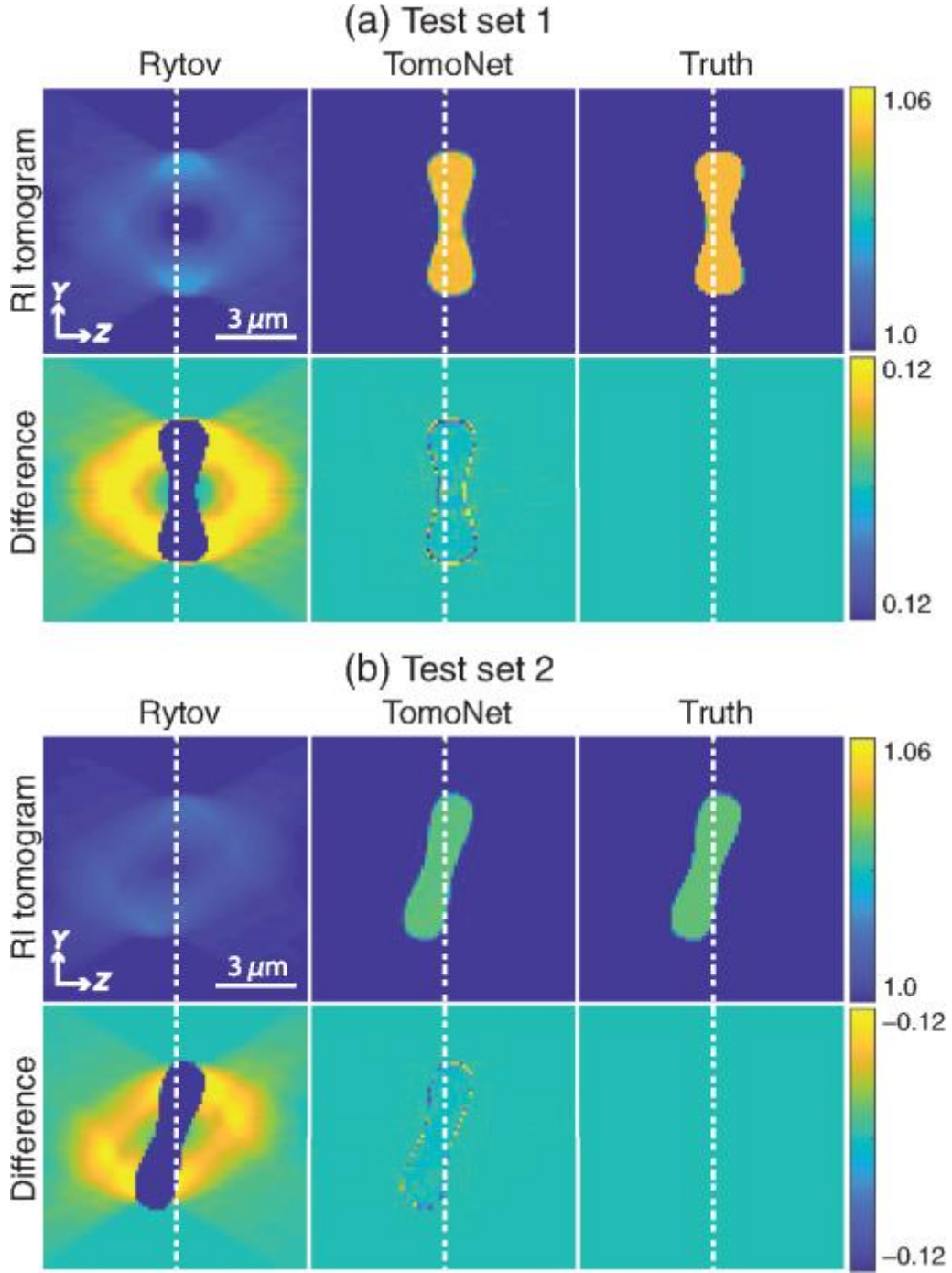


Figure 8-5. Reconstruction results using two examples from the test datasets. (a) Results for an RBC without rotation and (b) results for another RBC with rotation. The scale represents the normalized RI, which is calculated by dividing the RI values of a sample with the RI of background.

Three-dimensional tomography of red blood cells using deep learning

4.2. Experimental Data

We applied the network trained with digital phantoms to the Rytov reconstruction of a mouse RBC formed from experimental measurements. In the experiment, the samples were circularly scanned at the illumination angle of 36 deg in 9-deg steps resulting in 40 measurements, matching the parameters we used to generate the digital training data. As shown in Figure 8-6, the Rytov reconstructions using the measurements show severe distortions, especially at the dimple region as we also observed in the synthetic data. With the Rytov reconstruction as its input, the TomoNet reconstructs RI tomograms without those artifacts resulting in the biconcave morphology. We verified the great improvement in the quality of the reconstructions visible in Figure 8-6, by using a quantitative method [30] to evaluate the reconstruction accuracy of 3-D objects when the ground truth is not accessible. This was possible by generating semisynthetic measurements.

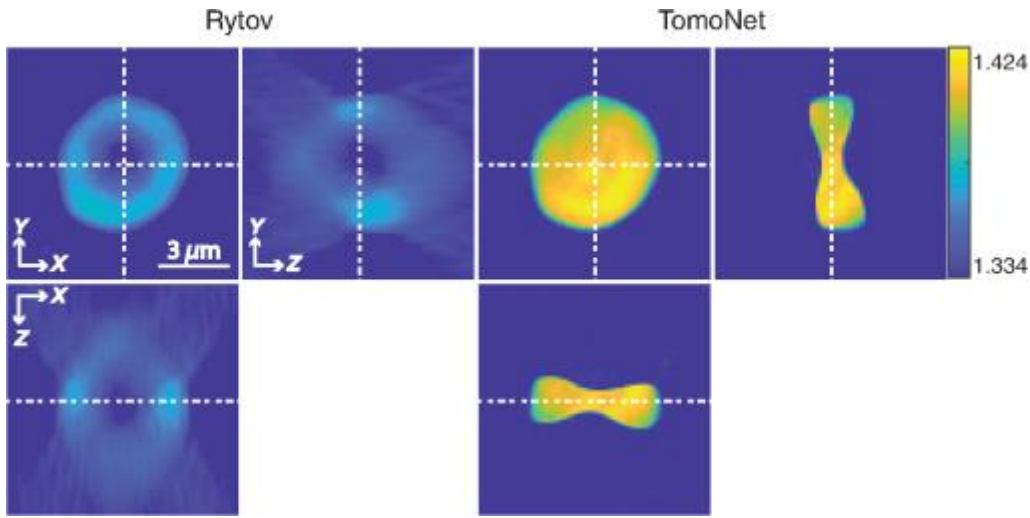


Figure 8-6. Reconstruction of mouse RBC from experimental data using the network trained on synthetic data. The images to the left show the Rytov reconstruction, which is the input to the network. The images to the right show the results of the TomoNet.

As described in Figure 8-7 (a), following the reconstruction of the RI distributions from the experimental measurements, we generated semisynthetic 2-D projections using an accurate forward model such as the DDA at each illumination angle. By comparing the digital projections with the corresponding 2-D experimental measurements, the difference between them reflects how close the 3-D reconstruction is to the ground truth. It is noteworthy that we did not use the forward model involved in the reconstruction to generate the digital projections to be fair.

Three-dimensional tomography of red blood cells using deep learning

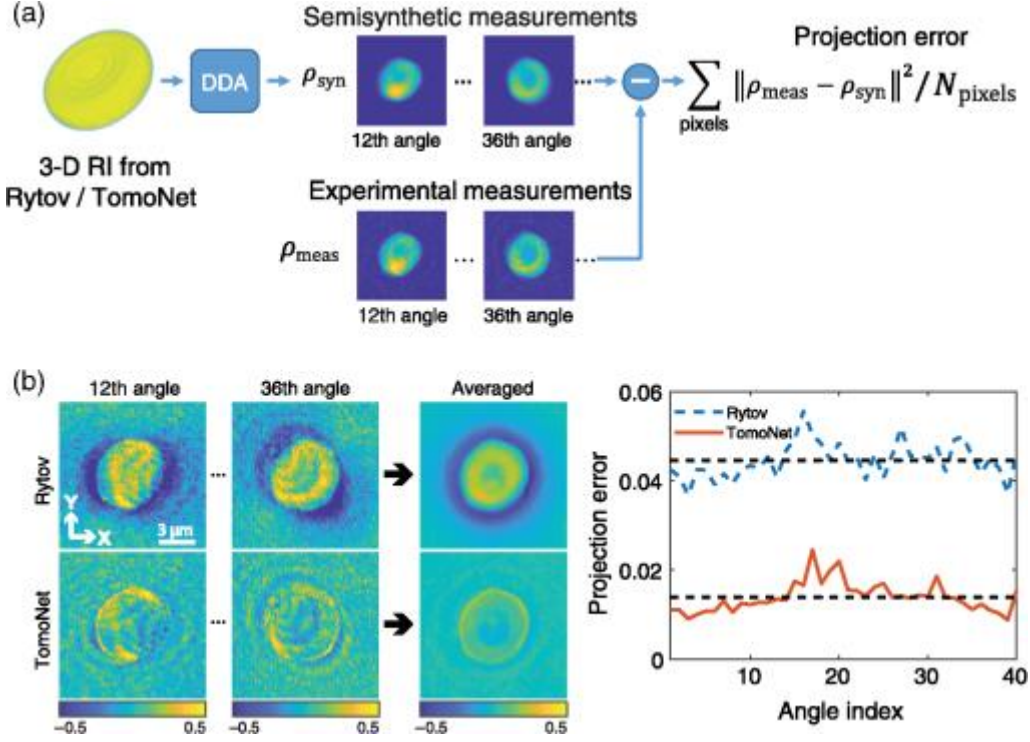


Figure 8-7. Validation of the experimental result using semisynthetic measurements. (a) Overall scheme of semisynthetic measurement generation using DDA. (b) Phase difference maps for two randomly selected angles and the average maps for all angles. The color bars are in radians. Calculation of projection errors in retrieved phase information from experimental and semisynthetic measurements.

Figure 8-7 (a) shows two examples of phase maps from digital projections. For each digital projection, we calculated the projection error map, the difference in phase information between experimental and simulated measurements, along with the mean projection error map over all angles. Figure 7(b) displays two randomly selected projection error maps as well as the mean projection error maps for the Rytov and the TomoNet. In the case of Rytov, we can clearly see the mismatch between experimental and digital projections in the mean projection error map. By contrast, the mean projection error map of TomoNet shows excellent consistency. We further quantitatively confirmed the improvement in performance of TomoNet over Rytov by calculating the metric,

$\sum_{l=1}^L \|\rho_{exp}^l - \rho_{syn}^l\|^2 / N$, where L is the total number of angles, N is the total number of pixels,

and ρ_{exp} and ρ_{syn} are the phase maps from experimental and semisynthetic measurements, respectively. As shown in Figure 8-7 (b), the average of the metric shows twofold improvement of TomoNet over the Rytov method.

5. Appendix A: Dataset Generation

The shape of the surface of an RBC can be modeled by the following equation:

$$\rho^4 + 2S\rho^2z^2 + z^4 + P\rho^2 + Qz^2 + R = 0 \quad (8.5)$$

Three-dimensional tomography of red blood cells using deep learning

where ρ is the radius in cylindrical coordinates ($\rho^2 = x^2 + y^2$) and S, P, Q, and R are the parameters derived from d, h, b, and c shown in Fig. 2(a) [144]. To generate various RBCs, the d, h, and b values in microns were randomly selected from normal Gaussian distributions whose mean values were 7.65, 2.84, and 1.44 and standard deviations were 0.67, 0.46, and 0.47. c/d and the normalized RI values, $(n - n_0)/n_0$, were sampled from uniform distributions whose ranges were (0.56, 0.76) for c and (1.0355, 1.596) for the normalized RI [144]. To avoid nonrealistic shapes, several criteria were applied to limit the parameter values in the following ranges: $h < 0.95 \times d/2$ and $b \leq h$. In addition, we limited the derived geometrical parameters such as cell volume ($V \mu m^3$), surface ($S \mu m^2$), and sphericity index (SI), $6\sqrt{\pi V/S^3/2}$, to fall within the normal ranges: $66 < V < 130$, $98 < S < 162$, and $0.494 < SI < 0.914$. The cell surface was calculated using the equation, $\pi d[d/2 + 2h \times (\sinh - 1)e]/e$, where $e = 2\sqrt{9d^2 - 4h^2}/5h$ [166]. Finally, RBC shapes were downsampled with a factor, 7.65/5.8, since the mean diameter of mouse RBCs is 5.8 μm , compared to the 7.65 μm for humans [167]. A total of 100 different RBCs were generated and each of them was randomly rotated in the yz plane (uniform distribution: $[0, \pi/6]$) and the xy plane (uniform distribution: $[0, 2\pi]$) resulting in 200 different RBCs (100 without rotation and 100 with rotation).

To generate synthetic measurements using the DDA, each RBC was illuminated at the incident angle of 36 deg for 40 angles, which were uniformly distributed on a circle. The illumination wavelength λ was 396 nm and the size of each dipole was set to $\lambda/12 = 33$ nm. The background medium in the simulation was air and the sample RI was set to the normalized RI. For 2-D measurements, the size of the grid was 256×256 with a pixel size of 99 nm. After that, the measurements were downsampled by cropping in k-space resulting in a pixel size of 122 nm. The original phantom defined using dipoles interpolated to a sampling grid that matched the pixel size of the measurements.

Measurements for 200 randomly generated RBCs were digitally refocused to five different planes resulting in 1000 pairs. Totally 800, 100, and 100 pairs were used for training, validation, and test, respectively. For the training and validation, we doubled the datasets by adding the randomly shifted sets on top of the original sets, resulting in 1600 and 200 pairs. The random shift varied at every iteration. For the rotated RBCs, after generating the measurements, we reversely rotated the Rytov reconstructions and the paired ground truth RBCs in the xy plane, resulting in rotations only in the yz plane to simplify the training. For the experimental data, since we do not know the rotation angle in the xy plane, we applied ellipsoidal fitting on a binary mask generated by applying Otsu thresholding on the maximum projection map of Rytov [168]. By analyzing the short and long axes, we extracted the orientation of the RBC. Since the Rytov reconstruction is shift-invariant in the xy plane, we simply interpolated in the xy plane for rotation.

6. Appendix B: Semisynthetic Simulation

The semisynthetic measurements were calculated using reconstruction results acquired from Rytov and TomoNet as samples for the DDA simulations. The pixel size of these reconstructions was 122 nm. Since the size of dipole was set to $\lambda / 6n_0 = 67$ nm, where $\lambda = 532$ nm, $n_0 = 1.334$, the reconstructions were interpolated to a grid, one pixel of which was the size of a dipole. Then, we discretized the RI values as $\text{round}(n / n_0 \times 1000) / 1000$, and the negative values were discarded.

Chapter 9 Conclusion

In chapter 1, optical imaging was described with its main 2 branches; fluorescent imaging and label-free imaging. Phase contrast imaging by Zernike was described in which a phase mask is inserted along the propagation to create a phase difference between the incident field and the scattered field from the sample. As a result, the phase delay originated from the different refractive index between the sample and the surrounding medium is converted to an intensity variation and high contrast images can be retrieved to highlight the sample from the surrounding medium. Another approach is to build an “off-axis” holographic system with a separate reference arm combined with the sample arm via a beam-splitter as suggested by Upatnieks and Leith as a continuation to the work started by Gabor. By doing so, one can retrieve the complex field from the intensity pattern (i.e. Hologram). This is usually referred to as Quantitative Phase Imaging (QPI) and is the driving principle in digital holography microscopy (DHM). However, to retrieve the 3D information about the refractive index, we would need to illuminate the sample from different illumination angles and then use inverse models to generate the 3D RI distribution out of the different 2D phase maps. We refer to this process as optical diffraction tomography (ODT). In this thesis we study different aspects of ODT including the assessment of 3D RI reconstruction without access to the ground truth, using “on-line” holography to generate 3D RI reconstruction and finally possibility to acquire images at a high pace with the help of light modulators such as DMDs.

In chapter 2, the theory underlying the light scattering from inhomogeneous media is explained. Starting from the wave-equation we can derive an expression that relates the scattering potential, incident field and the Green’s function to the total field. Such equation is usually referred to as the lippmann-schwinger equation (LSE). Out of this equation, different direct-inversion models based on weakly-scattering approximation (i.e. usually called first-order approximations) are derived including Born and Rytov approximations. While these models are direct and simple, they usually fail for samples that experience highly-scattering events. In addition, such reconstruction, usually suffer from the so-called “missing cone” problem where due to the limited NA of the objective results in missing spatial frequency around the axis of propagation. Different experimental and computational approaches are discussed to solve such problem. Experimentally, a proposed solution would be to image not in transmission but in a 90 degrees geometry (i.e. camera is at 90 degrees from the direction of the incident field), or to image in transmission but with including sample rotation in addition to illumination scanning approaches.

Conclusion

In chapter 3, a method to assess the performance of the fidelity of different 3D RI reconstruction is proposed. On the contrary of samples where the ground truth is known (i.e. fabricated samples), biological samples does not possess such property. As a result an assessment method for such reconstructions is highly needed. We showed how structured illumination can be used to assess the performance of different reconstruction schemes through the use of an SLM for both angular scanning and structured illumination. Having the same experimental setup for angular and structured illumination without the burden of alignment and/or mechanical instabilities, it is possible to evaluate the performance of the different reconstruction algorithms by quantifying the error between different reconstructions based on the retrieved field from the digitally back-propagated output field recorded on the detector using the LSE. This assessment method is useful when imaging biological samples where the ground-truth cannot be known while the reconstructions need to be validated.

However, there are some critical aspects to highlight. First, while in this chapter we showed only 3 different reconstructions (i.e. Born, Radon, and Rytov), any reconstruction method can be assessed with our technique. The second aspect is that while we described the assessment based on structured illumination, it is not limited to it. Plane-wave illumination can be used as well since the assessment technique is general to any illumination pattern (i.e. phase conjugation). As long as we have access to the illumination field and the total field after propagating through the sample, our technique is valid.

In chapter 4, we proposed a new technique for the 3D reconstruction of samples using the Wolf transform from intensity measurements. Compared to other reconstruction schemes (i.e. Born, Rytov) that require optical interferometry to extract the phase, our approach is less demanding in which it only requires 2D intensity maps to perform the 3D reconstruction. As compared to [14] where the far-field intensity was detected and the twin image was neglected, in this work, the twin image was carefully analyzed and was shown to strongly affect the final reconstruction from the intensity measurements. As a result of the twin image, the 3D reconstruction from the intensity measurement resulted in the high frequency features within the sample to prevail as compared to holographic measurements. Other approaches can be followed to obtain a quantitative measure of the refractive index from intensity measurements. One approach could be to illuminate with the maximum possible angle that passes through the objective lens to minimize the effect of the twin image, producing enhanced contrast and a quantitative measure of the RI. Another possible approach would be implementation of a neural network to map 3D RI maps (i.e. Born, Rytov) to the 3D reconstruction from the intensity measurement, implicitly removing the twin-image effect from the reconstructions. One limitation of neural networks is that their fidelity is strongly sample-dependent, meaning that they must be retrained for any given class of sample (e.g. cell type, tissue type, etc.), so their utility for biological application may be limited. The proposed method is only limited to the weak scattering assumption. For multiple scattering samples, iterative reconstruction schemes can be used with forward models that take multiple scattering into account. We expect this intensity-only reconstruction to serve as an initial guess for those iterative reconstruction algorithms which usually suffer from local minima when initialized with zero values. In conclusion, we observed intriguing results by applying the Wolf transform to intensity-only measurements, obtaining edge-enhanced reconstructions when compared to complex field measurements. By using a

Conclusion

holographic setup, we were able to investigate the physics behind this reconstruction method and compare the RI maps obtained from complex field measurements with the 3D reconstruction obtained from intensity only.

In chapter 5, as a continuation to chapter 4, we presented a technique for 3D refractive reconstruction using the Wolf transform based on intensity measurements. The technique relies on mapping the extracted scattered field into the 3D Fourier space and then taking an inverse 3D Fourier transform to retrieve the 3D RI in the spatial domain. The reconstructions showed signal-to-noise ratio due to the use of partially incoherent illumination source which led to minimizing the speckle noise usually detected in coherent detection. To retrieve the 3D RI distribution, the illumination and the imaging NA must be perfectly matched (i.e. using conical illumination) in which any slight mismatch will severely affect the reconstruction accuracy as we have shown. Finally, we investigated the effect of adding other illumination wavelength and showed how to correct for the chromatic aberrations from the objective lens.

In chapter 6, high speed complex wavefront shaping using the digital micro-mirror device was demonstrated. The DMD was used in a time-multiplexing mode which allows for 8-bit grayscale image representation on the DMD within 38.4 ms allowing for focusing in live samples or for other applications without compromising the accuracy. For higher modulation rates, amplitude modulation was demonstrated with maximum achievable frame rate for 8-bit images of 833Hz yielding a speed up by a factor of 32 as compared to time multiplexing schemes. The method we demonstrated relies on time integrating holographic recordings of the fields or intensity patterns corresponding to multiple binary patterns on the DMD. The method is particularly useful for optical systems that use digital holography. The method might also be useful in applications where the projected pattern is integrated in time by a light sensitive material such as a fluorescent molecule in imaging or a photo-initiator molecule in 3D printing.

In chapter 7, we have proposed a new tomographic reconstruction algorithm, the LT-SSNP, which is based on the SSNP forward model, for imaging complex highly scattering samples with fine details. By benefiting from the accuracy of the SSNP, the LT-SSNP extracts a maximum amount of information from measurements rather than relying on prior assumptions and generalizations about the sample structure. The LT-SSNP was quantitatively evaluated and compared with the previous algorithm, the LT-BMP, by using synthetic measurements. These synthetic measurements with a known solution were generated by using Mie theory for multiple cylinders, and the DDA for an arbitrarily shaped cluster of RBCs and a cell phantom. Importantly, the added capabilities of the LT-SSNP are dramatic for imaging biological samples containing information across many scales, as confirmed by applying it to tomographic images of a yeast cell. The reconstructed tomograms by using the LT-SSNP clearly reveal structures that are not observable in the case of Rytov and the LT-BPM. Semisynthetic measurements based on the RI reconstructions of the LT-BPM and the LT-SSNP numerically validate the accuracy of the LT-SSNP reconstructions.

Conclusion

Furthermore, we explored the capacity of learning approaches to enable data compression by reducing the number of scanning angles. The LT-SSNP shows a dramatic improvement in image quality by using a small number of illumination angles when compared with the conventional direct inverse method by using the Rytov approximation. Even with a low number of projections, the LT-SSNP benefits from its weak dependency on the regularization parameter.

In chapter 8, we presented a DNN approach for reconstructing tomograms of RBCs with greatly improved image quality and super-resolution capability, especially enhancing the axial resolution. We digitally generated various RBCs and used them to generate synthetic measurements using the DDA to overcome the lack of the ground truth. The network trained on the synthetic data accurately reconstructs RI distributions of RBCs resolving the problems caused by the missing cone problem. We applied the trained network on experimental data to utilize extracted features from the synthetic datasets. Despite the lack of the ground truth for the experimental result, we further validated the result of the network using semisynthetic measurements, and it confirmed the great improvement.

In this work, we focused on one specific cell type, RBCs, since it is relatively easy to model them. More importantly, RBCs are highly distorted by the missing cone problem, which prevents us from retrieving meaningful information for various applications. However, we believe that the proposed scheme can be further extended to other types of sample by carefully designing phantoms to statistically capture information in the generated dataset.

References

1. G. Popescu, K. Badizadegan, R. R. Dasari, & M. S. Feld, "Observation of dynamic subdomains in red blood cells," *J. Biomed. Opt. Lett.* 11, 040503 (2006).
2. K. Kim, et al., "High-resolution three-dimensional imaging of red blood cells parasitized by *Plasmodium falciparum* and in situ hemozoin crystals using optical diffraction tomography," *J. Biomed. Opt.* 19, 011005 (2013).
3. B. Kemper, et al., "Investigation of living pancreas tumor cells by digital holographic microscopy," *J. Biomed. Opt.* 11, 034005–034008 (2006).
4. W. C. Hsu, J. W. Su, C. C. Chang, & K. B. Sung, "Investigating the backscattering characteristics of individual normal and cancerous cells based on experimentally determined three-dimensional refractive index distributions," *Proc. SPIE* 8553, 85531O (2012).
5. P. Jourdain, et al., "Determination of transmembrane water fluxes in neurons elicited by glutamate ionotropic receptors and by the cotransporters KCC2 and NKCC1: a digital holographic microscopy study," *J. Neurosci.* 31, 11846–11854 (2011).
6. P. Marquet, C. Depeursinge, & P. J. Magistretti, "Review of quantitative phase-digital holographic microscopy: promising novel imaging technique to resolve neuronal network activity and identify cellular biomarkers of psychiatric disorders," *Neurophotonics* 1, 020901 (2014).
7. C. Hu and G. Popescu, "Quantitative Phase Imaging (QPI) in Neuroscience," in *IEEE Journal of Selected Topics in Quantum Electronics*, vol. 25, no. 1, pp. 1-9, Jan.-Feb. 2019, Art no. 6801309, doi: 10.1109/JSTQE.2018.2869613.
8. G. Popescu, T. Ikeda, R. R. Dasari, & M. S. Feld, "Diffraction phase microscopy for quantifying cell structure and dynamics," *Opt. Lett.* 31, 775–777 (2006).
9. W. Choi, et al., "Tomographic phase microscopy," *Nat. Methods* 4, 717–719 (2007).
10. A. Diaspro, "Optical Fluorescence Microscopy," (Springer, Berlin, 2011).
11. F. Zernike, "How I discovered phase contrast," *Science* 121, 345–349 (1955).
12. M. Born, & E. Wolf, "Principles of Optics: Electromagnetic Theory of Propagation, Interference and Diffraction of Light," 7th edn (Cambridge Univ. Press, 1999).
13. D. Gabor, "A new microscopic principle," *Nature* 161, 777–778 (1948).
14. K. Creath, "Phase-measurement interferometry techniques," *Prog. Opt.* 26, 349–393 (1988).
15. E. N. Leith, & J. Upatnieks, "Reconstructed wavefronts and communication theory," *J. Opt. Soc. Am.* 52, 1123–1130 (1962).
16. T. C. Poon, "Digital Holography and Three-dimensional Display: Principles and Applications," (Springer Science & Business Media, New York, 2006).
17. D. A. Boas, C. Pitris, & N. Ramanujam, "Handbook of Biomedical Optics," (CRC Press, Boca Raton, 2016).
18. E. CuChe, F. Bevilacqua, & C. Depeursinge, "Digital holography for quantitative phase-contrast imaging," *Opt. Lett.* 24, 291–293 (1999).
19. Emil Wolf, "Three-dimensional structure determination of semi-transparent objects from holographic data," *Optics communications*, 1(4):153–156, 1969.
20. Anthony J Devaney, "A filtered backpropagation algorithm for diffraction tomography," *Ultrasonic imaging*, 4(4):336–350, 1982.
21. Avinash C Kak, Malcolm Slaney, and Ge Wang, "Principles of computerized tomographic imaging," *Medical Physics*, 29(1):107–107, 2002.

References

22. Jos M Bioucas-Dias and Gonalo Valadao, "Phase unwrapping via graph cuts," *IEEE Transactions on Image processing*, 16(3):698–709, 2007.
23. Malcolm Slaney, Avinash C Kak, and Lawrence E Larsen, "Limitations of imaging with first-order diffraction tomography," *IEEE transactions on microwave theory and techniques*, 32(8):860–874, 1984.
24. Chansuk Park, Seungwoo Shin, and YongKeun Park, "Generalized quantification of three-dimensional resolution in optical diffraction tomography using the projection of maximal spatial bandwidths," *J. Opt. Soc. Am. A* 35, 1891-1898 (2018).
25. Bertrand Simon, Matthieu Debailleul, Mounir Houkal, Carole Ecoffet, Jonathan Bailleul, Joël Lambert, Arnaud Spangenberg, Hui Liu, Olivier Soppera, and Olivier Haeberlé, "Tomographic diffractive microscopy with isotropic resolution," *Optica* 4, 460-463 (2017).
26. U. S. Kamilov et al., "Optical Tomographic Image Reconstruction Based on Beam Propagation and Sparse Regularization," in *IEEE Transactions on Computational Imaging*, vol. 2, no. 1, pp. 59-70, March 2016, doi: 10.1109/TCI.2016.2519261.
27. Y. Bao, & T. K. Gaylord, "Clarification and unification of the obliquity factor in diffraction and scattering theories: discussion," *JOSA A* 34, 1738-1745 (2017).
28. A. Sharma, & A. Agrawal, "New method for nonparaxial beam propagation," *JOSA A* 21, 1082-1087 (2004).
29. A. Sharma, & A. Agrawal, "Non-paraxial split-step finite-difference method for beam propagation," *Optical and quantum electronics* 38, 19-34 (2006).
30. J. Lim, A. B. Ayoub, E. E. Antoine, and D. Psaltis, "High-fidelity optical diffraction tomography of multiple scattering samples," *Light: Science & Applications*, vol. 8, p. 82, 2019/09/11 2019.
31. E. Wolf, "Determination of the amplitude and the phase of scattered fields by holography," *J. Opt. Soc. Am.* 60, 18-20 (1970).
32. Florian Charrière, Anca Marian, Frédéric Montfort, Jonas Kuehn, Tristan Colomb, Etienne Cuche, Pierre Marquet, and Christian Depeursinge, "Cell refractive index tomography by digital holographic microscopy," *Opt. Lett.* 31, 178-180 (2006)
33. F. Merola, P. Memmolo, L. Miccio, R. Savoia, M. Mugnano, A. Fontana, G. D'Ippolito, A. Sardo, A. Iolascon, A. Gambale, and P. Ferraro, "Tomographic flow cytometry by digital holography," *Light: Science & Applications*, vol. 6, p. e16241, 2017.
34. K. Lee, K. Kim, J. Jung, J. Heo, S. Cho, S. Lee, G. Chang, Y. Jo, H. Park, and Y. Park, "Quantitative phase imaging techniques for the study of cell pathophysiology: From principles to applications," *Sensors*, vol. 13, no. 4, pp. 4170– 4191, 2013.
35. A. J. Devaney, "Mathematical Foundations of Imaging and Tomography and Wavefield Inversion," Cambridge Univ. Press, 2012.
36. O. Haeberle, K. Belkebir, H. Giovaninni, and A. Sentenac, "Tomographic diffractive microscopy: basics, techniques and perspectives," *Journal of Modern Optics* 57(9), 686-699 (2010).
37. Y. Sung, W. Choi, N. Lue, R. R. Dasari, and Z. Yaqoob, "Stain-free quantification of chromosomes in live cells using regularized tomographic phase microscopy," *Plos One* 7(11), e49502 (2012).
38. J. Radon, "Über die bestimmung von funktionen durch ihre integralwerte langs gewisser mannigfaltigkeiten," *Berichte der Sächsischen Akadamie der Wissenschaft*, vol. 69, pp. 262-277, 1917
39. D. Huang, et al. "Optical coherence tomography," *Science* 254(5035), 1178- 1181 (1991).
40. T. S. Ralston, D. L. Marks, P. S. Carney, and S. A. Boppart, "Real-time interferometric synthetic aperture microscopy," *Optics Express* 16(4), 2555-2569 (2008).
41. G. Popescu, "Quantitative Phase Imaging of Cells and Tissues," (McGraw Hill, 2011).
42. F. Zernike, "Phase contrast, a new method for the microscopic observation of transparent objects, Part 1," *Physica* 9(7), 686-698 (1942).
43. M. Mir, et al. "Visualizing Escherichia coli Sub-Cellular Structure Using Sparse Deconvolution Spatial Light Interference Tomography," *PLoS ONE* 7(6), e39816 (2012)
44. T. Kim, et al. "White-light diffraction tomography of unlabelled live cells," *Nat Photon* 8(3), 256-263 (2014).
45. H. F. Ding, Z. Wang, F. Nguyen, S. A. Boppart, and G. Popescu, "Fourier Transform Light Scattering of Inhomogeneous and Dynamic Structures," *Physical Review Letters* 101(23), 238102 (2008).

References

46. J. Kostencka, T. Kozacki, A. Kuś, B. Kemper, and M. Kujawińska, "Holographic tomography with scanning of illumination: space-domain reconstruction for spatially invariant accuracy," *Biomed. Opt. Express* 7, 4086-4101 (2016).
47. Y. J. Sung, et al. "Optical diffraction tomography for high resolution live cell imaging," *Opt Express* 17(1), 266-277 (2009).
48. J. Yoon, K. Kim, H. Park, C. Choi, S. Jang, Y. Park, "Label-free characterization of white blood cells by measuring 3D refractive index maps," *Biomed Opt Express*;6(10):3865–75, 2015.
49. Y. Kim, H. Shim, K. Kim, H. Park, S. Jang, Y. Park, "Profiling individual human red blood cells using common-path diffraction optical tomography," *Sci Rep*;4:6659, 2014.
50. TH Nguyen, ME Kandel, M Rubessa, M.B. Wheeler, G. Popescu, "Gradient light interference microscopy for 3D imaging of unlabeled specimens," *Nat Commun*;8(1):210, 2017.
51. E. N. Leith, & J. Upatnieks, "Holographic imagery through diffusing media," *J. Opt. Soc. Am. A* 56, 523–523 (1966).
52. Z. Yaqoob, D. Psaltis, M. Feld, & C. Yang, "Optical phase conjugation for turbidity suppression in biological samples," *Nature photonics* 2, 110 (2008).
53. M. Cui, & C. Yang, "Implementation of a digital optical phase conjugation system and its application to study the robustness of turbidity suppression by phase conjugation," *Optics Express* 18, 3444–3455 (2010).
54. C. L. Hsieh, Y. Pu, R. Grange, G. Laporte & D. Psaltis, "Imaging through turbid layers by scanning the phase conjugated second harmonic radiation from a nanoparticle," *Optics Express* 18, 20723–20731 (2010).
55. D. Tajik, A. D. Pitcher, and N. K. Nikolova, "Comparative Study of the Rytov and Born Approximations in Quantitative Microwave Holography," *Progress In Electromagnetics Research B*, Vol. 79, 1-19, 2017. doi:10.2528/PIERB17081003
56. D. Tajik, D. S. Shumakov and N. K. Nikolova, "An experimental comparison between the born and Rytov approximations in microwave tissue imaging," 2017 IEEE MTT-S International Microwave Symposium (IMS), Honolulu, HI, 2017, pp. 1391-1393. doi: 10.1109/MWSYM.2017.8058875
57. Joowon Lim, Alexandre Goy, Morteza H. Shoreh, Michael Unser, and Demetri Psaltis, "Learning Tomography Assessed Using Mie Theory", *Phys. Rev. Applied* 9, 034027 (2018).
58. M. H. Shoreh, A. Goy, J. Lim, U. Kamilov, M. Unser and D. Psaltis, "Optical Tomography based on a nonlinear model that handles multiple scattering," 2017 IEEE International Conference on Acoustics, Speech and Signal Processing (ICASSP), New Orleans, LA, 2017, pp. 6220-6224.
59. H. Liu, D. Liu, H. Mansour, P. T. Boufounos, L. Waller and U. S. Kamilov, "SEAGLE: Sparsity-Driven Image Reconstruction Under Multiple Scattering," in *IEEE Transactions on Computational Imaging*, vol. 4, no. 1, pp. 73-86, March 2018.
60. Emmanuel Soubies, Thanh-An Pham, and Michael Unser, "Efficient inversion of multiple-scattering model for optical diffraction tomography," *Opt. Express* 25, 21786-21800 (2017).
61. H. A. van der Vorst, "Bi-CGSTAB: A Fast and Smoothly Converging Variant of Bi-CG for the Solution of Nonsymmetric Linear Systems," *SIAM Journal on Scientific and Statistical Computing*, vol. 13, no. 2, pp. 631-644, 1992.
62. K. Haseda, K. KAnematcu, K. Noguchi, H. Saito, N. Umeda and Y. Ohta, "Significant correlation between refractive index and activity of mitochondria: single mitochondrion study," *Biomedical Optics Express*, 6(3), pp. 859-869, (2015).
63. J. D. Wilson, W. J. Cottrell and T. H. Foster, "Index-of-refraction-dependent subcellular light scattering observed with organelle-specific dyes," *Journal of Biomedical Optics*, 12(1), pp. 014010-014010, (2007).
64. J. A. Valkenburg and C. L. Woldringh, "Phase separation between nucleoid and cytoplasm in *Escherichia coli* as defined by immersive refractometry," *Journal of Bacteriology*, 160(3), pp. 1151-1157, (1984).
65. J. Van Roey, J. van der Donk, and P. E. Lagasse, "Beam-propagation method: analysis and assessment," *J. Opt. Soc. Am.* 71, 803-810 (1981).

References

66. T. Kim, R. Zhou, L. L. Goddard, and G. Popescu, "Solving inverse scattering problems in biological samples by quantitative phase imaging," *Laser & Photonics Reviews*, vol. 10, pp. 13-39, 2016/01/01 2016.
67. S. Shin, K. Kim, J. Yoon, and Y. Park, "Active illumination using a digital micromirror device for quantitative phase imaging," *Optics Letters*, vol. 40, pp. 5407-5410, 2015/11/15 2015.
68. K. L. Cooper, S. Oh, Y. Sung, R. R. Dasari, M. W. Kirschner, and C. J. Tabin, "Multiple phases of chondrocyte enlargement underlie differences in skeletal proportions," *Nature*, vol. 495, pp. 375-378, 2013/03/01 2013.
69. M. Beleggia, M. A. Schofield, V. V. Volkov, and Y. Zhu, "On the transport of intensity technique for phase retrieval," *Ultramicroscopy*, vol. 102, pp. 37-49, 2004/12/01/ 2004.
70. G.-z. Yang, B.-z. Dong, B.-y. Gu, J.-y. Zhuang, and O. K. Ersoy, "Gerchberg–Saxton and Yang–Gu algorithms for phase retrieval in a nonunitary transform system: a comparison," *Applied Optics*, vol. 33, pp. 209-218, 1994/01/10 1994.
71. M. H. Maleki and A. J. Devaney, "Phase-retrieval and intensity-only reconstruction algorithms for optical diffraction tomography," *Journal of the Optical Society of America A*, vol. 10, pp. 1086-1092, 1993/05/01 1993.
72. M. H. Maleki, A. J. Devaney, and A. Schatzberg, "Tomographic reconstruction from optical scattered intensities," *Journal of the Optical Society of America A*, vol. 9, pp. 1356-1363, 1992/08/01 1992.
73. A. Matlock, A. Sentenac, P. C. Chaumet, J. Yi, and L. Tian, "Inverse scattering for reflection intensity phase microscopy," *Biomedical Optics Express*, vol. 11, pp. 911-926, 2020/02/01 2020.
74. A. Matlock and L. Tian, "High-throughput, volumetric quantitative phase imaging with multiplexed intensity diffraction tomography," *Biomedical optics express*, vol. 10, pp. 6432-6448, 2019.
75. J. Li, A. Matlock, Y. Li, Q. Chen, C. Zuo, L. Tian, "High-speed in vitro intensity diffraction tomography," *Adv. Photonics*, vol. 1, pp. 066004, 28/12/2019 2019.
76. U. S. Kamilov, I. N. Papadopoulos, M. H. Shoreh, A. Goy, C. Vonesch, M. Unser, and D. Psaltis , "Learning approach to optical tomography," *Optica*, vol. 2, pp. 517-522, 2015/06/20 2015.
77. J. Lim, K. Lee, K. H. Jin, S. Shin, S. Lee, Y. Park, J. C. Ye, "Comparative study of iterative reconstruction algorithms for missing cone problems in optical diffraction tomography," *Optics Express*, vol. 23, pp. 16933-16948, 2015/06/29 2015.
78. L. Tian and L. Waller, "3D intensity and phase imaging from light field measurements in an LED array microscope," *Optica*, vol. 2, pp. 104-111, 2015/02/20 2015.
79. R. Horstmeyer, J. Chung, X. Ou, G. Zheng, and C. Yang, "Diffraction tomography with Fourier ptychography," *Optica*, vol. 3, pp. 827-835, 2016/08/20 2016.
80. T.-A. Pham, E. Soubies, A. Goy, J. Lim, F. Soulez, D. Psaltis, and M. Unser , "Versatile reconstruction framework for diffraction tomography with intensity measurements and multiple scattering," *Optics Express*, vol. 26, pp. 2749-2763, 2018/02/05 2018.
81. S. Chowdhury, M. Chen, R. Eckert, D. Ren, F. Wu, N. Repina, and L. Waller, "High-resolution 3D refractive index microscopy of multiple-scattering samples from intensity images," *Optica*, vol. 6, pp. 1211-1219, 2019/09/20 2019.
82. Ruilong Ling, Waleed Tahir, Hsing-Ying Lin, Hakho Lee, and Lei Tian, "High-throughput intensity diffraction tomography with a computational microscope," *Biomed. Opt. Express* 9, 2130-2141 (2018).
83. D. Gabor and W. L. Bragg, "Microscopy by reconstructed wave-fronts," *Proceedings of the Royal Society of London. Series A. Mathematical and Physical Sciences*, vol. 197, pp. 454-487, 1949/07/07 1949.
84. A. B. Ayoub, T.-A. Pham, J. Lim, M. Unser, D. Psaltis, "A method for assessing the fidelity of optical diffraction tomography reconstruction methods using structured illumination," *Opt. Commun.*, 454 124486 (2020).
85. W. Zhou, A. C. Bovik, H. R. Sheikh, and E. P. Simoncelli. "Image Qualify Assessment: From Error Visibility to Structural Similarity." *IEEE Transactions on Image Processing*. Vol. 13, Issue 4, April 2004, pp. 600–612.
86. T. Thomsen, A.B. Ayoub, D. Psaltis , and H.A. Klok, "Fluorescence-based and Fluorescent label-free Characterization of Polymer Nanoparticle Decorated T cells," *Biomacromolecules* (2020). Advance online publication. <https://doi.org/10.1021/acs.biomac.0c00969>

References

87. Lei Tian, Jingyan Wang, and Laura Waller, "3D differential phase-contrast microscopy with computational illumination using an LED array," *Opt. Lett.* 39, 1326-1329 (2014).
88. Lei Tian and Laura Waller, "Quantitative differential phase contrast imaging in an LED array microscope," *Opt. Express* 23, 11394-11403 (2015).
89. Lei Tian, Ziji Liu, Li-Hao Yeh, Michael Chen, Jingshan Zhong, and Laura Waller, "Computational illumination for high-speed in vitro Fourier ptychographic microscopy," *Optica* 2, 904-911 (2015).
90. Jiaji Li, Alex Matlock, Yunzhe Li, Qian Chen, Lei Tian, and Chao Zuo, "Resolution-enhanced intensity diffraction tomography in high numerical aperture label-free microscopy," *Photon. Res.* 8, 1818-1826 (2020)
91. Renhao Liu, Yu Sun, Jiabei Zhu, Lei Tian, Ulugbek Kamilov, "Zero-Shot Learning of Continuous 3D Refractive Index Maps from Discrete Intensity-Only Measurements," arxiv 2021.
92. A. Matlock, Y. Xue, Y. Li, S. Cheng, W. Tahir and L. Tian, "Model and learning-based computational 3D phase microscopy with intensity diffraction tomography," 2020 28th European Signal Processing Conference (EUSIPCO), 2021, pp. 760-764, doi: 10.23919/Eusipco47968.2020.9287407.
93. Ahmed B. Ayoub, Joowon Lim, Elizabeth E. Antoine, and Demetri Psaltis, "3D reconstruction of weakly scattering objects from 2D intensity-only measurements using the Wolf transform," *Opt. Express* 29, 3976-3984 (2021)
94. R. Eckert, Z. F. Phillips, and L. Waller, "Efficient illumination angle self-calibration in Fourier ptychography," *Appl. Opt.* 57(19), 5434-5442 (2018).
95. Christopher G. Rylander, Digant P. Davé, Taner Akkin, Thomas E. Milner, Kenneth R. Diller, and Ashley J. Welch, "Quantitative phase-contrast imaging of cells with phase-sensitive optical coherence microscopy," *Opt. Lett.* 29, 1509-1511 (2004)
96. Wonchan Lee, Daeseong Jung, Chulmin Joo, "Single-exposure quantitative phase imaging in color-coded LED microscopy (Conference Presentation)," *Proc. SPIE* 10074, Quantitative Phase Imaging III, 1007408 (24 April 2017); <https://doi.org/10.1117/12.2251746>
97. Poorya Hosseini, Yongjin Sung, Youngwoon Choi, Niyom Lue, Zahid Yaqoob, and Peter So, "Scanning color optical tomography (SCOT)," *Opt. Express* 23, 19752-19762 (2015).
98. I. M. Vellekoop, A. Lagendijk, and A. P. Mosk, "Exploiting disorder for perfect focusing," *Nat. Photonics* 4, 320-322 (2010).
99. H. Yilmaz, W. L. Vos, and A. P. Mosk, "Optimal control of light propagation through multiple-scattering media in the presence of noise," *Biomed. Opt. Express* 4, 1759-1768 (2013).
100. S. Popoff, G. Lerosey, M. Fink, A. C. Boccara, and S. Gigan, "Image transmission through an opaque material," *Nat. Commun.* 1, 81 (2010).
101. T. Chaigne, O. Katz, A. C. Boccara, M. Fink, E. Bossy, and S. Gigan, "Controlling light in scattering media noninvasively using the photoacoustic transmission matrix," *Nat. Photonics* 8, 58-64 (2014).
102. J. Yoon, K. Lee, J. Park, and Y. Park, "Measuring optical transmission matrices by wavefront shaping," *Opt. Express* 23, 10158-10167 (2015).
103. I. N. Papadopoulos, S. Farahi, C. Moser, and D. Psaltis, "Focusing and scanning light through a multimode optical fiber using digital phase conjugation," *Opt. Express* 20, 10583-10590 (2012).
104. C. L. Hsieh, Y. Pu, R. Grange, and D. Psaltis, "Digital phase conjugation of second harmonic radiation emitted by nanoparticles in turbid media," *Opt. Express* 18, 12283-12290 (2010).
105. Y. X. Ren, R. D. Lu, and L. Gong, "Tailoring light with a digital micromirror device," *ANNALEN DER PHYSIK*, 527: 447-470 (2015).
106. D. Akbulut, T. J. Huisman, E. G. van Putten, W. L. Vos, and A. P. Mosk, "Focusing light through random photonic media by binary amplitude modulation," *Opt. Express* 19, 4017-4029 (2011).
107. K. Nam, and J. H. Park, "Increasing the enhancement factor for DMD-based wavefront shaping," *Opt. Lett.* 45, 3381-3384 (2020)
108. A. Turpin, I. Vishniakou, and J. D. Seelig, "Light scattering control in transmission and reflection with neural networks," *Opt. Express* 26, 30911-30929 (2018)
109. T. Zhao, S. Ourselin, T. Vercauteren, and W. Xia, "Focusing light through multimode fibres using a digital micromirror device: a comparison study of non-holographic approaches," *Opt. Express* 29, 14269-14281 (2021).

References

110. S. Bianchi, and R. Di Leonardo, "A multi-mode fiber probe for holographic micromanipulation and microscopy," *Lab Chip* 12(3), 635–639 (2012).
111. S. Turtaev, I. T. Leite, K. J. Mitchell, M. J. Padgett, D. B. Phillips, and T. Čižmár, "Comparison of nematic liquid-crystal and DMD based spatial light modulation in complex photonics," *Opt. Express* 25, 29874-29884 (2017).
112. D. B. Conkey, A. M. Caravaca-Aguirre, and R. Piestun, "High-speed scattering medium characterization with application to focusing light through turbid media," *Opt. Express* 20, 1733–1740 (2012).
113. W. H. Lee, "Binary computer-generated holograms," *Appl. Opt.* 18, 3661-3669 (1979).
114. S. A. Goorden, J. Bertolotti, and A. P. Mosk, "Superpixel-based spatial amplitude and phase modulation using a digital micromirror device," *Opt. Express* 22, 17999-18009 (2014).
115. A. Drémeau, et al., "Reference-less measurement of the transmission matrix of a highly scattering material using a DMD and phase retrieval techniques," *Opt. Express* 23, 11898-11911 (2015).
116. A. Drémeau, and F. Krzakala, "Phase recovery from a bayesian point of view: the variational approach," *Proceedings of IEEE Trans. Acoust. Speech Signal Process.* (2015).
117. D. Wang, et al., "Focusing through dynamic tissue with millisecond digital optical phase conjugation," *Optica* 2, 728–735 (2015).
118. Y. X. Ren, et al., "Experimental generation of Laguerre-Gaussian beam using digital micromirror device," *Appl. Opt.* 49, 1838-1844 (2010)
119. L. Gong, et al., "Generation of nondiffracting Bessel beam using digital micromirror device," *Appl. Opt.* 52, 4566-4575 (2013).
120. A. A. Adeyemi, N. Barakat, and T. E. Darcie, "Applications of digital micro-mirror devices to digital optical microscope dynamic range enhancement," *Opt. Express* 17, 1831-1843 (2009).
121. X. Ding, Y. Ren, & R. Lu, "Shaping super-Gaussian beam through digital micro-mirror device," *Sci. China Phys. Mech. Astron.* 58, 1–6 (2015).
122. D. Jin, R. Zhou, Z. Yaqoob, and P. T. C. So, "Tomographic phase microscopy: principles and applications in bioimaging," *J. Opt. Soc. Am. B* 34, B64-B77 (2017).
123. K. Lee, K. Kim, G. Kim, S. Shin, and Y. K. Park, "Time-multiplexed structured illumination using a DMD for optical diffraction tomography," *Opt. Lett.* 42, 999-1002 (2017).
124. M. C. Park, B. R. Lee, J. Y. Son, and O. Chernyshov, "Properties of DMDs for holographic displays," *Journal of Modern Optics*, 62:19, 1600-1607 (2015), DOI: 10.1080/09500340.2015.1054445
125. J. W. Pan, and H. H. Wang, "High contrast ratio prism design in a mini projector," *Appl. Opt.* 52, 8347-8354 (2013)
126. J. W. Pan, C. M. Wang, W. S. Sun, and J. Y. Chang, "Portable digital micromirror device projector using a prism," *Appl. Opt.* 46, 5097-5102 (2007)
127. Texas Instruments Incorporated, DLP7000, DOI: <https://www.ti.com/product/DLP7000>
128. Yoon, J. et al. Label-free characterization of white blood cells by measuring 3D refractive index maps. *Biomed. Opt. Express* 6, 3865–3875 (2015).
129. Park, Y. et al. Refractive index maps and membrane dynamics of human red blood cells parasitized by *Plasmodium falciparum*. *Proc. Natl Acad. Sci. USA* 105, 13730–13735 (2008).
130. K. Kim, et al., "Three-dimensional label-free imaging and quantification of lipid droplets in live hepatocytes," *Sci. Rep.* 6, 36815 (2016).
131. K. Kim, et al., "Optical diffraction tomography techniques for the study of cell pathophysiology," *J. Biomed. Photonics Eng.* 2, 020201 (2016).
132. Y. Park, C. Depeursinge, & G. Popescu, "Quantitative phase imaging in biomedicine," *Nat. Photonics* 12, 578–589 (2018).
133. G. Mie, "Beiträge zur Optik trüber Medien, speziell kolloidaler Metallösungen," *Ann. der Phys.* 330, 377–445 (1908).
134. M.A. Yurkin, & A. G. Hoekstra, "The discrete-dipole-approximation code ADDA: capabilities and known limitations," *J. Quant. Spectrosc. Radiat. Transf.* 112, 2234–2247 (2011).
135. M. A. Yurkin, et al., "Systematic comparison of the discrete dipole approximation and the finite difference time domain method for large dielectric scatterers," *Opt. Express* 15, 17902–17911 (2007).

References

136. Y. Kaganovsky, et al., “Compressed sampling strategies for tomography,” *J. Opt. Soc. Am. A* 31, 1369–1394 (2014).
137. D. J. Brady, et al., “Compressive tomography,” *Adv. Opt. Photonics* 7, 756–813 (2015).
138. A. Beck, & M. Teboulle, “Fast gradient-based algorithms for constrained total variation image denoising and deblurring problems,” *IEEE Trans. Image Process.* 18, 2419–2434 (2009).
139. A. Beck, & M. Teboulle, “A fast iterative shrinkage-thresholding algorithm for linear inverse problems,” *SIAM J. Imaging Sci.* 2, 183–202 (2009).
140. P. Müller, M. Schürmann, & J. Guck, “ODTbrain: a Python library for full-view, dense diffraction tomography,” *BMC Bioinforma.* 16, 367 (2015).
141. Z. Wang, et al., “Image quality assessment: from error visibility to structural similarity,” *IEEE Trans. Image Process.* 13, 600–612 (2004).
142. J. Schäfer, S. C. Lee, & A. Kienle, “Calculation of the near fields for the scattering of electromagnetic waves by multiple infinite cylinders at perpendicular incidence,” *J. Quant. Spectrosc. Radiat. Transf.* 113, 2113–2123 (2012).
143. S. D’Agostino, et al., “Enhanced fluorescence by metal nanospheres on metal substrates,” *Opt. Lett.* 34, 2381–2383 (2009).
144. M. A. Yurkin, et al., “Discrete dipole simulations of light scattering by blood cells,” (Universiteit van Amsterdam, 2007).
145. P. W. Kuchel, & E. D. Fackrell, “Parametric-equation representation of biconcave erythrocytes,” *Bull. Math. Biol.* 61, 209–220 (1999).
146. D. Bhattacharya, & A. Sharma, “Split step non-paraxial finite difference method for 3D scalar wave propagation,” *Opt. Quantum Electron.* 39, 865–876 (2007).
147. Y. Sung and R. R. Dasari, “Deterministic regularization of three-dimensional optical diffraction tomography,” *J. Opt. Soc. Am. A*, 28 (8), 1554–1561 (2011). <https://doi.org/10.1364/JOSAA.28.001554>
148. Y. Rivenson et al., “Deep learning microscopy,” *Optica*, 4 (11), 1437–1443 (2017). <https://doi.org/10.1364/OPTICA.4.001437>
149. A. Sinha et al., “Lensless computational imaging through deep learning,” *Optica*, 4 (9), 1117–1125 (2017). <https://doi.org/10.1364/OPTICA.4.001117>
150. Y. Rivenson et al., “Phase recovery and holographic image reconstruction using deep learning in neural networks,” *Light: Sci. Appl.*, 7 (2), 17141 (2018). <https://doi.org/10.1038/lsa.2017.141>
151. Y. Rivenson et al., “Virtual histological staining of unlabelled tissue-autofluorescence images via deep learning,” *Nat. Biomed. Eng.*, 3 (6), 466–477 (2019). <https://doi.org/10.1038/s41551-019-0362-y>
152. N. Borhani et al., “Digital staining through the application of deep neural networks to multi-modal multi-photon microscopy,” *Biomed. Opt. Express*, 10 (3), 1339–1350 (2019). <https://doi.org/10.1364/BOE.10.001339> [BOEICL 2156-7085](https://doi.org/10.1364/BOE.10.001339)
153. Y. Jo et al., “Holographic deep learning for rapid optical screening of anthrax spores,” *Sci. Adv.*, 3 (8), e1700606 (2017). <https://doi.org/10.1126/sciadv.1700606> [STAMCV 1468-6996](https://doi.org/10.1126/sciadv.1700606)
154. J. Yoon et al., “Identification of non-activated lymphocytes using three-dimensional refractive index tomography and machine learning,” *Sci. Rep.*, 7 (1), 6654 (2017). <https://doi.org/10.1038/s41598-017-06311-y> [SRCEC3 2045-2322](https://doi.org/10.1038/s41598-017-06311-y)
155. J. Lee et al., “Deep-learning-based label-free segmentation of cell nuclei in time-lapse refractive index tomograms,” *IEEE Access*, 7, 83449–83460 (2019). <https://doi.org/10.1109/ACCESS.2019.2924255>
156. Y. Jo et al., “Quantitative phase imaging and artificial intelligence: a review,” *IEEE J. Sel. Top. Quantum Electron.*, 25 (1), 6800914 (2018). <https://doi.org/10.1109/JSTQE.2018.2859234> [IJSQEN 1077-260X](https://doi.org/10.1109/JSTQE.2018.2859234)
157. J. Yoo et al., “Deep learning diffuse optical tomography,” *IEEE Trans. Med. Imaging*, (2019). <https://doi.org/10.1109/TMI.2019.2936522> [ITMID4 0278-0062](https://doi.org/10.1109/TMI.2019.2936522)
158. Y. Sun, Z. Xia and U. S. Kamilov, “Efficient and accurate inversion of multiple scattering with deep learning,” *Opt. Express*, 26 (11), 14678–14688 (2018). <https://doi.org/10.1364/OE.26.014678> [OPEXFF 1094-4087](https://doi.org/10.1364/OE.26.014678)

References

159. T. C. Nguyen, V. Bui and G. Nehmetallah, “Computational optical tomography using 3-D deep convolutional neural networks,” *Opt. Eng.*, 57 (4), 043111 (2018). <https://doi.org/10.1117/1.OE.57.4.043111>
160. A. Goy et al., “High-resolution limited-angle phase tomography of dense layered objects using deep neural networks,” *Proc. Natl. Acad. Sci. U. S. A.*, 116 (40), 19848 –19856 (2019). <https://doi.org/10.1073/pnas.1821378116>
161. O. Ronneberger, P. Fischer and T. Brox, “U-Net: convolutional networks for biomedical image segmentation,” *Lect. Notes Comput. Sci.*, 9351 234 –241 (2015). https://doi.org/10.1007/978-3-319-24574-4_28
162. K. H. Jin et al., “Deep convolutional neural network for inverse problems in imaging,” *IEEE Trans. Image Process.*, 26 (9), 4509 –4522 (2017). <https://doi.org/10.1109/TIP.2017.2713099> IIPRE4 1057-7149
163. D. P. Kingma and J. Ba, “Adam: a method for stochastic optimization,” (2014).
164. T. Salimans and D. P. Kingma, “Weight normalization: a simple reparameterization to accelerate training of deep neural networks,” in *Adv. Neural Inf. Process. Syst.*, 901 –909 (2016).
165. J. L. Ba, J. R. Kiros and G. E. Hinton, “Layer normalization,” (2016).
166. I. Udriou, “Estimation of erythrocyte surface area in mammals,” (2014).
167. K. Namdee et al., “Effect of variation in hemorheology between human and animal blood on the binding efficacy of vascular-targeted carriers,” *Sci. Rep.*, 5 11631 (2015). <https://doi.org/10.1038/srep11631> SRCEC3 2045-2322
168. N. Otsu, “A threshold selection method from gray-level histograms,” *IEEE Trans. Syst. Man Cybern.*, 9 (1), 62 –66 (1979). <https://doi.org/10.1109/TSMC.1979.4310076>

Curriculum Vitae

Ahmed Bassam Ayoub

Chemin des Clos 6a, 1020 Renens VD, Switzerland

<mailto:ahmed.ayoub@epfl.ch> • (+41) 795-914-941 • [GoogleScholar](#)

EDUCATION

École polytechnique fédérale de Lausanne (EPFL), Lausanne, Vaud, Switzerland

- Ph.D. in Electrical Engineering Sep 2017 – Feb 2022
- Thesis: Advanced techniques in optical diffraction tomography

American University in Cairo (AUC), Cairo, Egypt

- M.S. in Physics Sep 2014 – Aug 2017
- Thesis: NanoPhotonic structures for biosensing applications

Alexandria University, Alexandria, Egypt

- B.S. in Electrical Engineering Sep 2008 – Jun 2013

RESEARCH EXPERIENCE

Laboratory of Optics (LO) -EPFL

- Spatial and Wavelength Diversity Optical Diffraction Tomography (ODT) Sep 2017 – now

My Role was the implementation of different optical setups for 3D reconstruction of different samples and especially biological samples. During the Ph.D., I built 2 optical setup with different imaging modalities. The first setup was used to perform 3D imaging in transmission configuration. In this setup spatial light modulator was used for angular scanning rather than the Galvo-mirrors to achieve better stability. In addition we employed a direct inversion model using intensity-only measurements in transmission to localize nano-particles and/or lipids inside cells. During the course of my study, I get to know more about sample preparation techniques, cell culture protocols for different biological cell lines, and fixation protocols for biological tissues.

InnoSuisse Project - TomoHoloK

- Tomographic Reconstruction and Mechanical Development Sep 2019 – now

In a project funded by InnoSuisse funding agency, we aimed at the design of a 3D tomographic imaging optical setup for imaging thick samples up to few hundreds of micrometers. My role was involved at two parts within the project. The first part was involved with the tomographic reconstruction and data acquisition of holographic images. My primary role was to acquire test data library with high angle/resolution. In the second part, I was involved in the process of designing fabricating microscope body with immersion stage compatible with conventional sample dishes.

NanoPhotonics Research Laboratory (NRL) - American University in Cairo (AUC)

- Photonic and Plasmonic Structures for Optical Sensing and Modulation Sep 2014 – Aug 2017

My research work was concerned with different projects related to sensing, modulation, demultiplexing, and computational techniques. In those projects, the light interaction with semiconductors and metallic structures was investigated. We aimed to find the best performance for each application in terms of maximum transmitted signal, and other key parameters depending on the application. In addition, I worked on different characterization techniques for samples

References

(i.e. Nanowires, nanotubes, wave-guides, etc.) by utilizing different technologies including scanning electron microscopy (SEM), and Raman spectroscopy.

TEACHING EXPERIENCE

École polytechnique fédérale de Lausanne (EPFL)

Biomedical Optics (Master's Level)

Sep 2020 – Dec 2020

Leading a one-hour exercise session to help master students get involved more into the course by solving problems.

American University in Cairo (AUC)

Mathematical Physics (Master's Level)

Sep 2016 – Dec 2016

Helping master's student to understand more the physical concept they have learned in the lecture sessions, help them in solving the exercise, and grading of the assignments and final exam.

Faculty of Engineering - Alexandria University

Digital Signal Processing (Bachelor Level)

Feb 2014 – Jun 2014

My role in that course included preparation of the assignments, exercise sessions, and grading of assignments and final exam.

AWARDS & SCHOLARSHIPS

■ Graduate Fellowship, AUC, Egypt

Sep 2014 – Aug 2017

Full Tuition coverage

■ Graduate Supplemental Fellowship, Misr-ElKheir Foundation, Egypt

Sep 2015 – Aug 2017

For Outstanding research work done through the master's degree

PROFESSIONAL AFFILIATIONS & ACTIVITIES

Optical Society of America (OSA)

■ Member

2019 – Present

CAMPUS ACTIVITIES

The International Society for Optics and Photonics (SPIE), AUC Student Branch, Egypt

■ President

Sep 2016 – Aug 2017

Institute of Electrical and Electronics Engineers (IEEE), Young Professionals, Egypt Section

■ Contents Team Lead

Sep 2014 – Sep 2015

Institute of Electrical and Electronics Engineers (IEEE), Alexandria Student Branch, Egypt

■ Reporting and Publications Team Lead

Sep 2012 – Jun 2013

LANGUAGES

■ Arabic (Native language), English (Proficient), French (Elementary)

SKILLS

Optics: Holography, microscopy, 3D imaging, spatial light modulation, metrology.

Biology: Cell Culture, Sample Preparation and Fixation Protocols, histology slides.

Materials: Raman spectroscopy, scanning electron microscopy, UV-VIS spectroscopy, ellipsometry.

Computer skills: Microsoft Office, MATLAB, Python, Lumerical, OptiFDTD, Adobe Illustrator.

INTERESTS

Running, Photography, Reading.

References

PUBLICATIONS

JOURNALS

- **Ahmed B. Ayoub**, Abhijit Roy, and D. Psaltis, “Optical Diffraction Tomography Using Nearly In-Line Holography with a Broadband LED Source,” MDPI Applied Sciences, Jan 2022.
- **Ahmed B. Ayoub**, and D. Psaltis, “High speed, complex wavefront shaping using the digital micro-mirror device,” Scientific Reports, Sep 2021.
- Amirhossein Saba, J. Lim, **Ahmed B. Ayoub**, Elizabeth E. Antoine, and D. Psaltis, “Polarization-sensitive optical diffraction tomography,” Optica, Mar 2021.
- **Ahmed B. Ayoub**, J. Lim, Elizabeth E. Antoine, and D. Psaltis, “3D reconstruction of weakly scattering objects from 2D intensity-only measurements using the Wolf transform,” Optics Express, Jan 2021.
- T. Thomson, **Ahmed B. Ayoub**, D. Psaltis, and H-A. Klok, “Fluorescence-based and Fluorescent label-free Characterization of Polymer Nanoparticle Decorated T cells,” ACS Biomacromolecules, Sep 2020.
- J. Lim, **Ahmed B. Ayoub** and D. Psaltis, “Three-dimensional tomography of red blood cells using deep learning,” Advanced Photonics, vol. 2, no. 2, pp. 026001, Mar 2020.
- T. Pham, E. Soubies, **Ahmed B. Ayoub**, J. Lim, D. Psaltis, and M. Unser, “Three-dimensional optical diffraction tomography with Lippmann-Schwinger model,” IEEE Transactions on Computational Imaging, vol. 6, pp. 727-738, Jan 2020.
- **Ahmed B. Ayoub**, T. Pham, J. Lim, M. Unser, and D. Psaltis, “A method for assessing the fidelity of optical diffraction tomography reconstruction methods using structured illumination,” Optics Communications, vol. 454, pp. 124486, Jan 2020.
- J. Lim, **Ahmed B. Ayoub**, Elizabeth E. Antoine, and D. Psaltis, “High-fidelity optical diffraction tomography of multiple scattering samples,” Light: Science and Applications, vol. 8, no. 1, pp. 1-12, Sep 2019.

CONFERENCES

- Amirhossein Saba, J. Lim, **Ahmed B. Ayoub**, Elizabeth E. Antoine, and D. Psaltis, “Tomographic diffraction microscopy of birefringence,” in Proceedings of OSA Digital Holography and Three-Dimensional Imaging, Jul 2021.
- **Ahmed B. Ayoub**, and D. Psaltis, “Complex field representation using digital micromirror device (DMD),” in Proceedings of SPIE Digital Optical Technologies Conference, Jun 2021.
- J. Lim, **Ahmed B. Ayoub**, and D. Psaltis, “Deep learning approach for solving the missing cone problem in optical diffraction tomography,” in Proceedings of Imaging and Applied Optics Congress, Washington DC, USA, Jun 2020.
- Elizabeth E. Antoine, J. Lim, **Ahmed B. Ayoub**, and D. Psaltis, “Optical Diffraction Tomography (ODT) for Label-Free Imaging of Large 3D Biological Samples,” in Proceedings of Imaging and Applied Optics Congress, Washington DC, USA, Jun 2020.
- T. Pham, E. Soubies, **Ahmed B. Ayoub**, J. Lim., D. Psaltis, and M. Unser, “Adaptive Regularization for Three-dimensional Optical Diffraction Tomography,” in Proceedings of IEEE 17th International Symposium on Biomedical Imaging, Iowa City, USA, Apr 2020.
- J. Lim, **Ahmed B. Ayoub**, Elizabeth E. Antoine, and D. Psaltis, “Learning tomography plus for highly scattering samples,” in Proceedings of Imaging and Applied Optics 2019 Conference Munich, Germany, Jun 2019.
- **Ahmed B. Ayoub**, J. Lim, Elizabeth E. Antoine, and D. Psaltis, “Optical Diffraction Tomography Based on a Spatial Light Modulator for Biological Imaging,” in Proceedings of Biophotonics Congress: Optics in the Life Sciences Congress 2019 Tucson, Arizona, USA, Apr 2019.